NASA Conference Publication 2046

Advanced Technology Airfoil Research

Volume II

Proceedings of a conference
held at Langley Research Center
Hampton, Virginia, March 7-9, 1978

NASA

NASA Conference Publication 2046

Advanced Technology Airfoil Research

Volume II

Proceedings of a conference
held at Langley Research Center
Hampton, Virginia, March 7-9, 1978

NASA

PREFACE

This NASA Conference Publication contains the proceedings of the NASA Conference on Advanced Technology Airfoil Research held at Langley Research Center on March 7-9, 1978, which have limited distribution. Conference cochairmen were Alfred Gessow, NASA Headquarters, and Robert F. Bower, Langley Research Center. Honorary cochairmen were Ira H. Abbott, NASA Headquarters (retired), and Richard T. Whitcomb, Langley Research Center.

The conference was planned to provide a comprehensive review of all NASA airfoil research, conducted both in-house and under grant and contract. In addition, a broad spectrum of airfoil research outside of NASA was reviewed. A total of 64 technical papers were presented at 12 sessions. Six workshops were also held to discuss progress, further immediate and long-range research needs, and important unresolved issues. A roundtable discussion summarized the technical sessions and workshops.

This volume contains papers presented at technical sessions covering the following subjects:

(1) Low- and Medium-Speed Applications
(2) Rotorcraft Airfoil Applications
(3) Other Airfoil Applications and Subjects

The major thrusts of the technical sessions were in three areas: development of computational aerodynamic codes for airfoil analysis and design, development of experimental facilities and test techniques, and all types of airfoil applications. The conference proceedings are presented in two volumes: Volume I is unclassified with unlimited distribution and Volume II is unclassified but with limited distribution.

The included papers are largely as submitted as camera-ready copy. Only minor editorial revisions have been made and a title page and abstract have been added.

Use of trade names or names of manufacturers in this report does not constitute an official endorsement of such products or manufacturers, either expressed or implied, by the National Aeronautics and Space Administration.

P. K. Pierpont, Conference Organizer

iii

CONTENTS

OTHER AIRFOIL APPLICATIONS AND SUBJECTS

Chairman: Bruce J. Holmes
NASA Langley Research Center

NASA LOW- AND MEDIUM-SPEED AIRFOIL DEVELOPMENT

Robert J. McGhee, William D. Beasley, and Richard T. Whitcomb
NASA Langley Research Center

SUMMARY

The status of NASA low- and medium-speed airfoil research, which was initiated in 1972 with the development of the GA(W)-1 airfoil and which has now emerged as a family of airfoils, is discussed. Effects of airfoil thickness-chord ratios varying from 9 percent to 21 percent on the section characteristics for a design lift coefficient of 0.40 are presented for the initial low-speed family of airfoils. Also, modifications to the 17-percent low-speed airfoil to reduce the pitching-moment coefficient and to the 21-percent low-speed airfoil to increase the lift-drag ratio are discussed. Representative wind-tunnel results are shown for two new medium-speed airfoils with thickness ratios of 13 percent and 17 percent and design lift coefficients of 0.30. These new airfoils were developed to increase the cruise Mach number of the low-speed airfoils while retaining good high-lift, low-speed characteristics. Applications of NASA-developed airfoils to general aviation aircraft are summarized.

INTRODUCTION

Research on advanced technology airfoils for low-speed general aviation applications has received considerable attention at Langley since the development of the GA(W)-1 airfoil in 1972. This airfoil was analytically developed using the subsonic viscous computer code of reference 1 which provided a low-cost analysis of the airfoil performance. References 2 and 3 report the experimental results for this airfoil and others derived from it, and references 4 to 6 report flap and control-surface results for several of these airfoils. Flight test results for the GA(W)-2 airfoil are reported in reference 7.

This research effort was initially generated to develop advanced airfoils for low-speed applications. Emphasis was placed on designing airfoils with largely turbulent boundary layers which had the following performance requirements: low cruise drag, high climb lift-drag ratios, high maximum lift, and predictable, docile stall behavior. However, in 1976 the need developed for airfoils with higher cruise Mach numbers than the low-speed airfoils provided, while retaining good high-lift, low-speed characteristics. Thus, two medium-speed airfoils were developed. These medium-speed airfoils are intended to fill the gap between the low-speed airfoils and the supercritical airfoils for application on light executive-type aircraft. In this paper the status of low- and medium-speed airfoil research is discussed and the applications of NASA-developed airfoils to general aviation aircraft are summarized.

c_p pressure coefficient

c airfoil chord

c_d section drag coefficient

c_l section lift coefficient

c_m section quarter-chord pitching-moment coefficient

l/d section lift-drag ratio

M Mach number

R Reynolds number

t airfoil thickness

x airfoil abscissa

α angle of attack

Subscripts:

d design

max maximum

SEP separation

T transition

AIRFOIL DESIGNATION

Sketches of the section shapes and airfoil designations for the low- and medium-speed airfoils are shown in figure 1. The airfoils are designated in the form LS(1)- or MS(1)-xxxx. LS(1) indicates low speed (first series) and MS(1) indicates medium speed (first series); the next two digits designate the airfoil design lift coefficient in tenths, and the last two digits are the airfoil thickness in percent chord. Thus, the GA(W)-1 airfoil becomes LS(1)-0417 and the GA(W)-2 airfoil becomes LS(1)-0413.

LOW-SPEED AIRFOILS

Initial Family

This initial family of low-speed airfoils was obtained by linearly scaling the mean thickness distribution of the 17-percent airfoil (LS(1)-0417).

2

Thus, all four airfoils have the same camber distribution and the design lift coefficient is 0.40. The effects of varying thickness-chord ratio from 9 to 21 percent on maximum lift coefficient and lift-drag ratio are shown in figure 2 for a Reynolds number of 4×10^6 with transition fixed near the leading edge of the airfoils. The maximum lift coefficient increases with thickness ratio up to a thickness ratio of about 13 percent; further increase in thickness ratio results in a decrease in maximum lift coefficient. For the 13-percent airfoil a value of maximum lift coefficient of about 1.9 is indicated. The lift-drag ratio decreases almost linearly with increasing thickness ratio over the entire thickness-ratio range at the design lift coefficient of 0.40. This decrease in lift-drag ratio is essentially a result of increased skin-friction drag because of the higher induced velocities for the thicker airfoils. However, at a typical climb lift coefficient of 1.0, this linear variation is indicated only up to a thickness ratio of about 17 percent. The large decrease in lift-drag ratio for the 21-percent airfoil is indicative of excessive turbulent boundary-layer separation. This effect has been reduced by redesign of the airfoil and is discussed later.

The scale effects on maximum lift coefficient for the low-speed airfoils for Reynolds numbers from about 2×10^6 to 9×10^6 are shown in figure 3. Increases in Reynolds number have a favorable effect on maximum lift coefficient for all thickness ratios shown. The increment in maximum lift coefficient with Reynolds number generally increases with increasing thickness ratio; however, note the differences in variation with Reynolds number. Application of a roughness strip just sufficient to trip the boundary layer resulted in only small effects on maximum lift coefficient for the 9- and 13-percent airfoils; however, large decreases occurred for the thicker airfoils.

Comparison of the maximum lift coefficients for this low-speed family with the older NACA airfoils is shown in figure 4 at a Reynolds number of 6×10^6 for the airfoils smooth. The comparison is made with the airfoils smooth because of the excessive roughness employed on the NACA airfoils. The largest value of $c_{l,max}$, 1.75, for the NACA airfoils was obtained for the forward-camber 230 airfoil series for a thickness ratio of 12 percent, which is probably the optimum thickness ratio. By contrast a value of $c_{l,max}$ greater than 2 is shown for the NASA low-speed series for a thickness ratio of 13 percent. Large improvements in $c_{l,max}$ performance for thickness ratios varying from 9 percent to 21 percent are shown for the NASA low-speed airfoils compared with the older NACA airfoils.

Refinements

21-percent-thick airfoil.- As previously discussed, the 21-percent airfoil displayed significantly lower values of lift-drag ratio compared to the thinner airfoils of the family because of turbulent boundary-layer separation at typical climb lift coefficients. Therefore, this thick airfoil has been reshaped to substantially decrease the upper-surface adverse pressure gradient and reduce the amount of separation on the airfoil. The changes in airfoil contour and pressure distribution are illustrated in figure 5. A theoretical analysis code with improved turbulent boundary-layer separation predictions (ref. 8) was used for the redesign of the airfoil. Note that the

start of the upper-surface pressure recovery was moved forward about 0.30c for the modified airfoil. At a lift coefficient of 0.40 the theory indicates a decrease in the extent of upper-surface separation of about 0.05c for the modified airfoil. Comparison of calculated and experimental pressure data indicate good agreement between experiment and theory for the modified airfoil. The experimental results were obtained in the Langley low-turbulence pressure tunnel.

Figure 6 compares lift-drag-ratio performance for the two airfoils for Reynolds numbers from 2×10^6 to 9×10^6. At the design lift coefficient of 0.40 some improvement in lift-drag ratio is shown for the modified airfoil at a Reynolds number of 2×10^6 even though there was no serious problem at this lift coefficient. However, at a typical climb lift coefficient of 1.0 large increases in lift-drag ratio are shown at all Reynolds numbers for the refined airfoil. The wind-tunnel results also indicated that the pitching-moment coefficient at design lift was reduced for the modified airfoil.

17-percent-thick airfoil.- Based on the significant increase in lift-drag ratio obtained for the redesigned 21-percent airfoil at typical climb lift coefficients, a redesign of the 17-percent airfoil was initiated. The objective of the redesign was twofold; to reduce the pitching-moment coefficient by increasing the forward loading and increase the climb lift-drag ratio by decreasing the aft upper-surface pressure gradient. The changes in airfoil contour and pressure distribution are illustrated in figure 7. A reduction in pitching-moment coefficient of about 28 percent is indicated by the theoretical calculations. Note that prior to the start of the aft upper-surface pressure recovery for the modified airfoil a flat pressure distribution or reduced pressure gradient region extends for about 0.20c. This reduced pressure gradient region with the "corner" located at $x/c = 0.60$ is considered to be an important feature of the airfoil design. Research reported in reference 9 for a modified 13-percent airfoil clearly indicated that this reduced pressure gradient region retards the rapid forward movement of upper-surface separation at the onset of stall and promotes docile stall behavior for airfoils which stall from the trailing edge. The chordwise location of the corner is determined by the aft pressure gradient which must be gradual enough to avoid separation at climb lift coefficients ($c_l = 1.0$). Thus, the chordwise location of the corner is dependent on airfoil thickness ratio and design lift coefficient. The chordwise extent of the reduced pressure gradient region must be determined from experimental tests, since we are concerned with stall behavior. The theoretical separation points and pressure distributions for both 17-percent airfoils are shown in figure 8 at a climb lift coefficient of 1.0. A reduction in the extent of separation of about 0.05c is indicated for the modified airfoil. Based on these theoretical predictions some improvement in lift-drag ratio at $c_l = 1.0$ would also be expected.

MEDIUM-SPEED AIRFOILS

Development

The design objective of the medium-speed airfoils was to increase the cruise Mach number of the low-speed airfoils but retain the good high-lift,

low-speed characteristics. Such new airfoils are intended to fill the gap between the low-speed airfoils and supercritical airfoils for application on light executive-type aircraft. Two medium-speed airfoils having thickness-chord ratios of 13 and 17 percent have been developed. The airfoils were designed for a lift coefficient of 0.30 and a Reynolds number of 14×10^6, and the design Mach numbers for the 13 and 17 percent airfoils were 0.72 and 0.68, respectively. The 13-percent medium-speed airfoil was obtained by reshaping the 13-percent low-speed airfoil as indicated in figure 9. The calculated pressure distribution shows that increasing the Mach number to 0.72 for the low-speed airfoil results in a region of high induced velocities near the midchord on the upper surface of the airfoil. Further increases in Mach number or lift coefficient would result in a shock wave developing on the air-foil. The airfoil has been reshaped to decrease the induced velocities near the midchord and increase the induced velocities in the forward region of the airfoil upper surface. The design criteria employed consisted of combining the best features of low-speed and supercritical airfoil technology for this application.

The design pressure distributions for both medium-speed airfoils are shown in figure 10. Note that the start of the aft upper-surface pressure recovery is located at about 0.50c for the 17-percent airfoil, compared with about 0.60c for the 13-percent airfoil. This is required in order to keep the aft pressure gradient gradual enough to avoid separation for the thicker airfoil. In order to retain good high-lift, low-speed characteristics for the new airfoils, the camber distribution was kept similar but not identical to the low-speed airfoil family.

Section Data

Low-speed section characteristics for the medium-speed airfoils are presented in figures 11 and 12 for a Reynolds number of 4×10^6. Comparison of the section data for the 13-percent low- and medium-speed airfoils (fig. 11) show that the stall characteristics for both airfoils are similar and that only a small decrease in $c_{l,max}$ occurred for the medium-speed airfoil. Also, the pitching-moment coefficient has been decreased through the lift-coefficient range for the medium-speed airfoil. The drag polars for both airfoils are essentially the same. A similar comparison for the 17-percent low- and medium-speed airfoils (fig. 12) show no decrease in $c_{l,max}$ and a decrease in drag coefficient at all lift coefficients for the medium-speed airfoil. Thus, the overall performance of the 17-percent medium-speed air-foil exceeds that for the earlier 17-percent low-speed airfoil. The small decrease in drag coefficient for the medium-speed airfoil at low lift coef-ficients is associated with the reduced aft upper-surface pressure gradient (fig. 13) and resulting boundary-layer development. The large decrease in drag coefficient at the higher lift coefficients for the medium-speed air-foil is a result of improved ability to design for and achieve less sepa-ration on the airfoil, as illustrated in figure 14 for a lift coefficient of 1.6. Turbulent trailing-edge separation is indicated by a region of nearly constant pressure upstream of the airfoil trailing edge.

The scale effects on maximum lift coefficient for the medium-speed airfoils for Reynolds numbers from about 2×10^6 to 9×10^6 are shown in figure 15. Increases in Reynolds number have a favorable effect on maximum lift coefficient for both airfoils. Application of roughness resulted in only a small decrease in $c_{l,max}$ for both the 13- and 17-percent airfoils. Comparison of figures 3 and 15 for the 17-percent low- and medium-speed airfoils illustrate two interesting features. The irregular variation of $c_{l,max}$ with Reynolds number at the lower Reynolds numbers and the sensitivity of $c_{l,max}$ to roughness for the low-speed airfoil have been improved for the newer medium-speed airfoil design.

The effects of Mach number on maximum lift coefficient for the 13- and 17-percent low- and medium-speed airfoils are summarized in figure 16. The medium-speed airfoils generally show smaller decreases in $c_{l,max}$ at the higher Mach number compared to the low-speed airfoils.

Theoretical calculated drag-rise characteristics (ref. 8) for the medium-speed airfoils at design conditions are shown in figure 17. Both airfoils indicate essentially no drag creep up to the design Mach numbers. The estimated drag-rise Mach numbers are about 0.76 and 0.72 for the 13- and 17-percent airfoils, respectively, which provide a margin of about 0.04 in Mach number above the design Mach numbers.

APPLICATIONS

Recently a number of United States general aviation manufacturers have announced the use of the NASA-developed low-speed airfoils on new aircraft; these are summarized as follows:

Aircraft	Airfoil
Hustler (American Jet)	Modified LS(1)-0413, formerly GA(W)-2
Model 77 (Beech)	LS(1)-0417, formerly GA(W)-1
Model 303 (Cessna)	LS(1)-0413
PA-38 Tomahawk (Piper)	LS(1)-0417

CONCLUDING REMARKS

An initial family of low-speed airfoils for general aviation applications has been investigated. These airfoils provide significant improvements in maximum lift coefficients compared to the older NACA airfoils. Refinements to the 17-percent low-speed airfoil to reduce the pitching-moment coefficient and to the 21-percent low-speed airfoil to increase the lift-drag ratio have been completed. Two medium-speed airfoils with thickness ratios of 13 and 17 percent have been developed. These new airfoils provide increased cruise Mach numbers over the low-speed airfoils, while retaining good high-lift, low-speed characteristics. The NASA-developed low-speed airfoils are now being used by several United States general aviation manufacturers.

REFERENCES

1. Stevens, W. A.; Goradia, S. H.; and Braden, J. A.: Mathematical Model for Two-Dimensional Multi-Component Airfoils in Viscous Flow. NASA CR-1843, 1971.

2. McGhee, Robert J.; and Beasley, William D.: Low-Speed Aerodynamic Characteristics of a 17-Percent-Thick Airfoil Section Designed for General Aviation Applications. NASA TN D-7428, 1973.

3. McGhee, Robert J.; and Beasley, William D.: Effects of Thickness on the Aerodynamic Characteristics of an Initial Low-Speed Family of Airfoils for General Aviation Applications. NASA TM X-72843, 1976.

4. Wentz, W. H., Jr.; and Seetharam, H. C.: Development of a Fowler Flap System for a High Performance General Aviation Airfoil. NASA CR-2443, 1974.

5. Wentz, W. H., Jr.: Effectiveness of Spoilers on the GA(W)-1 Airfoil With a High Performance Fowler Flap. NASA CR-2538, 1975.

6. Wentz, W. H., Jr.: Wind Tunnel Tests of the GA(W)-2 Airfoil With 20% Aileron, 25% Slotted Flap, 30% Fowler Flap, and 10% Slot-Lip Spoiler. NASA CR-145139, 1977.

7. Gregorek, G. M.; Hoffmann, M. J.; Weislogel, G. S.; and Vogel, G. M.: In-Flight Measurements of the GA(W)-2 Aerodynamic Characteristics. [Preprint] 770461, Soc. Automot. Eng., Mar.-Apr. 1977.

8. Bauer, Frances; Garabedian, Paul; Korn, David; and Jameson, Antony: Supercritical Wing Sections II. Volume 108 of Lecture Notes in Economics and Mathematical Systems, Springer-Verlag, 1975.

9. McGhee, Robert J.; and Beasley, William D.: Low-Speed Wind-Tunnel Results for a Modified 13-Percent-Thick Airfoil. NASA TM X-74018, 1977.
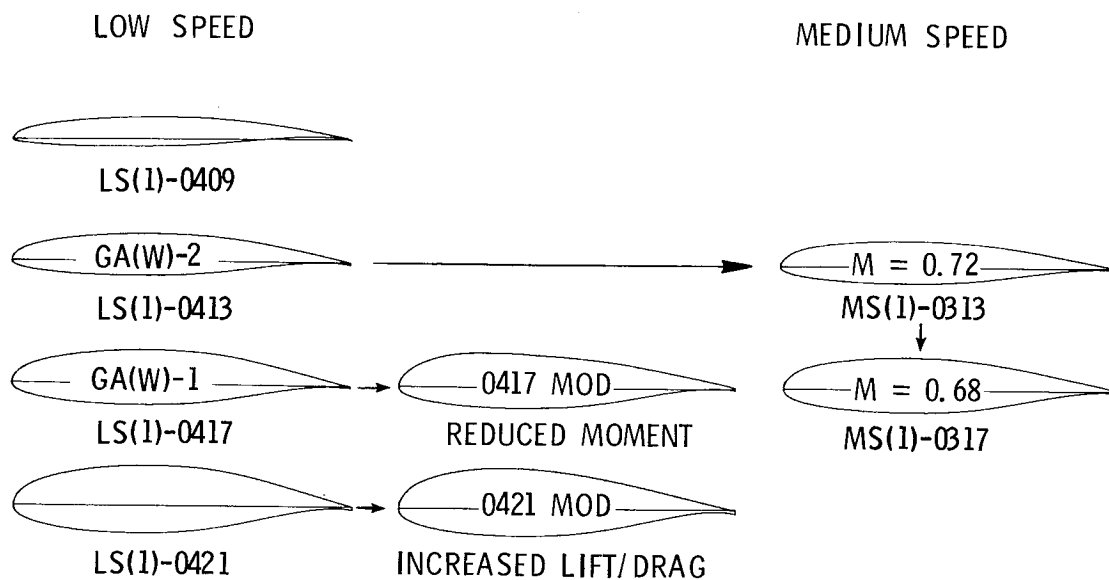
LOW SPEED   MEDIUM SPEED

LS(1)-0409

GA(W)-2 ————————————————————→ M = 0.72
LS(1)-0413   MS(1)-0313
                                                 ↓
GA(W)-1 ———→ 0417 MOD   M = 0.68
LS(1)-0417   REDUCED MOMENT   MS(1)-0317

LS(1)-0421 ———→ 0421 MOD
              INCREASED LIFT/DRAG

Figure 1.- Section shapes and airfoil designations for NASA low- and medium-speed airfoils.
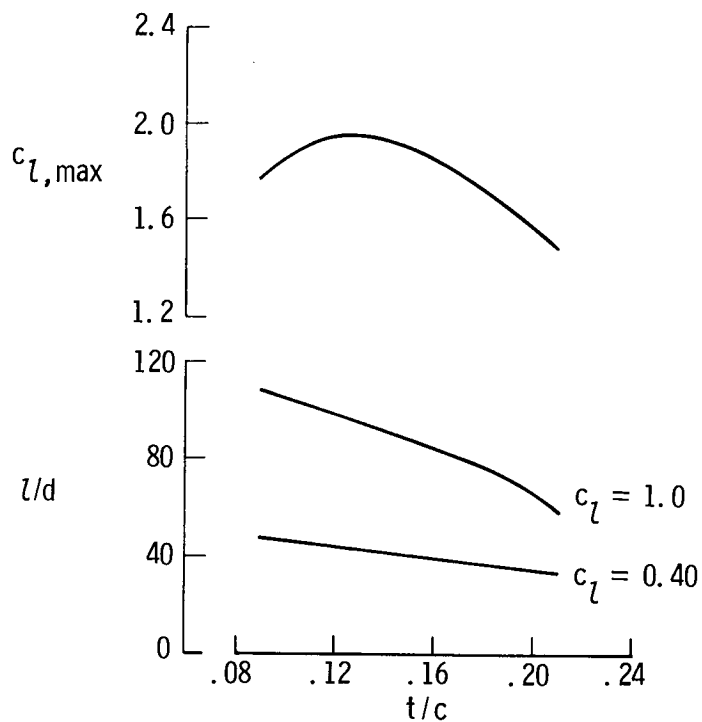

Figure 2.- Effect of airfoil thickness ratio on $c_{l,max}$ and lift-drag-ratio performance for low-speed airfoils. $M = 0.15$; $R = 4 \times 10^6$; $(x/c)_T = 0.075$.
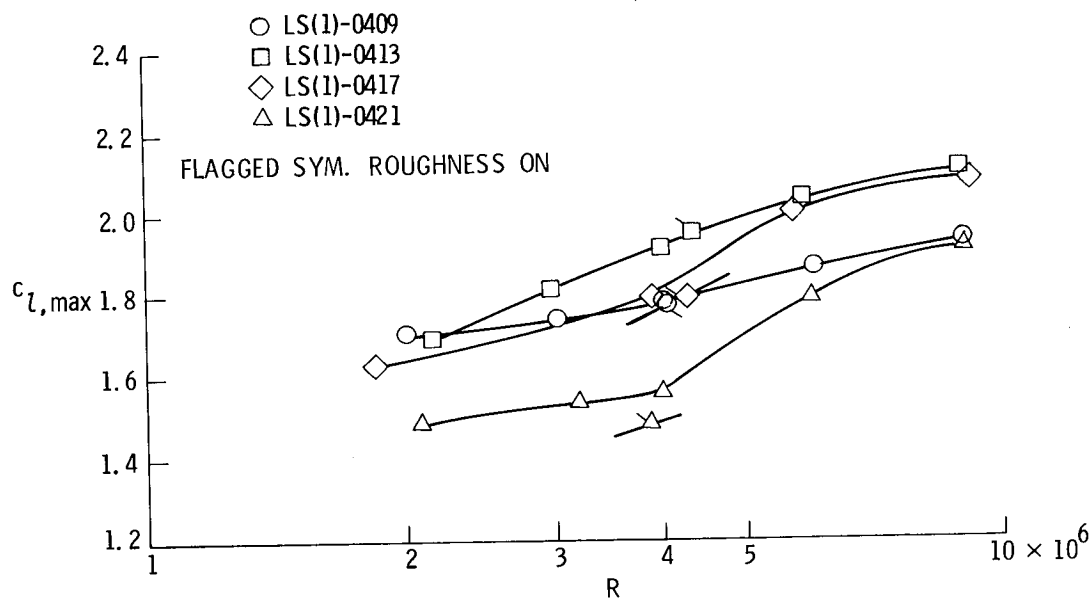
Figure 3.- Effect of Reynolds number on $c_{l,max}$ for low-speed airfoils. $M = 0.15$.
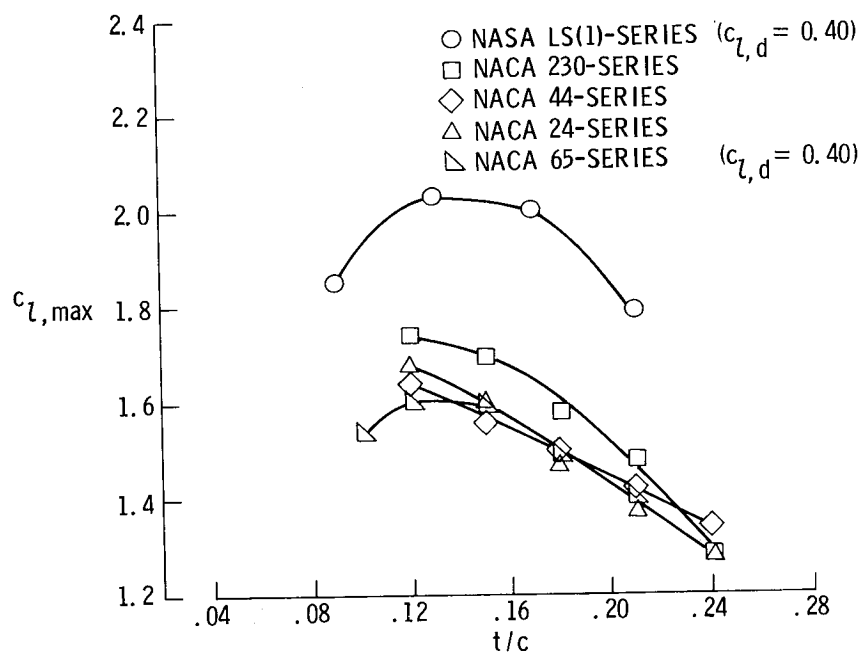

Figure 4.- Comparison of $c_{l,max}$ of NASA low-speed airfoils and NACA airfoils. $M = 0.15$; $R = 6 \times 10^6$; airfoils smooth.
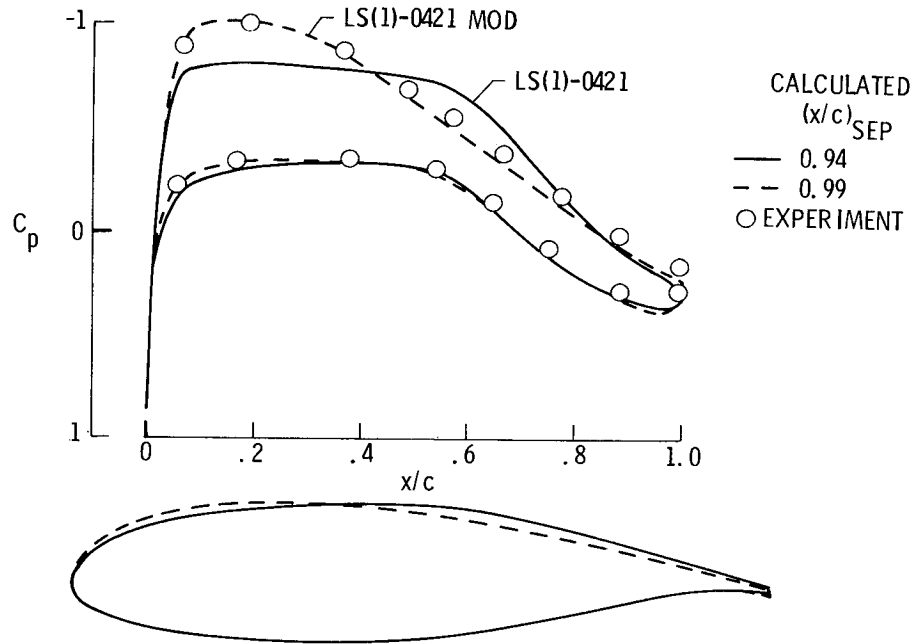
Figure 5.- Pressure distributions for 21-percent low-speed airfoils.
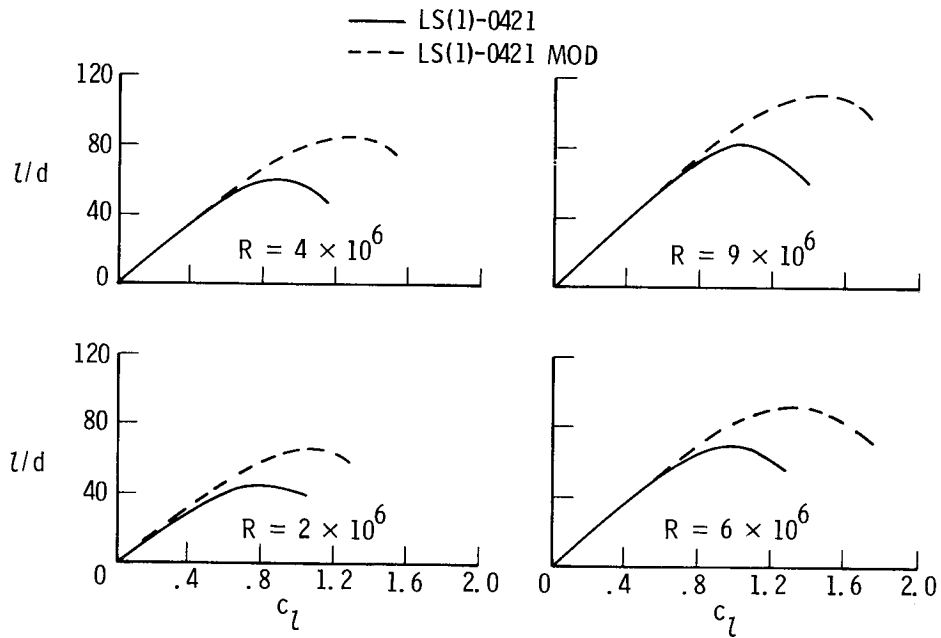$M = 0.15$; $R = 4 \times 10^6$; $c_l = 0.40$.

Figure 6.- Comparison of experimental lift-drag-ratio performance for 21-percent low-speed airfoils. $M = 0.15$; $(x/c)_T = 0.075$.
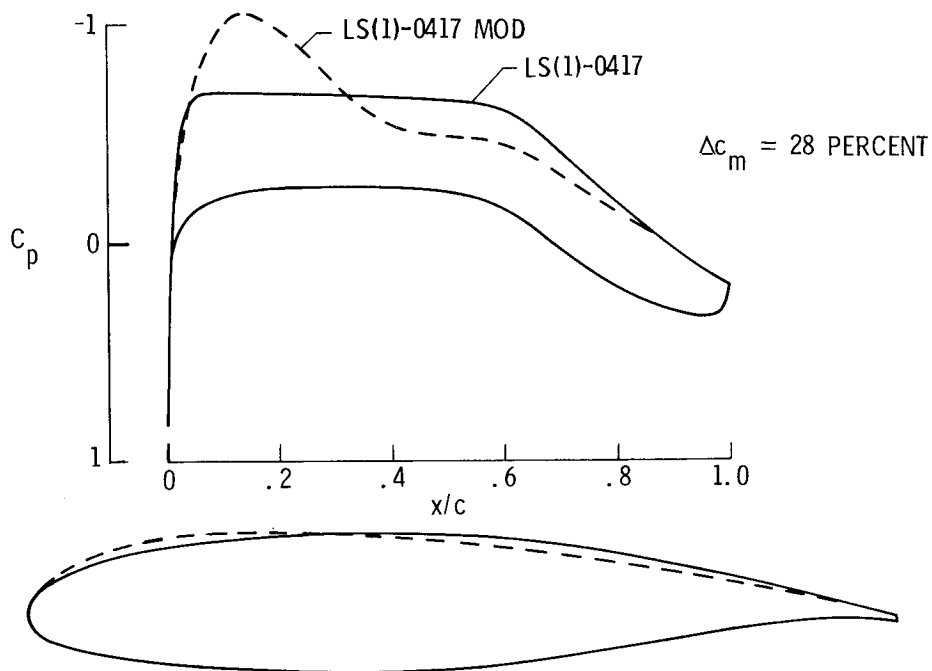
Figure 7.- Calculated pressure distributions for 17-percent low-speed airfoils. $M = 0.15$; $R = 4 \times 10^6$; $c_l = 0.40$.

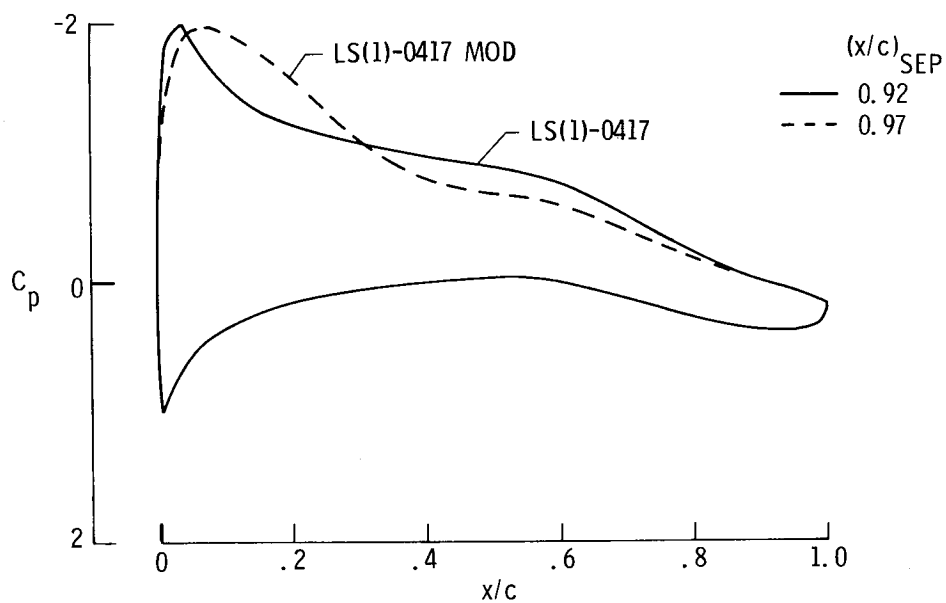Figure 8.- Calculated pressure distributions and separation points for 17-percent low-speed airfoils. $M = 0.15$; $R = 4 \times 10^6$; $c_l = 1.0$.

Figure 9.- Calculated pressure distributions for 13-percent low- and medium-speed airfoils. $M = 0.72$; $R = 14 \times 10^6$; $c_l = 0.30$.

Figure 10.- Calculated design pressure distributions for 13- and 17-percent medium-speed airfoils. $R = 14 \times 10^6$; $c_l = 0.30$.
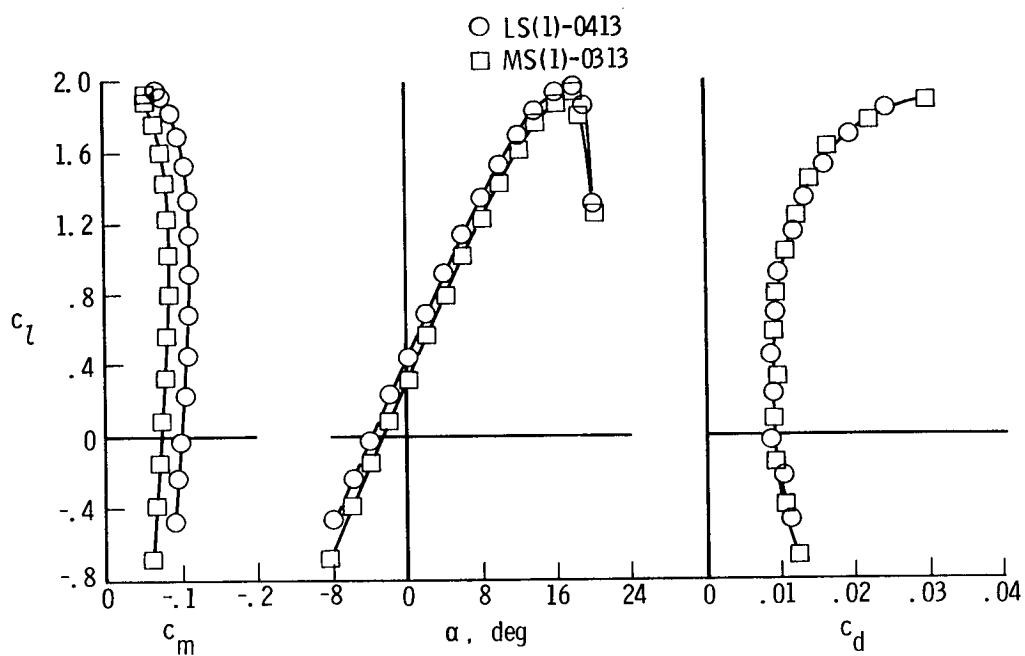
Figure 11.- Section data for 13-percent low- and medium-speed airfoils.
M = 0.15; R = 4 × 10⁶; (x/c)$_T$ = 0.075.
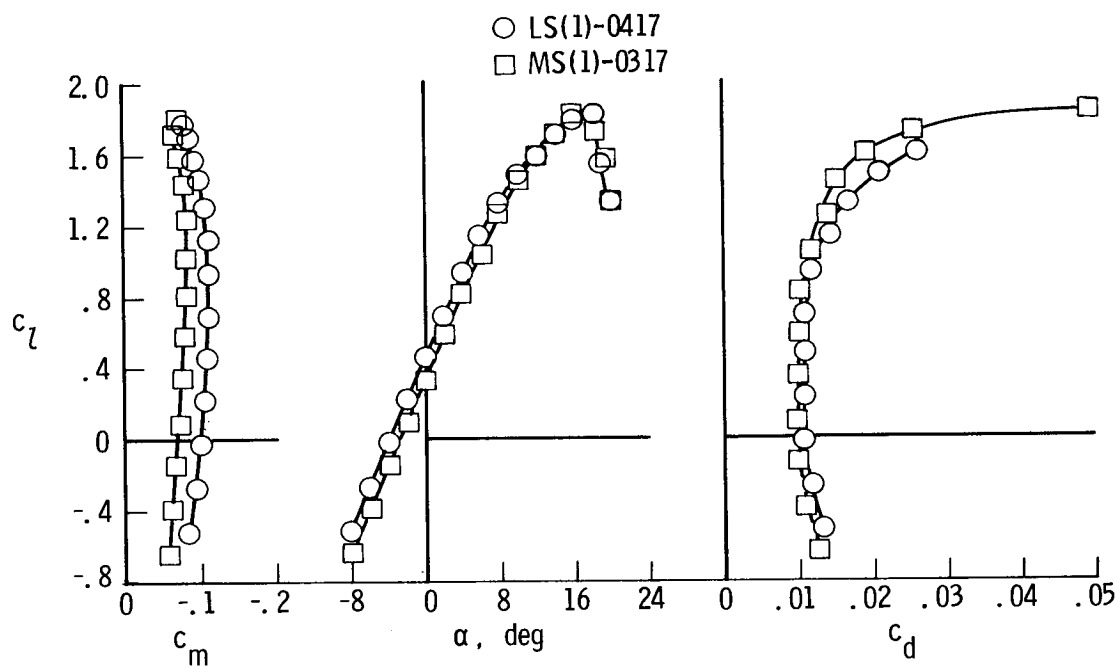
Figure 12.- Section data for 17-percent low- and medium-speed airfoils.
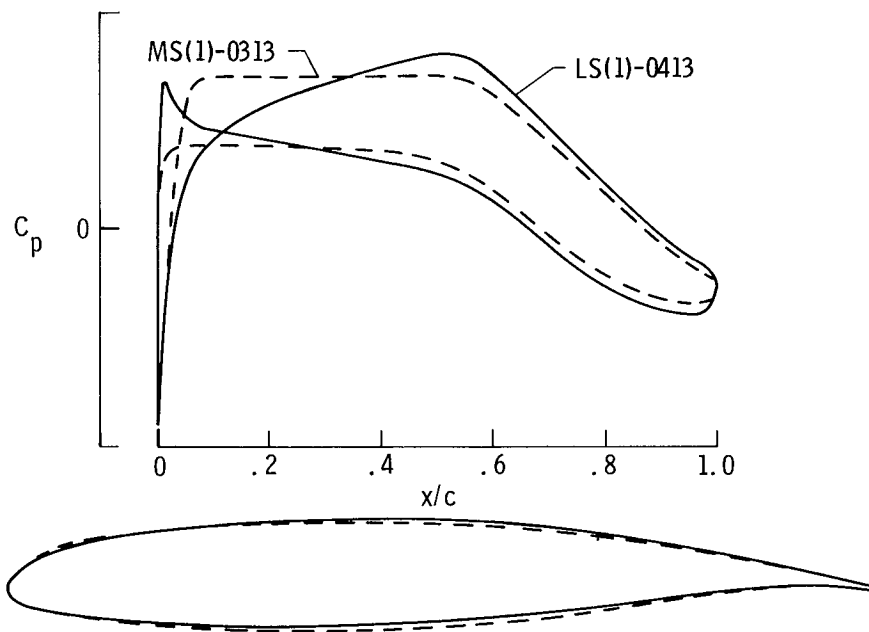M = 0.15; R = 4 × 10⁶; (x/c)$_T$ = 0.075.

13
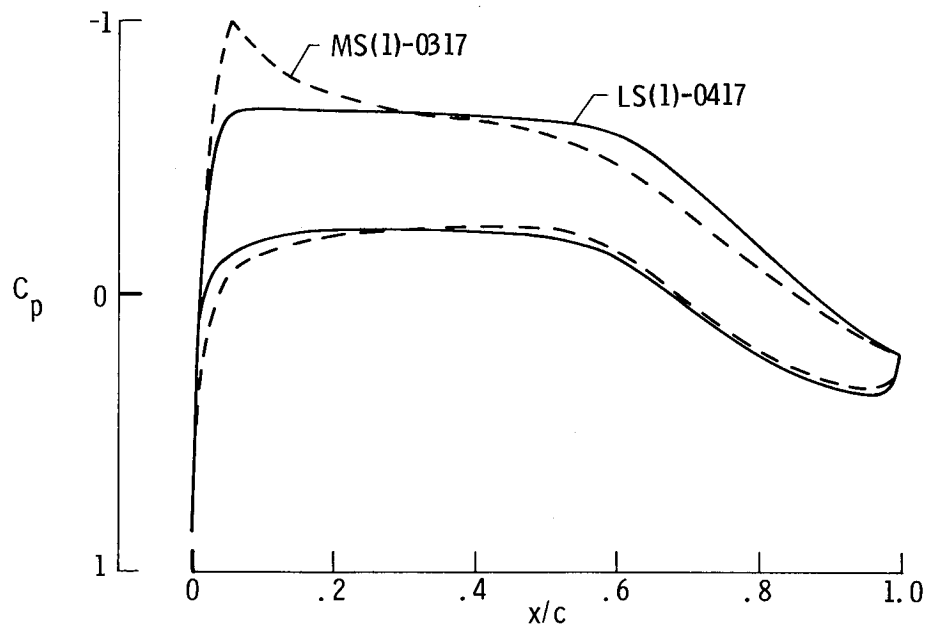
Figure 13.– Calculated pressure distributions for 17-percent low- and medium-speed airfoils. $M = 0.15$; $R = 4 \times 10^6$; $c_l = 0.40$.
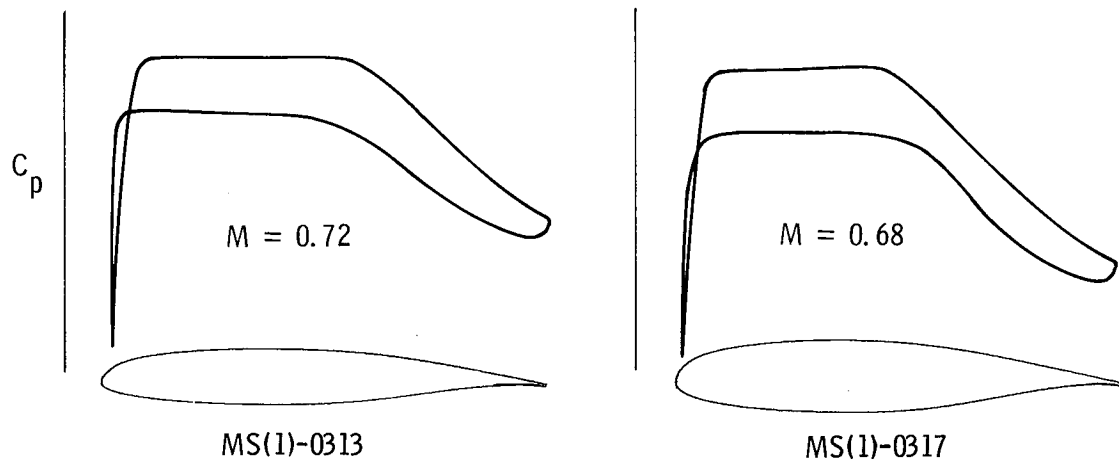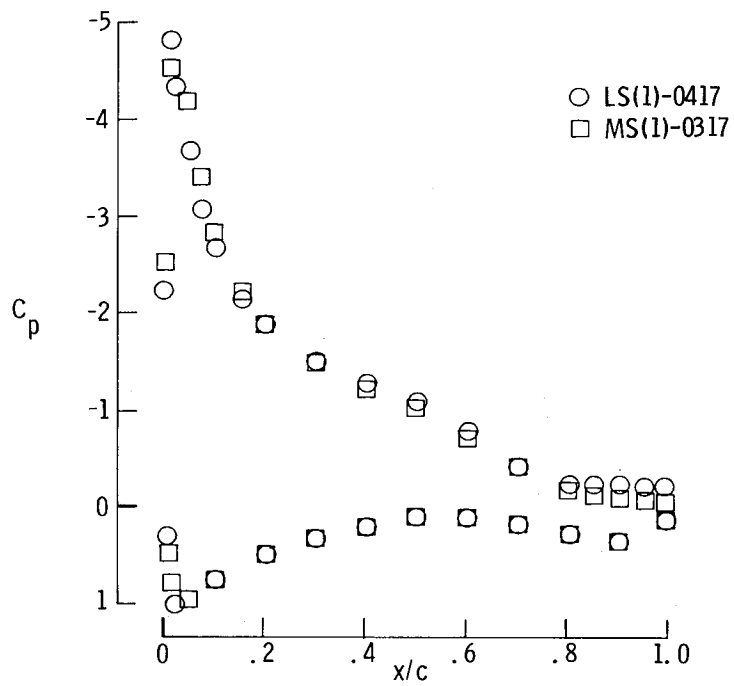

Figure 14.– Experimental pressure distributions for 17-percent low- and medium-speed airfoils. $M = 0.15$; $R = 4 \times 10^6$; $c_l = 1.6$.

Figure 15.- Effect of Reynolds number on $c_{l,max}$ for medium-speed airfoils. $M = 0.15$.

Figure 16.- Effect of Mach number on $c_{l,max}$ for low- and medium-speed airfoils. $R = 6 \times 10^6$; $(x/c)_T = 0.075$.
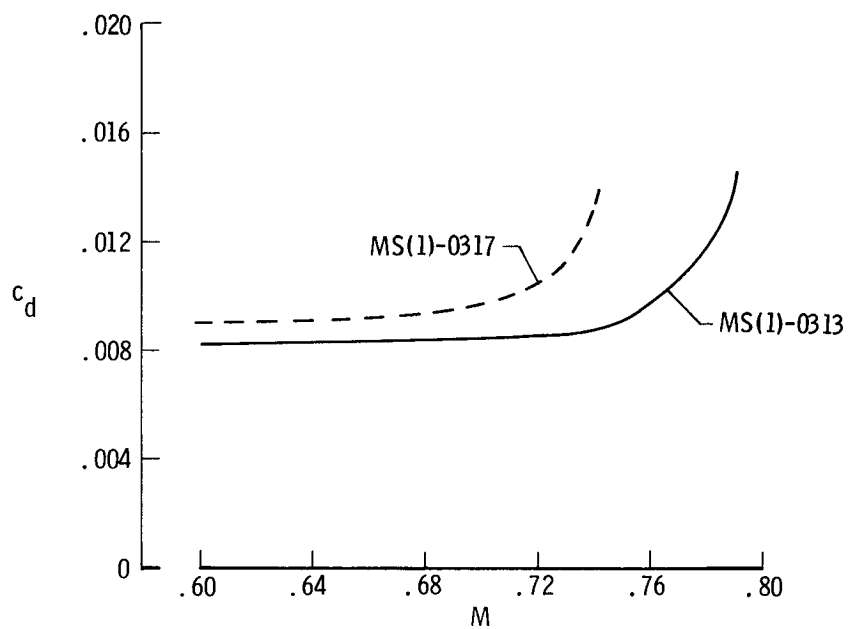
Figure 17.- Calculated drag-rise characteristics for medium-speed airfoils. $R = 14 \times 10^6$; $c_l = 0.30$.

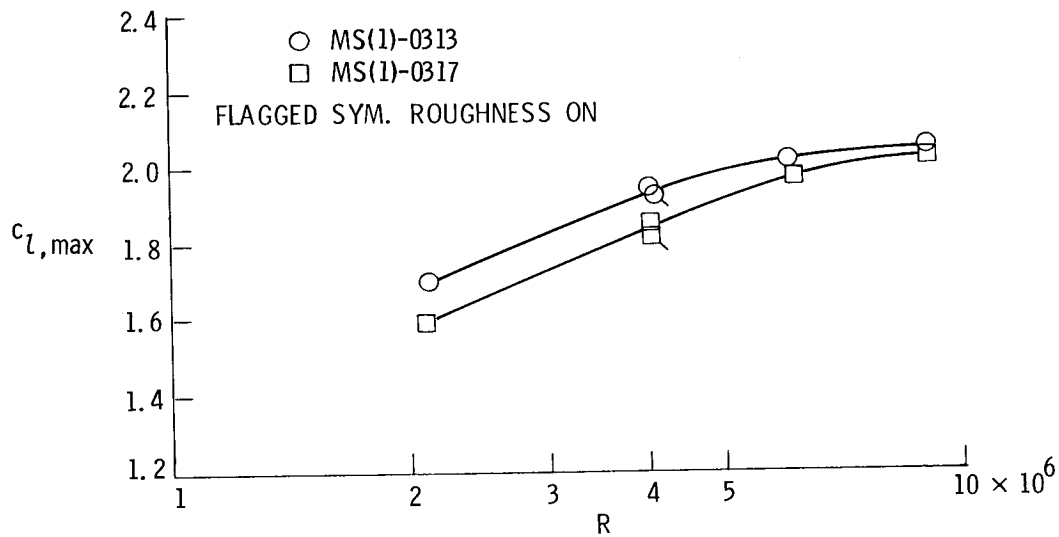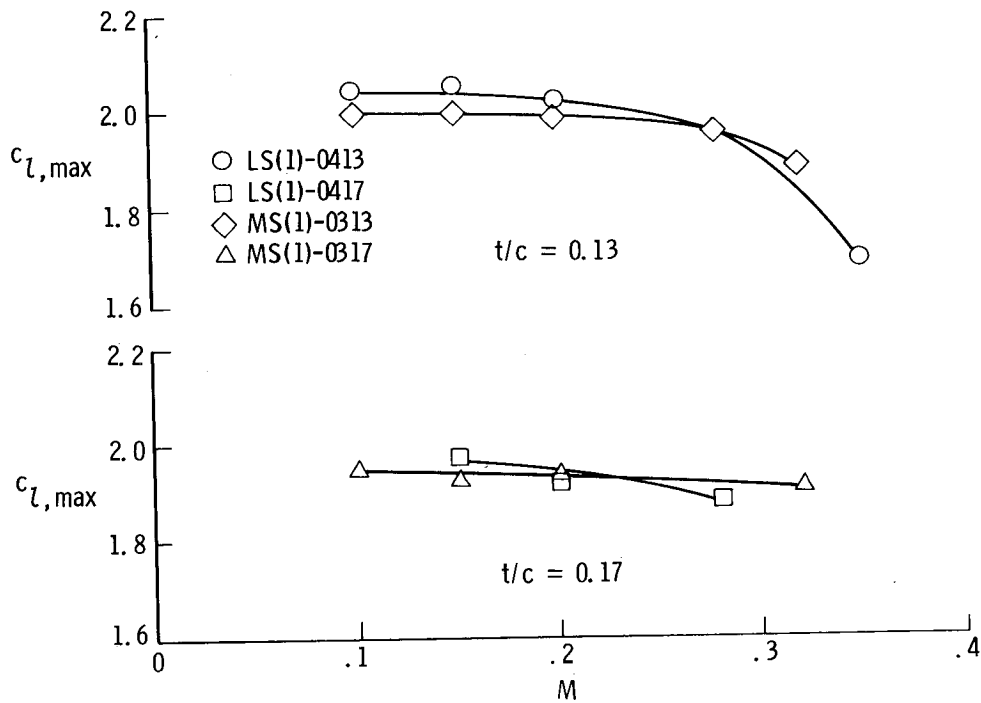# DEVELOPMENT OF HIGH LIFT FLAPS AND CONTROL SURFACES

FOR NEW GENERAL AVIATION AIRFOILS[*]

William H. Wentz, Jr.
Wichita State University

SUMMARY

Theoretical and experimental wind tunnel research has been conducted to develop flaps, ailerons and spoilers for use with NASA's new general aviation airfoils. Single-element flaps demonstrate good high-lift characteristics. Control response with either aileron or slot-lip spoiler is good, although hinge moments are rather high for both devices. Several needs for additional research are identified.

INTRODUCTION

Wichita State University has participated with NASA in advanced technology general aviation airfoil research since 1972. As the new series of general aviation airfoils has been developed at NASA's Langley Research Center, WSU has designed and tested flaps, ailerons, and spoilers for use with the new section shapes.

The detailed results of the WSU research have been published in a series of earlier reports (Refs. 1 through 11). The purpose of the present paper is to describe the scope of the flap and control surface development, the significant findings, and to suggest directions for further research.

SYMBOLS

All values are given in non-dimensional form. The measurements and calculations were made in U.S. Customary units.

c airfoil chord

c_d section drag coefficient

c_h control surface hinge moment coefficient

C_ℓ	section lift coefficient
$C_{\ell'}$	rolling moment coefficient for wing panel
$C_{m_{.25}}$	section pitching moment coefficient about .25 chord
C_p	pressure coefficient
x	chordwise coordinate
α	angle of attack
δ	control surface deflection angle
Δh	spoiler projection height normal to local surface

Subscripts:

a	aileron
max	maximum

SCOPE OF THE RESEARCH

Table 1 illustrates the scope of the WSU research, with the flap and control surface devices noted. For the 17% thick GA(W)-1 airfoil, 7.5% and 15% chord spoilers were evaluated. For the 13% thick GA(W)-2 and later airfoils, 10% slot-lip spoilers have been evaluated. Selected spoiler data will be presented in a later section of this paper.

Types of data obtained from this research program are:

1) flap-extended lift, drag, and pitching moment
2) optimum flap settings
3) effects of non-optimum flap settings
4) surface pressure distributions with flap and aileron
5) control surface effectiveness and hinge moment

Selected examples of each type data will be presented in the sections which follow. All testing was conducted at a Reynolds number of 2.2×10^6 and a Mach number of 0.13.

FLAP-EXTENDED RESULTS

Figures 1, 2, and 3 illustrate typical flap-extended lift, drag, and pitching moment. Theoretical results using the multi-element viscous analysis

18

method of reference 12 are also shown. The lift data show relatively good agreement at low α and modest flap deflections. For high angle of attack or high flap deflections, the theory over-predicts lift. This is as expected since the theory does not account for lift loss when separation is present. For $10°$ and $20°$ flap deflections the actual lift obtained is slightly higher than the theory. This trend has also been observed on every airfoil-flap combination studied in the present research. Evidently the discrepancy is the result of some deficiency in the theoretical model. Trends from the drag and pitching moment data are consistent with the lift.

Typical optimum flap settings for highest $c_{\ell max}$ are shown in figure 4. For low deflection angles a position with essentially zero overlap and a fairly generous gap is optimum. As deflection angle is increased the gap is narrowed considerably. It should be noted that the $10°$ flap position shown here is not a true optimum. Instead, the overlap for $10°$ flap was selected for practical track design somewhat arbitrarily as a value intermediate between the flap nested position and the fully aft position. Then the gap was varied to determine an optimum opening. For this case the $c_{\ell max}$ is quite insensitive to gap opening.

The effects of gap and overlap on $c_{\ell max}$ at a given high flap deflection are illustrated by figure 5. In this case $c_{\ell max}$ is quite sensitive to the flap positioning. These contour plots are intended to provide designers with data to evaluate the effects of the compromises necessary in practical flap track design.

The effects of gap on c_{ℓ} for a given flap deflection, overlap, and angle of attack are shown in figure 6, along with theoretical results. These data show that the theory not only overpredicts the lift for all gaps, but also that the theoretical predictions are much less sensitive to gap than the experimental results. This means that it is not presently possible to obtain either best gap setting or the value of $c_{\ell max}$ from the theory.

High-lift performance from the new airfoils with flaps is compared with similar flaps applied to the earlier NACA 23012 airfoil (Ref. 13) in Table 2. These data show that the new airfoils provide a substantial increment in $c_{\ell max}$ with flap extended. Since the new airfoils are noted for their ability to produce higher $c_{\ell max}$ values than earlier airfoils with flap nested, the results shown here illustrate clearly that the performance improvements are retained with flaps extended. This comparison is probably somewhat conservative because of the higher Reynolds number and smooth model condition of the earlier tests.

A method for comparing high-lift performance of flaps with various amounts of chord distribution between forward element and flap is shown in figure 7. For this study the reference chord has been taken as the sum of the forward element chord plus flap chord. These data again show that the new airfoils provide significant performance gains relative to the older NACA airfoil.

Pressure distributions with flap extended are compared with theory in figures 8, 9 and 10. For low and moderate angles of attack, the agreement is good. For $16°$ angle of attack, massive separation has occurred as evidenced

by a relatively constant pressure region on the airfoil forward element (and confirmed by tuft studies). For such cases the theory is inadequate.

AILERONS

Performance of ailerons applied to the new airfoils is shown in figure 11. Control response is similar to earlier airfoils, showing increasing non-linearity for large aileron deflections. Hinge-moment characteristics are nearly linear, although they are characterized by a substantial up-aileron moment at zero deflection, and this up-aileron moment is sensitive to angle of attack. This characteristic is a direct result of the substantial aft camber of the new airfoils. It introduces substantial loads into the control actuation system. While these are ordinarily balanced by right and left ailerons so that the pilot "feel" will not be affected, the cables, pulleys, brackets, etc., are loaded and must have added stiffness and strength as appropriate.

SPOILERS

Control effectiveness of unvented spoilers is shown in figure 12. For two-dimensional tests the effectiveness parameter is incremental lift, while for three-dimensional tests the appropriate parameter is rolling moment coefficient. The three-dimensional tests in this case were conducted with a reflection-plane wing panel representative of the ATLIT research airplane (Ref. 14). The control deflection parameter for spoiler studies is taken as the projection height divided by reference chord. This parameter is useful when spoilers of differing chords are being studied. The data for unvented spoilers show powerful roll effectiveness for large deflections, but a distinct region of control reversal for small spoiler deflections with flap extended. A number of spoiler cross-sectional shapes were tested as shown in figure 13, in attempts to eliminate the unsatisfactory control reversal. None of the shapes tested eliminated the reversal. Reversal was finally eliminated by providing an opening for venting of lower surface air to the upper surface as shown in figure 14. This solution had been used on the earlier spoiler studies of Reference 15.

Unfortunately the manual control system of the ATLIT airplane required clearance gaps at spoiler leading and trailing edges, and these gaps provide leak paths which lead to aerodynamic penalties. The magnitude of these penalties is shown in figure 15. With flap nested, a penalty in drag is shown which amounts to a 30% increase at the airfoil design lift coefficient of 0.4. With flap extended the leakage flow penalizes $c_{\ell max}$ about 10% at all flap deflections. These are extremely severe losses.

A more recent spoiler design is shown in figure 16. This slot-lip arrangement makes sealing the spoiler leading edge relatively easy and the trailing edge serves as the flap slot lip, so leakage losses are minimal. Vented

spoilers are characterized by large opening hinge moments and the attendant structural problems as described for ailerons in an earlier section of this paper.

FINDINGS

Significant findings from the present research are as follows:

1) Current theoretical methods are inadequate for flap optimization.
2) $c_{\ell max}$ performance of the new airfoils with single-element flap is considerably better than earlier airfoil-flap combinations.
3) Ailerons perform satisfactorily on the new airfoils.
4) Slot-lip spoilers have been developed for use with the new high-lift airfoil-flap combinations.

NEEDS

The following needs have been identified from the present research:

1) Improved theoretical models are needed for multiple-component configurations.
2) Theoretical models are needed for analyzing post-separated flows. Examples are:
   a) near-stall and post-stall angles of attack
   b) flap cove regions with separation and reattachment
   c) intentional separation with spoilers

Other needs:

1) New symmetrical airfoil sections with high $c_{\ell max}$ are needed for use as tail surfaces, streamline struts, etc.
2) Low Reynolds number ($< 1.0 \times 10^6$) airfoil designs and data are needed for special applications such as small RPV's, wind turbines, gas turbine compressor blades, etc.

CONCLUDING REMARKS

Flaps, ailerons, and spoilers have been developed for the new NASA airfoils through a combination of theoretical studies and wind tunnel tests. Some of these designs have been further demonstrated through flight research such as the ATLIT aircraft (GA(W)-1 airfoil, Fowler flaps, and spoilers) and the Ohio State University's tests of the modified Beech Sundowner (GA(W)-2 airfoil and ailerons). This technology is now appearing in commercially available products such as the Robertson Seneca II Mod, the recently introduced Beech model 76 and 77 aircraft, and the Piper Tomahawk aircraft.

REFERENCES

1. W.H. Wentz, Jr.: New Airfoil Sections for General Aviation Aircraft. SAE Paper 730876, 1973. (Included in SAE Transactons, 1974.)

2. W.H. Wentz, Jr., and H.C. Seetharam: Development of a Fowler Flap System for a High Performance General Aviation Airfoil. NASA CR-2443, 1974. (See also SAE paper No. 740365.)

3. J. Roskam, D.L. Kohlman and W.H. Wentz, Jr.: Spoilers for Lateral Control of Light Airplanes. AIAA Paper 74-861, 1974.

4. W.H. Wentz, Jr., H.C. Seetharam and J.T. Calhoun: Wind Tunnel and Flight Development of Spoilers for General Aviation Aircraft. SAE Paper 750523, 1975.

5. W.H. Wentz, Jr.: Effectiveness of Spoilers on the GA(W)-1 Airfoil with a High-Performance Fowler Flap. NASA CR-2538, 1975.

6. W.H. Wentz, Jr.: Reflection-Plane Tests of Spoilers on an Advanced Technology Wing. SAE Paper 760482, 1976. (Included in SAE Transactions, 1976.)

7. W.H. Wentz, Jr., and C.G. Volk: Reflection-Plane Tests of Spoilers on an Advanced Technology Wing with a Large Fowler Flap. NASA CR-2696, 1976.

8. W.H. Wentz, Jr., H.C. Seetharam, and K.A. Fiscko: Force and Pressure Tests of the GA(W)-1 Airfoil with a 20% Aileron, and Pressure Tests with a 30% Fowler Flap. NASA CR-2833, 1977.

9. W.H. Wentz, Jr.: Use of Simplified Flow Separation Criteria for Slotted Flap Preliminary Design. SAE Paper, 1977 Business Aircraft Meeting. SAE Paper No. 770481, 1977.

10. W.H. Wentz, Jr.: Wind Tunnel Tests of the GA(W)-2 Airfoil with 20% Aileron, 25% Slotted Flap, 30% Fowler Flap, and 10% Slot-Lip Spoiler. Wichita State University AR 76-2, 1976. (FEDD)

11. W.H. Wentz, Jr., and K. Fiscko: Pressure Distributions for the GA(W)-2 Airfoil with 20% Aileron, 25% Slotted Flap and 30% Fowler Flap. NASA CR-2948, 1978. (FEDD)

12. W.A. Stevens, S.H. Goradia, and J.A. Braden: Mathematical Model for Two-Dimensional Multi-Component Airfoils in Viscous Flow. NASA CR-1843, 1971.

13. Jones F. Cahill: Summary of Section Data on Trailing-Edge High-Lift Devices. NACA Report 938, 1949.

14. B.J. Holmes, D.L. Kohlman and H.L. Crane: Preliminary Flight-Test Results of an Advanced Technology Light Twin-Engine Airplane (ATLIT). SAE Paper 760497, 1976.

15. C.J. Wenzinger, and F.M. Rogallo: Wind Tunnel Investigation of Spoiler, Deflector, and Slot Lateral-Control Devices on Wings with Full-Span Split and Slotted Flaps. NACA Report 706, 1941.
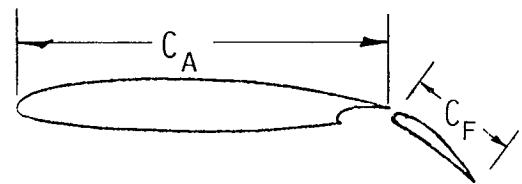
TABLE 1 - SCOPE OF FLAP AND CONTROL SURFACE DEVELOPMENT AT WSU

(NASA SPONSORED)

AIRFOIL	20% AILERON	30% FLAP	25% FLAP	10% SPOILER
17% LOW-SPEED	X	X		
13% LOW-SPEED	X	X	X	X
21% LOW-SPEED	1977		1977	1977
14% SUPERCRITICAL	1977		1977	1977
13% MEDIUM SPEED	1978		1978	1978

TABLE 2 - FOWLER AND SLOTTED FLAP PERFORMANCE
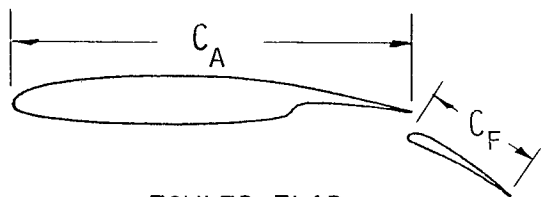
FOWLER FLAP

SLOTTED FLAP

AIRFOIL	C_F/C	C_A/C	$C_{L_{MAX}}$	AIRFOIL	C_F/C	C_A/C	$C_{L_{MAX}}$
GA(W)-1	.30	1.0	3.8	GA(W)-2	.25	.875	3.3
NACA 23012	.30	1.0	3.3	NACA 23012	.257	.83	2.8
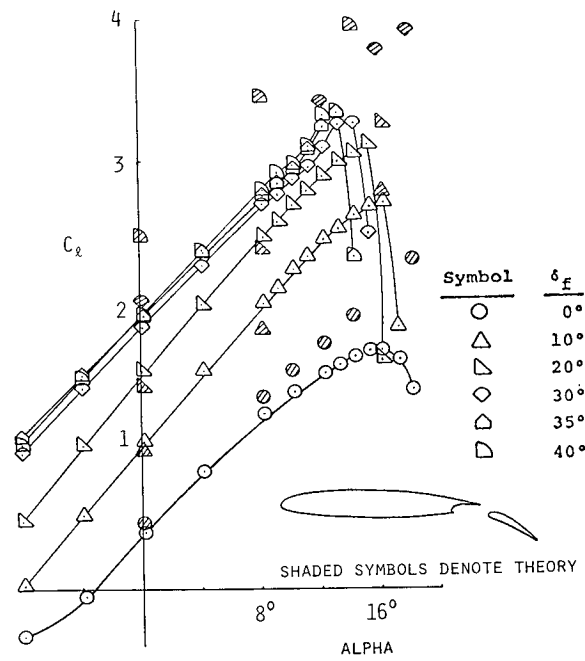
Figure 1.- Flap-extended lift.
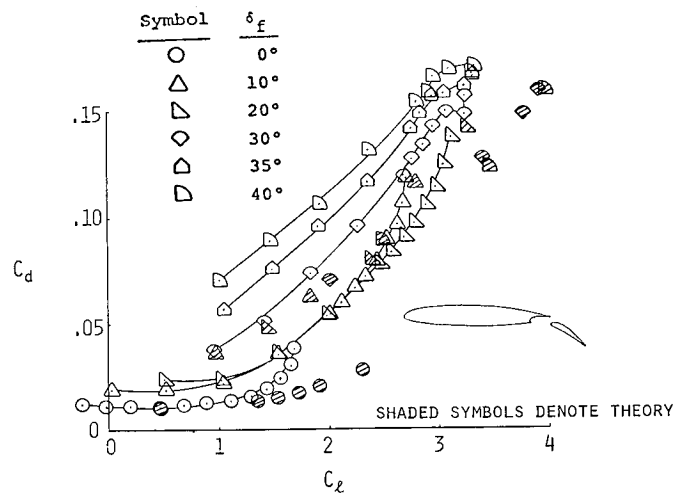
Figure 2.- Flap-extended drag.
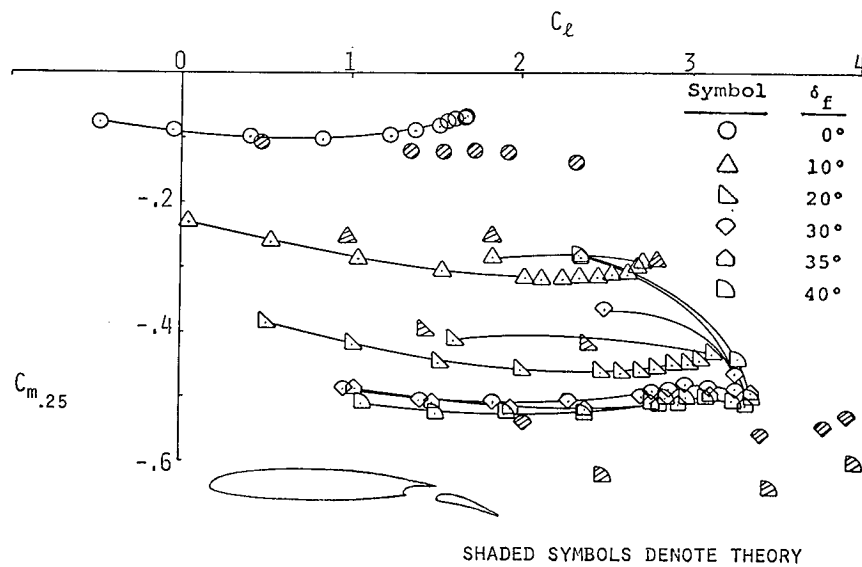
Figure 3.- Flap-extended pitching moment.
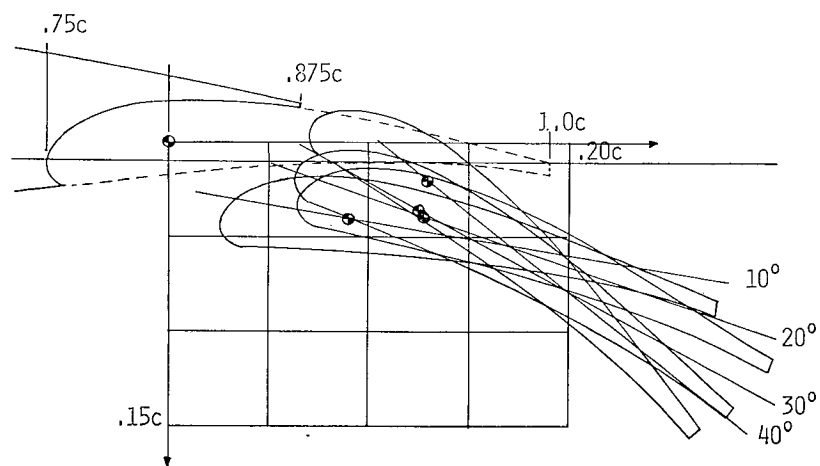
Figure 4.- Optimum flap settings.
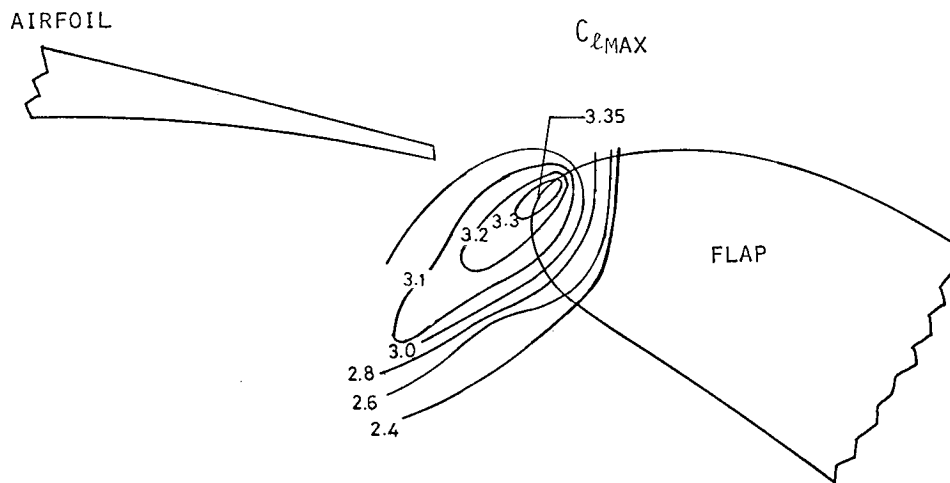
Figure 5.- Effects of nonoptimum flap settings.
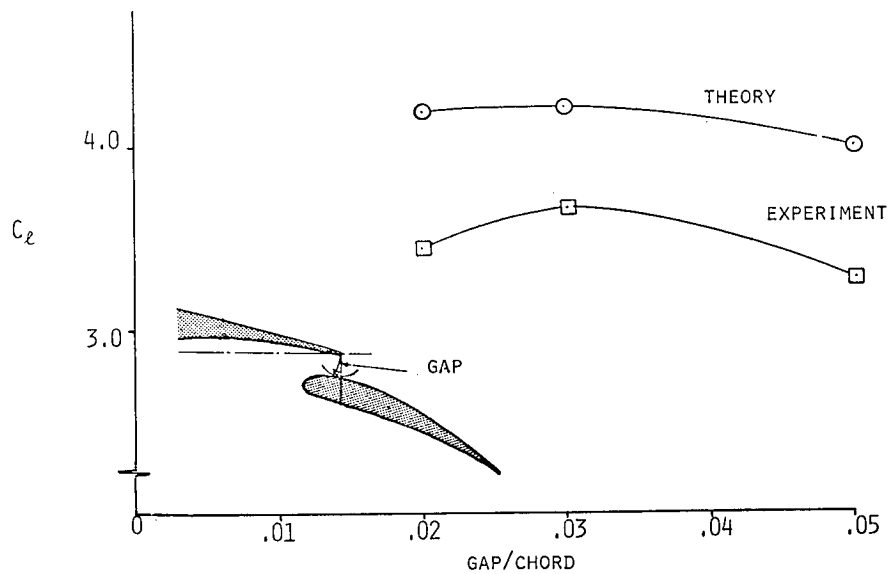
Figure 6.- Effects of gap on flap performance. $\alpha = 10^{\circ}$; Overlap/Chord, 0.012.
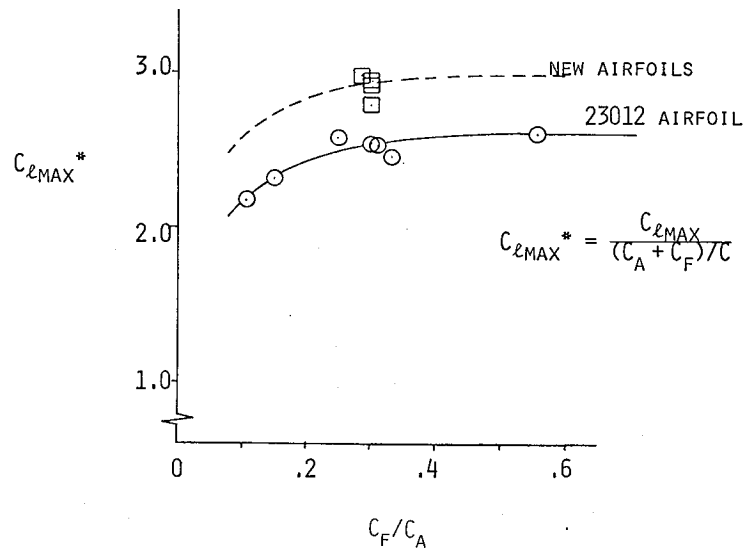
Figure 7.- High-lift performance with flaps.

$$C_{\ell MAX}{}^* = \frac{C_{\ell MAX}}{(C_A + C_F)/C}$$
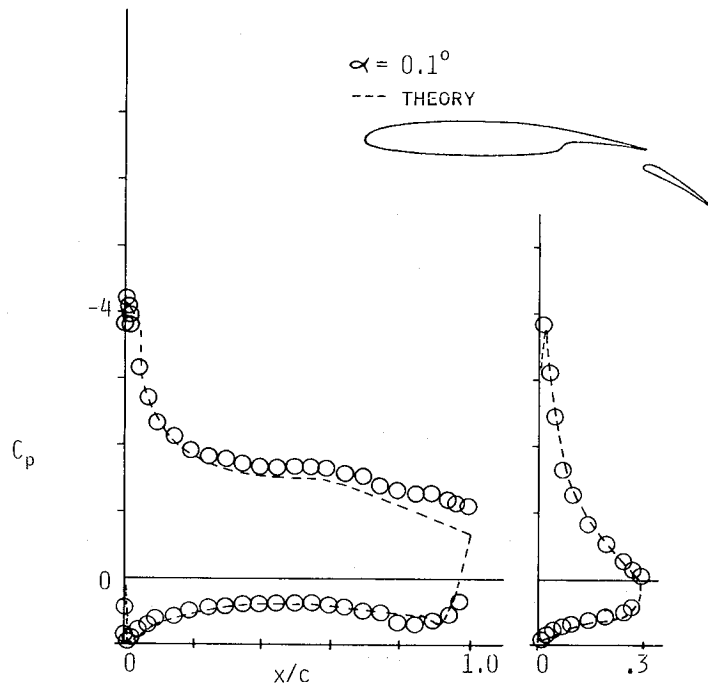
Figure 8.- Pressure distributions with flap extended. $\alpha = 0.1^{\circ}$.
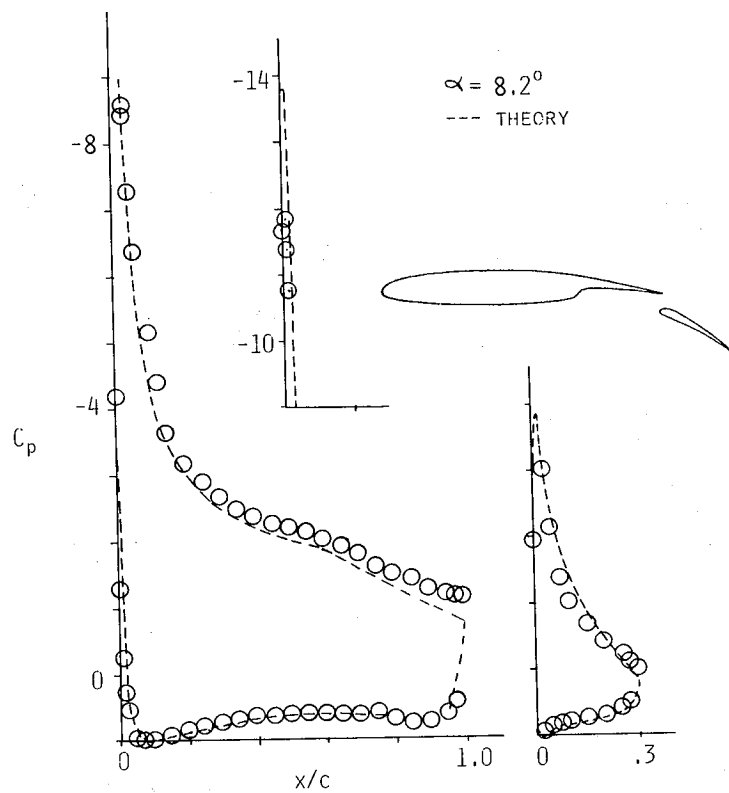
Figure 9.- Pressure distributions with flap extended. $\alpha = 8.2°$.
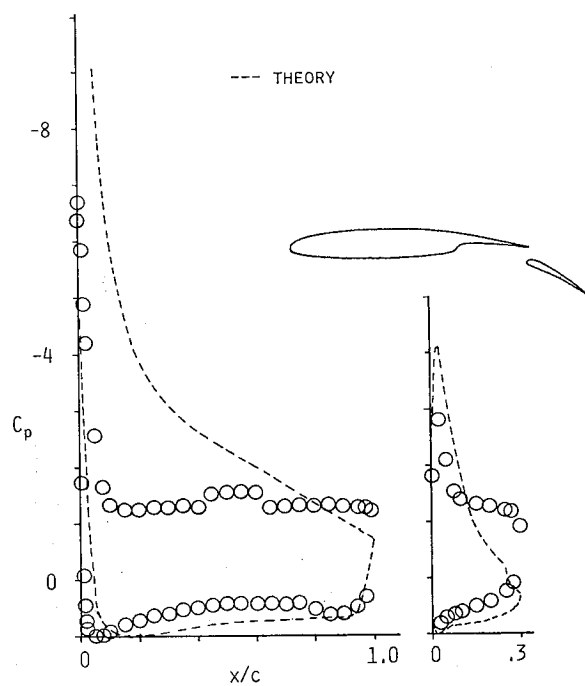
Figure 10.- Pressure distributions with flap extended. $\alpha = 16.0°$.

29
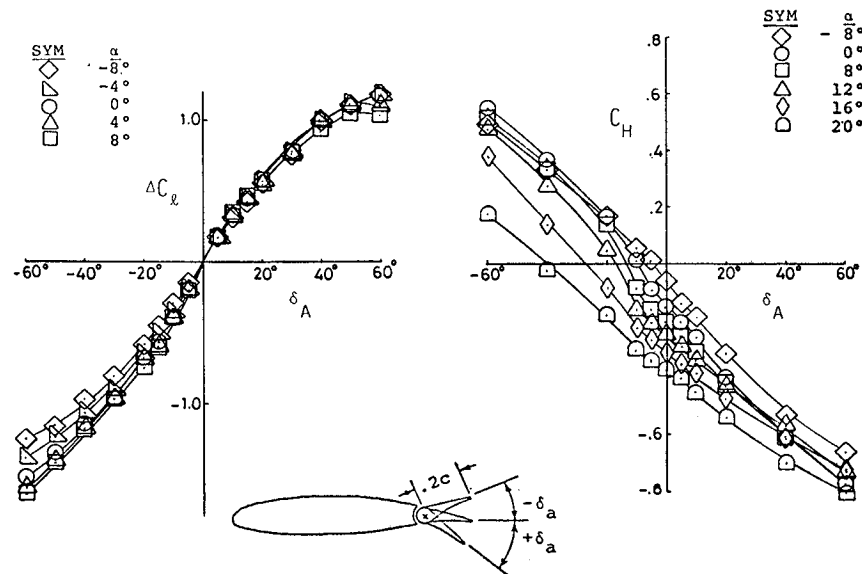
Figure 11.- Aileron effectiveness.
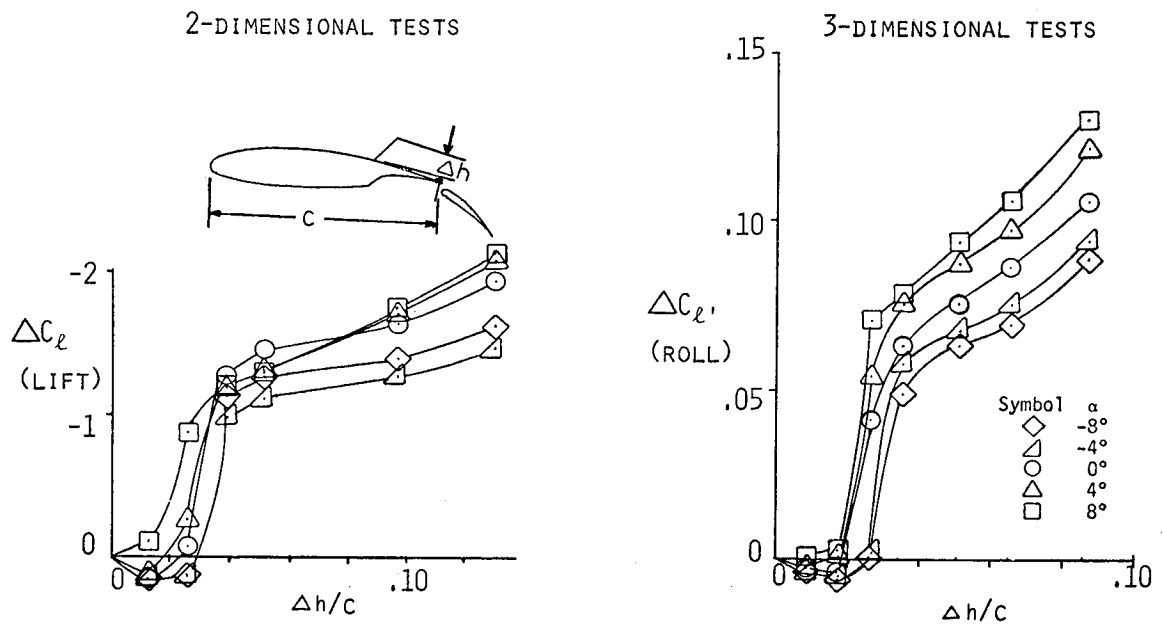
Figure 12.- Unvented spoilers.

SHARP TRIANGLE

TRIANGLE

MU-2

THICK FLAT PLATE

TEE
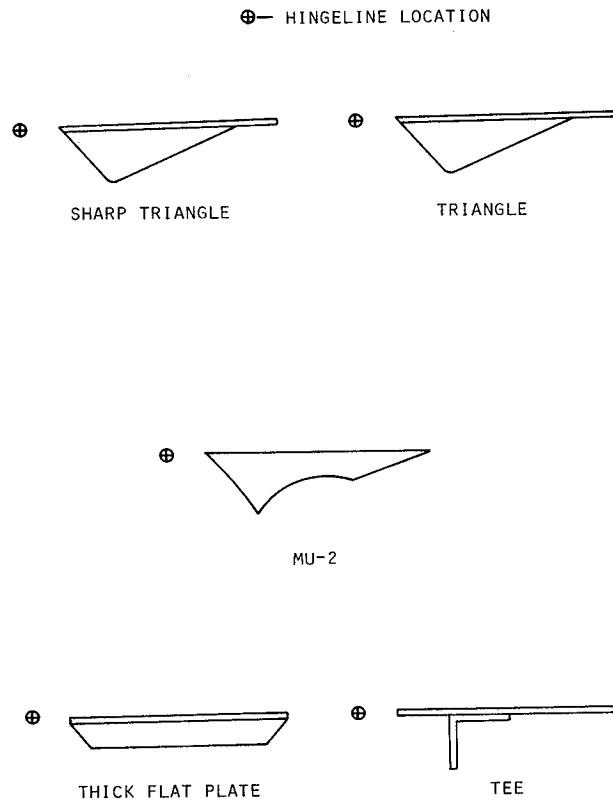
Figure 13.- Spoiler shapes tested.

2-DIMENSIONAL TESTS

3-DIMENSIONAL TESTS

Symbol	α
◇	-8°
◁	-4°
○	0°
△	4°
□	8°

ΔC_ℓ
(LIFT)

$\Delta C_{\ell'}$
(ROLL)

$\Delta h/c$

$\Delta h/c$

Figure 14.- Vented spoilers.

Figure 15.- Effects of spoiler gap leaks.
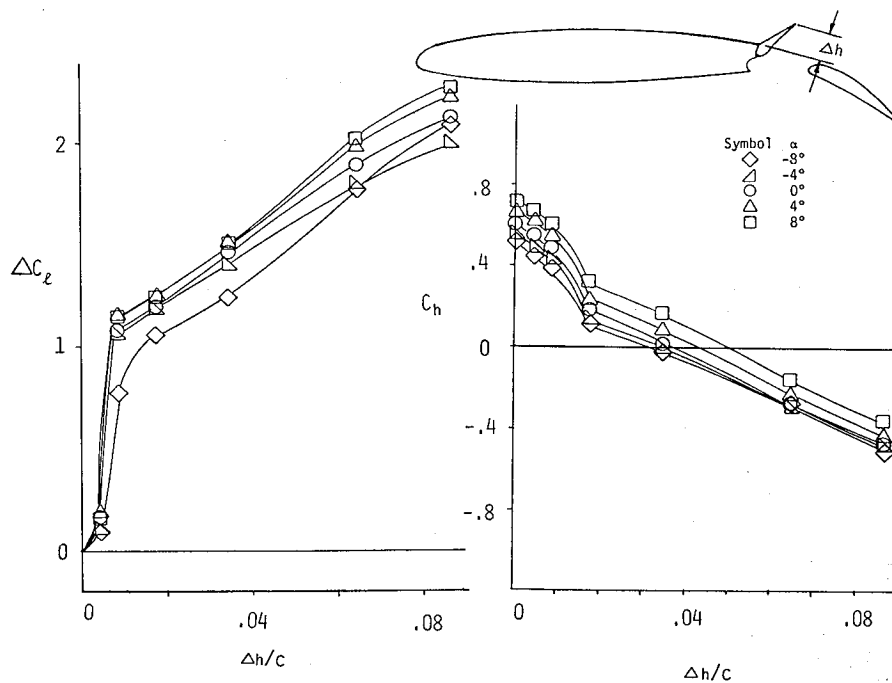
Figure 16.- Slot-lip spoiler.

COMPARISON OF WING PRESSURE DISTRIBUTIONS AND BOUNDARY-LAYER
CHARACTERISTICS FOR THE ADVANCED TECHNOLOGY LIGHT TWIN-ENGINE AIRPLANE
(ATLIT) WITH TWO-DIMENSIONAL SECTION DATA FOR THE GA(W)-1 AIRFOIL

Long P. Yip
NASA Langley Research Center

SUMMARY

An investigation was conducted in the Langley full-scale tunnel to measure
the aerodynamic characteristics of an Advanced Technology Light Twin-Engine
Airplane (ATLIT). The investigation included measurements of the performance
and stability and control characteristics of the airplane, wing-pressure
distributions, and boundary-layer characteristics. Samples of some pressure
and boundary-layer data are presented, and comparisons are made with two-
dimensional airfoil data. The results show that pressure distributions ob-
tained on the airplane wing at a station located at 75 percent of the semispan
were similar in shape to the pressure distributions obtained from two-
dimensional wind-tunnel results and theory. Pressure measurements obtained at
the 50-percent-semispan station, however, differed significantly from the
two-dimensional data because of interference effects of the nacelle on the
flow field of the airplane wing. Boundary-layer data indicated that laminar
flow was obtained on the ATLIT wing to at least the 30-percent chord for the
"in-service" condition airplane.

INTRODUCTION

Research on advanced technology airfoils over the last several years at
the Langley Research Center has resulted in the development of airfoils, such
as the 17-percent-thick GA(W)-1 airfoil, which offer substantial performance
improvements for propeller-driven light airplanes (see ref. 1). Flight tests
for verification of the potential performance benefits of the GA(W)-1 airfoil
have been conducted in the Advanced Technology Light Twin-Engine Airplane
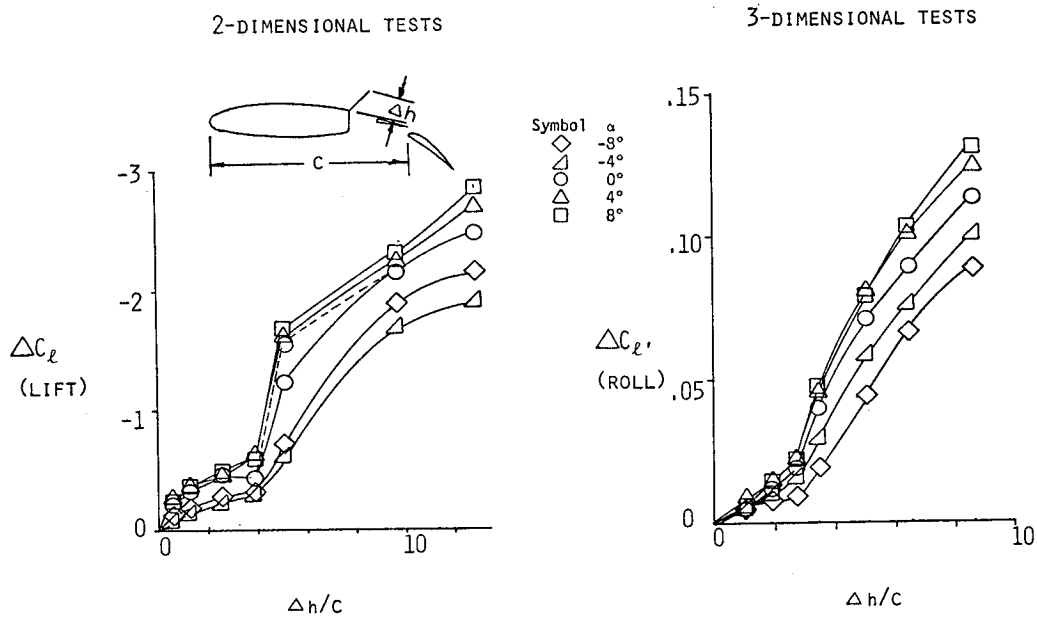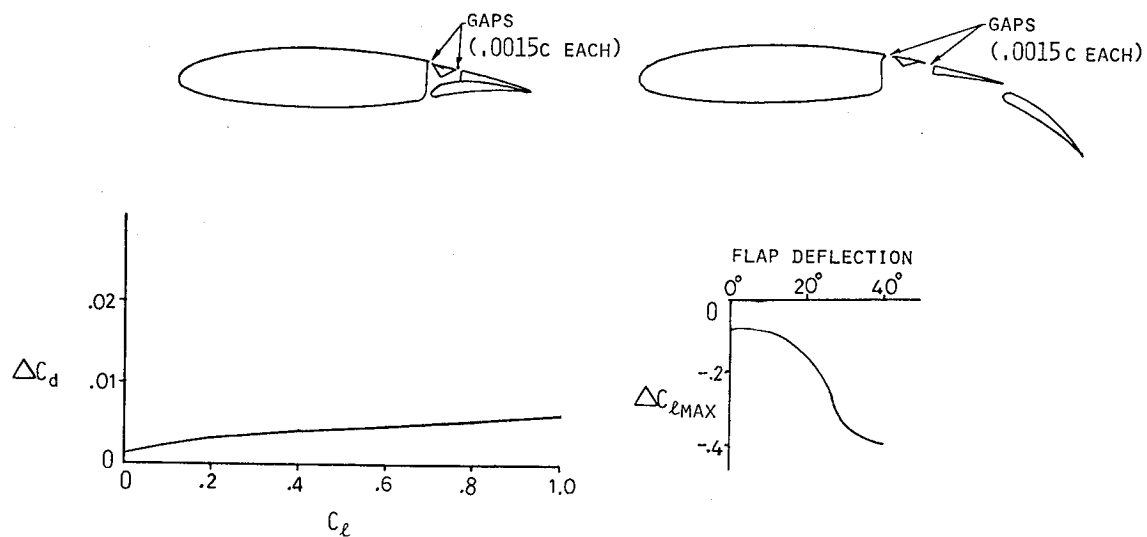(ATLIT). The ATLIT is a modified Piper Seneca airplane having a GA(W)-1 wing
section, full-span Fowler flap, and roll-control spoilers. The ATLIT has
completed initial flight tests at Langley and the results are presented in
reference 2. After the flight tests, the airplane was recently installed in
the Langley full-scale tunnel for further investigation. The wind-tunnel
investigation covered a broad range of objectives and included tests to
determine winglet performance, propeller performance using a propeller balance,
drag and drag cleanup, and pressure and boundary-layer flow characteristics.
This paper presents a sample of some of the pressure and boundary-layer data
measured on the ATLIT wing and correlates these results with two-dimensional
GA(W)-1 airfoil data.

C_p pressure coefficient, $\dfrac{p - p_\infty}{q_\infty}$

c local wing chord

$\bar{c}$ mean aerodynamic chord

c_n section normal-force coefficient, $\displaystyle\int (C_{p,ls})\ d\left(\dfrac{x}{c}\right) - \int (C_{p,us})\ d\left(\dfrac{x}{c}\right)$

p local static pressure

p_∞ free-stream static pressure

q_∞ free-stream dynamic pressure

u local velocity in chordwise direction

u_e velocity at edge of boundary layer

x distance in chordwise direction

y distance above surface of wing

α angle of attack

α_e effective angle of attack

δ boundary-layer thickness

δ^* displacement thickness

Subscripts:

ls   lower surface

us   upper surface

TEST CONDITIONS

Wind-tunnel tests of the ATLIT airplane were conducted over an angle-of-attack range from 0° to 10° to obtain pressure distributions and boundary-layer velocity distributions on the wing and wake momentum surveys behind the wing. The winglets and propellers were removed for this phase of the test. Pressure measurements were obtained by mounting belts of plastic tubing having an outside diameter of 4.75 mm (0.1875 in.) on the left wing at several semispan locations. Boundary-layer measurements were obtained using a boundary-layer mouse consisting of a series of total head probes set at different heights above the surface. Wake momentum measurements were obtained using a wake rake

of 120 total head probes set 6.35 mm (0.25 in.) apart. In addition to the total head probes, six static probes measured the static pressure variation in the wake. Test conditions for the study included a Reynolds number of 3.39×10^6 and a free-stream velocity of 78 knots (90 mph), which corresponds to about the climb speed of the airplane. Figure 1 shows the ATLIT with winglets mounted in the Langley full-scale tunnel.

FACTORS INFLUENCING APPLICATION OF TWO-DIMENSIONAL AIRFOIL DATA

It is well known that many factors must be considered in the application of two-dimensional airfoil data to a finite wing. The three-dimensional effects of a finite wing change the local flow conditions on the wing section through such factors as tip shape, planform shape, and twist distribution. A lifting-line method, documented in reference 3, was used with inputs of the ATLIT wing planform and twist distribution to determine the effects of these configuration features on local angle of attack. Results of the calculations are shown in figure 2 as a plot of the effective angle of attack against semispan location for several airplane angles of attack. As would be expected, the results show a reduction in local effective angle of attack, especially near the wing tip. Lifting-line theory was used for a quick estimate of local induced angle of attack for the wing only and does not take into account interference effects and variation of downwash in the chordwise direction.

Interference effects from components such as the fuselage, nacelles, and flap brackets also influence the performance of airfoils on wing sections. On general aviation light twin-engine airplanes, such as the ATLIT, treatment of the nacelle area on the wing is critical to the span loading and resulting aerodynamic performance of the airplane. Interference effects and section lift losses must be minimized for optimum cruise and climb performance. The section lift loss in the nacelle region is illustrated in figure 3, where the measured span loading is compared with predicted span loading for the ATLIT wing without nacelles. The span loading was obtained by integrating the pressure distributions at several spanwise stations and is shown as a plot of $c_n c/\bar{c}$ against semispan location. The comparison of measured and theoretical data of figure 3 indicates a severe loss in section lift due to the interference effects of the nacelle. Such lift losses and distortions of the span load distribution have severe adverse effects on the aerodynamic efficiency of the wing.

Another factor that influences the application of two-dimensional airfoil data is the difference between "real world" airfoils and the two-dimensional airfoils tested in wind tunnels. These differences include airfoil coordinate deviations due to manufacturing tolerances, surface contour irregularities such as rivet heads, and surface cutouts for aerodynamic controls such as flaps, ailerons, and spoilers. Several wing section contours were measured on the ATLIT (see ref. 2); the coordinates at the 70-percent-semispan location of the left wing are compared with the GA(W)-1 airfoil coordinates in figure 4. The contours of figure 4 show that there is generally good agreement between the ATLIT and the GA(W)-1 airfoil section, especially on the upper surface;

however, on the lower surface near the trailing edge, the ATLIT thickness is twice the thickness of the GA(W)-1 section. The discrepancy in the airfoils at the wing trailing edge is due to the full-span Fowler flap used on the ATLIT wing. Because of manufacturing tolerances on the ATLIT wing, there is a gap at the trailing edge between the flap and wing when the Fowler flap is fully retracted.

PRESSURE DATA

Pressure distributions were obtained on the ATLIT at six semispan stations on the left wing. Pressure distributions measured at a station located at 75 percent of the ATLIT wing semispan and of a two-dimensional airfoil (ref. 1) are compared in figures 5 and 6 for normal-force coefficients representative of cruise and climb, respectively. The comparison shows that the two- and three-dimensional pressure distributions are similar in shape; however, on the lower surface, there is a slight discrepancy in the pressure data, which may be due to coordinate differences or to contour and thickness changes brought about by the addition of the pressure belt to the ATLIT surface. This discrepancy in the lower surface pressures was investigated by using a two-dimensional viscous theory (ref. 4) to predict the pressure distributions while taking into account the thickness of the pressure belt. In figures 7 and 8, results of the calculations are compared with pressures measured at 75 percent of the ATLIT wing semispan. The comparison of figures 7 and 8 shows better overall agreement than that of figures 5 and 6, but the discrepancy in the pressures on the lower airfoil surface is still present.

Pressure data at the 50-percent-semispan station near the nacelle are compared with data from two-dimensional measurements (ref. 1) in figure 9. A comparison of the pressure distributions shows a noticeable difference between the three-dimensional and two-dimensional data, particularly on the upper surface. The differences in the two- and three-dimensional results are believed to be caused by the aerodynamic interference effects of the nacelle on the ATLIT wing at the 50-percent-semispan location.

In summary, pressure distributions at the 75-percent-semispan station of the ATLIT wing were generally similar to those for the two-dimensional airfoil. However, the pressure data indicated that at the 50-percent-semispan location, the flow field of the ATLIT wing was drastically affected by the presence of the nacelle.

BOUNDARY-LAYER DATA

Boundary-layer measurements were made at the 75-percent-semispan station of the left wing for chordwise positions from 15 percent to 70 percent of the chord. The measurements were obtained on the wing with the airplane in an "in service" condition. The results of the boundary-layer measurements, in the form of velocity distributions at several chordwise positions, are presented

in figure 10 for a wing-section angle of attack of 0°. The ratio of the velocity at each height u to the velocity at the edge of the boundary layer u_e is plotted for each chordwise station against height y normalized by the boundary-layer thickness δ. The results of figure 10 show two distinct characteristics: (1) the data collapsed into one curve (dashed line) for chordwise stations forward of the 30-percent chord and (2) the data showed a fuller profile indicated by the solid lines for chordwise stations aft of the 35-percent chord. This fullness in the profiles aft of the 35-percent chord is indicative of turbulent flow, and the data in this figure imply that transition occurred between the 30-percent and the 35-percent chord.

The transition point is also indicated from figure 11 in which the velocity ratio u/u_e is cross-plotted from figure 10 at a height very close to the surface. This plot shows that the velocity ratio decreases from the leading edge to the 30-percent chord and then increases from the 30-percent to the 40-percent chord. The sudden increase in boundary-layer velocity indicates transition in this region.

A plot of displacement thickness as a function of x/c is shown in figure 12. Theoretical results from a two-dimensional viscous theory (ref. 4) indicate that an ideally smooth GA(W)-1 airfoil exhibits transition at 55-percent chord for an angle of attack of 0°. The measured displacement thickness on the ATLIT indicates that transition was moved forward to about 35-percent chord.

CONCLUDING REMARKS

An investigation was conducted in the Langley full-scale tunnel to measure the aerodynamic characteristics of an Advanced Technology Light Twin-Engine Airplane (ATLIT). Pressure distributions and boundary-layer characteristics of the ATLIT airplane were compared with results from two-dimensional experimental and theoretical investigations. At the 75-percent-semispan location of the ATLIT wing, good correlation was obtained among the experimental and theoretical two-dimensional and the experimental three-dimensional pressure distributions. At the 50-percent-semispan location, the two-dimensional and three-dimensional pressure distributions differed because of interference effects of the nacelle on the wing.

Boundary-layer data indicated that laminar flow was obtained on the ATLIT wing to at least the 30-percent chord for an "in service" condition airplane.

REFERENCES

1. McGhee, Robert J.; and Beasley, William D.: Low-Speed Aerodynamic
   Characteristics of a 17-Percent-Thick Airfoil Section Designed for
   General Aviation Applications. NASA TN D-7428, 1973.

2. Holmes, Bruce J.: Flight Evaluation of an Advanced Technology Light
   Twin-Engine Airplane (ATLIT). NASA CR-2832, 1977.

3. Smetana, Frederick O.; Sumney, Delbert C.; Smith, Neill S.; and Carden,
   Ronald K.: Light Aircraft Lift, Drag, and Moment Prediction - A Review
   and Analysis. NASA CR-2523, 1975.

4. Stevens, W. A.; Goradia, S. H.; and Braden, J. A.: Mathematical Model
   for Two-Dimensional Multi-Component Airfoils in Viscous Flow. NASA
   CR-1843, 1971.

Figure 1.- ATLIT installed in Langley full-scale tunnel.
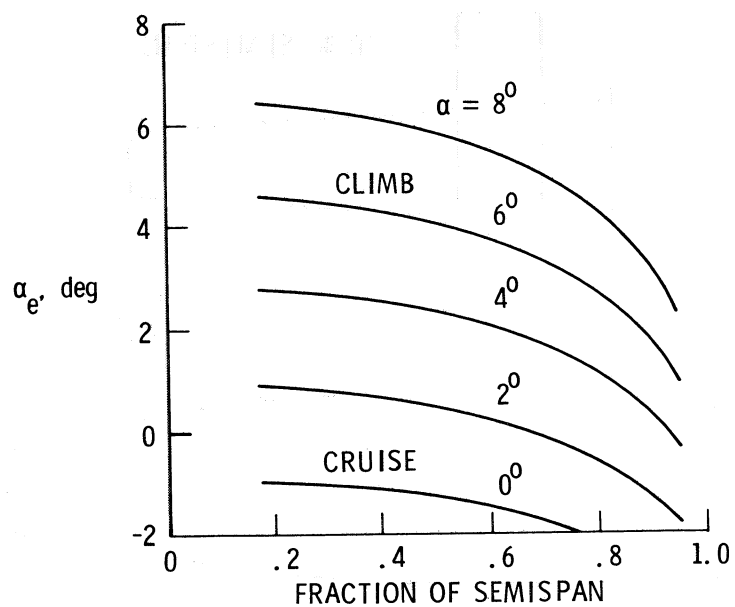
Figure 2.- Local effective angle of attack for ATLIT wing from lifting-line theory (ref. 3).
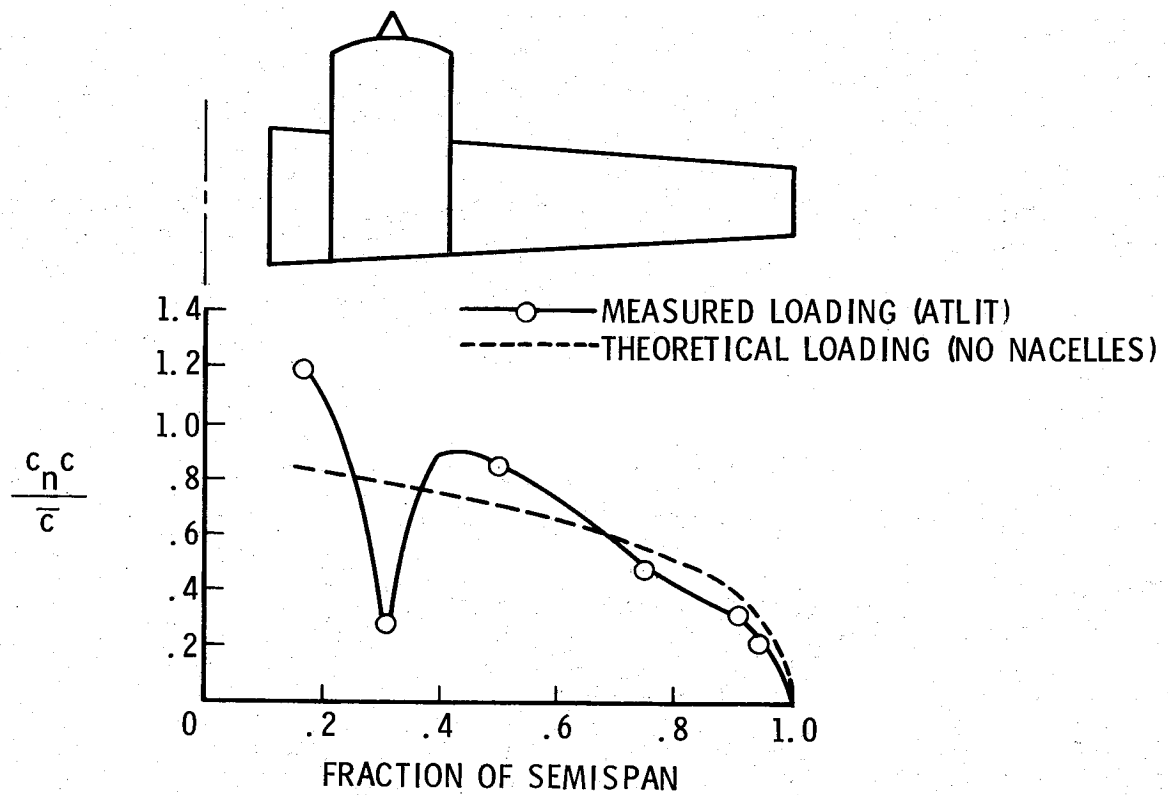
Figure 3.- Span loading on ATLIT wing.
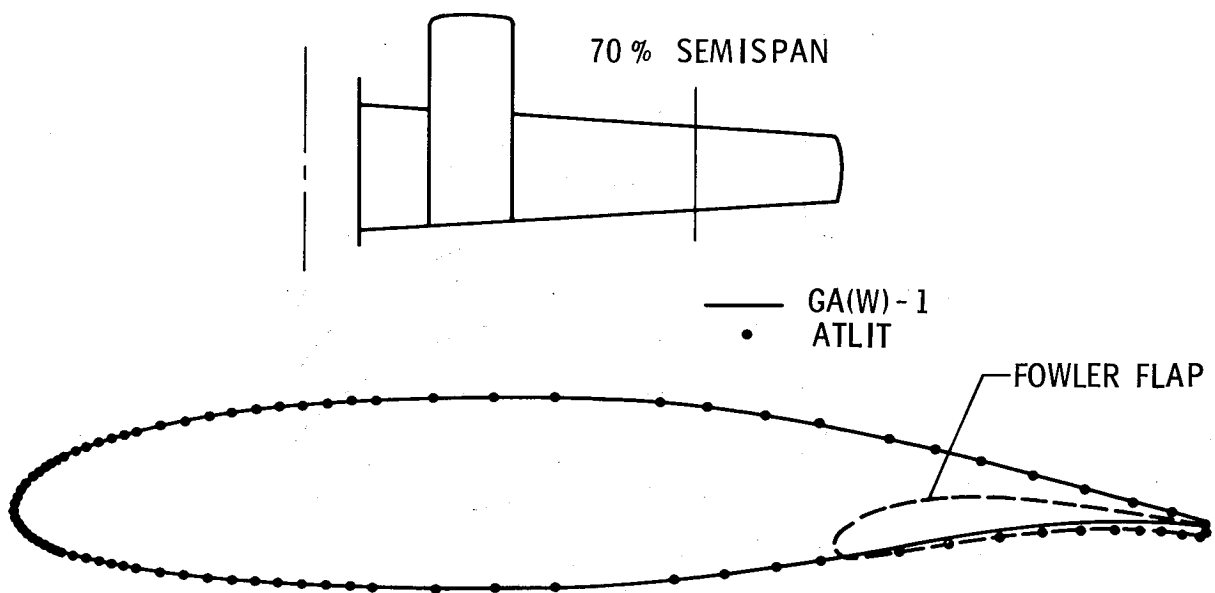
Figure 4.- Wing section contour measured on ATLIT wing at
70-percent semispan.
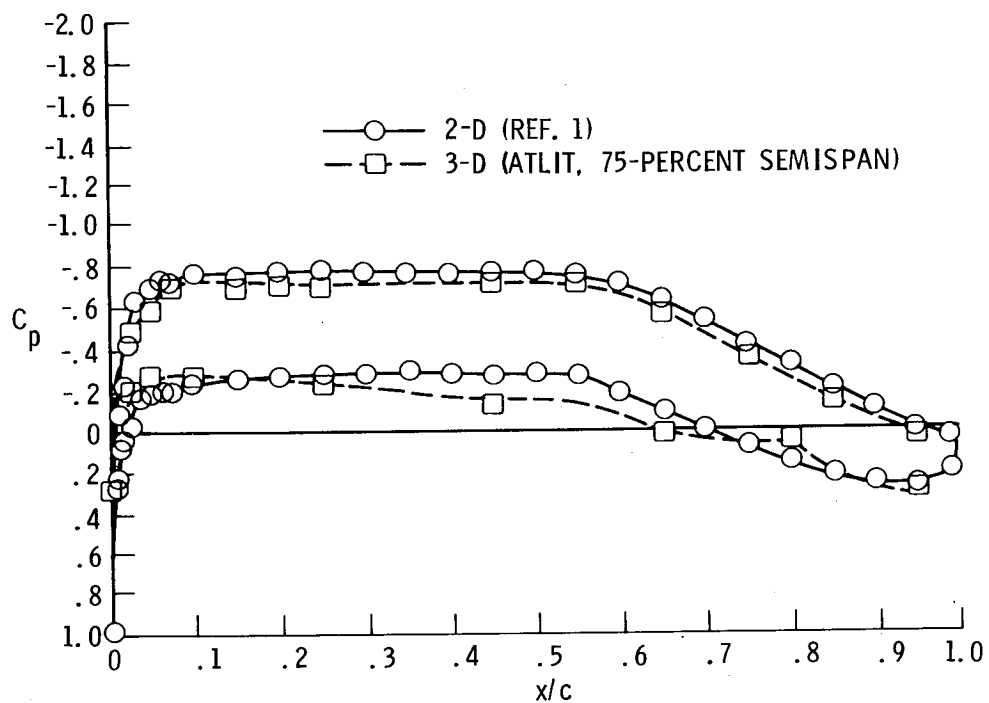
Figure 5.- Chordwise pressure distributions compared with experimental two-dimensional airfoil data. $c_n = 0.4$.
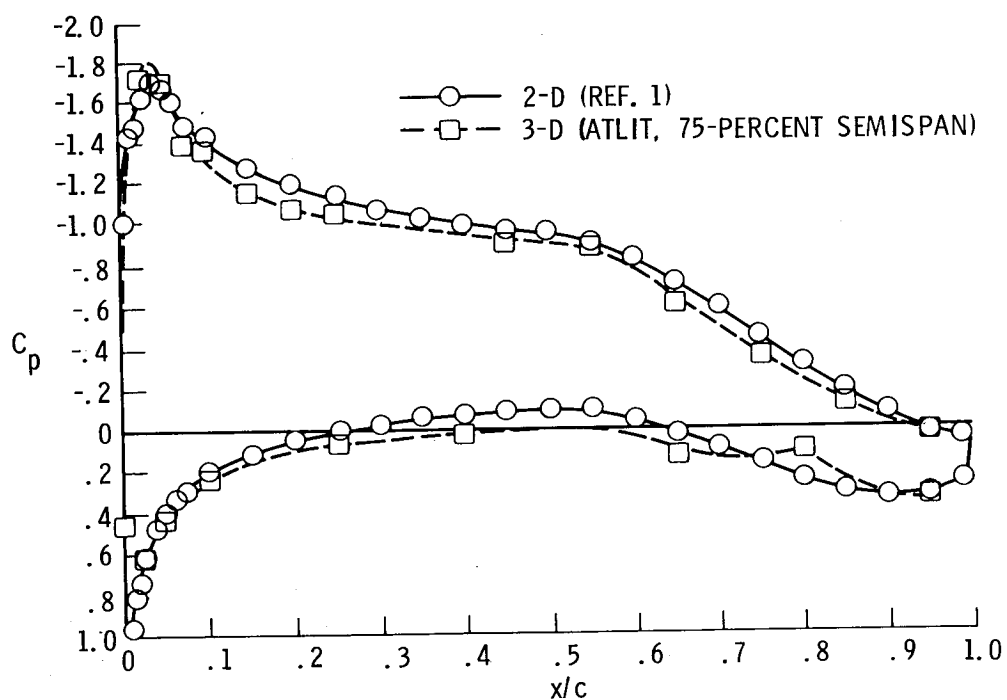
Figure 6.- Chordwise pressure distributions compared with experimental two-dimensional airfoil data. $c_n = 0.9$.

41
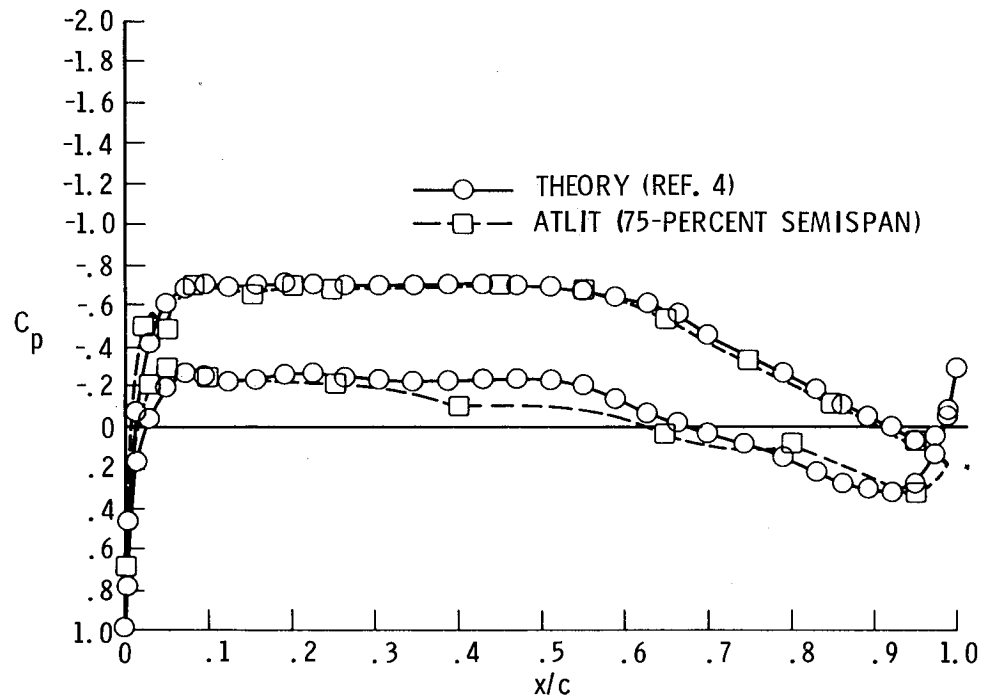
Figure 7.- Chordwise pressure distributions compared with theory. $c_n = 0.4$.
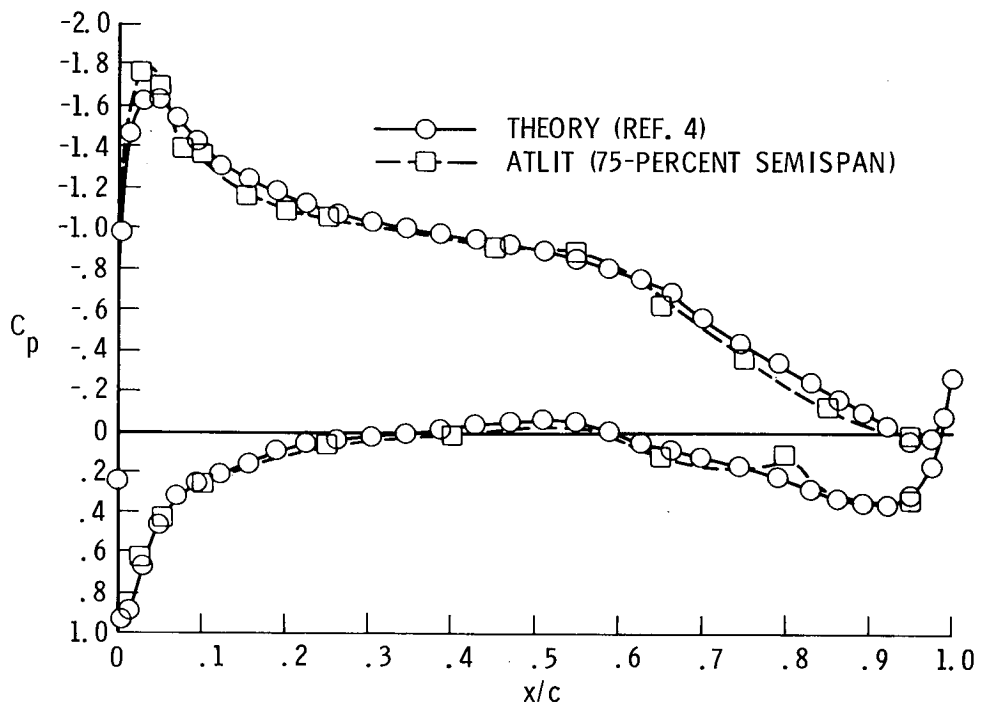
Figure 8.- Chordwise pressure distributions compared with theory. $c_n = 0.9$.
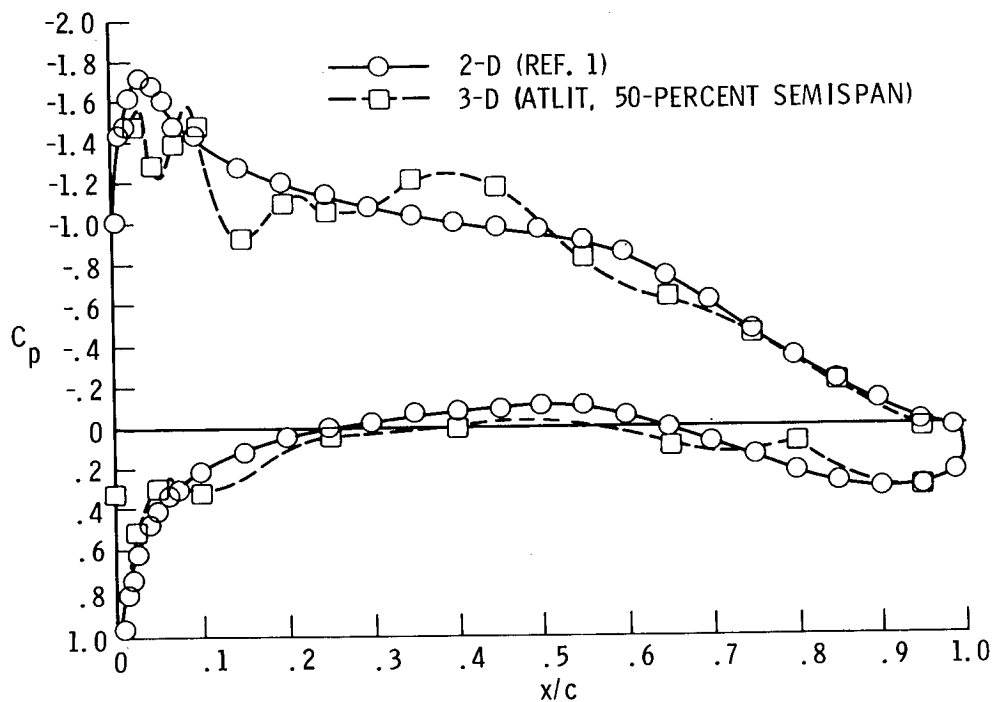
Figure 9.- Chordwise pressure distributions at 50-percent semispan compared with experimental two-dimensional airfoil data. $c_n = 0.9$.
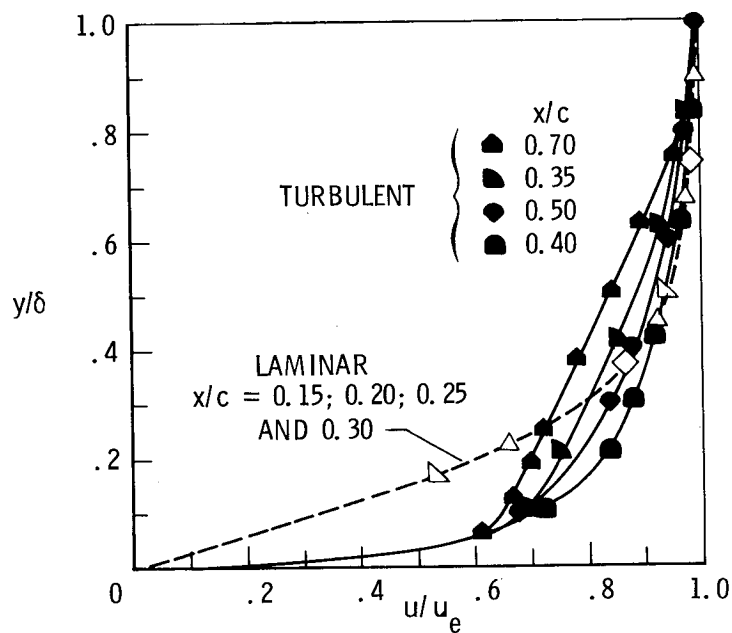
Figure 10.- Measured velocity distribution in boundary layer at 75-percent semispan. $\alpha = 0^o$.
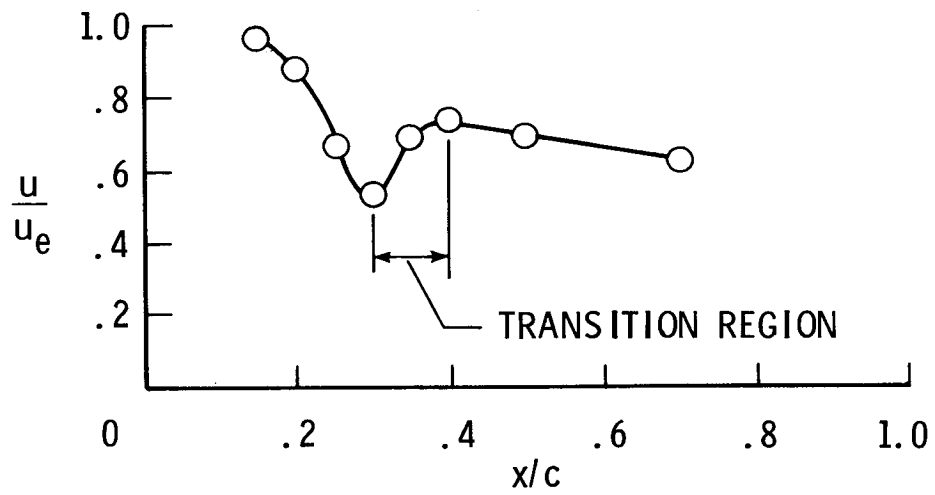
Figure 11.- Velocity ratio along chord at y = 0.064 cm (0.025 in.).
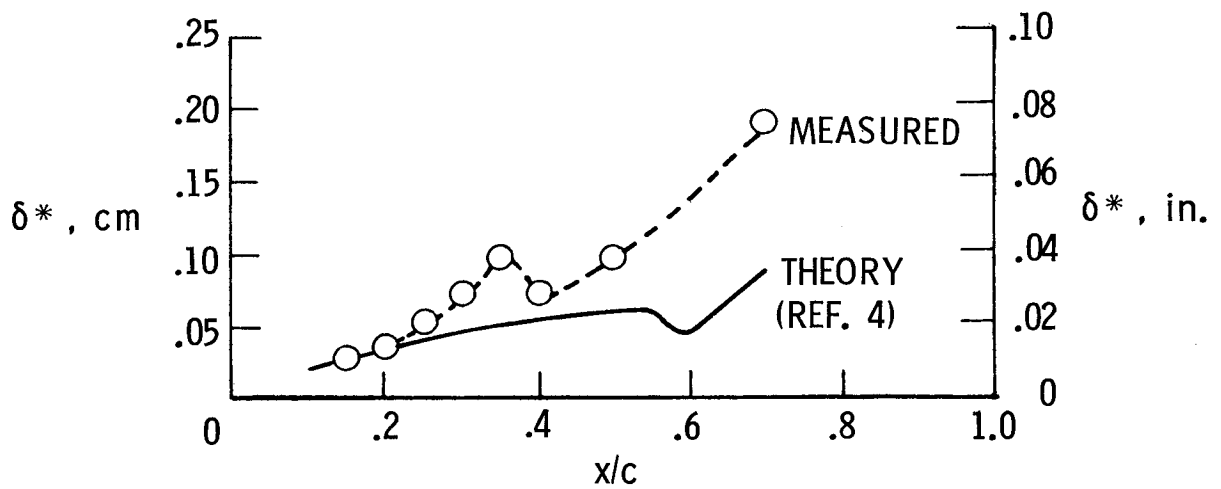
Figure 12.- Measured displacement thickness compared with theory at α = 0°.

AN EVALUATION OF NUMERICAL OPTIMIZATION
IN SUPERCRITICAL AIRFOIL MODIFICATION
AND DESIGN*

Manuel E. Lores, Kenneth P. Burdges, George D. Shrewsbury
Lockheed-Georgia Company

Raymond M. Hicks
Ames Research Center, NASA

SUMMARY

Numerical optimization was used with an inviscid, full potential equation, transonic flow analysis computer code to design two contour modifications of a representative C-141 airfoil section. One modification consisted of a re-design of the forward 12% of the airfoil upper surface and the other was a change of the entire airfoil upper surface. The baseline and the two modified airfoils were tested in the Lockheed-Georgia Compressible Flow Wind Tunnel. Analyses of the experimental and theoretical data showed that the leading edge modification performed as expected, but that the upper surface re-design failed to achieve its predicted performance. This failure is shown to be attributable to the inability of the viscous transonic airfoil analysis code used in this study to treat the trailing edge flow which resulted when the entire upper surface was re-designed.

INTRODUCTION

Efficient transonic performance continues to be an important design requirement for many new aircraft. Specialized airfoils whose contours are dependent upon design conditions are needed to achieve the desired transonic performance. To design the airfoils rapidly and effectively, aerodynamicists must have accurate and easy-to-use theoretical design methods. The numerical optimization technique which originated at NASA-Ames (refs. 1, 2, and 3) offers a means for developing the needed transonic theoretical design method. In this approach, a minimization scheme is coupled with aerodynamic analysis methods to design airfoils which are in some sense optimized for specific flight conditions. Since analysis methods are used, the need to specify a priori a design pressure distribution can be avoided. Also, because analysis methods applicable to mixed transonic flows are available, the technique is not limited to shock-free flows. In the current study, the inviscid full potential equation transonic airfoil analysis code developed by Jameson (ref. 4) was used to provide the needed aerodynamics.

The purpose of the work reported herein was to determine the applicability of numerical optimization using inviscid aerodynamics in both a limited and an extensive re-design of a conventional airfoil to improve its transonic performance. The specific design problem selected was the re-contouring of (1) the forward 12% of the upper surface of·a representative C-141 airfoil, and (2) the entire airfoil upper surface. This problem was selected because a leading edge modification of the C-141 wing is being investigated as a means to improve that aircraft's efficiency and a test program was already planned. The data from that test would serve as a standard against which the entire upper surface modification could be compared.

In this report, the aerodynamic design of both the leading edge and the upper surface modifications using numerical optimization are discussed, the wind tunnel model design and test are described, the performances of the re-designed airfoils are compared with that of the baseline airfoil, and the design procedure is evaluated. A more complete discussion of the leading edge modification and the upper surface re-design can be found in reference 5.

SYMBOLS

Values are given both in SI and U.S. Customary Units. The measurements and calculations were made in U.S. Customary Units.

C	airfoil chord
C_p	pressure coefficient
c_d	section drag coefficient
c_{d_w}	section wave drag coefficient
c_m	section pitching-moment coefficient about quarter chord
c_n	section normal-force coefficient
M_∞	free stream Mach number
P	airfoil perturbation shape functions
R_N	Reynolds number based on free stream conditions and airfoil chord
V	optimization design variables
x	coordinate along airfoil chord line measured from airfoil leading edge, cm (in.)
y	coordinate normal to airfoil chord line, cm (in.)

α geometric angle of attack, degrees

τ wind tunnel wall porosity, %

AIRFOIL DESIGN

Problem Definition

The design goals of this study were to minimize the cruise drag of the baseline C-141 airfoil and to increase the drag divergence Mach number and lift coefficient. The section Mach number and lift coefficient corresponding to airplane cruise conditions are 0.72 and 0.57, respectively. The inviscid design condition was established by computing a solution for the baseline airfoil at $M_\infty = 0.72$ and $c_n = 0.57$ using the NYU viscous transonic program (ref. 6), and using the resulting angle of attack ($\alpha = 2°$) as the design α. Consequently, the inviscid design condition was taken to be:

$$M_\infty = 0.72$$

$$\alpha = 2°$$

Numerical Optimization

The upper surface contours needed to attain the design goals were determined using the NASA-Ames aerodynamic numerical optimization scheme. The optimization objective was to minimize inviscid wave drag, c_{d_w}, at the inviscid design conditions.

Four constraints were imposed. The first constraint was that c_{d_w} be less than twenty counts at $M_\infty = 0.74$ and $\alpha = 2°$. This constraint was used to obtain an airfoil with good off-design performance and to increase the drag divergence Mach number by permitting only a modest increase in drag between $M_\infty = 0.72$ and $M_\infty = 0.74$. The second constraint was that c_n be greater than 0.77 so that when viscous effects were taken into account, c_n would be greater than or equal to 0.57. Two geometric constraints were used. The first was that the modified airfoils be at least as thick as the baseline section, and the second was that they retain a certain degree of leading edge bluntness to avoid poor stall characteristics.

Proper selection of design variables is imperative if the design objective is to be efficiently attained in numerical optimization. In the leading-edge modification, a single polynomial representation of the forward 12% of the upper surface was used. The design variables (i.e., the parameters perturbed during the optimization scheme) were the coefficients of the polynomial and/or the exponents in the polynomial terms as shown in figure 1. This approach proved to be successful because only a few terms were required to achieve sufficient design flexibility and hence computation times were small.

However, numerous polynomials which must maintain ordinate and at least first derivative continuity at their match points would be required to provide an entire upper surface parameterization with adequate design flexibility. Such an approach would not only be complex, it would also be computationally expensive. Therefore, an alternative airfoil parameterization scheme was used for the upper surface modification. The scheme was developed by Ames researchers and it involves the use of perturbation shape functions to distort the upper surface contour of the baseline airfoil. The shape functions used in this work are shown in figure 2 with their defining equations. In this case, the design variables are the pre-multiplying coefficients which determine the magnitude of the individual shape functions. These pre-multiplying (or participation) coefficients are adjusted by the optimization scheme until the design objective is met without violating the constraints. Thus, twelve (12) geometric design variables were used in this study. Eleven are the coefficients and the twelfth was an exponent term used in the first two shape functions to control leading edge bluntness. An additional design variable, the angle of attack, α, was tried and found to be unnecessary.

Optimization Results

The numerical optimization was done by starting with the baseline airfoil at $\alpha = 2°$ and computing solutions for $M_\infty = .72$ and $M_\infty = .74$ for perturbations of the design variables until the design objective and the four constraints were attained. The initial and final pressure distributions for the baseline and the modified airfoils at $M_\infty = .72$ and $M_\infty = .74$ are shown in figure 3. The amelioration of the inviscid flow field and the attendant reduction in wave drag are evident in these data.

The initial and modified airfoil geometries are shown in figure 4. Evident in this figure is the attempt by the optimization scheme to use aft-camber in the upper surface modification. Since the lower surface was fixed, the only way to incorporate aft-camber was to raise the upper surface contour at about the 75% chord station. A half percent chord trailing edge bluntness was also produced by the upper surface modification. Apparent in the geometries is the increased leading edge bluntness used to improve airfoil performance when only the leading edge region was changed.

WIND TUNNEL TESTS

Wind tunnel models having 17.78 cm (7.00 in.) chords and spans of 50.80 cm (20.00 in.) were tested in the Lockheed-Georgia Compressible Flow Wind Tunnel. The tunnel is of the blow-down type, and its test section is 50.80 cm (20.00 in.) wide by 71.2 cm (28.00 in.) high by 183 cm (72.0 in.) long. The top and bottom walls of the two-dimensional test section have variable porosity capability ranging from 0% to 10% porosity. The 2-D test section side walls are solid.

Model aerodynamics were obtained from fifty-three (53) airfoil surface static-pressures and a fixed wake-survey rake used for section drag measurements.

The rake has a total of 90 total head measurement tubes and four static pressure tubes. Data were obtained for angles of attack from 0° to 5°, and for Mach numbers between 0.45 and 0.78. Most of the tests were conducted at a nominal chord Reynolds number of 11 million using free transition, and a wind-tunnel wall porosity of 4%. A limited amount of data were obtained for a Reynolds number of 4 million, and for wall porosities between 2% and 6%. The boundary layer was tripped at the 5% chord station on both upper and lower surfaces during the tests at $R_N = 4$ million.

RESULTS

Experiment

The variation of measured drag with Mach number for the three airfoils at $c_n = 0.57$ is shown in figure 5. The following observations can be made from these data:

1. The complete upper surface modification produced the largest drag rise Mach number.

2. For Mach numbers less than the baseline airfoil's drag rise, the upper surface modification has substantially more drag.

3. The leading-edge modification reduces the supercritical drag of the baseline airfoil and increases the drag divergence Mach number.

The reasons for these results can be deduced from the chordwise pressure distributions shown in figure 6. For $M_\infty = 0.55$, the flows are subcritical, and in the absence of any indications of flow separation, the higher drag of the modified airfoil is probably attributable in the main to its blunt trailing edge. The rapid drag increase produced by the upper surface modification at approximately $M_\infty = 0.68$ (fig. 6(b)) can be seen to be due to the formation of a strong leading-edge shock. As M_∞ increases and the design Mach number is approached (fig. 6(c) to 6(e)), the shock on the modified upper surface moves downstream and decreases in strength. At the same time, a shock wave forms on the other two airfoils and increases rapidly in strength. This behavior results in the increased drag divergence Mach number associated with the upper surface modification.

Design Method Evaluation

The performance improvements predicted for the leading edge modification were confirmed in the wind tunnel test. However, even though *inviscid* numerical optimization of the entire upper surface reduced wave drag at the design point, experimental data show that the drag reduction was not realized. The lack of performance by the modified upper surface, then, must be due to adverse viscous effects which were not taken into account. The effects of viscosity were examined by computing solutions using the viscous NYU program and comparing

the solutions with experimental data. The solutions were generated using non-conservative theory with corrected wave drag and employing "default" boundary layer parameters.

The agreement between theoretical drag predictions and experimental data is in general poor, as demonstrated in figure 7. The reasons for this failure can be deduced by comparing theoretical and experimental pressure distributions at the same Mach number and lift coefficient. These data are shown for the baseline and modified upper surface airfoils in figures 8 and 9, respectively.

The results shown in figure 8 indicate that the baseline airfoil pressure distributions are fairly well predicted by theory, with the major discrepancies being the shock location, trailing edge pressure recovery, and the lower surface pressure level. The failure to properly compute the trailing edge pressure recovery is probably due to the large (approximately 20 degrees) trailing edge included angle which produces a thick boundary layer. The NYU code uses a conventional (albeit adjusted) boundary layer method, which is not applicable to thick boundary layers.

The theoretical pressures for the modified upper surface airfoil bear little resemblance to their experimental counterparts, as evidenced by the results shown in figure 9. At $M_\infty = .72$, the entire character of the leading edge shock is missed, while at $M_\infty = .74$, a dual shock is predicted when only one shock occurred. In both cases, the trailing edge pressure recovery is over-predicted; even more so than for the baseline airfoil. Also, the lower surface pressures are under-predicted, but not quite to the same degree which they were missed for the baseline airfoil.

All of these discrepancies are probably attributable mainly to improper modeling of the viscous trailing edge flow. This failure is accentuated for the modified upper surface airfoil because the "hump" in the upper surface produces a reflex in the upper surface contours near the trailing edge. The resulting concavity produces a thicker boundary layer than can be predicted by simple boundary layer theory. This thick boundary layer produces a reduced trailing edge pressure recovery when compared to the baseline airfoil, a result which is not predicted by theory.

Experiences both at Lockheed and elsewhere have shown the NYU code to yield reliable transonic results for other airfoils. Consequently, alternate reasons for the failure to predict the modified upper surface airfoil's aerodynamics were explored. One possibility examined was wind tunnel wall interference. Previous tests in the Lockheed CFWT (including the baseline airfoil tests) indicate that 4% porosity best simulates free-air conditions. Was it possible, however, that good agreement could be attained between theory and experiment using a different wall porosity? This question was answered by using the limited variable porosity data taken in this test and comparing them with theoretical solutions at the same lift coefficients. The result of this side-study was that good agreement could not be found for any porosity (2% to 6%) investigated.

Various computer code options such as quasi-conservative theory and different boundary layer modeling parameters were examined in an attempt to obtain

50

improved correlation. Although some improvements were made, completely satis-factory correlation could not be found. Hence, the observation can be made that an improved transonic viscous airfoil method is required to make airfoil design practical and reliable. The most needed improvement seems to be a better trailing edge flow formulation.

CONCLUDING COMMENTS

The salient results of the study are summarized below:

1. Numerical optimization using inviscid aerodynamics worked well for the re-design of the baseline airfoil's leading edge region.

2. The upper surface modification increased the drag divergence Mach number at the expense of a larger pre-drag-rise drag which is attributable to the premature formation of a relatively strong shock wave.

3. Numerical optimization did produce an upper surface modification with reduced inviscid wave drag. However, viscous analyses failed to predict either the premature shock formation or the airfoil's drag level.

4. The failure of the viscous airfoil analysis method in this application is probably due to its inability to compute the thick trailing edge boundary layer which can be expected to result from the modified airfoil's trailing edge geometry.

5. The use of a quasi-conservative formulation in lieu of the standard non-conservative scheme did not have a significant effect on the theoretical results.

6. The concept of numerical optimization offers an efficient and versatile method for aerodynamic design. However, inviscid optimization should be re-stricted to limited modifications which do not significantly affect the viscous flow (e.g., the leading edge re-design study briefly discussed herein), or to airfoil design for which viscous effects are well-understood.

REFERENCES

1. Vanderplaats, G. N.: CONMIN-A Fortran Program for Constrained Function Minimization - User's Manual. NASA TM X-62282, Aug. 1973.

2. Hicks, J. M. and Vanderplaats, G. N.: Design of Low-Speed Airfoils by Numerical Optimization. SAE Business Aircraft Meeting, Wichita, April 1975.

3. Hicks, R. M.; Mendoza, J. P.; and Bandettini, A.: Effects of Forward Contour Modification on the Aerodynamic Characteristics of the NACA 64, -212 Airfoil Section. NASA TM X-3243, Sept. 1975.

4. Jameson, A.: Iterative Solution of Transonic Flows Over Airfoils and Wings. Comm. Pure Applied Mach, Vol. 27, 1974.

5. Blackerby, W. T. and Carlton, M. E.: Experimental Investigation of Subsonic Creep Drag Phenomena on a Cl41 Airfoil Using Modified Leading Edges. Lockheed–Georgia Rpt. LG78ER0010, March 1978.

6. Bauer, F.; Garabedian, P.; Korn, D.; and Jameson, A.: Supercritical Wing Sections II. *Lecture Notes in Economics and Mathematical Systems*, Vol. 108, Springer–Verlag, New York, 1975.
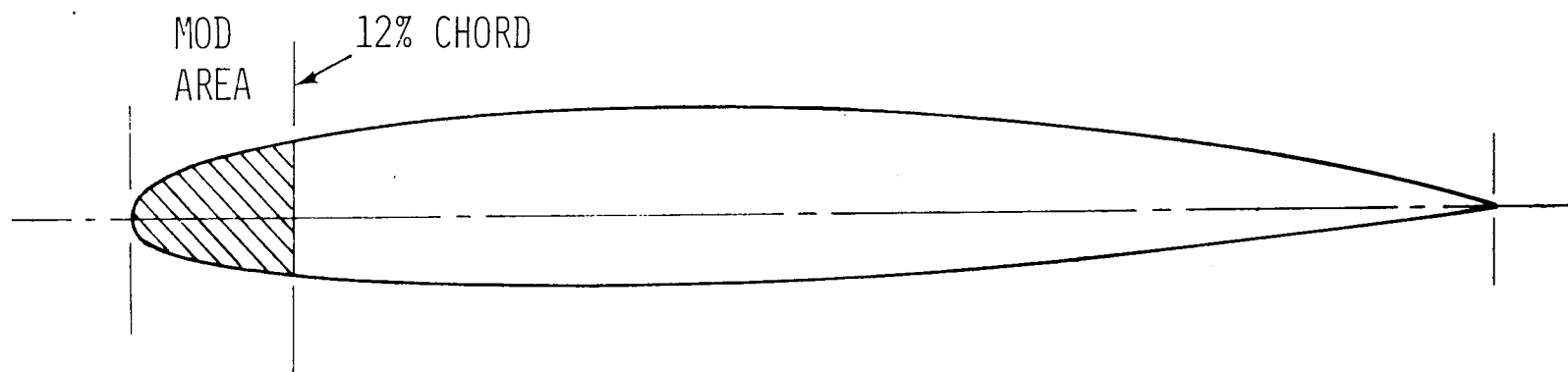
UPPER SURFACE

$$Y = V(1) \cdot X^{V(4)} + F \cdot X + V(2) \cdot X^2 + V(3) \cdot X^3 + FF \cdot X^4$$

Figure 1.- Leading edge parameterization.

TERM	EQUATION
P(1)	$10(1 - X)X^{V(12)}/e^{20X}$
P(2)	$10(1 - X)X^{V(12)}/e^{40X}$
P(3)	$\sqrt{X}(1 - X)/e^{3X}$
P(J), J=4, 10	$\sin^5(X^{n_j})$
P(11)	X^{10}

WHERE X IS INTERPRETED AS X/C

EXPONENT TABLE	
j	n
4	.5757166
5	.7564708
6	1.
7	1.356915
8	1.943358
9	3.106283
10	6.578813

$$y/c = \sum_{N=1}^{11} V(N)\, P(N)$$
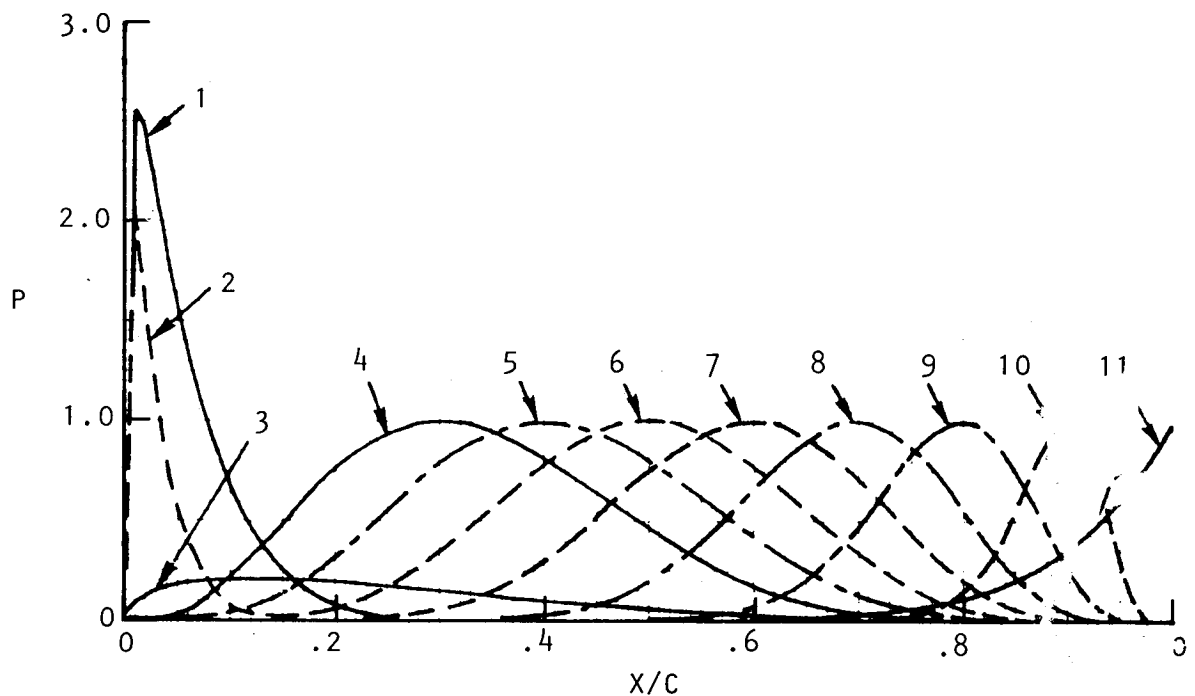
Figure 2.- Upper surface modification; airfoil parameterization.
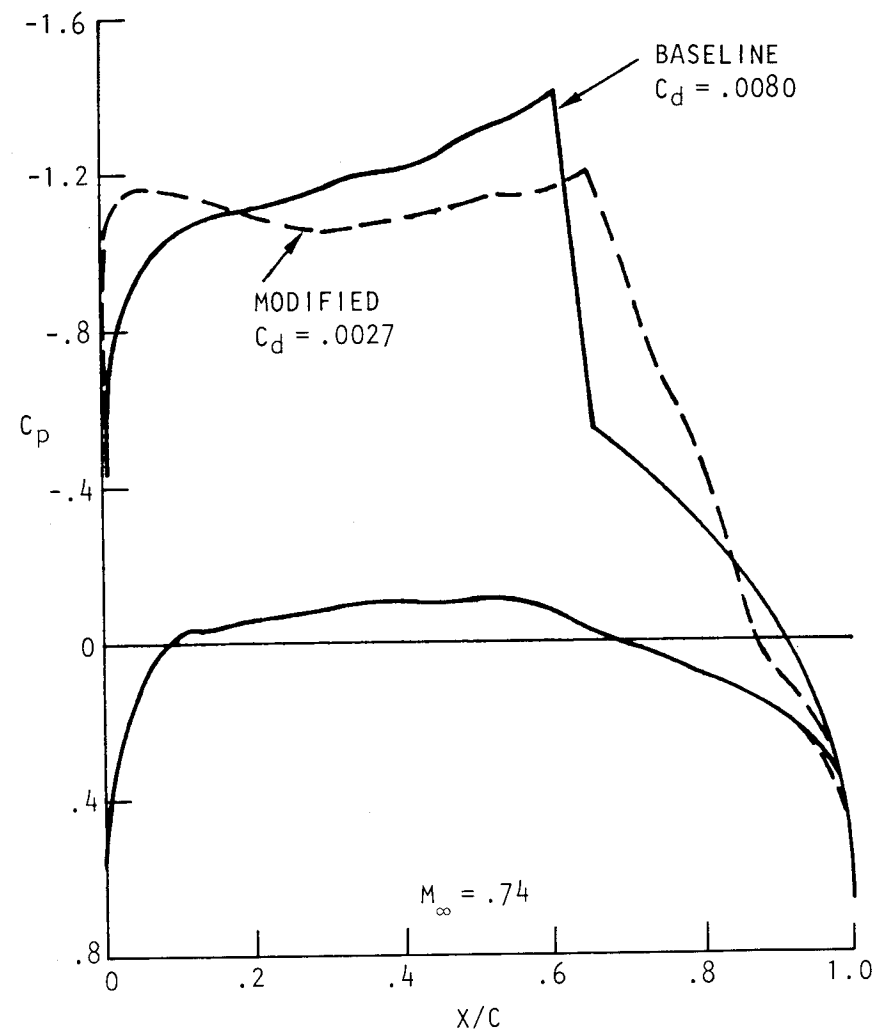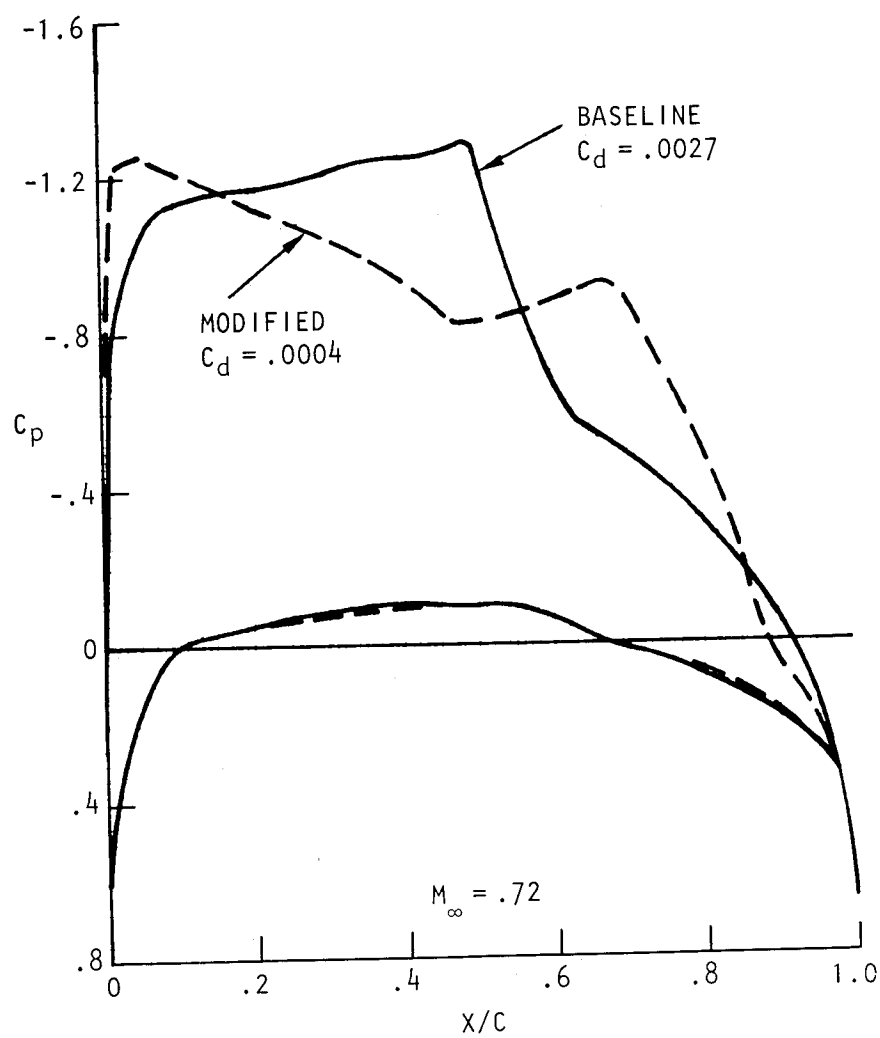
Figure 3.- Upper surface modification; inviscid design pressures. $\alpha = 2^{\circ}$.

BASELINE (——) AND LEADING EDGE MODIFICATION (---)
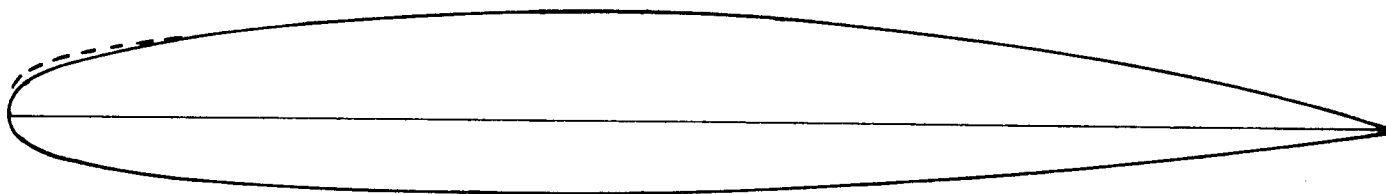
UPPER SURFACE MODIFICATION
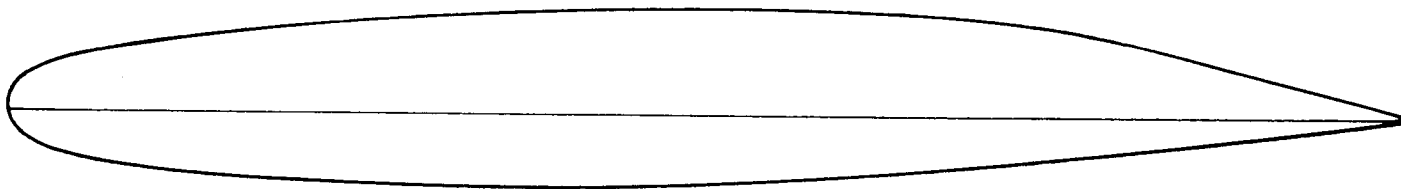
Figure 4.- Comparison of airfoil geometries.

.0180

.0140

c_d

.0100

.0060

MODIFIED UPPER SURFACE

BASELINE

MODIFIED LEADING EDGE

.52   .56   .60   .64   .68   .72   .76   .80

MACH NUMBER, M_∞
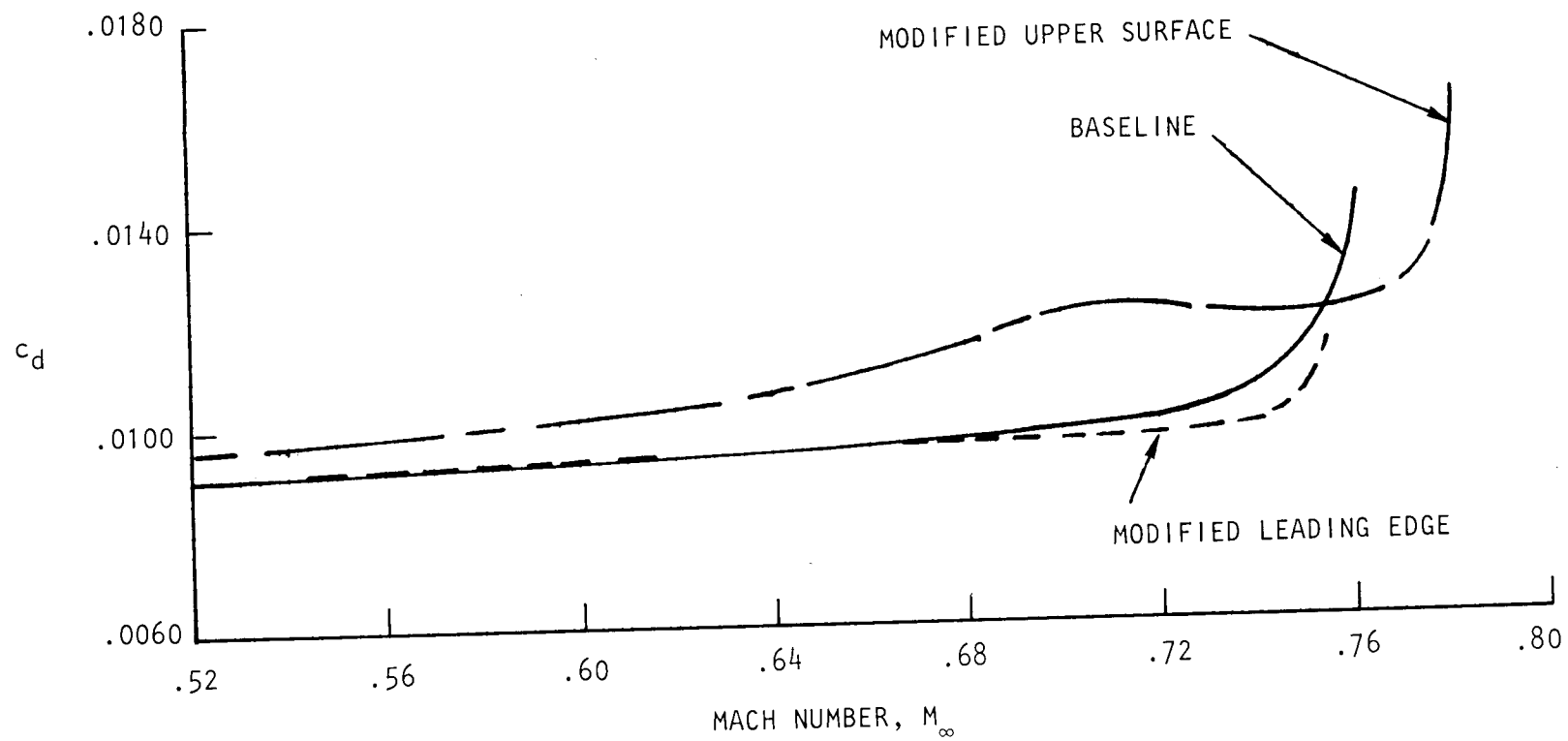
Figure 5.- Comparison of measured airfoil performances at $c_n = 0.57$.
$R_N = 11 \times 10^6$; $\tau = 4\%$.

SYMBOL	AIRFOIL	c_n	c_d	c_m
△	BASELINE	.567	.0092	-.0433
⬡	MOD.	.531	.0090	-.0406
⊡	MOD. U.S.	.569	.0096	-.0417

(a) $M_\infty = 0.55$
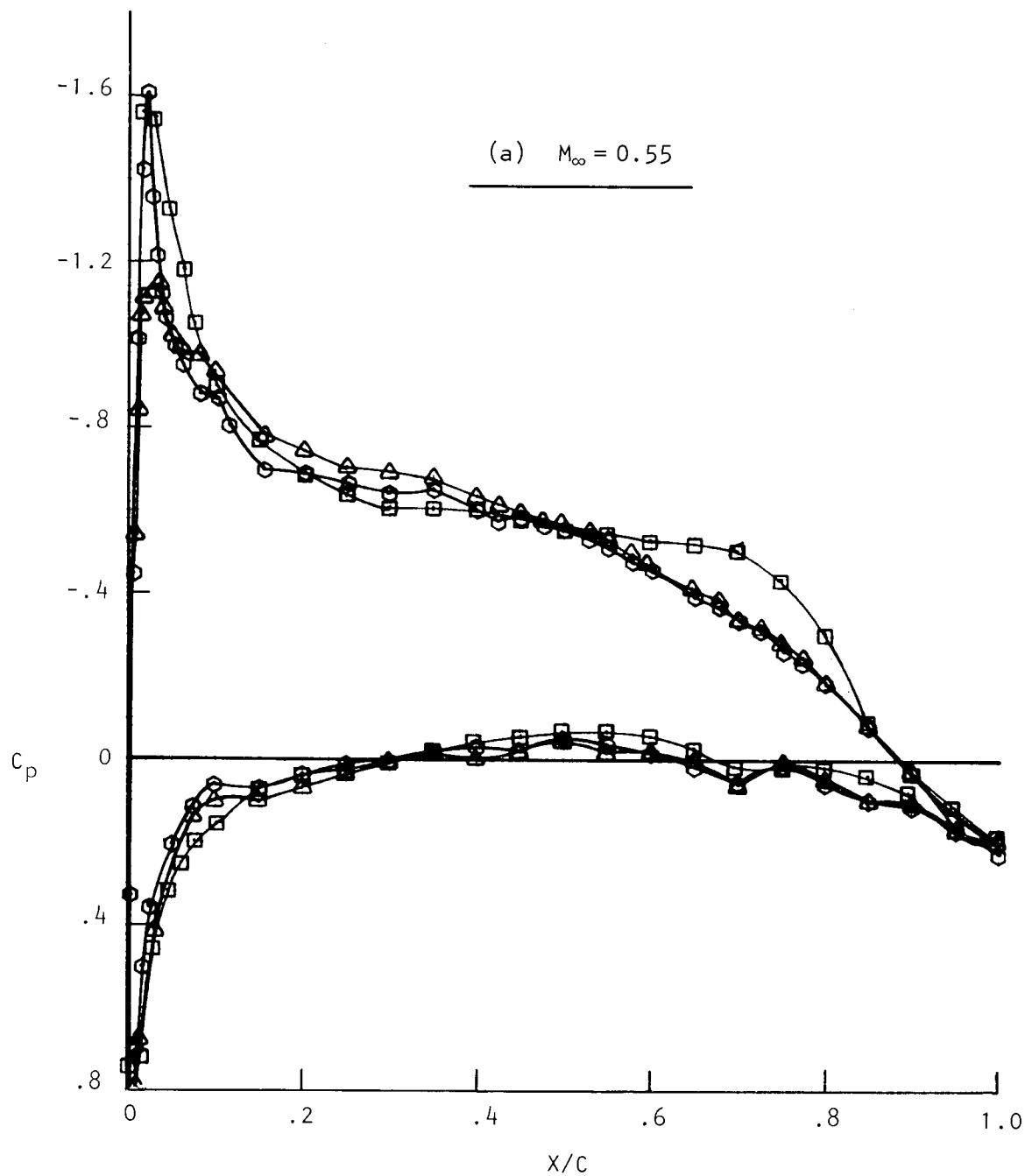
Figure 6.- Comparison of measured airfoil pressures.

SYMBOL	AIRFOIL	C_n	C_d	C_m
△	BASELINE	.562	.0097	-.0431
⬡	MOD L.E.	.579	.0095	-.0373
⊡	MOD U.S.	.558	.0116	-.0333

(b) $M_\infty = 0.68$
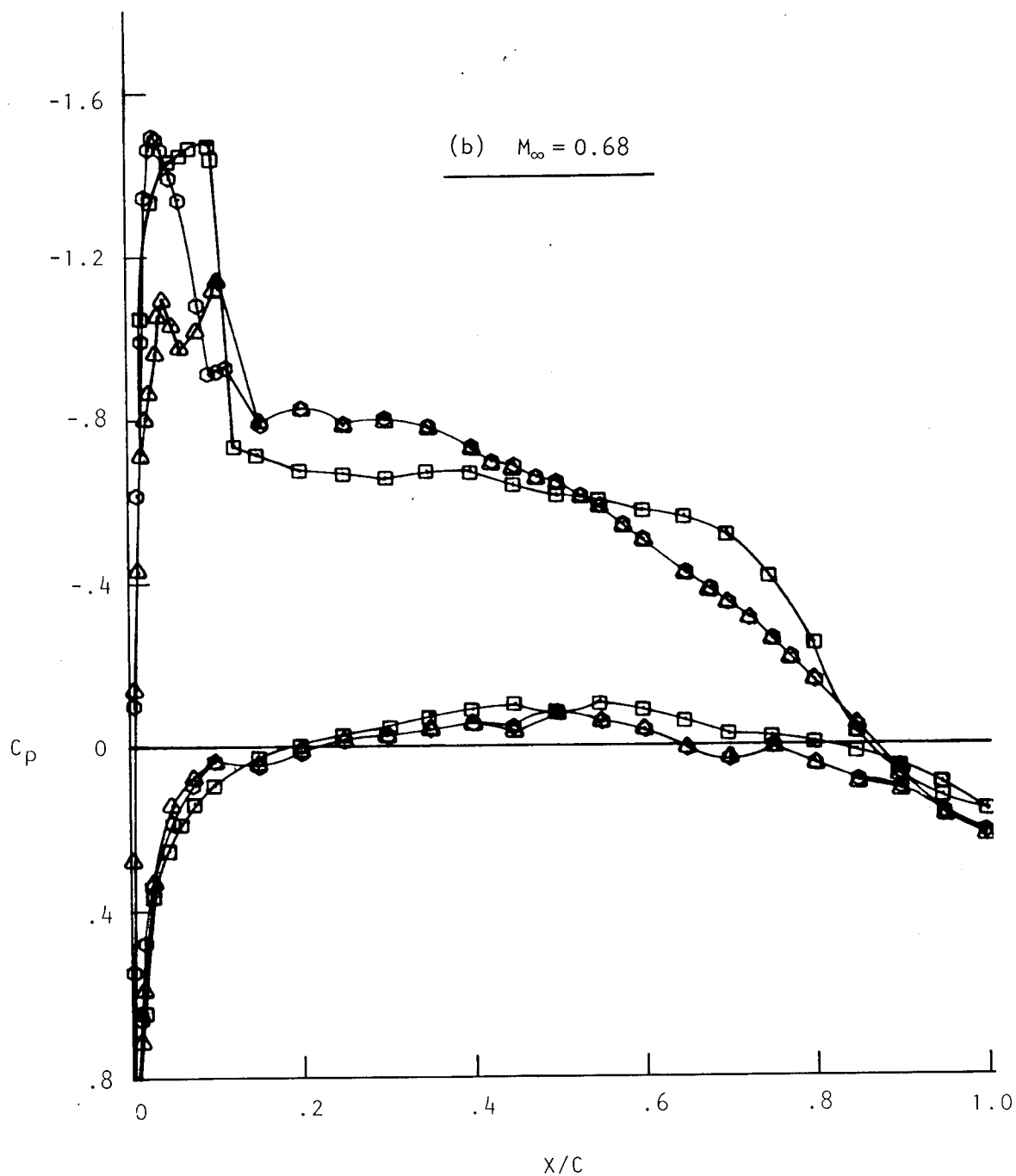
Figure 6.- Continued.

SYMBOL	AIRFOIL	C_n	C_d	C_m
△	BASELINE	.566	.0101	-.0413
⬡	MOD L.E.	.546	.0095	-.0413
⊡	MOD U.S.	.571	.0121	-.0322

(c) $M_\infty = 0.72$
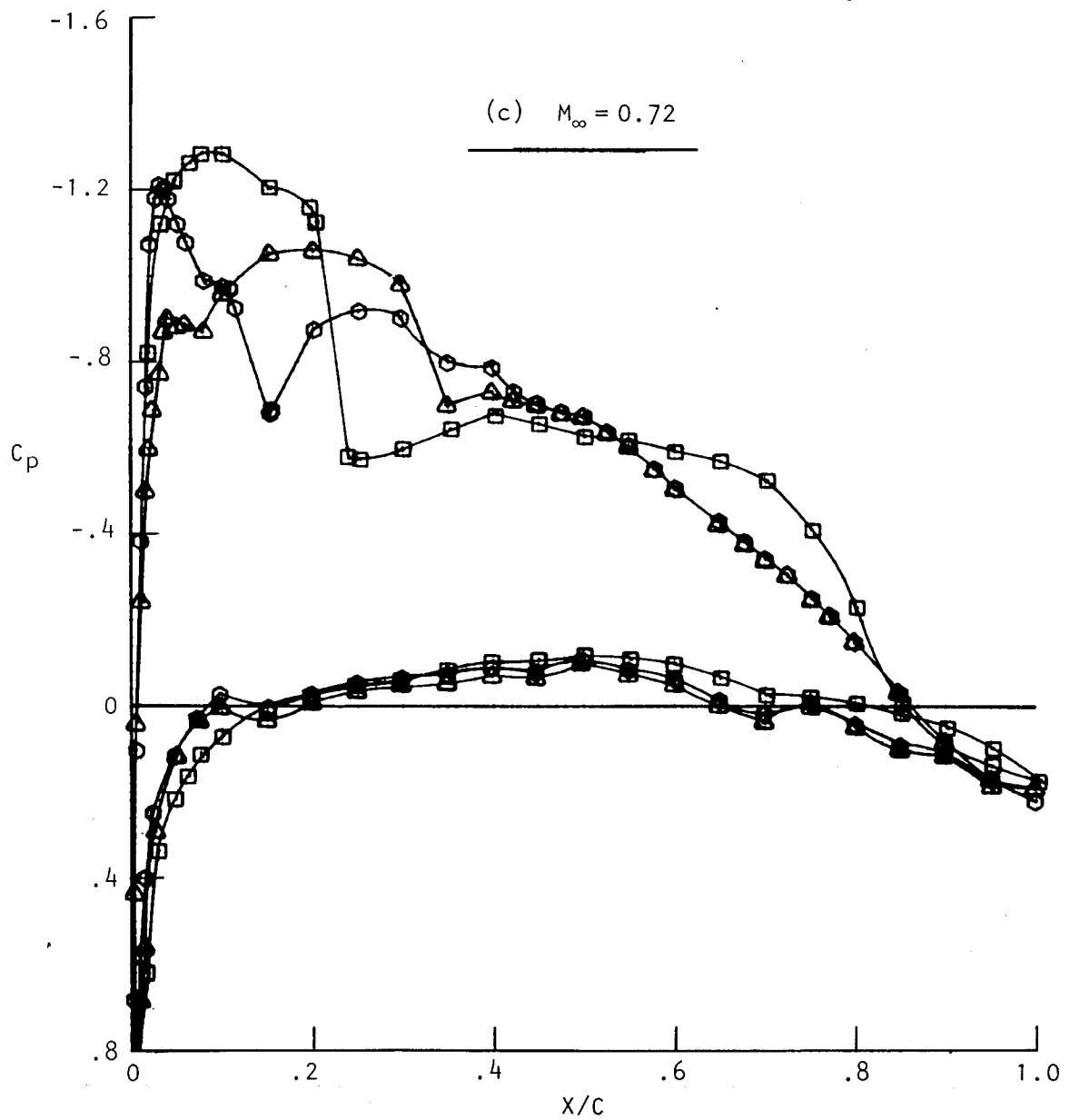
Figure 6.- Continued.

SYMBOL	AIRFOIL	c_n	c_d	c_m
△	BASELINE	.566	.0109	-.0490
⬡	MOD L.E.	.569	.0099	-.0430
⊡	MOD U.S.	.572	.0120	-.0333

(d) $M_\infty = 0.74$
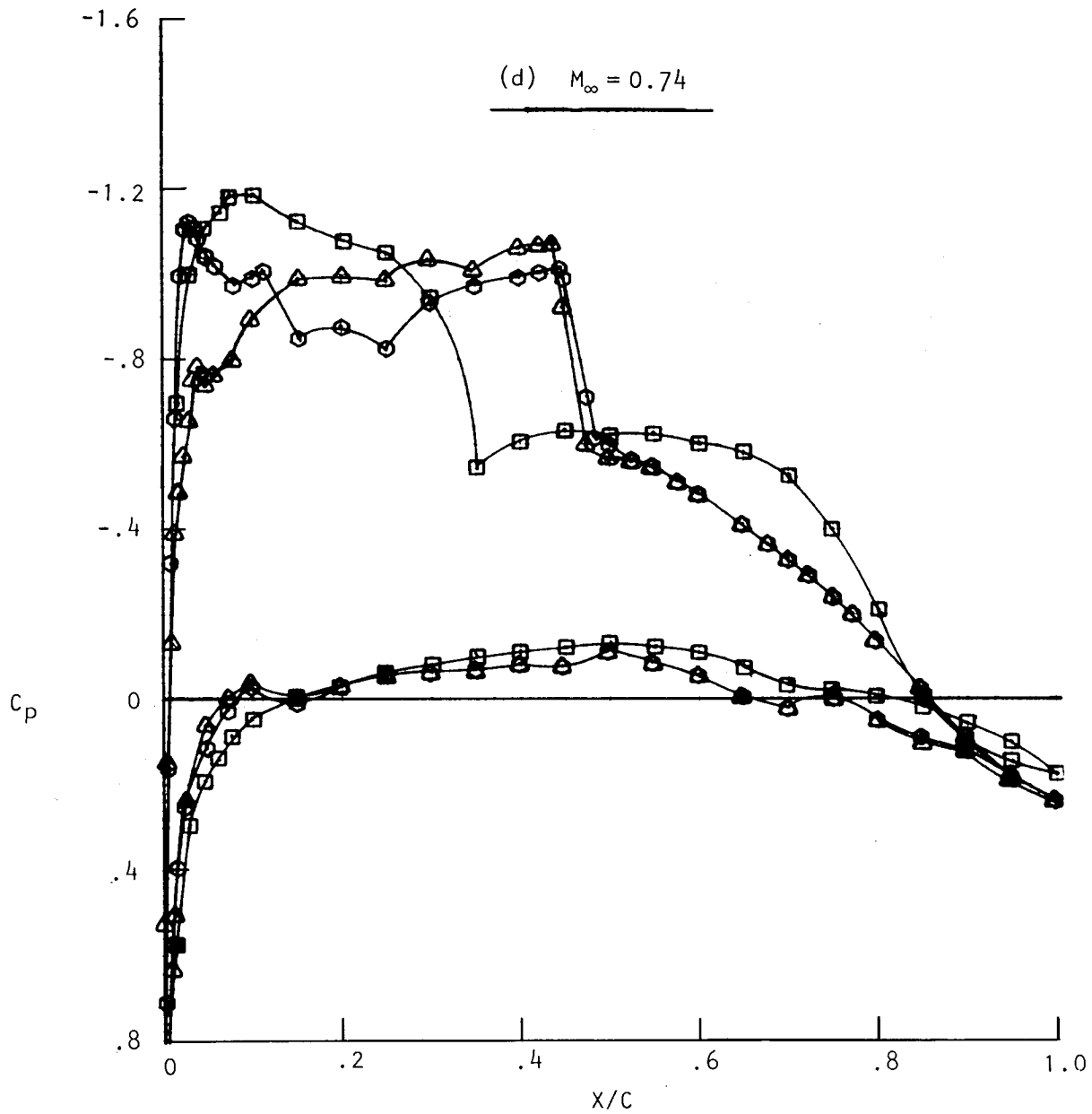
Figure 6.- Continued.

SYMBOL	AIRFOIL	C_n	C_d	C_m
△	BASELINE	.557	.0139	-.0561
⊙	MOD L.E.	.610	.0147	-.0568
⊡	MOD U.S.	.563	.0120	-.0367

(e) $M_\infty = 0.76$
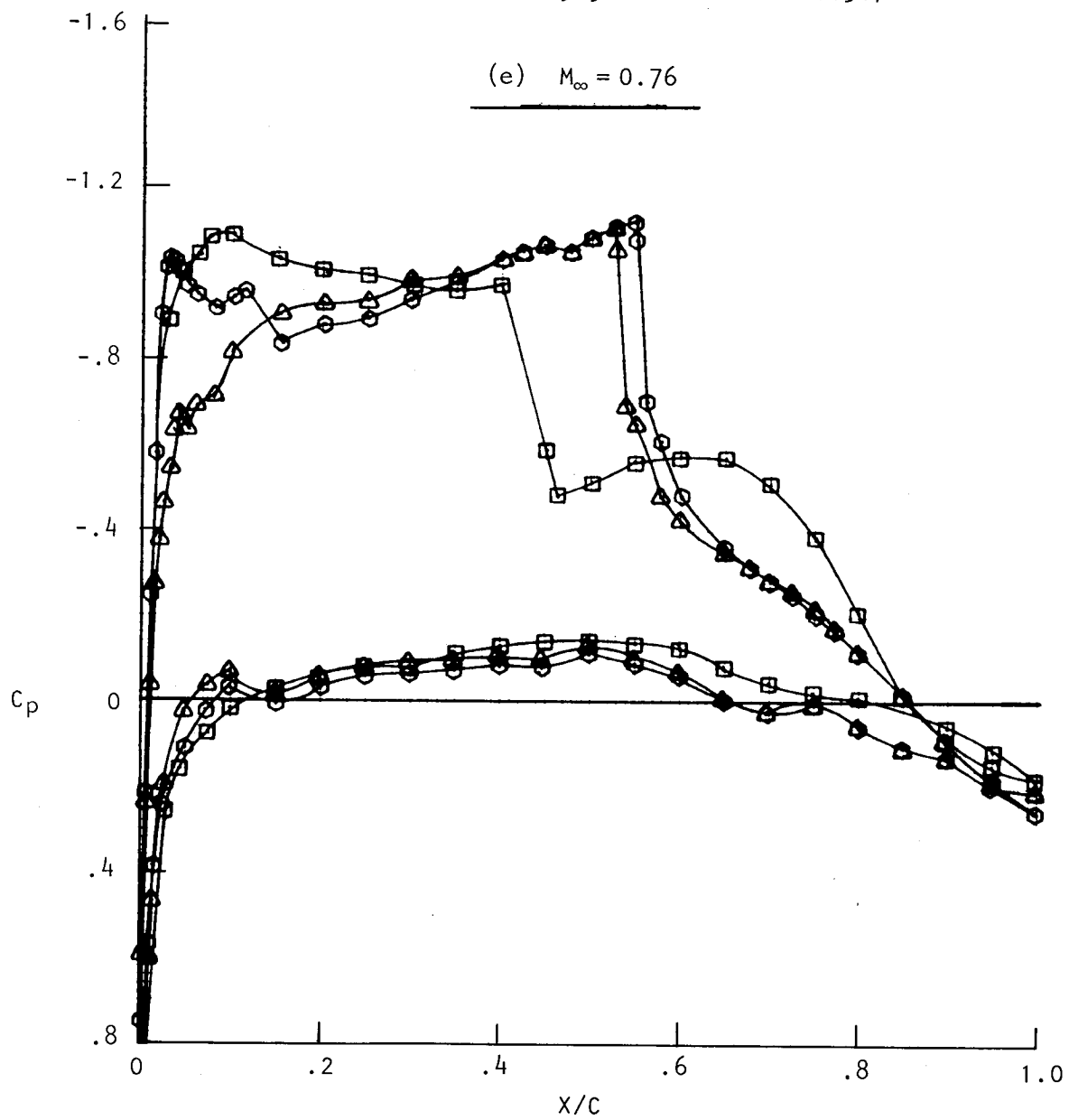
Figure 6.- Concluded.
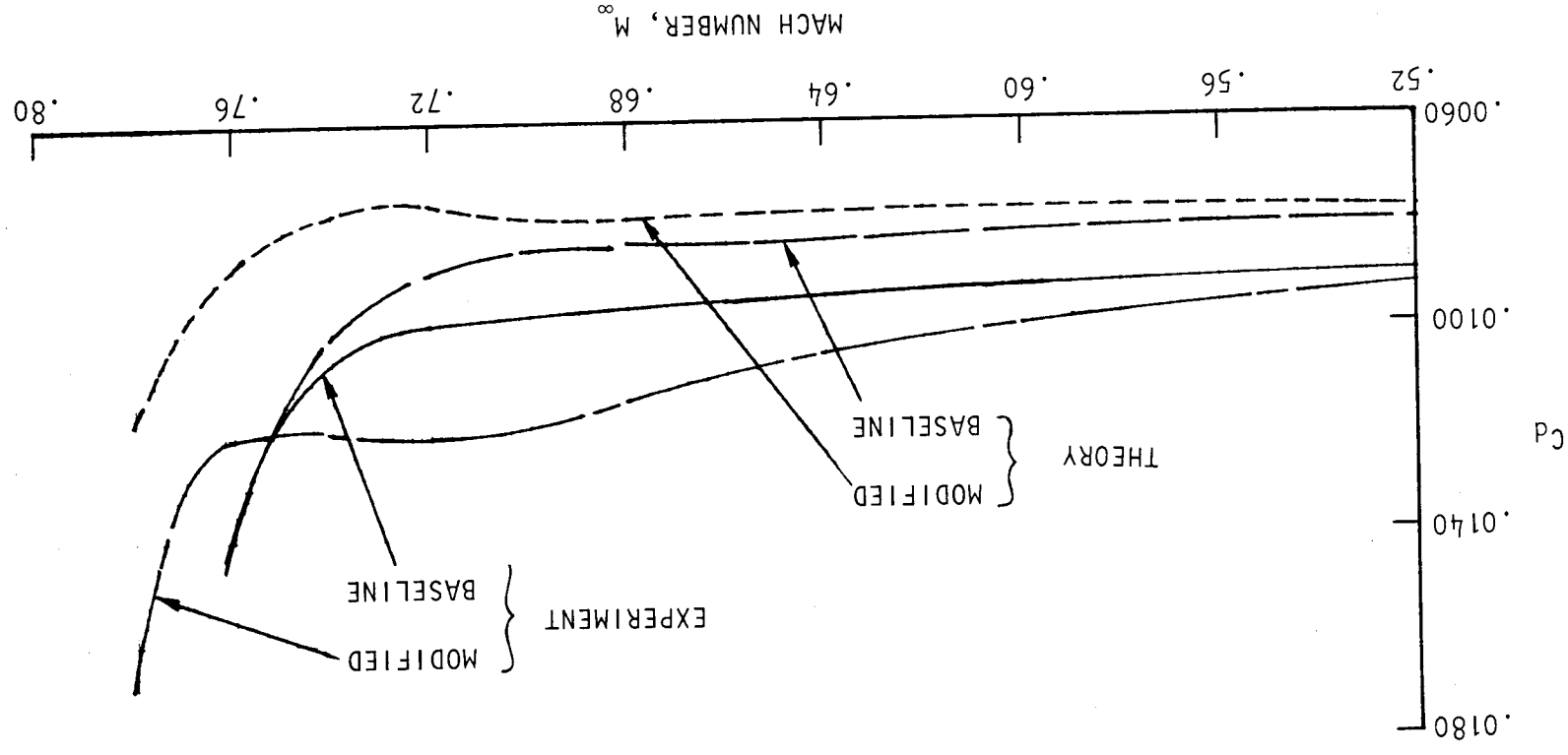
Figure 7.- Theoretical and experimental drag for the baseline airfoil and upper surface modification. $C_n = 0.57$; $R_N = 11 \times 10^6$; $\tau = 4\%$.

MACH NUMBER, M_∞

.52 .56 .60 .64 .68 .72 .76 .80

c_d

.0060 .0100 .0140 .0180

THEORY { MODIFIED / BASELINE

EXPERIMENT { MODIFIED / BASELINE
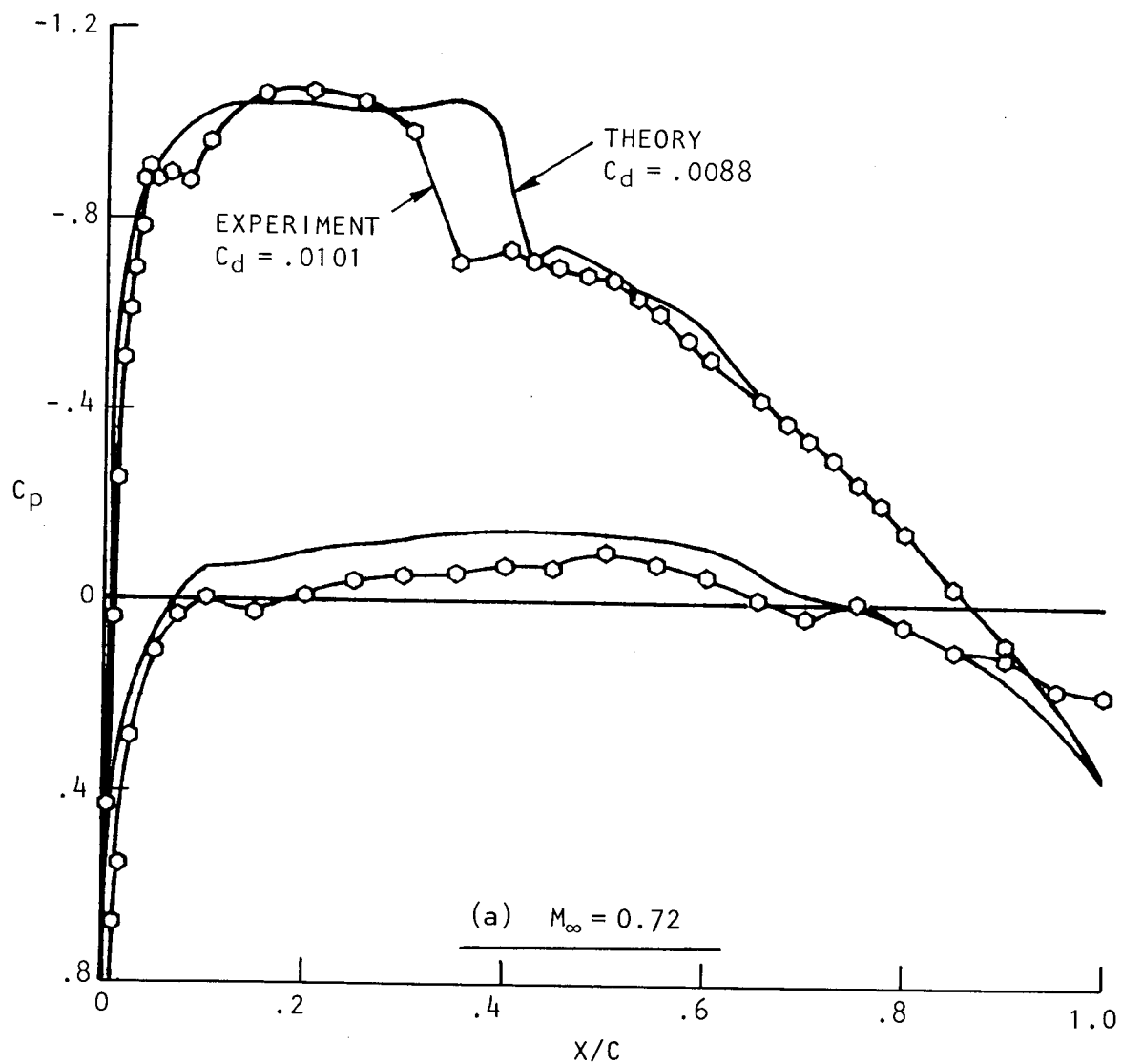
Figure 8.- Baseline airfoil theoretical and experimental pressures at $c_n = 0.57$.

(b) $M_\infty = 0.74$
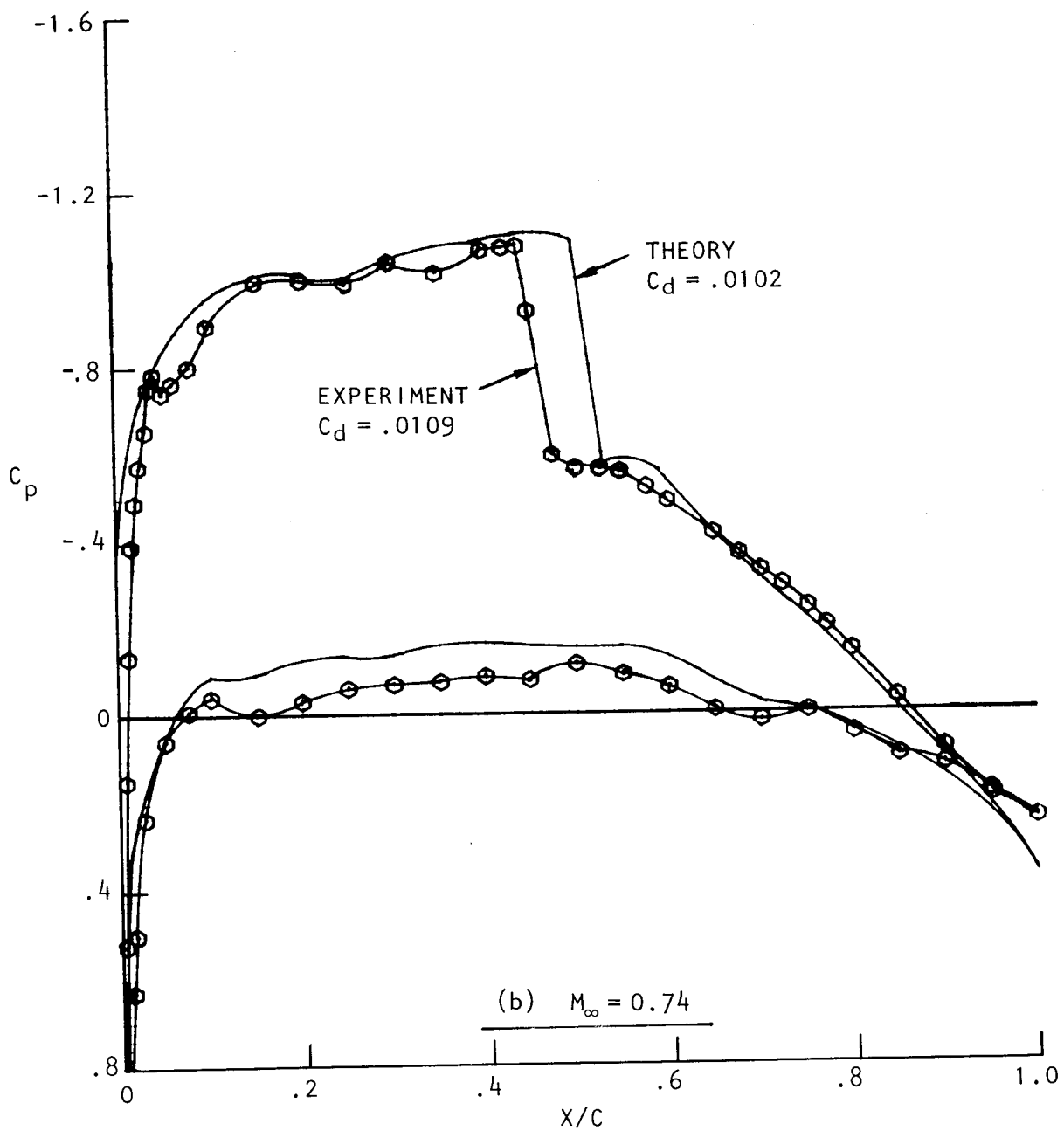
Figure 8.- Concluded.
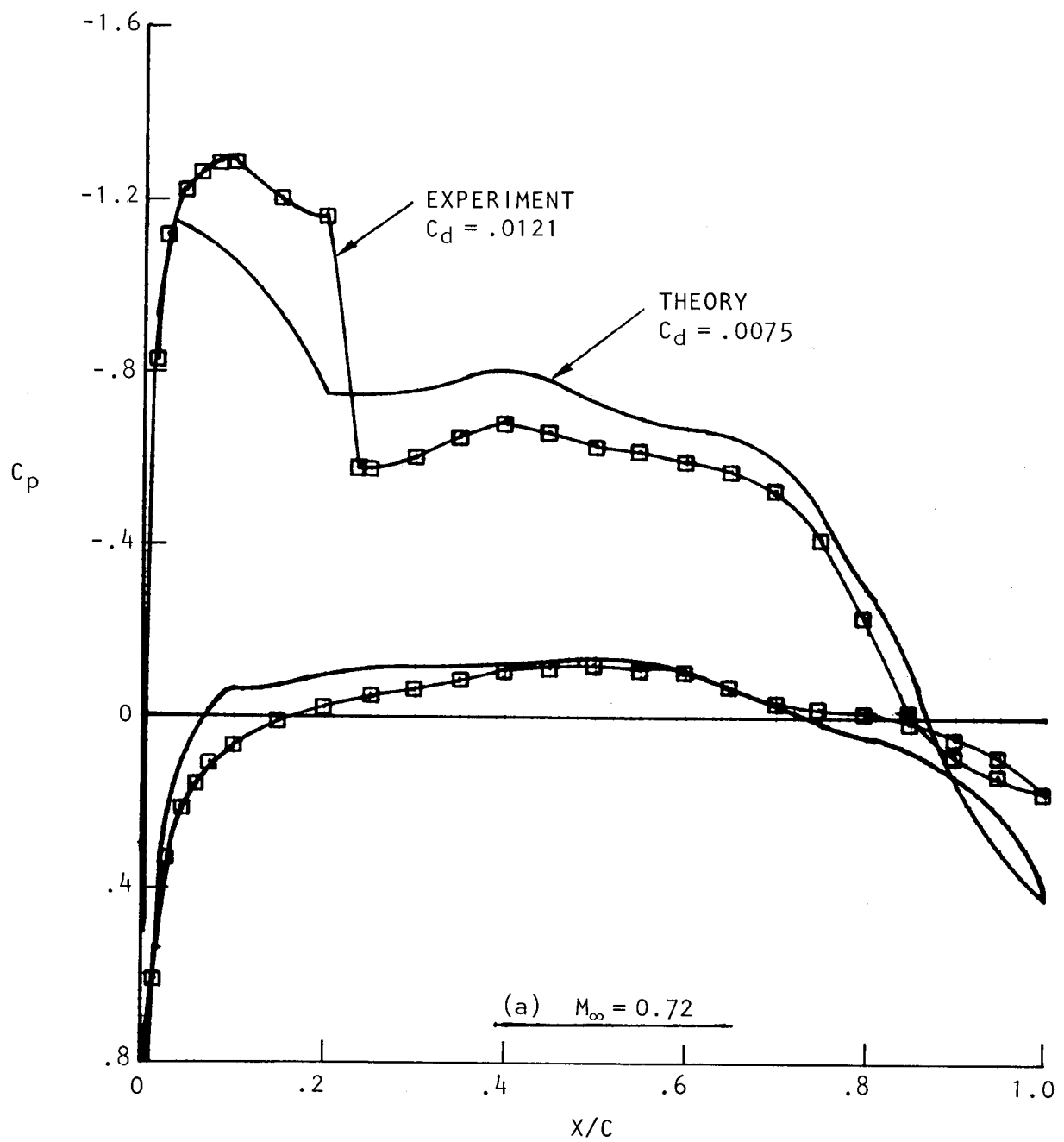
Figure 9.- Modified upper surface theoretical and experimental pressures at $c_n = 0.57$.
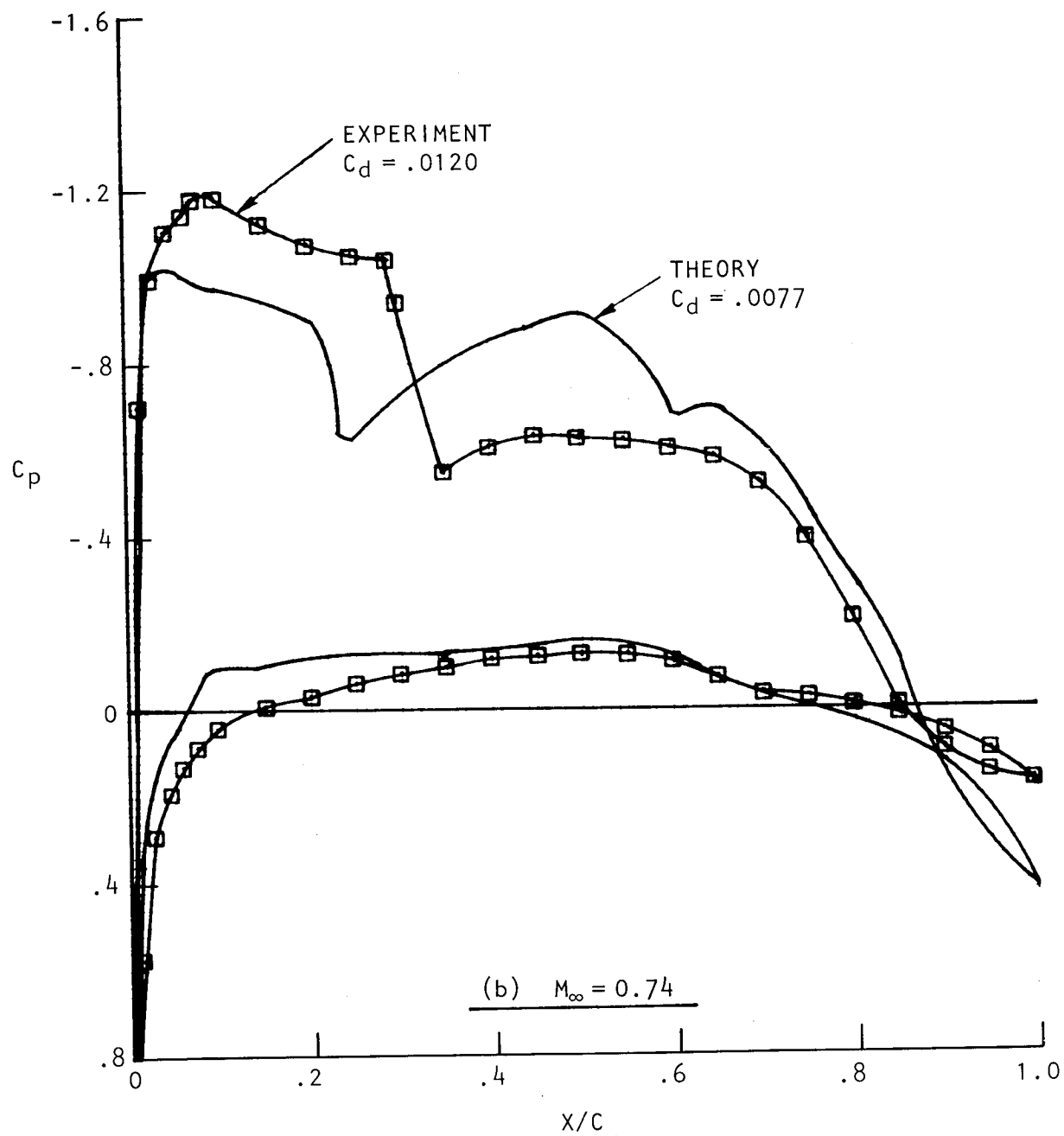
Figure 9.- Concluded.

AIRCRAFT PERFORMANCE IMPROVEMENTS

THROUGH AIRFOIL REFINEMENTS

Paul C. Bavitz

Grumman Aerospace Corporation

Carl P. Hellsten

Grumman American Aviation Corporation

SUMMARY

Computational airfoil design and analysis methods were applied to improve the cruise performance of an executive jet aircraft. These methods were used to identify those regions of the wing which could be improved at transonic cruise speeds and to appropriately modify airfoil section contours. Anticipated performance gains were verified by wind tunnel tests.

INTRODUCTION

This paper describes the application of some of the latest two-dimensional inviscid design and viscous analysis methods (references 1 through 4) to improve the transonic cruise capability of an executive jet aircraft. The baseline configuration was developed in the mid-1960's, primarily through extensive wind tunnel testing and prior to the revolutionary advancements in the field of computational aerodynamics. The modified configuration incorporates a wing redesign which was developed using two-dimensional computational methods to minimize cruise drag between speeds of 0.75 and 0.80 Mach number. Specifically, the elimination of approximately twenty counts of drag creep at cruise lift and 0.75 Mach number, as well as a modest increase in drag rise Mach number, were pursued.

SYMBOLS

b	wing span
C_d	section drag coefficient
C_D	aircraft drag coefficient
C_l	section lift coefficient

SYMBOLS   (Continued)

C_L	aircraft lift coefficient
C_p	pressure coefficient
L/D	lift-to-drag ratio
M	aircraft Mach number
S	wing area
X/C	chord station
η	semi-span station

DISCUSSION

The baseline and modified configurations are illustrated in figure 1. To derive the new planform, optimization studies were conducted considering weight, drag, fuel volume, cost and performance. The results indicated modest extensions of both the leading edge and the tip regions were required and that winglets should also be incorporated. The new planform maintained the aspect ratio of the baseline wing, provided three degrees additional leading edge sweep, and increased the wing area about fifteen percent. The destabilizing effect of the leading edge extension was nearly balanced by the stability contributions from the tip extension and the winglet.

The two-dimensional analytical tools not only produced the final airfoil coordinates for the new wing, but also were instrumental in shaping this new planform. For example, analyses indicated that contour modifications constrained to the region between the existing leading edge and front beam would yield almost no improvement in performance. Conversely, the tools showed that modifications aft of the rear beam would enhance the cruise characteristics, but these solutions were not cost effective. Ultimately, the calculations demonstrated that the rear two-thirds of the baseline wing structure could be preserved, including the rear beam and the lateral control and high lift systems, while meeting the performance objectives.

The following discussion highlights the airfoil related analyses and experimental verification. The winglet design and test data are not included in this paper, although they are an integral feature of the updated configuration. Results from the application of the tools are emphasized rather than the methodology. In addition to the improved section performance, note that careful attention to the wing span load, twist requirements, stability levels, and

trim drag was necessary to insure overall design success.

Figure 2 presents the estimated cruise pressure distributions at two stations in the baseline wing, and it reveals the motivation behind the planform extension. The station at 35 percent semispan is typical of the wing outer panel, and the one at 18 percent semispan lies in the plane of the nacelle centerline. Shock waves of moderate strength are evident at the cruise conditions. In order to eliminate the shock losses, improved upper surface curvature distributions are required starting forward of the existing leading edge and continuing just downstream of the shock location to limit the local velocities in this region to subcritical levels. Since the basic wing is constructed using three upper surface wing cover plates, the effort focused on redesigning the forward cover plate.

Figures 3 and 4 illustrate the estimated effects of the resulting airfoil modifications at the same two wing stations. To derive these modifications for the wing outer panel, a coordinate transformation was applied to the baseline wing section in the process of relating the 3-D design conditions to the appropriate 2-D design conditions. This transformation essentially modifies section slopes to account for planform taper effects. Once the effective 2-D section shape was defined, airfoil design and analysis techniques were applied to improve the baseline contours. Then the transformation process was reversed to place the new airfoil section back into the wing. The resulting pressure distribution, as depicted in figure 3, is entirely subcritical at the cruise conditions. Local lift at supercritical speeds on the baseline section near the leading edge has been replaced by lift at subcritical speeds forward of the baseline leading edge, with curvatures tailored to prevent local accelerations which could promote the development of a shock wave.

For the inboard wing station, an additional step was incorporated in the above procedure to produce the effective 2-D shape. The baseline wing had been successively treated in the inboard region, through several wind tunnel tests, in order to accommodate 3-D root effects. As a result of this experimental evolution, an analytic definition for the parent (untreated) wing root section was lacking. Thus, an inverse solution from a wing/body analysis and design program (reference 5) was used to analytically isolate these root effects and thereby produce an untreated wing root section for transformation into the 2-D coordinate system. Since the nacelle/wing interference problem was extensively treated and optimized on the baseline configuration, and since the modified configuration did not alter the wing pressure distributions aft of the section crestline in the vicinity of the nacelle overlap, no attempt was made to perturb the delicate nacelle/wing geometric relationship. Figure 4 shows the estimate for the resulting pressure distribution and an accompanying leading edge geometry schematic. This schematic depicts the large increase in fuel volume afforded by the leading edge extension, an important facet in the selection of the new planform.

Section drag rise characteristics for three wing stations are summarized in figure 5 at local lift coefficients consistent with the wing spanload at total cruise lift. At the inboard station, the drag coefficient at Mach 0.75 is reduced by 20 counts. The reduction for this section significantly affects the wing drag creep characteristics. The drag divergence Mach number is also improved by 0.04, but about one-third of this increment can be attributed to decreased thickness ratio. There was some concern about the drag rise characteristics of the sections near the baseline tip, because the tip extension led to increased local lift coefficients for these sections with the spanload stretched to the new tip. However, the drag coefficient for the wing sections in this region (station 387) ultimately proved to remain nearly constant up to the design Mach number.

At this stage in the design process, contour development of the entire wing from the three control stations was initiated. In addition to preserving the rear two-thirds of the baseline wing, the development of the new contours was constrained by existing root structure at the side of the fuselage. This root constraint forced a slight modification to the initial definition of the new inboard control section, but this modification is already incorporated in the section results herein presented. Three-dimensional transonic analysis programs were subsequently used to confirm the anticipated wing characteristics, and these tools indicated no additional treatment was necessary (references 6, 7, and 8).

A wind tunnel test of both the baseline and modified configurations was then conducted to define incremental forces and moments. A 1/8.8 scale reflection plane model was used for the test, and a common wing reference area system was adopted for coefficient definition. This reference system afforded greater visibility between incremental coefficients and incremental performance because a reference area change was avoided. Since the reference area is smaller than the actual wing area for the modified planform, the reference aspect ratio (b^2/S_{REF}) of the new planform is increased (i.e., the contribution of the additional area to lifting efficiency is manifested in the force coefficients as an apparent aspect ratio change).

Figure 6 summarizes the drag reduction measured for the modified configuration relative to the baseline. The increase in span (reduced vortex drag) and the increase in chord length (reduced profile drag) contribute to a net drag reduction of approximately 25 counts at 0.60 Mach number and the cruise C_L of 0.45. The refined contours then lead to a further reduction of 20 counts at Mach 0.75 by eliminating the baseline drag creep. Note that these results include trim effects at the flight design center of gravity.

The validity of the wing design methodology is conclusively verified by the pressure distribution correlations presented in figure 7. At all three design stations, very good agreement between the estimates and the test data is demonstrated. The cruise drag summary in figure 8, based on the test data, indicates the aerodynamic cruise efficiency is improved 16 percent at Mach 0.75 and 23 percent at Mach 0.78. While the drag coefficient for the baseline

configuration starts to rise at Mach 0.70, it remains constant up to Mach 0.78 for the modified configuration (the estimated section drag divergence characteristics of the refined contours are slightly conservative, particularly for the tip station).

The cruise performance summary, with 8 passengers, is shown in figure 9. Effects of the wing modification and of the additional fuel volume are individually assessed. The performance calculations utilized the baseline engine and mission format, with emphasis again placed on isolating incremental results. At Mach 0.75, the wing refinement provides an increase in range of approximately 325 nautical miles. Using all the available fuel volume, the total range improvement is in excess of 1000 nautical miles. In addition, the increase in best cruise speed directly reflects the drag rise character-istics noted above.

CONCLUSIONS

The applicability of computational airfoil design and analysis methods to enhance the cruise performance of an executive jet has clearly been demonstrated. These tools led to refined airfoil contours for the redesign of the baseline wing, while constrained to preserve much of the existing structure. Expectations of improved cruise efficiency were confirmed by wind tunnel tests. The wing modifications provided a 12% increase in range at the design Mach number of 0.75 with the baseline fuel load, and a 36% range extension resulted when the accompanying increase in fuel volume was utilized.

REFERENCES

1. Melnik, R.E., Chow, R. and Mead, H.R., "Theory of Viscous Transonic Flow Over Airfoils at High Reynolds Number, "AIAA Paper No. 77-680, June 1977.

2. Bauer, F., Garabedian, P., Korn, D. and Jameson, A., "Supercritical Wing Sections II. A Handbook," Lecture Notes in Economics and Mathematical Systems, No. 108, Springer-Verlag, 1975.

3. Bavitz, P., "An Analysis Method for Two-Dimensional Transonic Viscous Flow," NASA TN D-7718, January 1975.

4. Volpe, G., "Recent Advances in Airfoil Analysis and Design," Grumman Aerodynamics Memorandum 75-27, February 1975.

5. Boppe, C., "A Computer Program for Calculating the Subsonic Aerodynamics of Complex Wing-Body Configurations," Grumman Aerodynamic Technical Data Report 393-73-1, October 1973.

REFERENCES (Continued)

6. Ballhaus, W.F., Bailey, F.R. and Frick, J. "Improved Computational Treatment of Transonic Flow About Swept Wings," _Advances in Engineering Sciences_, NASA CP-2001, 1976.

7. Mason, W., MacKenzie, D.A. and Stern, M.A., "A Numerical Three-Dimensional Viscous Transonic Wing-Body Analysis and Design Tool," AIAA Paper No. 78-101, January 1978.

8. Jameson, A. and Caughey, D., "Finite Volume Method for Transonic Potential Flow Calculations," AIAA Paper No. 77-635, June 1977.
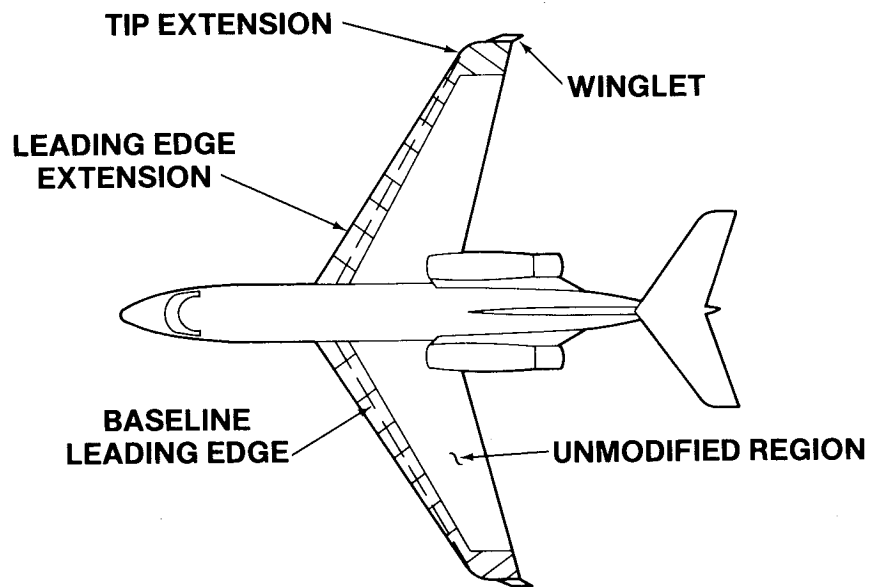
Figure 1.- Executive jet aircraft configuration.
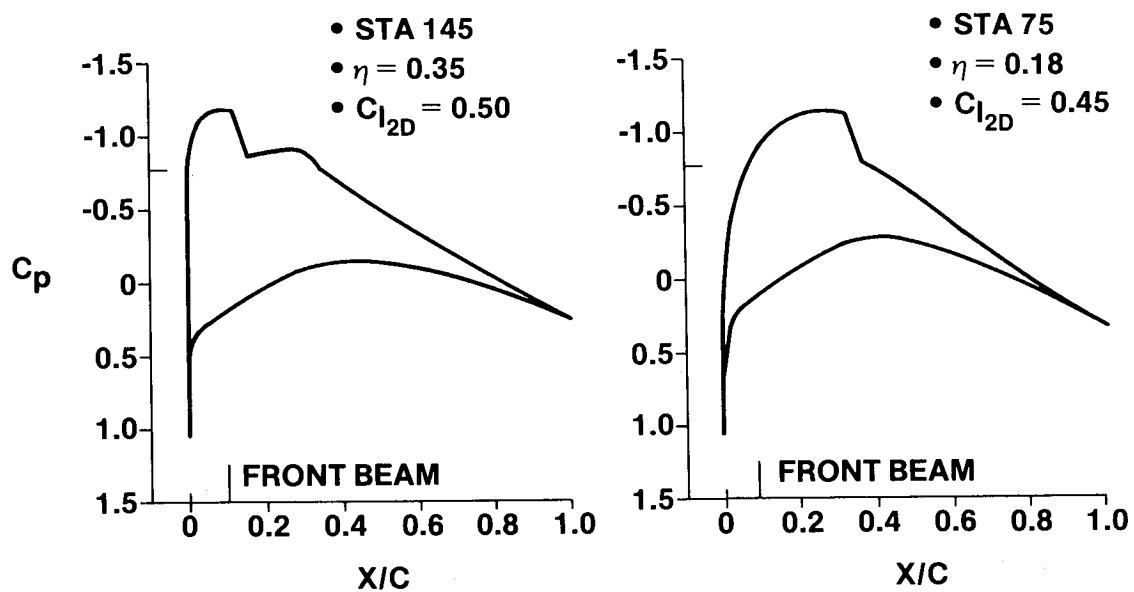
Figure 2.- Baseline cruise pressure distributions. 2-D viscous analysis;
M = 0.75.
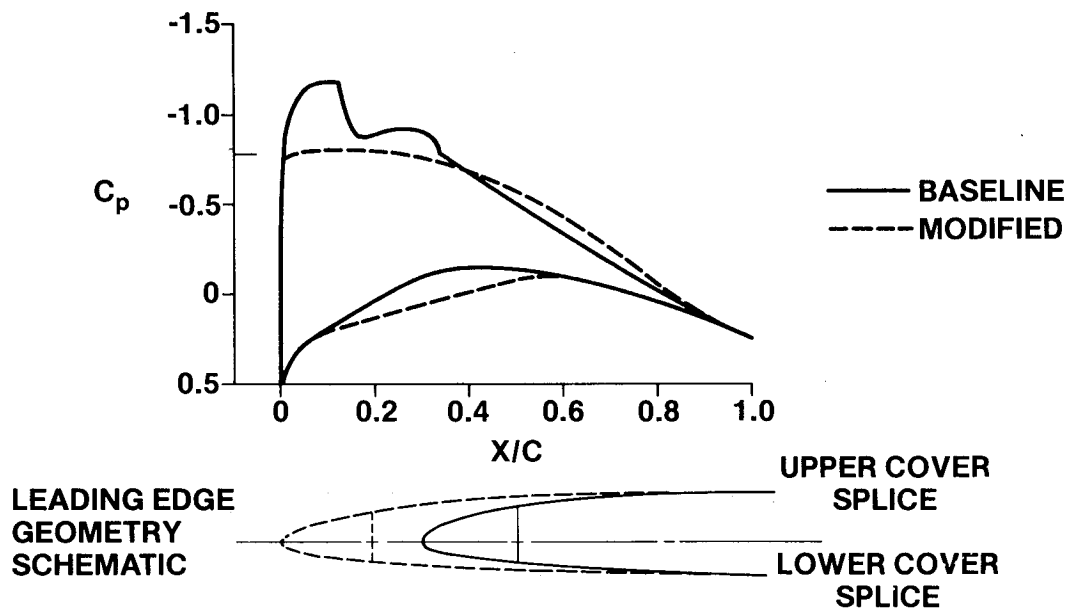
Figure 3.- Estimated effect of airfoil modifications at station 145.
$M = 0.75$; $C_{\ell_{2D}} = 0.50$.
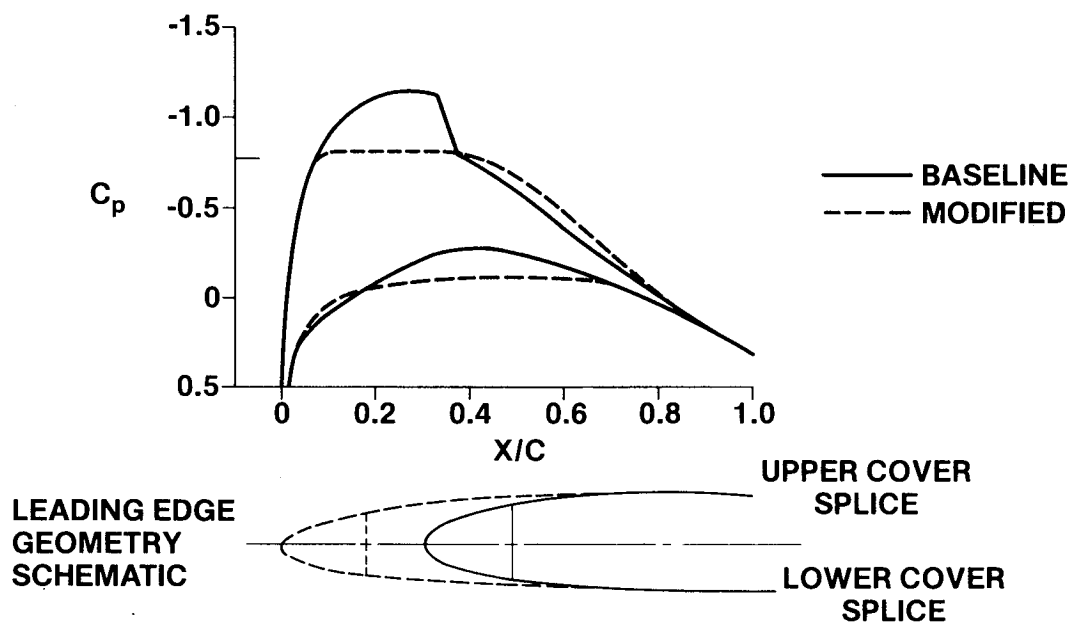
Figure 4.- Estimated effect of airfoil modifications at station 75.
$M = 0.75$; $C_{\ell_{2D}} = 0.45$.
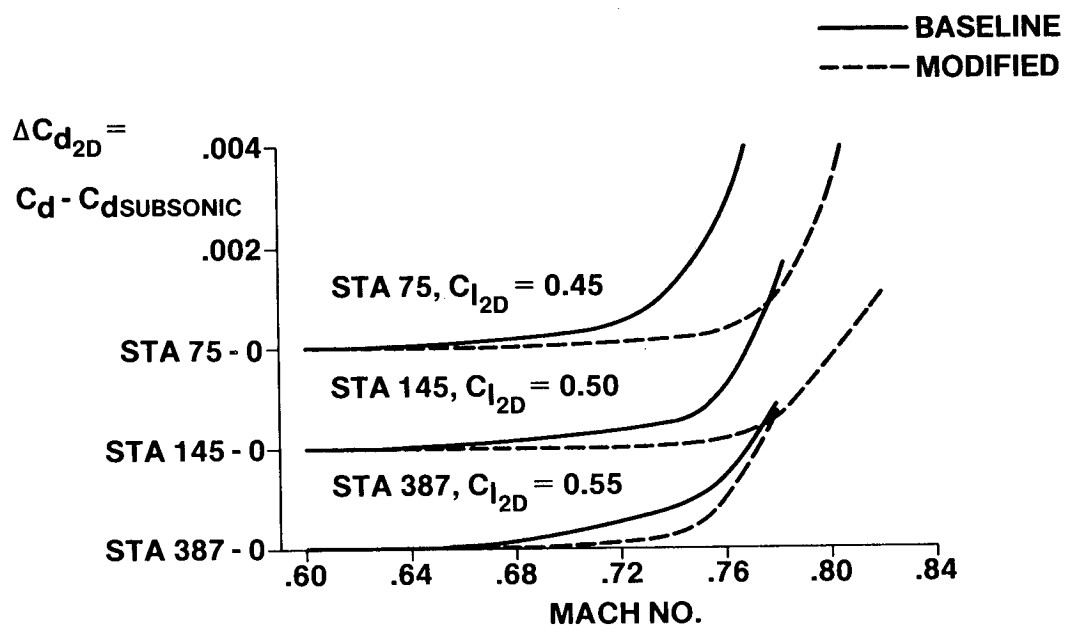
Figure 5.- Estimated section drag-rise characteristics.
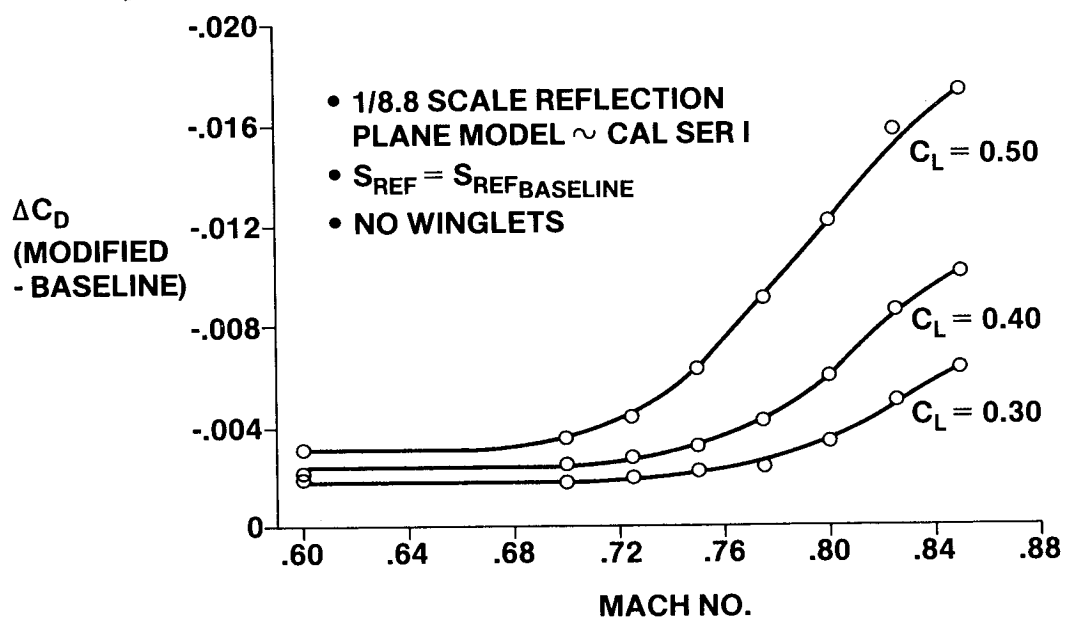
Figure 6.- Configuration drag increment.

STA 75

C_p

X/C

ANALYSIS $C_L = 0.47$

○ σ TEST $C_L = 0.49$

STA 145

C_p

X/C

STA 387

C_p

X/C
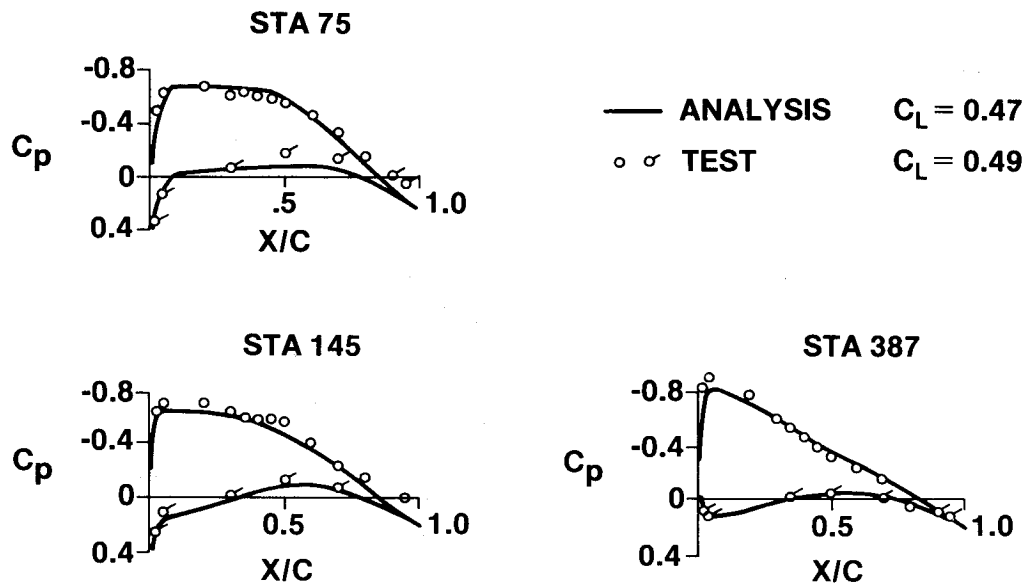
Figure 7.- Cruise pressure-distribution correlations for modified wing. M = 0.75.

• $S_{REF} = S_{REF_{BASELINE}}$

• NO WINGLETS

C_D

L/D IMPROVEMENT: 11%

16%

23%

BASELINE

--- MODIFIED

MACH NO.
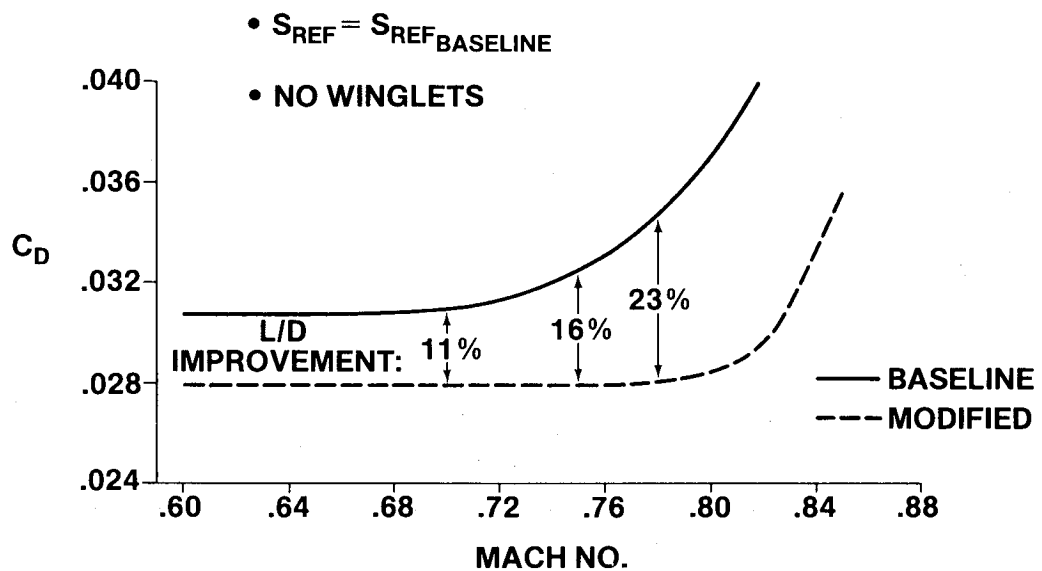
Figure 8.- Cruise drag summary. $C_L = 0.45$.
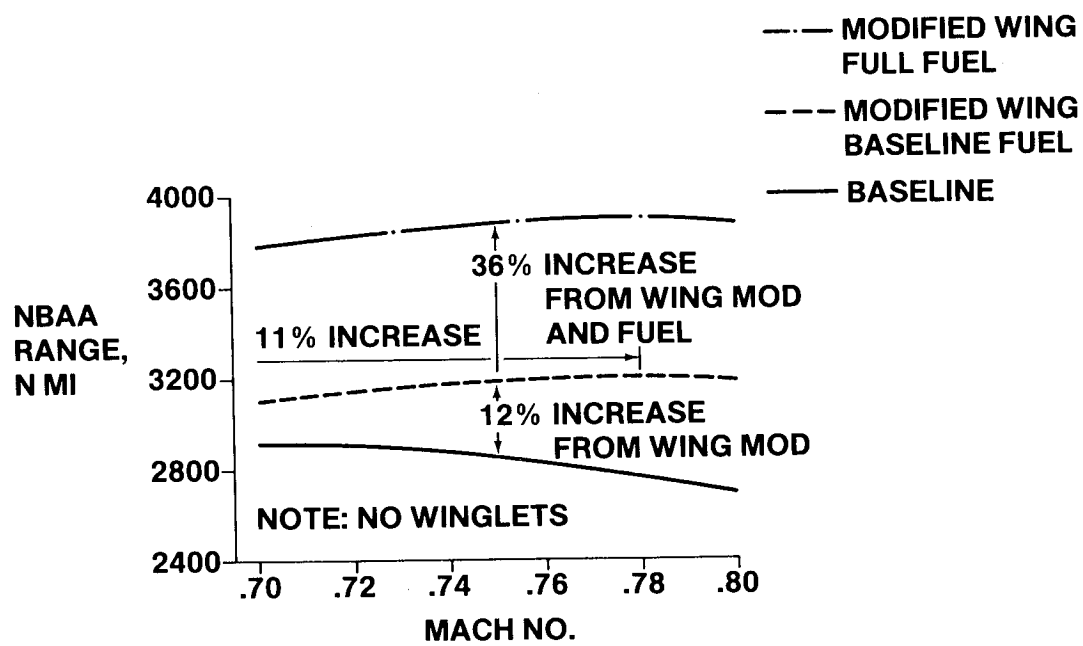
Figure 9.- Performance summary with eight passengers.

THE USE OF SMALL COMPUTERS IN A SUBSONIC

AIRFOIL DESIGN APPLICATION

J. C. Narramore
Cessna Aircraft Company

SUMMARY

The application of a desk top mini-computer system to the problem of sub-sonic airfoil design is considered. It is shown that if methods which do not require large memory are employed, a complete design sequence may be integrated into a small computer. An example of an airfoil designed to satisfy specified aerodynamic and geometric requirements using a subsonic airfoil design method program in conjunction with an inverse conformal mapping program on a mini-computer is given.

INTRODUCTION

One of the continually recurring tasks in the business of aerodynamic design is the selection of the best airfoil for a particular application. Historically, this involved searching through the existing wind tunnel data to locate an airfoil with characteristics close to those desired. Recent advances in aerodynamic computational methods have allowed designers to produce sections specifically tailored to the design requirements. Progress in electronic computers has decreased the size of the machine required to take advantage of these methods.

SYMBOLS

C_d Airfoil section drag coefficient

C_l Airfoil section lift coefficient

C_m Airfoil section pitching moment coefficient

C_p Pressure coefficient

K   Coefficient in generalized velocity distribution

l/d Airfoil section lift to drag ratio

Re   Reynolds number based on chord length

S	Airfoil surface length
S_o	Maximum velocity location
S_p	Stagnation point location
V	Velocity along airfoil surface
V_∞	Freestream velocity
V_o	Maximum velocity
w_{TE}	Pressure recovery parameter
α	Angle of attack of airfoil
μ	Coefficient in generalized velocity distribution
σ	Non-dimensional surface coordinate originating at the effective origin of the equivalent constant pressure length
σ_o	Non-dimensional equivalent constant pressure length

Subscripts:

L	Refers to conditions on the lower surface
o	Refers to conditions at velocity peak on airfoil surface
TE	Refers to conditions at the trailing edge
U	Refers to conditions on the upper surface

MINI-COMPUTER CAPABILITIES

As micro-miniaturization of electronic components has progressed, so has the development of small computing systems. Recent advances have put the same computing power in a desk top mini-computer that was available in some of the large computing systems only ten years ago. These small computers do have limitations which may include small read/write memory size and slow input/output compared to most large systems (fig. 1). However, the advantages (fig. 2) of mini-computer systems stem from their low cost, small size, and programmer-controlled operation. These advantages may in some cases justify use of a mini-computer instead of, or in addition to, a large computer system.

SUBSONIC AIRFOIL APPLICATIONS

An area where the mini-computer has shown a usefulness is subsonic air-foil applications. Direct and inverse conformal transformations and thin air-foil theories may easily be programmed on most mini-computers and recently a subsonic airfoil design procedure (ref. 1) has been developed which utilizes a desk top mini-computer system.

Airfoil design entails producing the best two-dimensional shape that will satisfy a set of given design requirements. These may include aerodynamic specifications such as low drag, low pitching moment, high maximum lift, and gentle stall; and geometric specifications such as maximum thickness and thickness distribution for structural and fuel volume considerations (fig. 3).

The current design procedures used to obtain airfoils with specified characteristics are depicted in figure 4. With the iterative-direct (ref. 2) and geometric optimization (ref. 3) techniques, an initial airfoil is selected and analyzed to determine its aerodynamic characteristics. The results are compared to the requirements and if they are not satisfied the shape of the airfoil is modified. This process is repeated until the requirements are met and the design is complete. With an inverse airfoil design procedure, an initial guess for the velocity distribution is made and the resulting airfoil determined. The aerodynamic characteristics are determined and compared to the requirements. If they are not satisfied, the velocity distribution is modified, and this process is repeated until all of the requirements are met. The problem with all of these procedures is that they require a large number of iterations which must be done by hand or by complex computer programs.

A desired design procedure would be one in which no iterations occur and is depicted in figure 5. First, the velocity distribution which will satisfy the design requirements is determined, and this is used as the input to an inverse program to determine the airfoil shape.

The approach taken here to approximate this procedure is to assume gener-alized equations for the velocity distribution along the perimeter of the air-foil. Since the lower surface velocity distributions are similar to the upper surface distributions it is convenient to evaluate each independently. In the analysis carried out here, an airfoil surface is divided into an acceler-ation region and a deceleration region as shown in figure 6.

In the acceleration region the velocity is constant in this case.

$$\frac{V}{V_o} = 1 \text{ for } 0 \leq \sigma \leq \sigma_o$$

However, any arbitrary acceleration velocity distribution may be used.

In the deceleration region the velocity is an equation of the form

$$\frac{V}{V_o} = \left[1 + K\left(\frac{\sigma-\sigma_o}{1-\sigma_o}\right)\right]^{-\mu} \quad \text{for } \sigma_o \leq \sigma \leq 1$$

which was developed by F.X. Wortmann (ref. 4) to produce a turbulent boundary layer with constant form parameter $\left(H = \dfrac{\text{Displacement Thickness}}{\text{Momentum Thickness}}\right)$.

Using these equations for the velocity distribution the airfoil lift and pitching moment may be determined by integration. The drag is calculated by using a Squire-Young drag method in conjunction with Truckenbrodt's boundary layer theory (ref. 5) and the separation location is determined by a method of B.S. Stratford (ref. 6). Reference 1 presents the derivation of these results.

The design parameters lift, pitching moment, drag, and separation location then become equations which are a function of the velocity distribution parameters σ_o, K, and μ. It is a relatively easy task to program these equations on a mini-computer that can analyze a large number of velocity distributions in a short period of time and therefore, determine the distribution which will best satisfy the design requirements. As a result, this design process is faster and much less expensive than either modifying the input velocity distribution of an inverse program or modifying the input geometry to a direct analysis program.

In order to determine the coordinates of the airfoils which will produce the given velocity distributions some inverse airfoil design method must be used. A mini-computer is also capable of handling this problem if the method does not require large matrices. Conformal mapping procedures for subsonic airfoils usually utilize the flow about a circle and determine a transformation to an airfoil plane.

The method used in this analysis was developed by Eppler (ref. 7) and is quite applicable to mini-computer systems. In this approach, the velocity

$$V = \frac{dF}{dz} = \frac{\dfrac{dF}{d\zeta}}{\dfrac{dz}{d\zeta}}$$

is written as

$$\ln \frac{dz}{dF} = \ln \frac{dz}{d\zeta} - \ln \frac{dF}{d\zeta}$$

Taking the real part of this expression gives

$$-\ln V = \text{Real}\left[\ln \frac{dz}{d\zeta} - \ln \frac{dF}{d\zeta}\right]$$

84

which with input velocity and known flow about a circle $\frac{dF}{d\zeta}$ can be used to determine the proper transformation $\frac{dz}{d\zeta}$ and thereby the desired coordinates.

EXAMPLE

Now that these airfoil design tools have been developed for the mini-computer, an example of their usage can be presented. Figure 7 illustrates the entire design and analysis sequence employed in this study. Input for the design of a new airfoil comes in as design requirements to the airfoil design method mini-computer program while input for the analysis of a defined section comes in as coordinates to the North Carolina State University single element version of the Lockheed two-dimensional analysis program (ref. 8). This allows the aerodynamic performance of airfoils designed by the mini-computer design programs to be directly compared with airfoils designed by some other method.

Consider the design of an airfoil with the requirements shown in figure 8. The aerodynamic specifications include high lift to drag ratio at a lift coefficient of 1.0, low drag coefficient at a lift coefficient of 0.2, and a pitching moment coefficient whose magnitude is less than −0.05 at a Reynolds number of 5 million; or stated differently: drag coefficients similar to NASA LS-Series (GAW) airfoils with pitching moment coefficients similar to NACA 24-Series airfoils are required. An airfoil will be designed having a maximum thickness of 15% with the geometric constraint that the thickness distribution allow for spars located at 10 and 55% chord.

In order to determine the form of the upper surface velocity, a family of velocity distributions is investigated by the design method computer program in which the location of the start of the pressure recovery is varied. Figure 9 depicts plotted output from the mini-computer program. The abscissa represents the non-dimensional surface distance from the effective origin of the equivalent constant pressure length to the trailing edge and the ordinate is the local velocity divided by the peak velocity and squared; W_{TE} is the ratio of trailing edge velocity to maximum velocity, $C_{p_{TE}}$ is the trailing edge pressure coefficient, and Re is the Reynolds number. The curves represent a family of velocity distributions produced by varying the parameter σ_0 in the velocity distribution equations. Along each of these curves the lift, drag, pitching moment, and separation location is calculated by the mini-computer. Notice that separation is calculated along the curves for which σ_0 is greater than or equal to 0.8.

The calculated results for the design parameters as a function of the location of the start of the pressure recovery are shown in table 1. As σ_0 is increased, the lift, drag, pitching moment, and lift-drag ratio increase. At values of σ_0 greater than 0.5, the pitching moment values become much larger than −0.05 so that a value of σ_0 of 0.5 is chosen to obtain the highest lift-drag ratio with a pitching moment of approximately −0.05.

At $\sigma_0 = 0.5$, a family of velocity distributions is produced by varying the μ parameter in the velocity equation as shown in figure 10. Notice that for convex pressure recovery distributions, the possibility of separation exists. However, there exists a region in this family of curves for which separation does not exist. The design parameters in the region where no separation exists are shown in table 2. As μ becomes more positive, the lift, drag, pitching moment, and lift-drag ratio increase. At $\mu = 0.4$ the pitching moment constraint boundary is met at a high lift-drag ratio. Therefore, the velocity distribution that results from this selection of the parameters of μ and σ_0 represents a good selection for the design requirements on the upper surface.

Using this velocity as input to an inverse program produces the airfoil shape shown in figure 11. It is not a practical airfoil since at any angle higher than the design angle of attack a spike in the velocity will be produced at the leading edge due to the sharp nose. This spike causes a premature thickening of the boundary layer which may lead to early stall. Also, since no pressure recovery took place on the lower surface, the inverse program calculated the reflex shape in order to properly close the airfoil which is only 7.5% thick.

To produce desired airfoils the velocity can be modified to change the leading edge radius by changing the slope of the velocity at the leading edge and by recovering pressure on the lower surface.

A family of curves (fig. 12) may be produced for the lower surface in which the location of the start of the pressure recovery is varied. Notice that a nominal value of $W_{TE} = 0.8$ was chosen for this analysis even though this parameter will be the one which is varied to produce an airfoil with the desired thicknesses. However, the trends can be surmised from this example. On the lower surface as σ_0 is increased, the airfoil drag increases and the lift decreases. Therefore, to minimize the drag at low lift coefficients the pressure recovery should start at the leading edge on the lower surface. However, this would produce a thin highly cambered airfoil. Since a requirement for a spar to be located at 55% chord was stipulated, the geometric considerations dictate a high thickness over this portion of the airfoil chord. Based on this, the start of the pressure recovery can be set at $\sigma_0 = 0.6$.

A family of velocity distributions with $\sigma_0 = 0.6$ is produced (fig. 13) and the design parameters along each curve calculated. The results of the computer program show that the drag is minimized with $\mu = 0.05$. However, this extremely concave velocity distribution would require a large discontinuity in the curvature of the lower surface, and would produce an airfoil which might not provide sufficient room for flap or aileron actuators. Therefore, as a good compromise between low drag and geometric considerations, the selection $\sigma_0 = 0.6$ and $\mu = 0.8$ for the lower surface and the previously defined upper surface parameters can be used as input to the inverse program. As was mentioned before, the amount of pressure recovered on the lower surface is varied to produce an airfoil with the specified thicknesses.

The inverse program takes this information and determines the coordinates of the airfoil that will produce that velocity distribution in potential flow, and the results are plotted (fig. 14) and printed in the proper format for NC State program input. Also, at this time, the coordinates of LS-Series and 24-Series airfoils of 15% thickness are written on the NC State input form. All of this information is processed by the NC State program and the output is punched on cards. Another mini-computer program reads this data, stores it on tape for later reference, and plots sets of comparative data as shown in figure 15. In this figure, the circles represent the results for the airfoil produced by using the airfoil design procedure, the squares represent LS-Series airfoil results, and the triangles represent the results for 2415 airfoil.

Remembering that the requirements for this airfoil were to obtain LS-Series levels of drag with 24-Series levels of pitching moment, an investigation of the drag and pitching moments is appropriate. Notice that at a lift coefficient of 0.2, the new airfoil has about 2.5% lower predicted drag level than both the LS(1) - 0415 and the 2415. At a lift coefficient of 1.0, the new airfoil has approximately 1% higher lift-drag ratio than the LS-Series airfoil and 10.5% higher lift-drag ratio than the 2415. The pitching moment curves show that the new airfoil has a pitching moment level similar to the 2415 and 50% lower than the LS(1) - 0415 airfoil.

CONCLUDING REMARKS

It has been shown that subsonic airfoils can be developed using a desk top mini-computer as the primary design tool. A theoretical analysis of a section produced by this method indicates that this approach to subsonic airfoil design is a viable one.

REFERENCES

1. Narramore, J.C.: An Approach to Subsonic, Turbulent Flow Airfoil Design Using Mini-Computers. SAE Paper 770479, 1977.

2. Kennedy, J.L. and Marsden, D.J.: A Potential Flow Design Method for Multicomponent Airfoil Sections. J. Aircraft, Vol. 15, No. 1, January 1978, pp. 47-52.

3. Hicks, R.M.; Murman, E.M.; and Vanderplaats, G.N.: An Assessment of Airfoil Design by Numerical Optimization. NASA TM X-3092, 1974.

4. Wortmann, F.X.: A Contribution to the Design of Laminar Profiles for Gliders and Helicopters, Ministry of Aviation Translation TIL/T, 4903, 1960.

5. Schlichting, H.: Boundary Layer Theory, McGraw-Hill Book Company, 1968.

6. Stratford, B.S.: The Prediction of Separation of the Turbulent Boundary Layer, Journal of Fluid Mechanics, Vol. 5, 1959.

7. Eppler, R.: Direct Calculation of Airfoils from Pressure Distribution, NASA TT F-15,417, 1974.

8. Smetana, F.O.; Summey, D.C.; Smith, N.S.; and Carden, R.K.: Light Aircraft Lift, Drag, and Moment Prediction – A Review and Analysis, NASA CR-2523, 1975.

Table 1

Design Parameters as a Function of σ_0 with $K = 0.615$

σ_0	C_l	C_d	C_m	l/d
.1	.33	.0045	−.018	73.11
.2	.37	.0047	−.024	78.40
.3	.41	.0050	−.032	83.26
.4	.45	.0052	−.044	87.75
.5	.49	.0054	−.058	91.93
.6	.54	.0056	−.076	95.82
.7	.58	.0058	−.096	99.46
.8	Separation			

Table 2

Design Parameters as a Function of μ with $\sigma_0 = 0.5$

μ	C_l	C_d	C_m	l/d
.05	.40	.0049	−.018	80.86
.1	.44	.0051	−.033	85.49
.2	.47	.0053	−.046	89.14
.4	.49	.0054	−.050	91.22
.8	.50	.0054	−.059	92.28
−.4	.53	.0056	−.075	95.42
−.2	Separation			

- Memory

   8-64K byte memory

- Input/Output

   Printer
   Magnetic Tape
   Cards
   Plotter
   CRT Display

- Word Length

   16-64 bit word

- Speed of Processing

Figure 1.- Capabilities and limitations of desk-top mini-computers.

- Low Cost

- Small Size

- Programmer Controlled Operation

- Flexibility

Figure 2.- Advantages of desk-top mini-computers.

AERODYNAMIC

- ## LOW DRAG AT SPECIFIED LIFT VALUES
- ## LOW PITCHING MOMENT
- ## HIGH MAXIMUM LIFT
- ## GENTLE STALL

GEOMETRIC

- ## PROFILE MAXIMUM THICKNESS
- ## PROFILE THICKNESS DISTRIBUTION

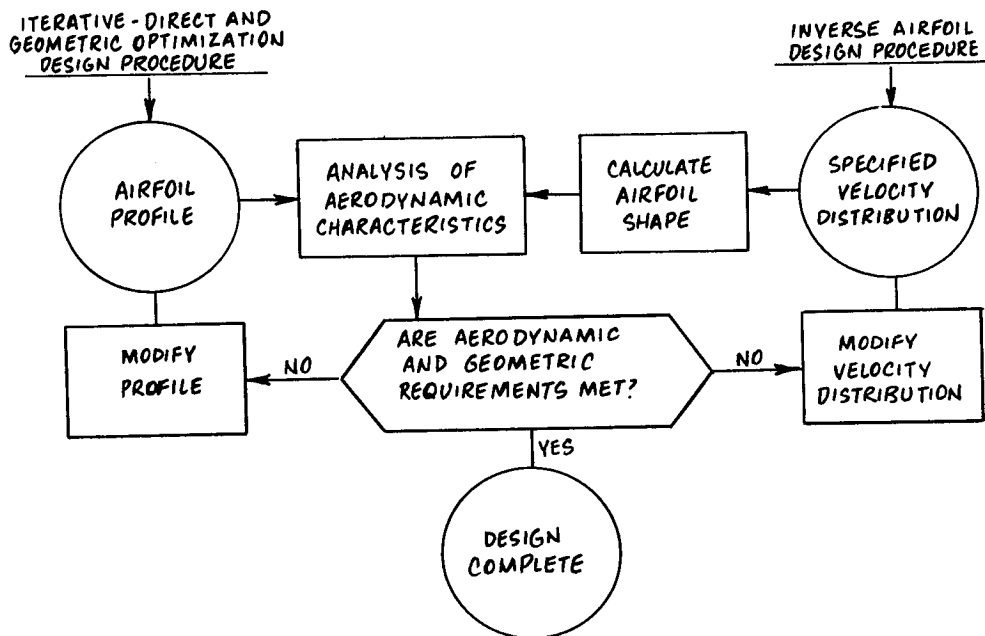Figure 3.- Characteristic given airfoil design requirements.

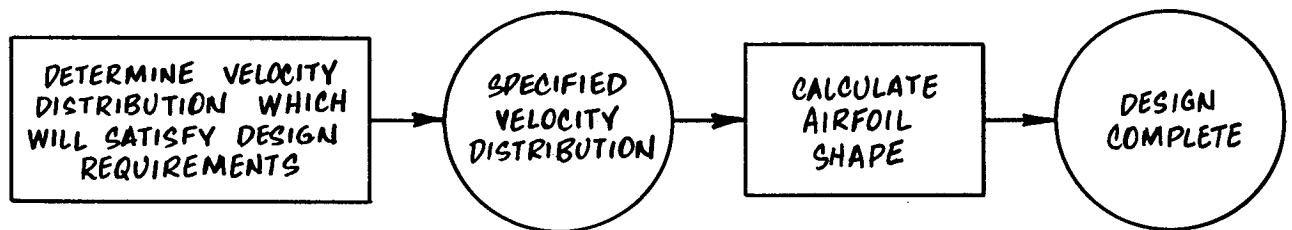Figure 4.- Simplified flow chart depicting most airfoil design procedures.

Figure 5.- A desired design procedure with no iterations.
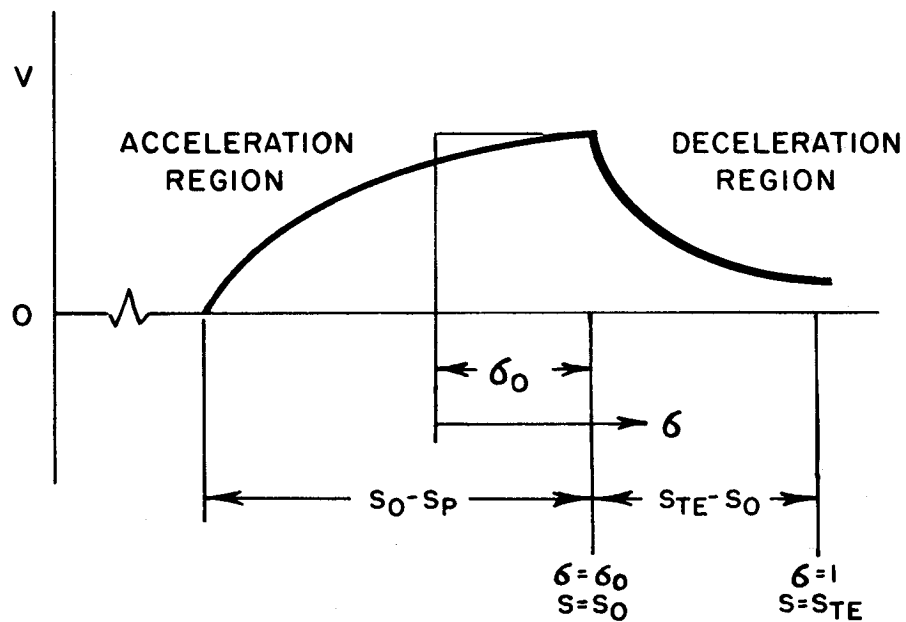
Figure 6.- Upper or lower surface velocity distribution.
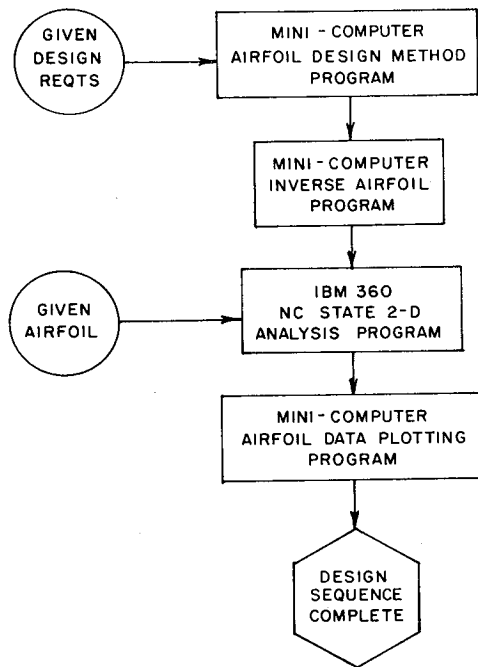
Figure 7.- Airfoil design and analysis sequence.

AERODYNAMIC

HIGH LIFT-DRAG RATIO AT $C_l = 1.0$
LOW DRAG AT $C_l = 0.2$
PITCHING MOMENT MAGNITUDE LESS THAN 0.05
REYNOLDS NUMBER OF 5×10^6

OR

DRAG COEFFICIENTS SIMILAR TO LS SERIES AIRFOIL
WITH PITCHING MOMENT COEFFICIENT SIMILAR
TO 24 SERIES AIRFOIL

GEOMETRIC

AIRFOIL WITH 15 PERCENT MAXIMUM THICKNESS
THICKNESS DISTRIBUTION SUCH THAT SPARS CAN
BE LOCATED AT 10 AND 55 PERCENT CHORD

Figure 8.- Airfoil requirements.

Figure 9.– Velocity distributions produced by varying σ_o on the upper surface.
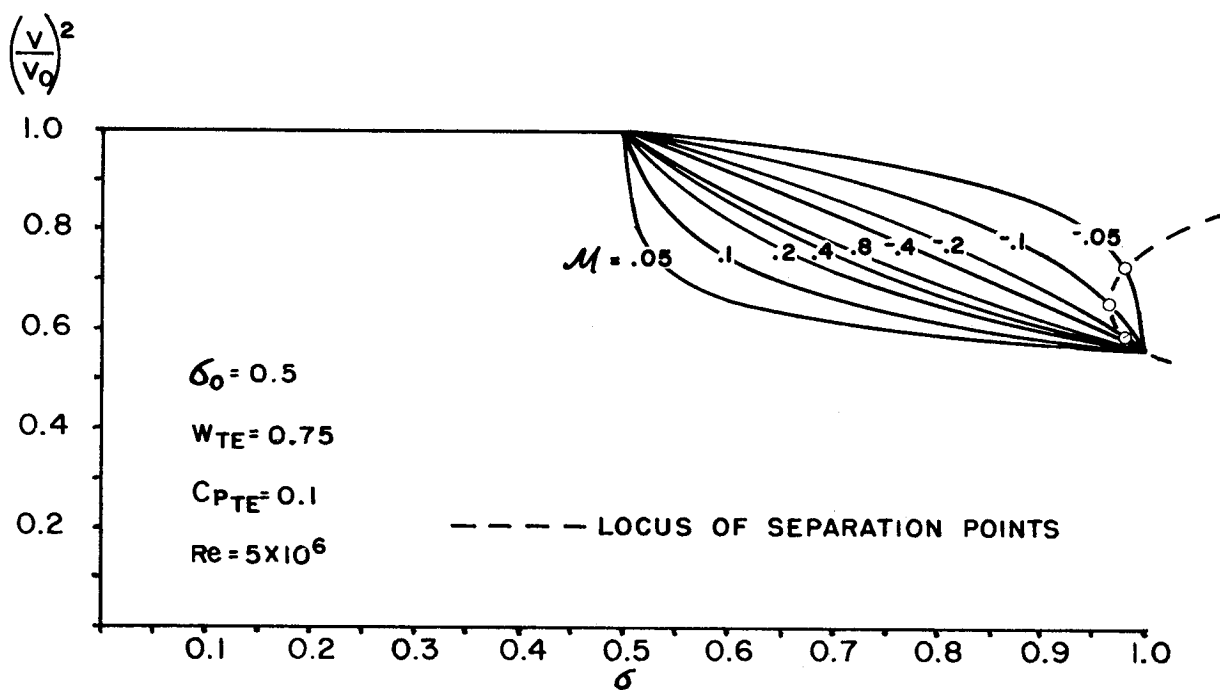
Figure 10.– Velocity distributions produced by varying μ on the lower surface.

Figure 11.- Airfoil resulting from upper surface input.

Figure 12.- Velocity distributions produced by varying σ_o on the lower surface.
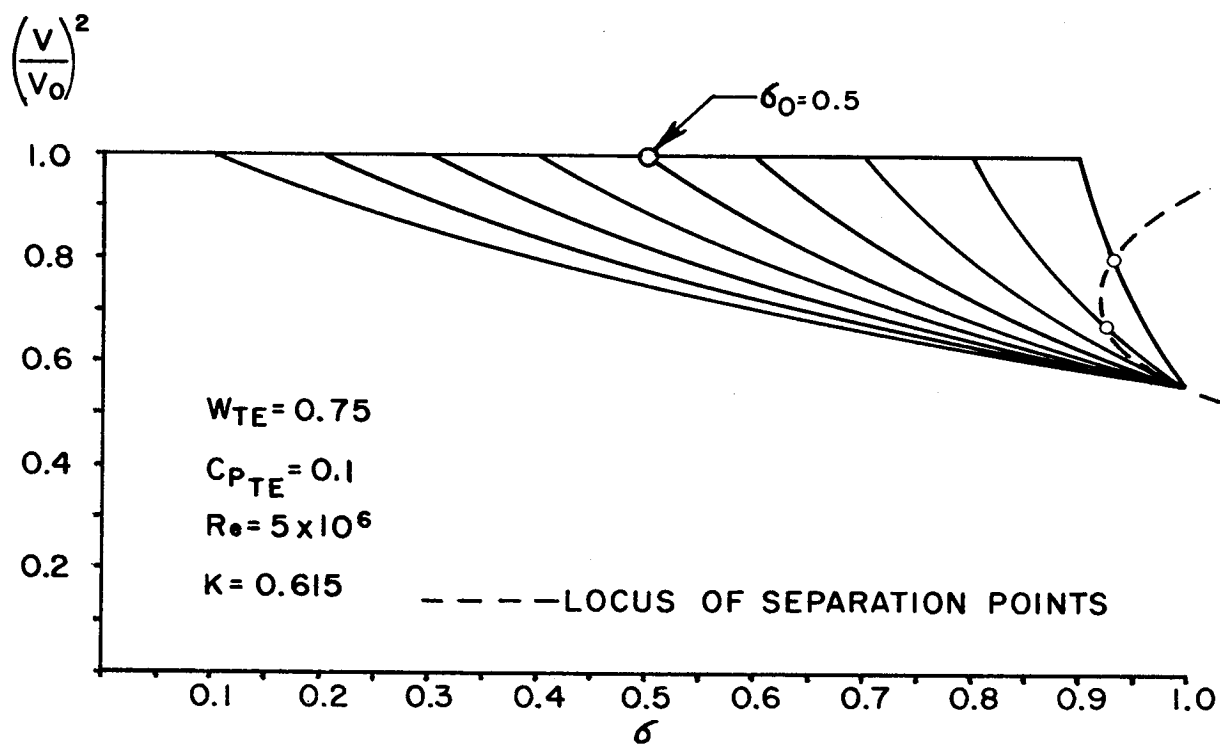
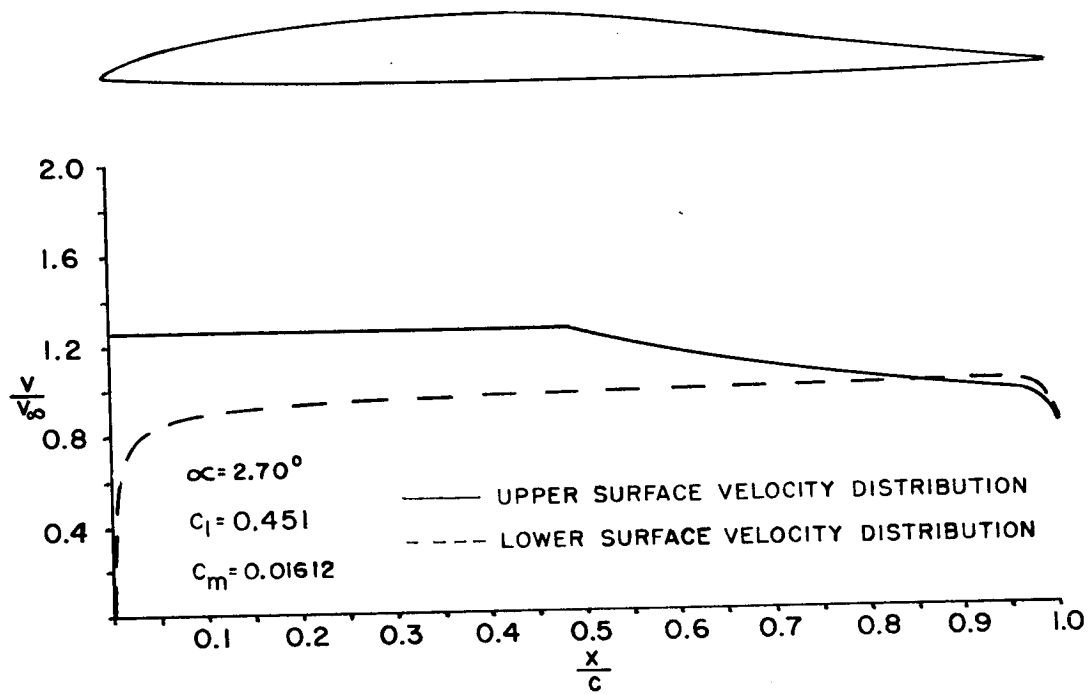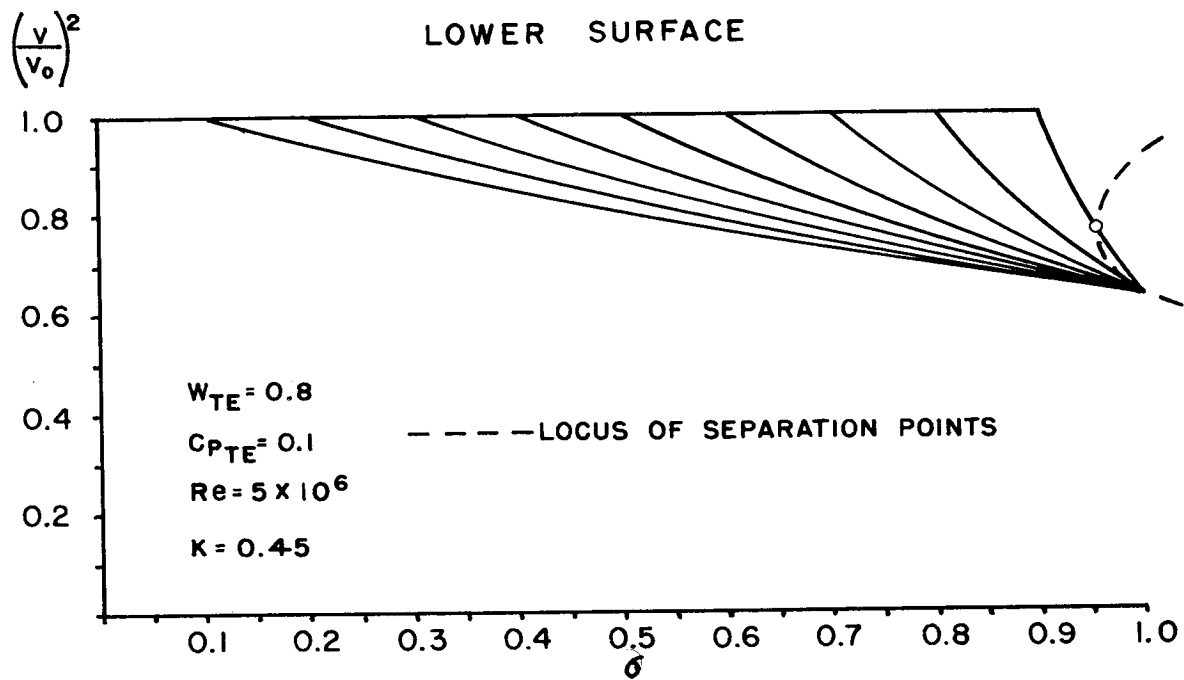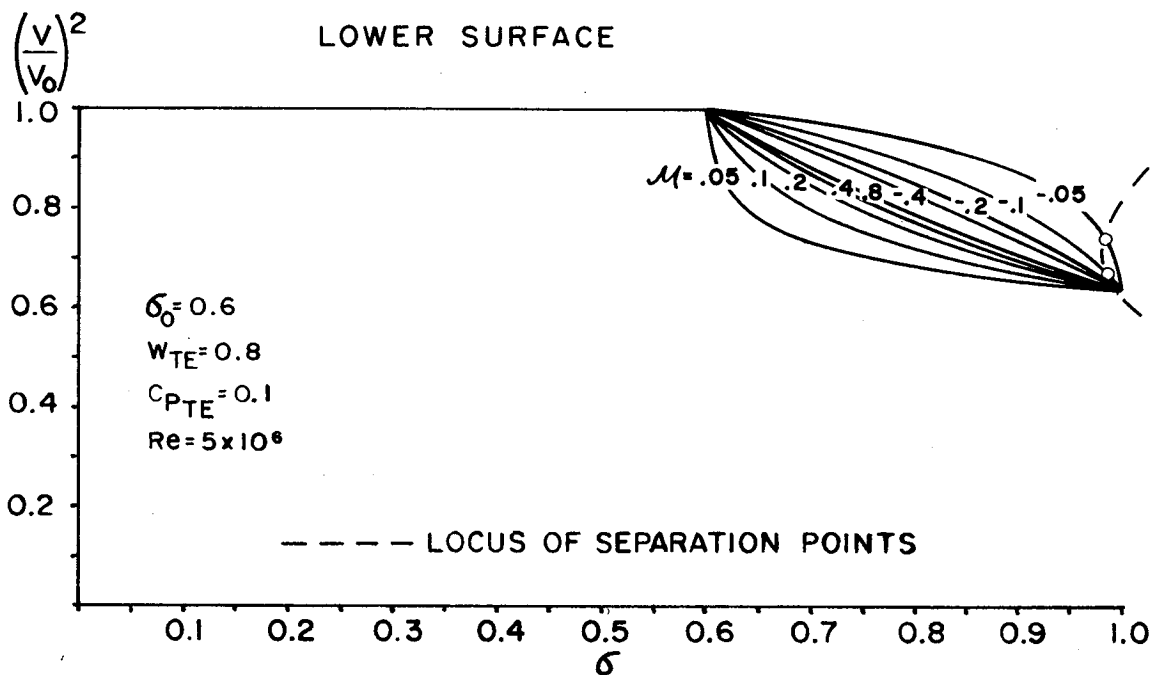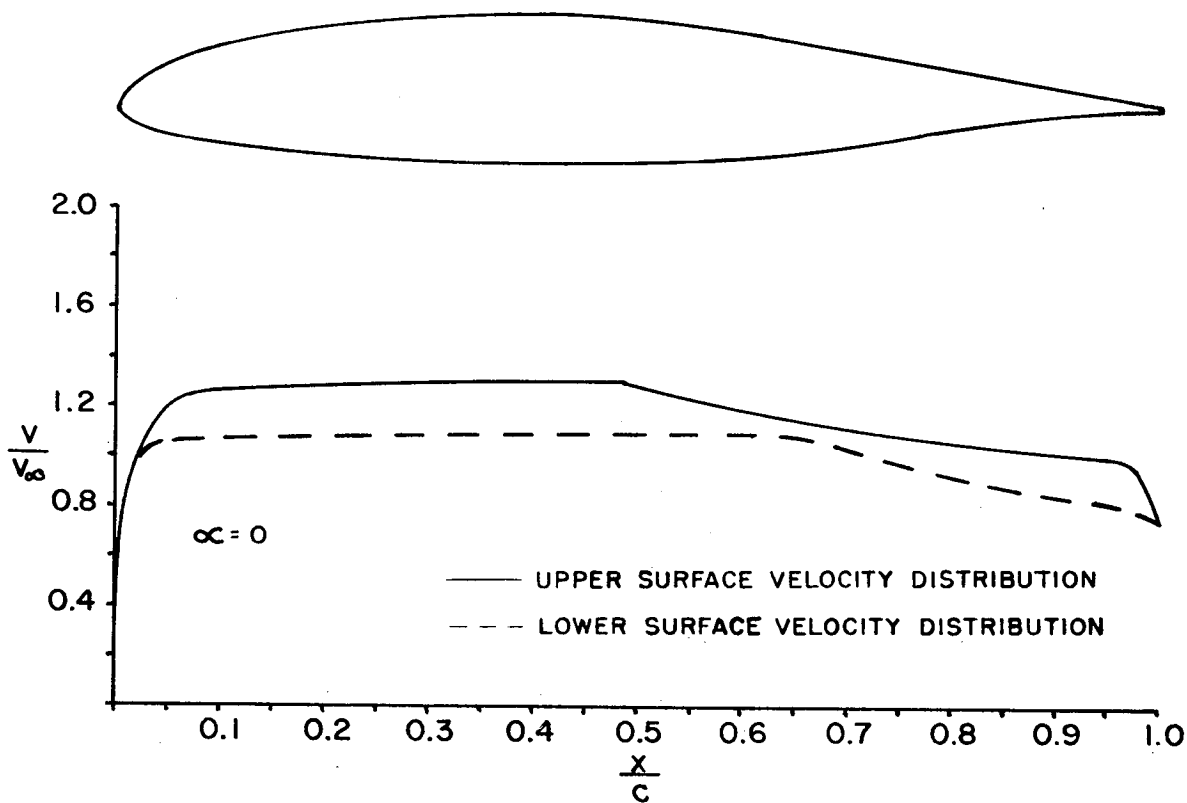Figure 13.- Velocity distributions produced by varying μ on the lower surface.

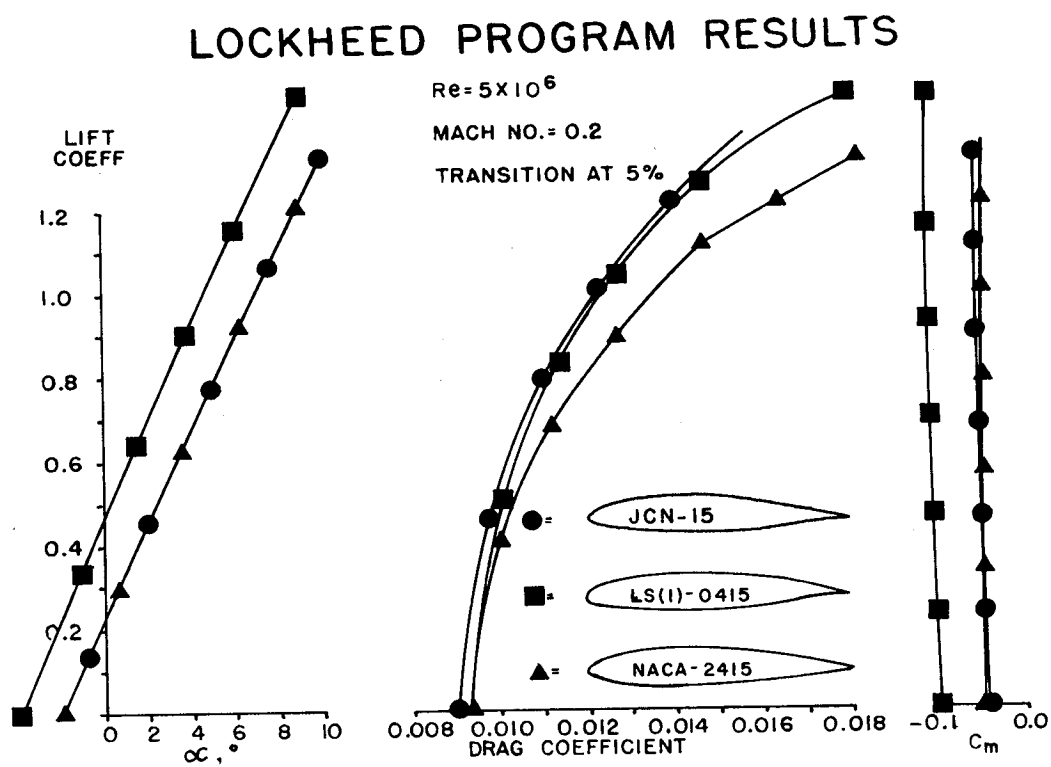Figure 14.- Results of inverse airfoil design program for 15-percent-thick airfoil.

LOCKHEED PROGRAM RESULTS

Figure 15.- Theoretical performance of three 15-percent-thick airfoils.

THE GENERAL AVIATION AIRFOIL DESIGN

AND ANALYSIS SERVICE - A PROGRESS REPORT

G. M. Gregorek, K. D. Korkan, and R. J. Freuler
The General Aviation Airfoil Design & Analysis Center
The Ohio State University

SUMMARY

Under contract to the NASA Langley Research Center, The Ohio State University established an airfoil design and analysis service for the general aviation industry. This paper presents the status of that service, 20 months after its initiation.

INTRODUCTION

In June 1976, The Ohio State University (OSU) was awarded a contract by NASA Langley Research Center to initiate an airfoil design and analysis service for use by the general aviation technical community. The primary objective of this contract, as noted in the Statement of Work, was "to develop the capabilities to perform design, selection and development of advanced two-dimensional airfoil shapes, high lift flap systems and trailing edge controls by use of advanced analytic methods and computer programs". This capability was to be used to develop airfoils tailored to the particular requirements of general aviation and to provide other technical and consultation services applicable to airfoil selection and development.

In response to these requirements, the General Aviation/Airfoil Design and Analysis Center (GA/ADAC) was established at the Aeronautical and Astronautical Research Laboratory (AARL) in July, 1976. AARL, located at The Ohio State University Airport is a modern research facility, equipped with wind tunnels operating at all speed regimes and supported by excellent data handling and numerical computing capability. GA/ADAC personnel are part of the research staff of AARL and have experience in the analysis, wind tunnel, and flight testing of airfoils.

The key airfoil computer methods to be utilized by the service were provided by NASA Langley Research Center. These codes, categorized as single element analysis, single element design and multi-element analysis programs, were tuned for the AARL Harris Computer System. Once these codes were tested and declared operational at GA/ADAC, and after NASA Langley Research Center personnel reviewed its organizational and contractual procedures, GA/ADAC was certified for use by industry. Thus in November 1977, the airfoil design and analysis service was ready to aid the industry in single element design and analysis for both low

speed and transonic airfoils and for low-speed multi-element airfoil analysis.

This paper reviews the capability of GA/ADAC and the progress made since the certification process was completed.

GA/ADAC CAPABILITIES

Organization

The structure of the General Aviation Airfoil Design and Analysis Center is shown in figure 1. The organization consists primarily of two areas with associated personnel, i.e., applied aerodynamics and numerical analysis. These areas are then supported by both graduate and undergraduate student assistants providing them valuable experience in airfoil design and analysis. GA/ADAC is further enhanced by having available consultants when needed in theoretical/experimental aerodynamics in AARL and GA Operations through the Department of Aviation located at Don Scott Field. Further, all contractual items such as the basic contract and purchase orders are handled by The Ohio State University Research Foundation.

AARL Computer Facilities

The AARL Digital Computer and Data Acquisition System (fig. 2) is an example of state-of-the-art techniques in the computer and electronics fields applied to experimentally and theoretically oriented research. The system can be broken into four groups of components for descriptive purposes: (1) the analog front end consisting of various analog and signal conditioning devices; (2) the central processing units (CPU); (3) the various input and output peripheral devices (I/O devices) to handle assorted I/O functions associated with more typical computer systems; and (4) the Remote Job Entry (RJE) subsystem which enables communication with any remote host computer in a dial-up mode of operation.

The AARL Digital Computer and Data Acquisition System utilizes two central processing units which are operated in a non-redundant dual processor configuration. The processors are directly connected via a CPU-to-CPU link and, in addition, they share a disc cartridge mass storage device.

The input-output system, exclusive of the devices which comprise the analog front end, consists of the following peripheral devices: (1) a removable pack disc system; (2) a cartridge disc system including one fixed disc platter and one removable disc cartridge; (3) a dual density 800/1600 bits/inch 9 track industry compatible magnetic tape drive; (4) an 800 bits/inch 9 track magnetic tape drive; (5) a 300 cards/minute card reader; (6) a 135 characters/line 400 line printer; (7) an ASR-33 standard teletype with paper tape facilities; (8) a Tektronix 4010 cathode ray tube (CRT); and (9) a four pen 36 inch drum type plotter.

The Remote Job Entry (RJE) subsystem supports communication with a remote host computer. Such communications are carried out concurrently with other computer tasks including real-time data acquisition and reduction. Included in the RJE subsystem are: (1) a synchronous controller with baud rate to 9600 bits/second; (2) a Bell system compatible modem with dial-up telephone dataset; and (3) a CRT display device providing 24 lines with 80 characters/line of display.

The computer system is operated in an "open-shop" mode, where all users have full access at both the hardware and software levels to the majority of the features of the system. The computer system is used extensively in on-line, real-time, interactive data acquisition/reduction and theoretical calculations performed within GA/ADAC. Further, as shown in figure 2, students are encouraged and trained to use the various computer codes on the AARL computer available through GA/ADAC.

GA/ADAC Computer Program Library

GA/ADAC includes an extensive library of computer codes developed for and by NASA. A listing of the current programs is given in table I and covers both single and multi-element analysis and design in addition to the necessary utility codes. Theoretical analyses of sub- and supercritical airfoils have been conducted with these computer programs, with numerous comparisons, as indicated in figures 3 and 4, between the numerical methods and wind tunnel data. The limitations of each code have been explored and documented.

More recently, propellers have been studied, specifically the effect of airfoils on the aerodynamic and acoustic performance of propellers. This effort was started at the beginning of the second year of the NASA contract; the current capability allows an evaluation of propeller performance coupled with the numerical calculation of the acoustic environment. Typical results are shown in figures 5 and 6 showing the satisfactory spectral and acoustic pressure signature agreement with experiment.

GA/ADAC EXPERIENCE

Industry Interactions

In the early stages of the service, GA/ADAC staff contacted many of the potential users in the industry, describing the proposed service and inquiring of the interest and needs of the particular company.

One area touched upon consistently by industry was the protection of proprietary data. The question was one of tempering the desire for confidentiality of a user with the needs for eventual dissemination of technical information generated by a government supported activity. While GA/ADAC personnel could assure industry officials that this data would remain confidential for two years - the duration NASA had suggested for restricting the information -

industry felt this period insufficient. Discussions with NASA resulted in a compromise; company data would be withheld automatically for three years before becoming part of the public domain. Should a user desire, yearly extensions to this period could be negotiated on an individual basis.

The second area that was explored during these company contacts was the type of service that would most fit their needs, in addition to those proposed services. Immediately apparent was the necessity for improvement in the prediction of maximum lift coefficient for both single and multi-element airfoils, for general improvements in mult-element performance at high flap angles, for integrating the advanced airfoil designs into three dimensional predictions and for more information on propellers. These desirable goals for GA/ADAC were noted and targeted for study during the second year.

Industry Users

Since the certification of GA/ADAC by NASA was made known to industry, many inquiries have been received. Of these inquiries, as of 1 March 1978, six have resulted in contracts for services. The tasks cover the range from simple consultation and selection of an airfoil through analysis tasks for modified airfoils to complete airfoil design problems. Costs for these services have varied from a few hundred to several thousand dollars. As noted in table II, these users vary from small concerns to large corporations and government agencies.

CONCLUSIONS

From the initial operating experiences of GA/ADAC several pertinent observations may be drawn.

i)   Basing GA/ADAC at AARL has proven valuable; expert help may be drawn in from AARL as required.

ii) As senior GA/ADAC staff are assigned part-time to the NASA sponsored part of the service, their efforts may be expanded to support industry sponsors as necessary.

iii) Use of undergraduate and graduate engineering students as an integral part of GA/ADAC operations has been successful, with one graduate and two undergraduate students trained in airfoil computation methods entering the industry job stream.

iv) The interest in new airfoils is quite high with groups such as the the Experimental Aircraft Association (EAA) continually seeking data; some mechanism must be set up to serve this important segment of aviation.

To these observations may be added the final comment that GA/ADAC - with its comprehensive and expanding library of airfoil computer codes - is operational.

TABLE I. GA/ADAC COMPUTER PROGRAM LIBRARY

COMPUTER CODE	NUMBER AVAILABLE AT GA/ADAC
Single Element	
- Analysis	5
- Design	7
Multi-Element	
- Analysis	4
- Design	1
Propeller	
- Performance Analysis	3
- Acoustic Analysis	1
- Design	1
Utility	
- Airfoil Section Generation	2
- Contour Smoothing	1
- Coordinate Enrichment	1
- Hicks Optimizer	1

TABLE II. GA/ADAC USERS AS OF 1 MARCH 1978

USER	TASK
Branson Aircraft Corp........Airfoil Modification/Analysis	
Hamilton Aviation Corp.......Airfoil Selection/Consultation	
Piper Aircraft Corp.........Airfoil Analysis	
Rockwell International.......Airfoil Design	
Scheutzow Corp...............Airfoil Selection/Consultation	
USAF Flight Dynamics Lab.....Airfoil Design	
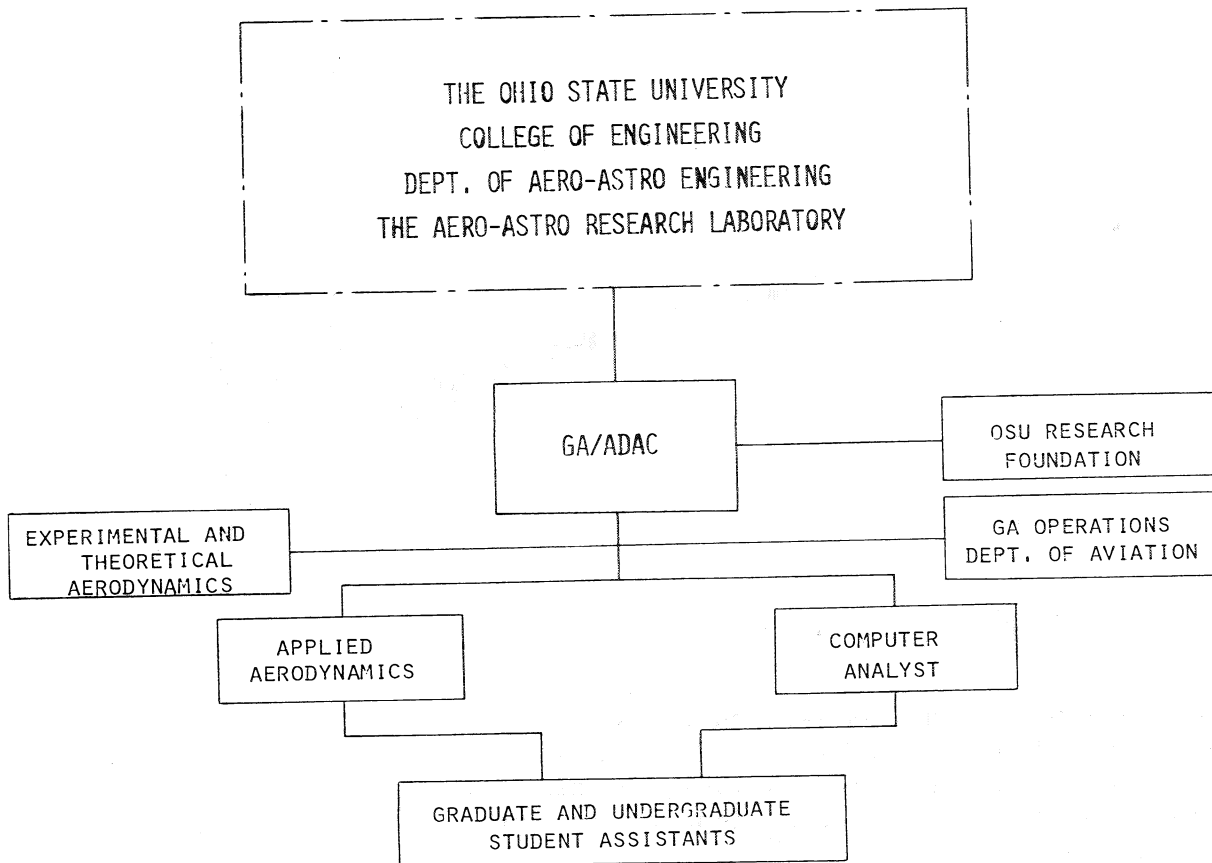
Figure 1.- Organization chart showing General Aviation Airfoil Design and Analysis Center.

Figure 2.- AARL Computer Center.
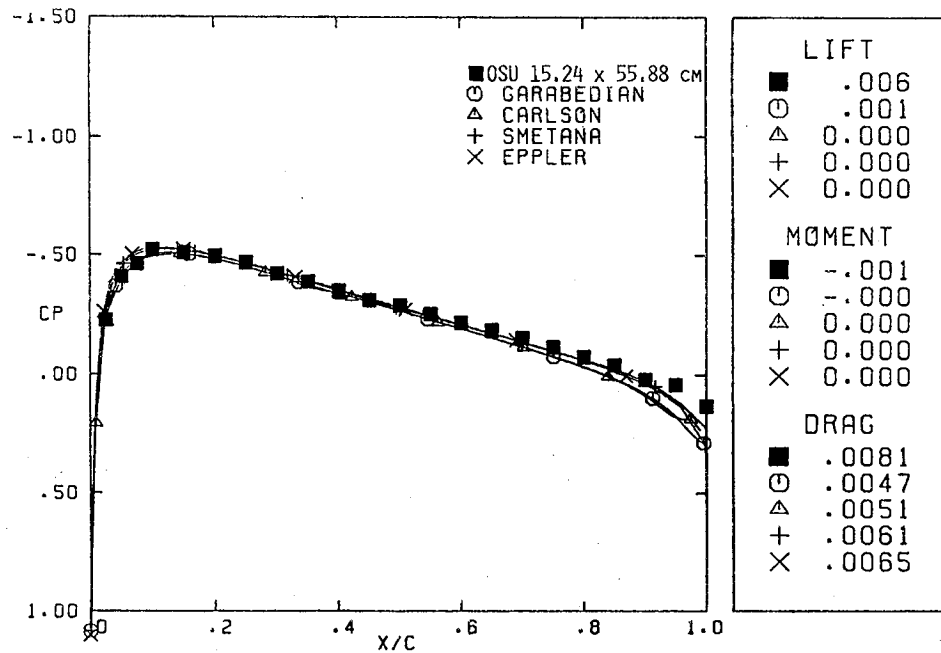
Figure 3.- Subcritical comparison of four computer codes with OSU wind tunnel results. NACA 0012 airfoil; M = 0.575; Re = 4.68 × 10^{6}; α = 0°. The symbol M denotes Mach number, Re denotes Reynold's number, α denotes angle of attack, C_p denotes pressure coefficient, and x/c denotes fraction of chord.

Figure 4.- Supercritical comparison of two airfoil analysis codes with OSU wind tunnel results. NACA 0012 airfoil; M = 0.808; Re = 6.12 × 10^{6}; α = 0°.

Figure 5.- Comparison between acoustic experimental measurements on a propeller and predicted computational results.
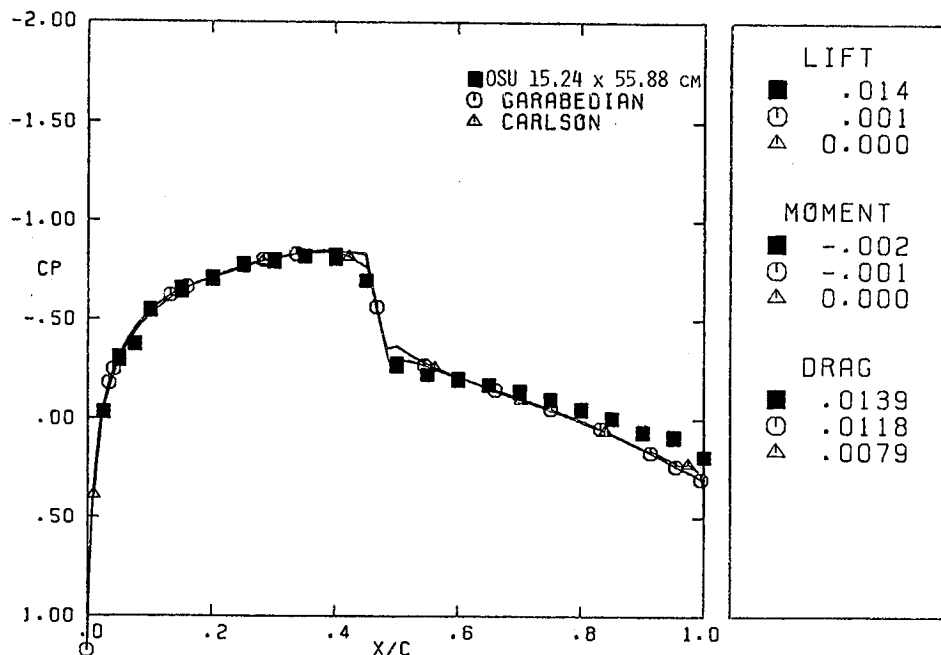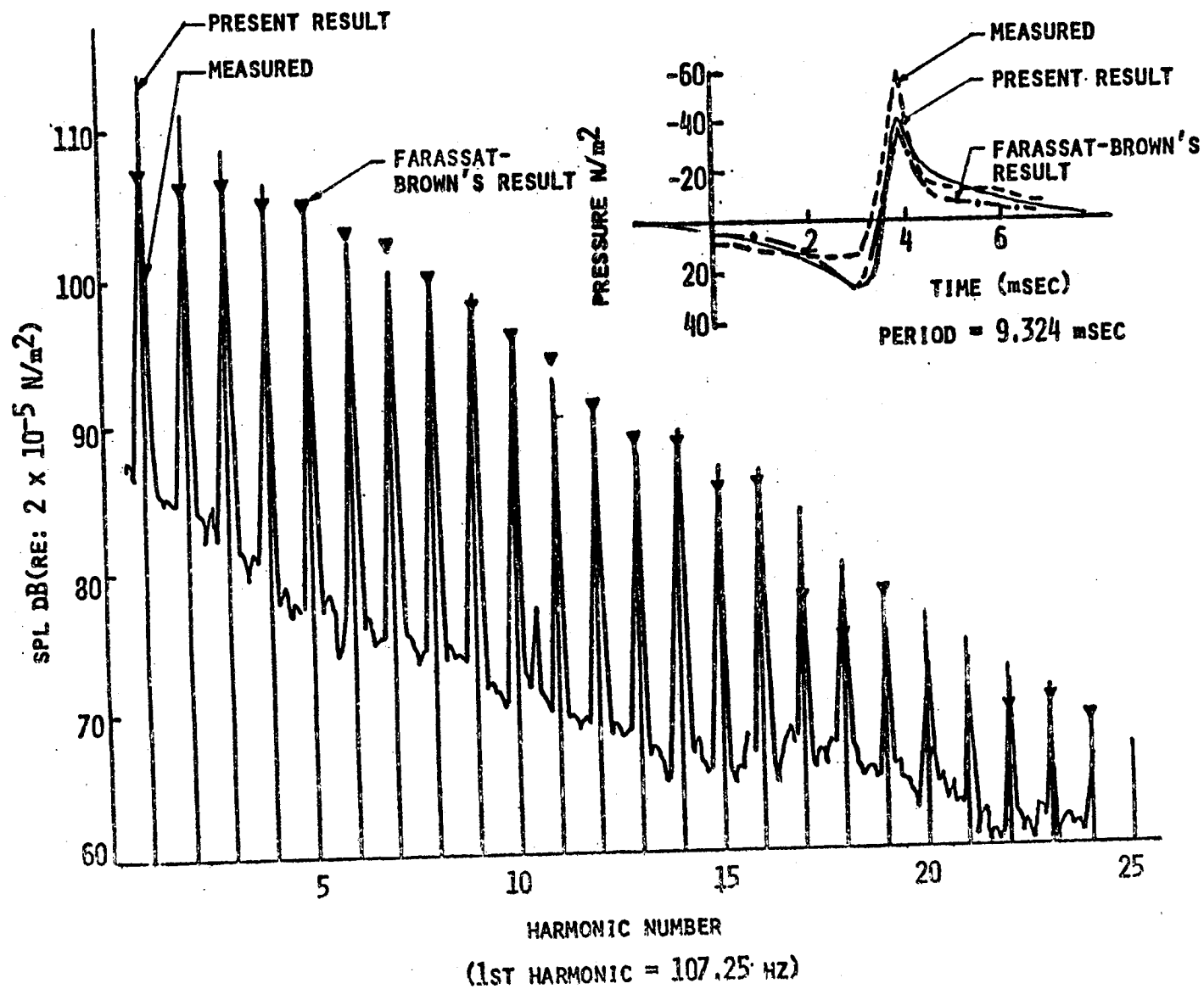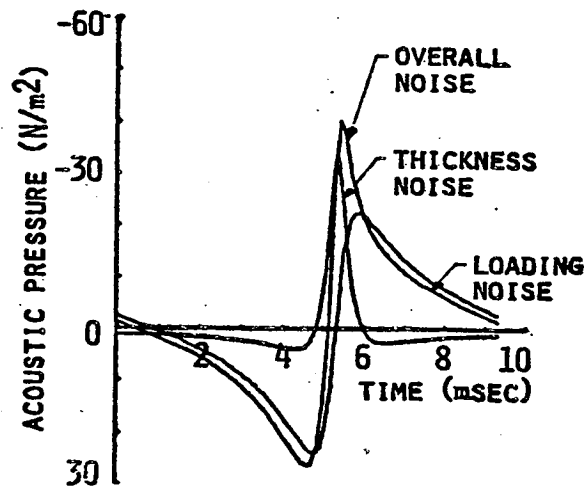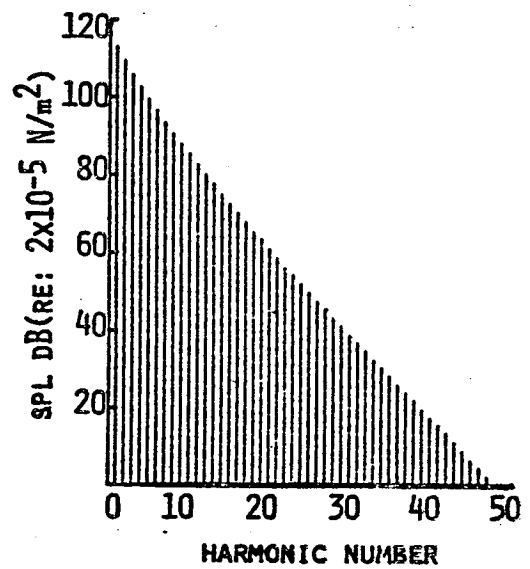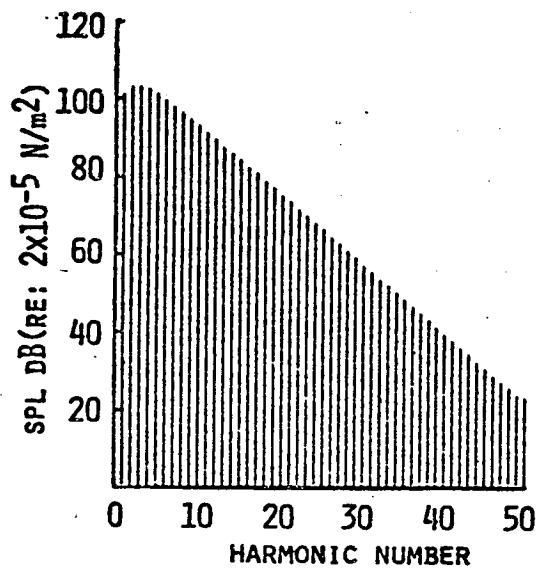
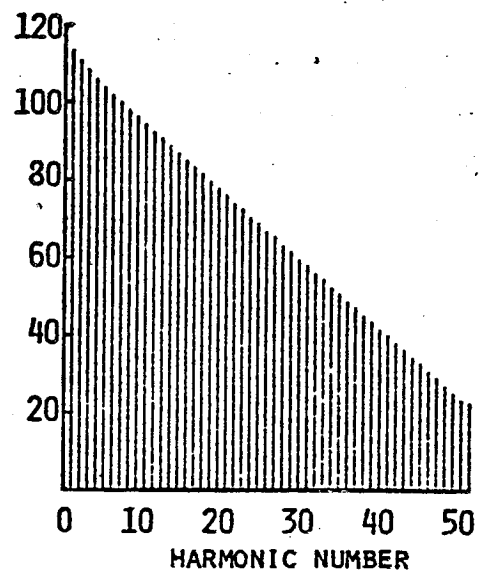Figure 6.- Propeller acoustic pressure signature and spectrum.

RESULTS OF AN INVESTIGATION OF SEVERAL NEW ROTORCRAFT AIRFOILS

AS RELATED TO AIRFOIL REQUIREMENTS

Gene J. Bingham, Kevin W. Noonan, and Henry E. Jones
Structures Laboratory, AVRADCOM Research and Technology Laboratories

SUMMARY

The results of an analytical investigation indicate that the airfoil design requirements for a helicopter rotor depend strongly on the specific rotor application. In addition, the investigation indicates that improvements in the airfoil drag-divergence and/or lift characteristics provide added flexibility to the rotor designer.

Based on these results, a set of three airfoil sections has been designed by applying a crestline criteria and has been experimentally evaluated in the Langley 6- by 28-inch transonic tunnel. The test results indicate that the new airfoils provide a higher drag-divergence Mach number (over a range of lift coefficients) than other sections of comparable thickness-to-chord ratios. The maximum normal-force coefficients were determined to be lower than the airfoils used in the comparison. Other airfoils are currently being developed to provide improvements in maximum normal-force coefficient.

INTRODUCTION

During a single revolution of a helicopter rotor in forward flight, the airfoil sections can experience lift coefficients from negative values up to the maximum lift coefficient and Mach numbers from near zero to values greater than that for drag divergence. Therefore, the airfoil design challenge is to identify and satisfy all of these operating conditions. Of course, the operating conditions can be expanded as the airfoil characteristics are improved.

An analytical and experimental investigation has been conducted to identify and expand rotor-airfoil operating conditions. The analytical investigation defined the operating envelopes of the CH-53A, UH-1H, AH-1G, OH-58, OH-6A, and CH-54B aircraft. The experimental investigation of three new airfoil designs was conducted in the Langley 6- by 28-inch transonic tunnel at Mach numbers from about 0.35 to 0.90 and at respective Reynolds numbers (based on chord) of about 4.0×10^6 to 11.0×10^6.

DISCUSSION OF RESULTS

The operating conditions for a CH-53A rotor are presented in figure 1 at the indicated weight and velocity at sea level standard conditions (SLS). Lift

coefficient is presented as a function of Mach number at three radial stations. The three curves define the lift coefficient and Mach number relationship as the rotor turns one revolution. For example, at the rotor tip (1.0 R where R denotes radius), the section advancing into the wind experiences a Mach number of about 0.82 at a slightly negative lift coefficient. Then, as the blade rotates 180° to the retreating side, the lift coefficient increases to about 1.1 at a Mach number of about 0.45. The corresponding lift coefficient for the other two radial stations on the retreating side (for example, those at the respective minimum Mach number) are lower than that at the tip. At 0.4 R the lift coefficient is significantly lower because of the combination of rotational and inflow velocity that results in a significantly lower section angle of attack.

The values of lift coefficient and Mach number shown in figure 1 were obtained by using a rotor performance prediction program (in this case, C-81). The program accepts airfoil characteristic data as a function of Mach number and angle of attack and, with inputs of aircraft geometry and operating conditions, the conditions for trimmed flight are determined and outputs of section lift coefficient and Mach number can be obtained. NACA 0012 airfoil data adjusted for practical construction tolerances, roughness, and so forth, were used.

The next figure (fig. 2) shows the same lift coefficient-Mach number curves, but lines indicating the maximum lift coefficient and the drag divergence Mach number of the airfoil are added. The added curves were obtained by cross-plotting the NACA 0012 airfoil characteristic data in the rotor performance prediction program used initially to define the operational lift coefficient-Mach number curves. The maximum lift coefficient is reached at the retreating-tip section which results in high drag coefficients. Even more significant from the rotor power-requirement point of view is the operation of the tip region at Mach numbers greater than the drag-divergence value. As indicated in figure 3, the largest increment between the drag divergence Mach number and the operating line occurs at the higher lift coefficients. In this case, the computed results indicate that the power absorbed by the retreating tip is about 70 percent as great as that of the advancing tip even though the advancing-tip Mach number and dynamic pressure are significantly higher. With these factors considered, the airfoil design challenge for the tip section is to increase both the section maximum lift coefficient at a Mach number of about 0.5 and the drag-divergence Mach number at all operational lift coefficients.

It should be noted here that the selected operating conditions presented on figures 1 and 2 and the next three figures are boundary conditions, so near-maximum Mach numbers and angles of attack are indicated for level flight.

Operating conditions for the UH-1H aircraft are indicated on figure 3. As before, NACA 0012 data were used and the weight and flight velocity are indicated. In this case, the advancing-tip Mach number is about 0.9 at a negative lift coefficient and decreased to about 0.55 at a lift coefficient of 0.8 on the retreating side. The lift coefficients are higher for the retreating side at the inboard stations. The maximum lift coefficient and drag-divergence Mach number curves are again superimposed on figure 4. Here, the maximum lift coefficient is not reached and the drag divergence line is exceeded on the

advancing side only. The design challenge for the tip section is to increase the drag-divergence Mach number at lift coefficients below 0.5 or 0.6.

The operating lift coefficient-Mach number curves for a given aircraft can be significantly altered by applying composite-blade technology because it permits a wide range of blade planform and airfoil section changes which were not economically feasible with metal-blade technology. In addition, blade twist can be altered to improve both hover and forward-flight performance. If a tapered tip region is applied instead of the usual rectangular planform and the blade is retwisted, the inboard lift coefficients can be increased and the outboard can be decreased to improve both profile and induced-power requirements. The retreating-tip lift coefficients would be more negative and the overall airfoil design requirements would be somewhat altered. The point is, the airfoil design and the rotor design should be an integrated effort and the planform and twist distribution should be adjusted to take advantage of the new airfoil's enlarged lift-coefficient—drag-divergence-Mach-number boundaries.

Operating envelope curves are defined for a number of rotors in figure 5. The curves indicate boundaries such as those on the previous figures. The circle symbols indicate the part of the curve defined by the tip region, and the square and diamond symbols indicate boundary points defined by the curves at 0.7 R and 0.4 R, respectively. The point to be made here is that a wide range of airfoil requirements are encountered for different rotors. The advancing-tip Mach number varies from about 0.7 to 0.9 and the envelope lift coefficients vary from 0.9 to 1.3. Fortunately for the airfoil designer, it appears that if the drag-divergence Mach number requirements are higher, the lift coefficient requirements are generally lower. For example, the previously discussed UH-1H has a Mach number at the tip of about 0.9 (fig. 5) but the retreating-tip lift coefficient is about 0.8. However, the OH-58 has an advancing-tip Mach number of 0.7 but a retreating-tip lift coefficient of about 1.15.

With requirements such as these in mind, a family of airfoils has been designed at the Langley Research Center. Thickness-to-chord ratios of 8, 10, and 12 percent were included so multiple thicknesses could be applied at different radial stations, for reasons already mentioned. The design was made using the crestline criteria discussed in earlier papers and by analyzing the potential improvements in performance with the North Carolina State University version of the Lockheed program and the Korn-Garabedian program. One section for each thickness-to-chord ratio was selected for two-dimensional tests in the Langley 6- by 28-inch transonic wind tunnel (fig. 6). The sections are designed for easy transition from one thickness to another and to provide the maximum lift capability in the inboard regions of the rotor. Each section has the maximum thickness located at 40 percent chord because earlier analysis indicated that the drag divergence Mach number could be increased at midrange lift coefficients if this were done. The maximum camber was located at 40 percent chord for the same reason. The leading-edge radius was increased compared to the conventional NACA airfoils to increase the maximum lift coefficient. The lower surface is somewhat flattened to delay the onset of supercritical flow at negative angles of attack. Finally, the trailing edge was reflexed to provide near-zero pitching moment coefficient about the aerodynamic center, at least at subcritical Mach numbers.

Data from the 6- by 28-inch tunnel indicate that the near-zero pitching moment was attained. It should be noted here that different manufacturers specify different design pitching-moment coefficients. However, the value most used in the literature is absolute 0.02. The 8-percent-thick section meets this requirement at Mach numbers to about 0.90 (fig. 7), the 10-percent-thick section to about 0.82, and the 12-percent-thick section to about 0.72. By using the thicker sections inboard, the pitching-moment coefficient greater than absolute 0.02 can generally be avoided.

The normal-force coefficient boundaries indicated by the test results are indicated by figure 8. Normal-force coefficients are presented to eliminate possible lift interference correction errors required to account for the presence of the wind-tunnel walls. The differences in lift coefficient and normal-force coefficient are second or third decimal place values so the two can be used interchangeably. Also, it should be noted that the actual maximum normal-force coefficients for the airfoil sections are greater than that indicated. It has been determined that, as with a number of other wind tunnels, the boundary-layer separation from the airfoil occurs at the tunnel wall juncture prior to the occurrence of separation in the airfoil center line region. Based on comparisons of data from the 6- by 28-inch tunnel with data believed to be free of the tunnel wall separation problem, it has been concluded that the actual maximum normal-force coefficient should be about 0.10 to 0.15 higher than that indicated. A solution to the wall separation problem is under development with first tests of a wall boundary-layer suction system planned this summer.

A comparison of the data of figure 8 with the requirements indicated by figure 7 suggest that the requirements can be satisfied with these airfoil sections. For example, for the UH-1H the three sections would be distributed radially, and for the OH-58 the 12-percent-thick section alone would satisfy the requirements. Again, the requirements curves could be altered by changing planform and twist distribution to provide an even greater compatibility between requirements and airfoil section characteristics.

As mentioned earlier, the airfoils tested in the Langley 6- by 28-inch transonic tunnel were selected from a group of airfoils. The selection was made on the basis of analytical comparisons of aerodynamic characteristics of these airfoils and other airfoils applied to current helicopter configurations. The analysis indicated that the Langley airfoils would provide increases in drag-divergence Mach number in each case and that the maximum normal-force coefficient would be equal to or greater than that of the other airfoils of comparable thickness.

Figures 9, 10, and 11 show 6- by 28-inch wind tunnel results for the listed airfoil sections and indicate that the anticipated drag divergence improvements were realized but the maximum normal-force coefficients were generally lower.

A comparison of the RC12(B)3 airfoil with the classic NACA 0012 and the Boeing Vertol VR-7 with a -4.6° trailing-edge tab (to provide near-zero pitching moment) is presented in figure 9. The NACA 0012 provides the higher drag divergence Mach numbers at near-zero normal-force coefficient primarily

because of the absence of camber. The lack of camber also results in a lower drag-divergence Mach number at normal-force coefficient above about 0.3 and lower maximum normal-force coefficients. Again, the drag-divergence Mach number of the RC12(B)3 is generally slightly higher than that of the VR-7 but the maximum normal-force coefficient is about 0.1 lower.

A comparison of airfoil sections with thickness-to-chord ratios of about 10 percent is presented in figure 10. Included in the comparison is the Wortmann FX-098 (9.8 percent thick) designed for Bell Helicopter and the SC1095 (9.5 percent thick) designed by Sikorsky Aircraft. The largest gain in drag-divergence Mach number with the RC(B)3 series was obtained for the figure 10 case. The increase is greatest at normal-force coefficients above about 0.2. As before, the maximum normal-force coefficient is about 0.1 lower than the other two configurations.

The sections at or near 8 percent thick are compared in figure 1 and include the Wortmann FX-080 (8.0 percent thick) and FX-083 (8.3 percent thick) airfoils designed for Bell Helicopter, and the NLR-1 (8.6 percent thick) airfoil designed for Bell Helicopter and NASA. Again, the drag-divergence characteristics of the RC08(B)3 are favorable but the maximum normal-force coefficient is up to 0.1 lower than that of other airfoils shown.

Current plans are to make a more complete analysis of the data obtained during tests of the airfoils (fig. 6) previously described and to update the profiles of the family of airfoils from which the sections were selected. This effort will be accomplished using the analytical tools previously applied. The updated designs will then be evaluated and, as appropriate, the number of configurations tested in the wind tunnel will be expanded. One primary objective will be to increase the maximum normal-force coefficient capability of the airfoil family.

CONCLUDING REMARKS

The following points are to be made:

1. The airfoil design requirements are, to a large degree, a function of the specific rotor application.

2. Improved airfoil characteristics can give added flexibility to the rotor designer.

3. A set of airfoils has been defined by applying crestline criteria and has been experimentally evaluated.

4. New airfoils are being developed to improve the maximum normal-force coefficient characteristics without substantial degradation of the drag-divergence characteristics.
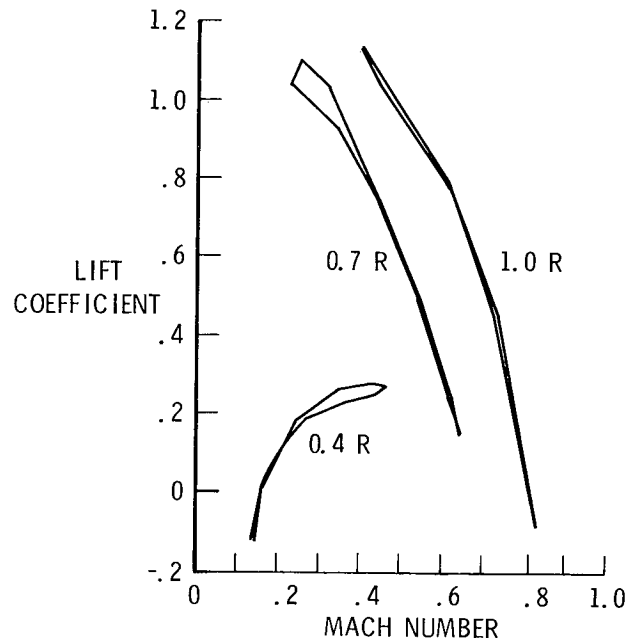
Figure 1.- Operating conditions for CH-53A rotor (19 000 kg; sea level standard; 140 knots). R denotes radius.

Figure 2.- Operating conditions for CH-53A rotor compared with maximum lift coefficient $c_{l,max}$ and drag-divergence Mach number M_{dd}.

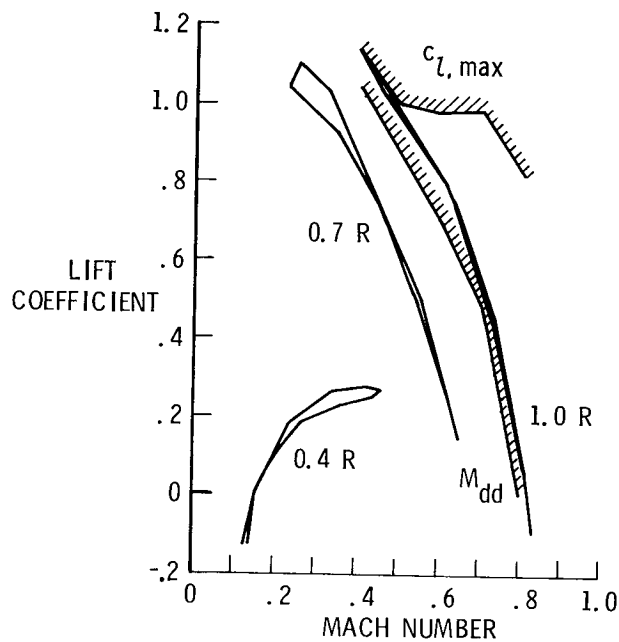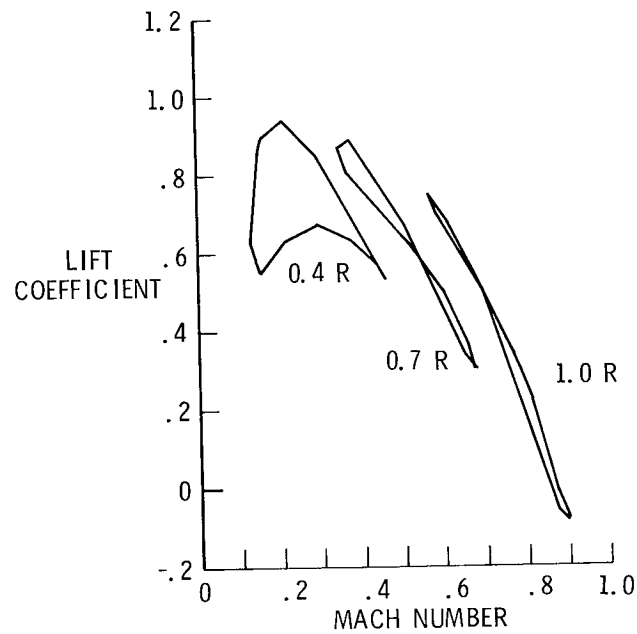Figure 3.- Operating conditions for UH-1H rotor (4300 kg; sea level standard; 110 knots).
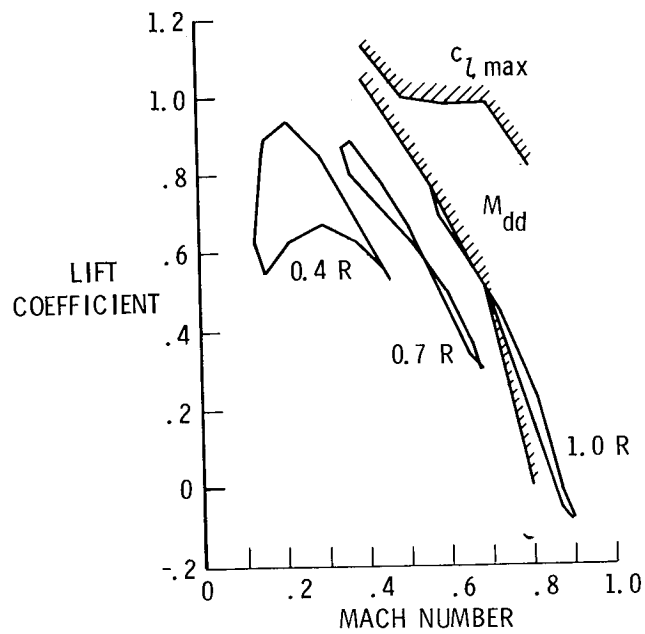
Figure 4.- Operating conditions for UH-1H rotor compared with maximum lift coefficient $c_{l,max}$ and drag-divergence Mach number M_{dd}.
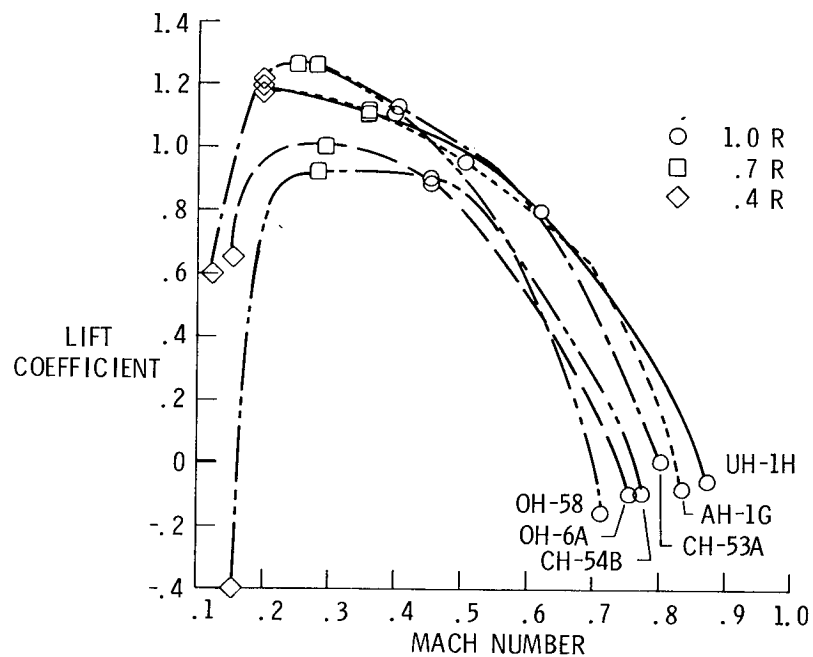
Figure 5.- Comparison of several helicopter boundaries.
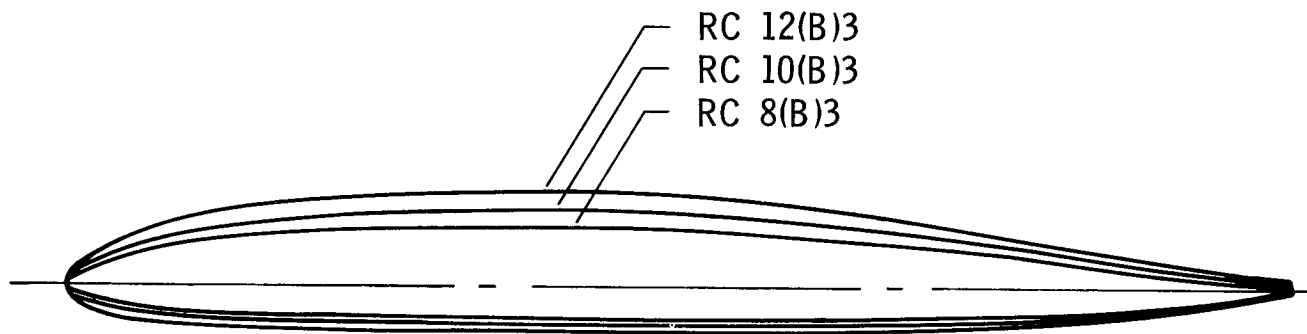
Figure 6.- Airfoil profiles.
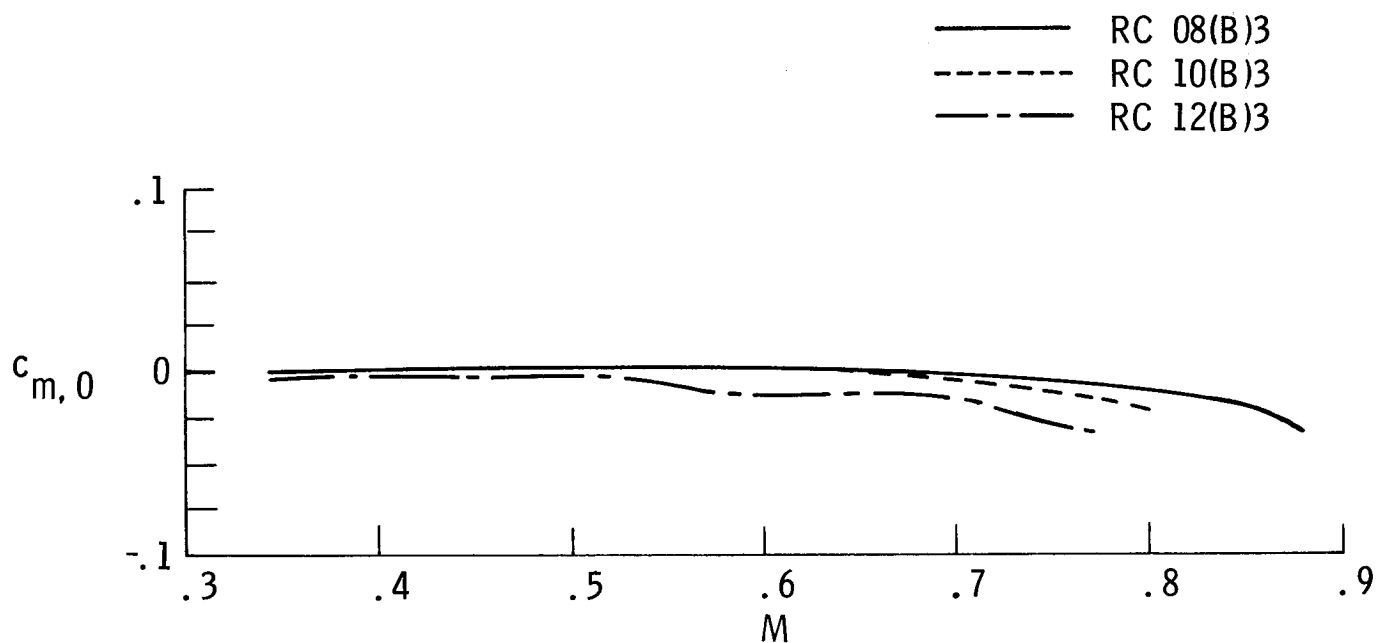
Figure 7.- Pitching-moment coefficient $c_{m,0}$ about aerodynamic center for RC08(B)3, RC10(B)3, and RC12(B)3 airfoils (Langley 6- by 28-inch transonic tunnel data). M denotes free-stream Mach number.
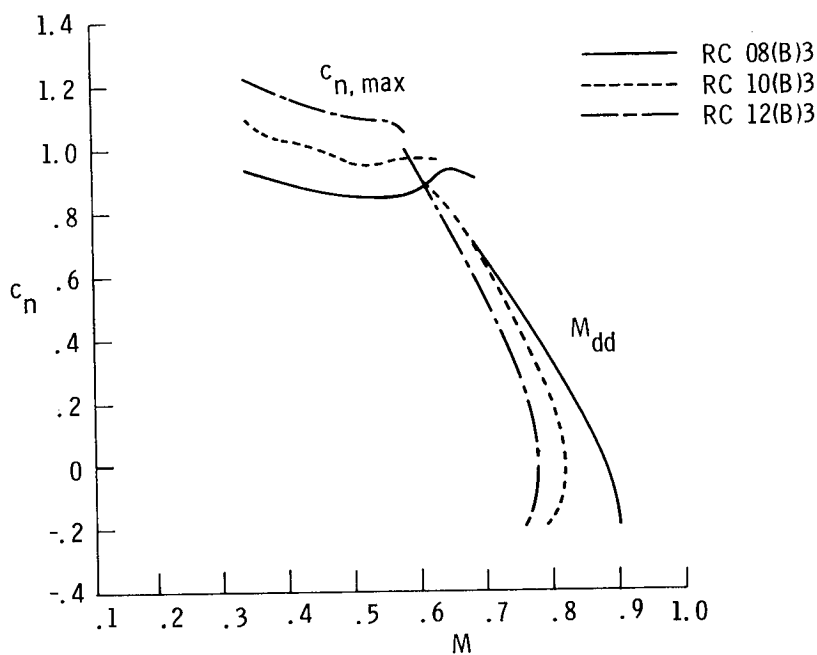
Figure 8.- Maximum normal-force coefficient $c_{n,max}$ and drag-divergence Mach number M_{dd} for RC08(B)3, RC10(B)3 and RC12(B)3 airfoils (Langley 6- by 28-inch transonic tunnel data).

117
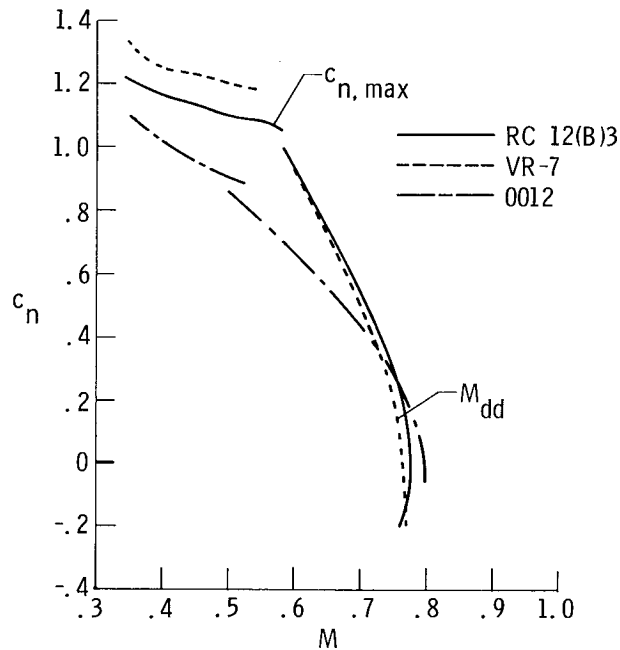
Figure 9.- Comparison of maximum normal-force coefficient $c_{n,max}$ and drag-divergence Mach number M_{dd} for 12-percent-thick airfoils (Langley 6- by 28-inch transonic tunnel data).

Figure 10.- Comparison of maximum normal-force coefficient $c_{n,max}$ and drag-divergence Mach number M_{dd} for near-10-percent-thick airfoils (Langley 6- by 28-inch transonic tunnel data).

Figure 11.- Comparison of maximum normal-force coefficient $c_{n,max}$ and drag-divergence Mach number M_{dd} for near-8-percent-thick airfoils (Langley 6- by 28-inch transonic tunnel data).

9

THE AERODYNAMIC DESIGN OF AN ADVANCED ROTOR AIRFOIL

James A. Blackwell, Jr., and Bobby L. Hinson
Lockheed-Georgia Company

SUMMARY

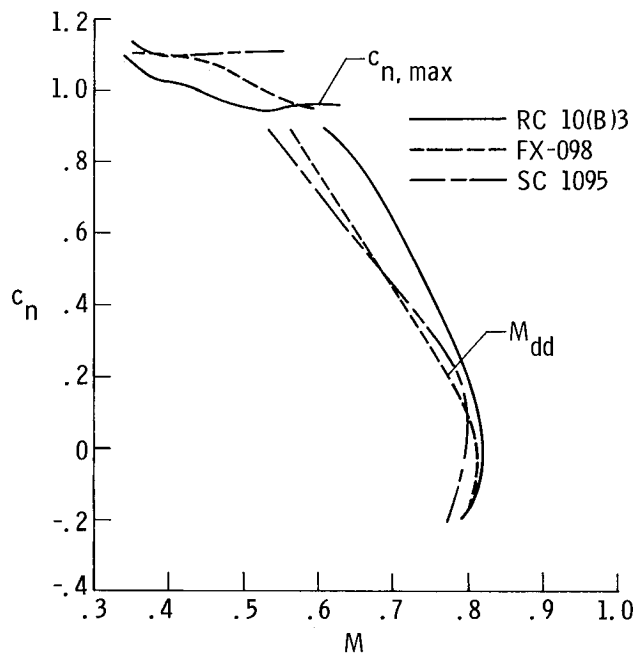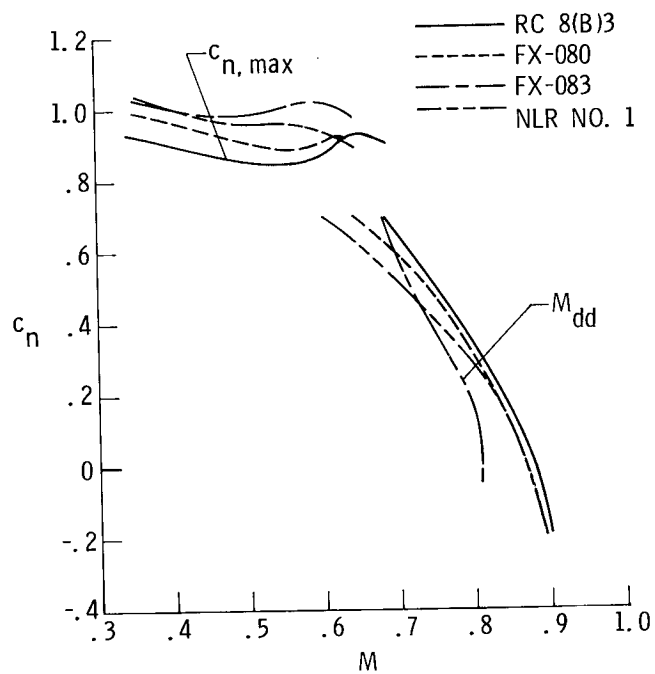A new rotor airfoil has been designed utilizing supercritical airfoil design concepts and an advanced design-and-analysis methodology. The new airfoil was designed subject to a stringent set of aerodynamic performance objectives. The design was accomplished using the Carlson viscous transonic inverse design procedure and the NASA-Ames constrained-function minimization technique for optimizing the airfoil leading-edge shape. The new airfoil has a maximum thickness-to-chord ratio of 10% and has a small amount of nose camber. Analysis of the new airfoil using the viscous transonic code of Bauer, et al. indicated the section generally achieved the specified aerodynamic performance objectives. The most important of the achieved objectives were low pitching-moment characteristics throughout the operating range, a maximum lift coefficient of 1.5 at a Mach number of 0.4, and a drag-rise Mach number of 0.81 at zero-lift conditions.

INTRODUCTION

Recently, several new airfoil concepts have been developed that indicate potential gains in performance may be possible over the wide spectrum of rotor operating conditions sketched in figure 1. For example, in Region 1 (fig. 1) significant progress has been made over the last ten years in increasing the airfoil drag-rise Mach number through the application of "supercritical" airfoil technology. Early applications (1969) of supercritical airfoil technology to rotor airfoil design (ref. 1) indicated large gains in drag-rise Mach number were possible, with respect to conventional airfoils, at low lift coefficients. Unfortunately, the maximum-lift characteristics (Region II) of this section were disappointingly low. Relative to Region II, new airfoil designs by Liebeck (ref. 2) and others have shown that the maximum lift of the airfoil can be significantly increased through proper design. These airfoils are not suitable, however, for rotor applications due to poor performance at the operating conditions of Region I.

Several attempts (ref. 3) have been made to synthesize the above advanced concepts developed for improving the performance in a single region into a unified approach that would yield good performance over the entire helicopter flight regime. This work has met with some success. The primary limiting factor in implementing the synthesized design approach and, hence, in achieving improved overall airfoil performance has been the lack of an adequate analytical design and analysis methodology.

Over the past five years, significant advances (refs. 4 to 6) have been made in theoretical methods for the design and analysis of airfoil sections. The use of these advanced programs will substantially increase the rotor designer's chance of developing a new airfoil that will best suit his particular helicopter mission and result in optimum rotor performance.

It is the objective of this paper to present results on the application of new theoretical methods to design an advanced rotor airfoil on the basis of a representative set of airfoil performance objectives. Emphasis is also placed on defining the total design methodology which includes the design logic and the coupled use of design and analysis tools.

SYMBOLS

c	airfoil chord, m
C_d	section drag coefficient
C_ℓ	section lift coefficient
C_m	section pitching-moment coefficient about quarter chord
C_n	section normal-force coefficient
C_p	pressure coefficient
M	freestream Mach number
M_D	drag-rise Mach number ($dC_d/dM = 0.1$)
M_ℓ	local Mach number
M_S	local Mach number immediately upstream of shock
M_T	Mach number for pitching moment break, or Mach tuck ($dC_m/dM = -.25$)
x,y	coordinates along and normal to airfoil chord, m

AERODYNAMIC PERFORMANCE OBJECTIVES

In order to guide the design of the new rotor airfoil, a prioritized set of aerodynamic performance objectives was developed (table I). Most of these objectives are graphically illustrated in figure 2. The attainment of the aerodynamic performance objectives is constrained by imposition of several geometric constraints (see ref. 7). The most important was that the maximum thickness-to-chord ratio be greater than or equal to 10 percent.

AERODYNAMIC DESIGN CRITERIA

In this section, a synthesized set of aerodynamic design criteria for each of the operating regions of figure 1 will be presented.

Region I — High Mach Number/Low Lift

The aerodynamic design criteria pertinent to achieving the aerodynamic performance objectives in Region I are illustrated in figure 3 in terms of the required pressure distribution shapes. The paragraph number of the individual design criteria which follow are keyed to the numbers depicted in figure 3.

1. In order to achieve good drag-rise characteristics, a rapid change in curvature must occur near the airfoil leading-edge on both the upper and lower airfoil surfaces. The presence of the required leading-edge curvature is evidenced by the "peaky" subcritical pressure distributions near the airfoil leading-edge (fig. 3(a)). At transonic speeds, the rapid change in curvature produces supersonic expansion waves that result in a near isentropic or isentropic recompression of the supercritical flow. The chordwise location of the subcritical pressure-distribution peak (fig. 3(a)) is very important. The closer the location of the pressure-distribution peak to the leading edge, the higher the drag-rise Mach number will be. By moving the region of rapid curvature closer to the nose of the airfoil, a considerable reduction in curvature over the crest region of the airfoil can occur. This reduces the supervelocities over the crest region resulting in a delay of the drag-rise Mach number. The magnitude of the subcritical pressure peak is also very important. A subcritical peak that is too large may result in excessive subcritical creep drag (objective no. 12, table I). The correct level of subcritical pressure peak is one that produces a near flat pressure distribution back to the shock at transonic speeds (fig. 3(b)).

For the lower surface, the rapid change in curvature should be located near the airfoil leading-edge. On the upper surface, the chordwise location of the rapid change in curvature must be compromised with Region II design criteria (to follow) which requires that the rapid change in curvature be located as far aft as possible. For the current design, a compromise location of approximately 10% chord was selected for the upper surface position.

2. The surface Mach number preceding the shock waves on the upper and lower airfoil surfaces must be less than 1.16 at the design point for Region I ($M = 0.83$, $C_l = 0$). The weak shock wave can be obtained by using "supercritical" design concepts (see ref. 7). Using these design concepts, the strength of the shock wave can be diminished to near-isentropic or to an isentropic flow recompression.

Application of supercritical concepts requires the airfoil shape following the regions of rapid curvature at the airfoil leading edge back to the airfoil crests to have a minimum of surface curvature. This can be achieved by locating

the airfoil crest (at the angle of attack corresponding to $C_\ell = 0$) for each surface as far aft as possible.

3. *The pressure recovery following the shocks on the airfoil surfaces (fig. 3(b)) should be mild.* Region I criteria would dictate near-zero pressure gradient behind the shock and a maximum gradient near the trailing edge. The selected shape represents a compromise with Region II where a minimum pressure gradient near the trailing edge is required.

4. *The flow must remain attached over the entire airfoil surface.*

5. *To achieve well behaved boundary-layer characteristics at the airfoil trailing-edge, the trailing-edge pressure coefficient should be minimized as much as possible (more negative).* This requirement results in a boundary-layer near the airfoil trailing edge that is less likely to separate. This can generally be accomplished with no increase in profile drag (ref. 7). The geometric effect resulting from minimizing the trailing-edge pressure coefficient is that the trailing-edge included angle of the airfoil basic thickness form is reduced.

6. *The airfoil trailing-edge bluntness should be less than one-half the boundary layer thickness at the trailing-edge.* This criterion (ref. 8) ensures that excessive base drag due to the blunt trailing-edge will not occur. This criterion is important to achieving aerodynamic performance objective no. 12 in table 1.

7. *In order to achieve a low drag level at Mach numbers below the on-set of drag-rise (objective no. 12, table I), the upper and lower surface boundary-layers must remain laminar back to approximately 30% chord.* Since subcritical pressure peaks which would precipitate transition (fig. 3(a)) are required near the leading-edge to achieve a high drag rise Mach number, it does not appear that aerodynamic performance objective no. 12 can be fully achieved.

Region II — Low Mach Number/High Lift

The aerodynamic design criteria for Region II operating conditions are illustrated in figure 4 and discussed below:

1. *The Mach number ahead of the leading-edge shock should be less than 1.4 at the conditions corresponding to maximum lift at $M = 0.40$.* For shock Mach numbers approaching or in excess of 1.4, the condition of the boundary layer is substantially weakened and flow separation occurs at the shock (ref. 9), or near the airfoil trailing-edge thereby limiting the maximum lift of the airfoil. To minimize the strength of the leading-edge shock at these high-lift/low-speed conditions, "supercritical" design concepts similar to those discussed for Region I can be used. This approach was first recognized by Wortmann (ref. 3).

As with Region I, maximum reduction in shock strength is achieved for Region II when the crest is as far aft on the airfoil as possible. Coupled with the rapid curvature requirement from Region I, a visual "corner" is produced on the airfoil surface near 10% chord.

2. *The pressure distribution ahead of the leading-edge shock should be shaped to promote isentropic recompression (fig. 4(a)).* In order to achieve a level of supervelocity over the forward part of the airfoil that culminates in a shock strength no greater than 1.4, the curvature of the airfoil must be low following the leading-edge. This gives the appearance of a flat over the leading-edge region.

3. *Pressure recovery following the shock should be designed to maintain attached flow up to 90% chord for the condition corresponding to maximum lift.* This criterion is partially achieved by moving the airfoil maximum thickness point as far forward as possible. This results in the majority of flow deceleration taking place over the forward portion of the airfoil where the boundary layer is thin. A forward maximum-thickness location also allows a smaller included trailing-edge angle which in turn produces a more negative trailing-edge pressure coefficient. This has the effect of minimizing the pressure drop between the leading and trailing edges and reduces the tendency of the flow to separate. It should be noted that this criterion is in conflict with the design criteria of Region I where it is desirable to have the maximum thickness as far rearward as possible. Obviously a compromise must be made.

4. *In order to achieve aerodynamic performance objective no. 1, the design pressure distribution (fig. 4(b)) must be constrained such that the pitching-moment coefficient is minimized.* To achieve a low value of the pitching moment, the amount of airfoil camber must be minimized and limited to the forward region of the airfoil.

Region III — Moderate Mach Number/Moderate Lift

The airfoil aerodynamic design criteria for Region III operating conditions are illustrated in figure 5 and discussed below.

1. *In order to meet the target drag level of $C_d = .0080$ at $M = 0.60$ and $C_\ell = 0.60$ (aerodynamic performance objective no. 5), the wave drag must be virtually zero.* Wave-drag minimization requires that the entire pressure distribution be subcritical or if supercritical flow is present then the flow must either recompress isentropically or the shock waves must be very weak.

2. *The lower surface pressure distribution should be shaped to promote laminar flow and hence reduce the airfoil profile drag.*

3. *The flow must remain attached to the airfoil trailing edge.*

DESIGN AND ANALYSIS METHODOLOGY

The aerodynamic design considerations previously discussed dictate the design of an airfoil section with good performance at conditions which produce extensive regions of supercritical flow over the airfoil. Therefore, the required theoretical design-and-analysis methodology must be able to treat

transonic flows. The selected methodology is illustrated in figure 6. A combination of three methods is used: (1) viscous, transonic design program of Carlson (ref. 4); (2) the airfoil-optimization program of Vanderplatts, et al. (ref. 5); and (3) the viscous, transonic analysis program of Bauer, et al. (ref. 6). The approach that was selected for designing the rotor airfoil involves the use of the Carlson inverse method for designing the aft region of the airfoil (approximately the aft 85% chord) and use of the Ames optimization technique to design the leading-edge region. The transonic, viscous analysis method of Bauer, et al. (ref. 6) was selected for analysis of the airfoil at design and off-design conditions.

ROTOR SECTION DEVELOPMENT

Design Evolution

The airfoil design was initiated using the design criteria formulated for Region I. The design conditions of $M = 0.83$, $C_\ell = 0$, and $R_N = 8.3 \times 10^6$ with boundary layer transition fixed at 5% chord were chosen to be indicative of Region I performance.

The first task was to develop a design pressure distribution consistent with the above operating conditions, the geometric constraints, and the aerodynamic design criteria for Region I. The resulting pressure distribution used for input to the Carlson design program is shown in figure 7. The initial design distribution was selected such that a symmetrical airfoil would be produced.

The final airfoil shape resulting from several applications of the Carlson inverse design technique is presented in figure 8 along with the computed (ref. 6) pressure distributions for operating conditions indicative of Region I and Region II. As can be seen, the resulting pressure distribution for $M = 0.83$ and $C_\ell = 0$ has a weaker shock ($M_S = 1.19$) than the original input distribution (fig. 7). However, the resulting pressure distribution for the low Mach number/high-lift condition indicates a shock strength in excess of the desired level of $M_S \leq 1.4$. This solution is inviscid since a strong shock was expected and considerable separation would be present in a viscous calculation. The angle of attack is approximately that which would yield $C_\ell = 1.5$ in viscous flow if separation did not occur ahead of 90% chord. Thus it appears from the above analysis that forward camber will have to be applied in order to reduce the shock strength at Region II operating conditions to acceptable levels.

The Vanderplaats optimization program was used to modify the airfoil shape in figure 8 to achieve the target leading-edge upper-surface pressure distribution in figure 4(a). In the Vanderplaats program the object function selected for minimization in Region II was the airfoil drag (wave drag). The following constraints were imposed:

o Maximum and minimum values of permissible pitching moment

o Maximum value of upper surface suction peak

o   Gradient aft of suction peak

o   Nose shape would have no inflexion points (constrained by y'')

o $M_S \le 1.4$

o   Airfoil shape to be unchanged aft of 20% chord

The final airfoil shape resulting from application of the Ames optimization design procedure is presented in figure 9. A list of the airfoil coordinates is included as table II.

Design Evaluation — Performance Objectives

In the following discussion the performance of the new airfoil will be theoretically evaluated relative to the target characteristics under each aerodynamic performance objective. All data presented have the boundary-layer transition locations fixed at 5% chord, unless otherwise indicated, and are calculated for a Reynolds number equal to $M \times 10^7$.

Aerodynamic Performance Objective No. 1. - This objective requires *the magnitude of the section pitching-moment coefficient for the new airfoil to be less than or equal to 0.010 at a lift coefficient of zero and a Mach number of 0.30*. As indicated in figure 10, this objective was achieved.

Aerodynamic Performance Objective No. 2. - This objective requires *the maximum lift coefficient of the new airfoil to equal or exceed a value of 1.5 at a Mach number of 0.40*. The pressure distribution corresponding to this condition is presented in figure 11 and compares well with figure 4(a). In particular, the shock Mach number is approximately 1.4 and the predicted separation location on the upper surface is at approximately 90% chord indicating that a maximum lift coefficient of 1.5 can probably be achieved at M = 0.40 with the new airfoil design.

Aerodynamic Performance Objective No. 3. - This objective requires *the drag-rise Mach number of the new airfoil be equal to or exceed 0.81 at $C_\ell = 0$*. As can be seen in figure 10, this objective is achieved.

The pressure distribution for the new airfoil at M = 0.81 and $C_\ell = 0$ is presented in figure 12. The local Mach number preceeding the upper surface shock is 1.18 which is slightly higher than desired. The lower-surface leading-edge pressure peak, which was precipitated at this flow condition by the nose droop, is undesirable. However, the pressure peak is tolerated since nose droop is required to meet the higher-priority $C_{\ell max}$ objective (no. 2).

Aerodynamic Performance Objective No. 4. - This objective requires *the magnitude of the pitching-moment coefficient for the new airfoil to be less than or equal to 0.015 at Mach numbers less than 0.70 for a lift coefficient of zero*. From figure 10 it can be seen that the new airfoil meets the required objective.

Aerodynamic Performance Objective No. 5. - This objective requires *the drag level of the new airfoil be less than or equal to 0.0080 at a Mach number of 0.60, a lift coefficient of 0.60, and a Reynolds number of 6 x 10^6.* With transition fixed at 5% chord, the predicted drag level at $M = 0.60$ is shown in figure 13 to be significantly higher than the target level. For free transition, the target drag level is achieved; however, the predicted transition locations (9% and 73% chord on the upper- and lower-surfaces, respectively) cannot be expected in practice. Therefore, it can generally be concluded that this objective cannot be met by the new airfoil at the specified Reynolds number.

The pressure distribution indicative of this aerodynamic performance objective is presented in figure 14. Comparison of this pressure distribution to the Region III design pressure distribution in figure 5 indicates the maximum upper-surface Mach number (1.21) for the new airfoil to be slightly higher than the target value of 1.16. Separation of the upper-surface boundary-layer was indicated at $x/c = .96$. The possibility of additional pressure drag due to separation further minimizes the chances of the new airfoil to achieve the drag level of 0.0080 required by this objective.

Aerodynamic Performance Objective No. 6. - The objective requires *the section lift coefficient of the new airfoil to equal or exceed a value of 1.5 at a Mach number of 0.50 and a section drag coefficient of 0.0500.* A calculated pressure distribution for $C_{\ell} = 1.5$ and $M = 0.50$ is shown in figure 11. This pressure distribution is probably not representative of the real flow since the shock Mach number is very strong ($M_S = 1.70$). No doubt, considerable separation is present. Current analytical analysis methods do not properly account for separation; hence, little can be said as to whether the airfoil can support a lift coefficient of 1.5, or what the resulting drag level would be. It is conjectured, however, that the lift coefficient for the new airfoil would approach 1.5 for $C_d = .0500$ and $M = .50$ since little degradation in $C_{\ell max}$ is noted for a similarly shaped airfoil (FX69-H-098) between $M = 0.4$ and $M = 0.5$ (ref. 10).

Aerodynamic Performance Objective No. 7. - This objective requires *the magnitude of the pitching-moment coefficient of the new airfoil be less than or equal to 0.020 at a Mach number of 0.30 and over a lift coefficient range of zero to one.* The computed pitching-moment results for the new airfoil are given in figure 10 for the flow conditions of this performance objective. As can be seen, the new airfoil meets the required aerodynamic performance.

Aerodynamic Performance Objective No. 8. - This objective requires *the drag coefficient of the new airfoil be less than or equal to 0.0100 at a Mach number 0.02 above the drag-rise Mach number at zero lift.* A measure of the performance of the new airfoil with respect to this objective can be obtained from figure 10. As indicated previously, the drag-rise Mach number is approximately 0.81. For transition fixed, the predicted drag level of the new airfoil at $M_D + 0.02$ (or $M = 0.83$) is approximately 0.0122 which is considerably higher than the target value of 0.0100. The target incremental drag between $M = 0.70$ (aerodynamic performance objective no. 12) and $M = 0.83$ is 30 drag counts. This compares with a drag increment of 42 drag counts for the new airfoil. With

free boundary layer transition (fig. 10), the drag coefficient at $M = 0.83$ and $C_\ell = 0$ is 0.0106 which is close to the target value. Predicted boundary layer transition locations were approximately 30% and 5% chord on the upper and lower surfaces respectively.

The pressure distribution representative of this performance objective is presented in figure 12. A comparison with the design pressure distribution in figure 3(b) indicates general agreement with the design criteria specified for good high-speed/low-lift performance. The Mach number preceding the shock wave on the upper surface is 1.20 and is slightly higher than desired.

Aerodynamic Performance Objective No. 9. - This objective requires *the Mach number for rapid increase in pitching-moment coefficient due to compressibility, referred to as the "pitching-moment break" and indicated by a slope of $dC_m/dM = -0.25$, be equal to or greater than the drag-rise Mach number.* Inspection of figure 10 indicates the pitching moment break for the new airfoil to occur at $M_T = 0.825$ which exceeds the drag rise Mach number of 0.81. Hence, the requirements of this performance objective are met.

Aerodynamic Performance Objective No. 10. - This objective requires *the parameter $M^2 C_m$ be maintained less than 0.01 and greater than -0.04 for all Mach numbers less than M_D and for a lift coefficient of zero.* This requirement is translated into the target pitching-moment coefficient curve presented in figure 10. From this figure, it can be seen that the pitching-moment results for the new airfoil are within the permissible limits specified by this performance objective.

Aerodynamic Performance Objective No. 11. - This objective requires *the gentlest possible stall to occur near maximum lift over a Mach number range of 0.3 and 0.4.* It is well known that the gentlest stall occurs when the flow separates first at the trailing-edge and progressively moves forward. As discussed above under objective no. 2, primary emphasis in the design was placed on suppressing the leading-edge stall. Although no quantitative statement can be made concerning the type of stall, it is anticipated that a gentle stall will occur. This conjecture is supported by the gentle stall results observed on the FX69-H-098 airfoil (ref. 10) and its aerodynamic similarity to the present design.

Aerodynamic Performance Objective No. 12. - This objective requires *the section drag coefficient for the new airfoil be less than 0.0070 at Mach numbers less than 0.71 (M_D-0.10) for a lift coefficient of zero.* As shown in figure 10 for fixed transition at 5% chord, the drag is 9 to 12 counts higher for the new airfoil than the target value. For free transition ($M = 0.6$ typical), the drag level is 0.0074 (fig. 10) with the transition locations at approximately 20% and 4% chord, respectively, on the upper and lower surfaces. The lower-surface leading-edge pressure spike (i.e., fig. 12) prohibits a long run of laminar flow on the lower surface at low lift coefficients.

CONCLUDING REMARKS

A new rotor airfoil has been designed utilizing supercritical technology and advanced theoretical transonic design-and-analysis methods to meet stringent geometric design constraints and numerous weighted aerodynamic performance objectives. The overall design-and-analysis methodology, as described in this paper, was found to greatly facilitate rotor section design. Theoretical analysis of the new airfoil design indicated the section generally has the potential to achieve the most important aerodynamic performance objectives.

REFERENCES

1. Blackwell, James A. Jr.: Aerodynamic Characteristics of an 11-Percent-Thick Symmetrical Supercritical Airfoil at Mach Numbers Between 0.30 and 0.85. NASA TM X-1831, July 1969.

2. Liebeck, R. H.: A Class of Airfoils Designed for High Lift in Incompressible Flow. *Journal of Aircraft*, Vol. 10, No. 10, 1973.

3. Sloof, J. W.; Wortmann, F. X.; and Duhon, J. M.: The Development of Transonic Airfoils for Helicopters. Preprint 901, 31st Annual National Forum, American Helicopter Society, May 1975.

4. Carlson, L. A.: Transonic Airfoil Design Using Cartesian Coordinates. NASA CR-2578, December 1975.

5. Vanderplaats, Garret N.; Hicks, Raymond N.; and Murman, Earll M.: Application of Numerical Optimization Techniques to Airfoil Design. NASA SP-347, 1975.

6. Bauer, F.; Garabedian, P.; Korn, D.; and Jameson, A.: Supercritical Wing Sections II. *Lecture Notes in Economics and Mathematical Systems*, Vol. 108, Springer-Verlag, New York, 1975.

7. Blackwell, James A. Jr.; Hinson, Bobby L.: The Aerodynamic Design of an Advanced Rotor Airfoil. NASA CR-2961, May 1977.

8. Hoerner, Sighard F.: Fluid-Dynamic Drag. Hoerner Fluid Dynamics (Brick Town, N.J.), c.1965.

9. Lindsey, W. F.; and Johnston, P. J.: Some Observations on Maximum Pressure Rise Across Shocks Without Boundary-Layer Separation on Airfoils at Transonic Speeds. NACA TN 3820, November 1956.

10. Kemp, Larry D.: An Analytical Study for the Design of Advanced Rotor Airfoils. NASA CR-112297, March 29, 1973.

TABLE I. AERODYNAMIC PERFORMANCE OBJECTIVES

		FIRST PRIORITY	SECOND PRIORITY	THIRD PRIORITY
REGION I	M	(3) $M_D \geq 0.81$ @ • $C_\ell = 0$		(9) $M_T \geq M_D$
REGION I	C_d		(8) $C_d \leq 0.0100$ @ • $M = M_D + 0.02$ • $C_\ell = 0$	(12) $C_d \leq 0.0070$ @ • $M \leq M_D - 0.10$ • $C_\ell = 0$
REGION I	C_m	(4) $|C_m| \leq 0.015$ @ • $M \leq 0.70$ • $C_\ell = 0$		(10) $0.01 \geq M^2 C_m \geq -0.04$ @ • $M \leq M_D$ • $C_\ell = 0$
REGION II	C_ℓ	(2) $C_\ell \geq 1.5$ @ • $M = 0.40$ • $C_{\ell_\alpha} = 0$	(6) $C_\ell \geq 1.5$ @ • $M = 0.50$ • $C_d = 0.0500$	
REGION II	C_m	*(1) $|C_m| \leq 0.010$ @ • $M = 0.30$ • $C_\ell = 0$	(7) $|C_m| \leq 0.020$ @ • $M = 0.30$ • $0 \leq C_\ell \leq 1.0$	(11) GENTLEST POSSIBLE STALL @ • $0.30 \leq M \leq 0.40$
REGION III	C_d		(5) $C_d \leq 0.0080$ @ • $M = 0.60$ • $C_\ell = 0.60$	

* Lowest numbers have highest priority.

TABLE II. — DESIGN COORDINATES OF ROTOR AIRFOIL

| X/C	Y/C UPPER SURFACE	Y/C LOWER SURFACE
.00000	.00000	.00000
.00106	.00529	-.00411
.00433	.01115	-.00729
.00972	.01724	-.01001
.01722	.02349	-.01267
.02678	.02973	-.01525
.03844	.03594	-.01773
.05206	.04164	-.02010
.06767	.04668	-.02238
.08428	.05079	-.02444
.09928	.05369	-.02605
.12942	.05782	-.02881
.15972	.06037	-.03107
.19018	.06187	-.03292
.22077	.06266	-.03445
.25148	.06298	-.03569
.28231	.06294	-.03667
.32000	.06246	-.03753
.35000	.06181	-.03797
.37500	.06111	-.03817
.40000	.06026	-.03823
.42500	.05926	-.03813
.45000	.05813	-.03791
.47500	.05684	-.03753
.50000	.05543	-.03703
.52500	.05388	-.03638
.55000	.05219	-.03561
.57500	.05037	-.03470
.60000	.04842	-.03366
.62500	.04634	-.03250
.65000	.04415	-.03122
.67500	.04183	-.02981
.70000	.03938	-.02828
.72500	.03682	-.02664
.75000	.03415	-.02489
.77500	.03136	-.02302
.80000	.02846	-.02104
.82500	.02545	-.01895
.85000	.02234	-.01676
.87500	.01911	-.01446
.90000	.01579	-.01206
.92500	.01236	-.00957
.95000	.00884	-.00697
.97500	.00521	-.00428
1.00000	.00150	-.00150
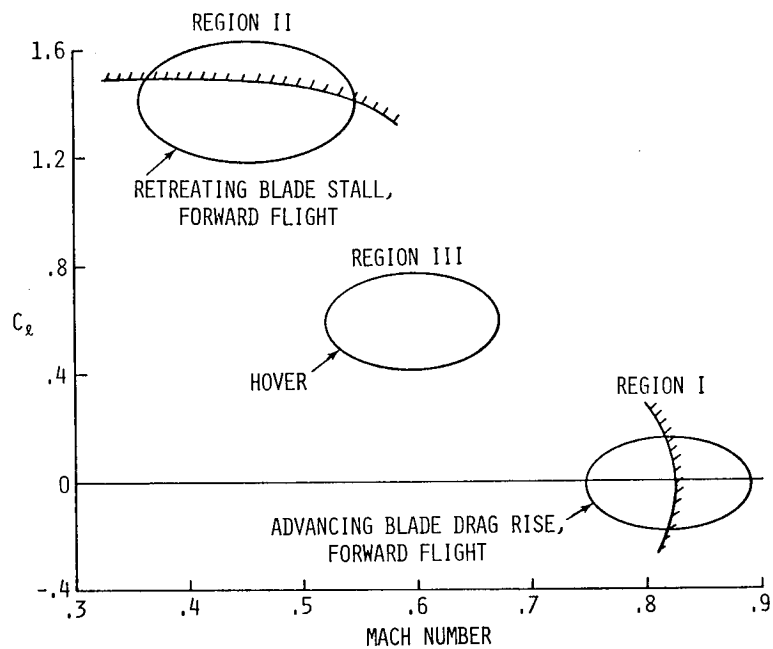
Figure 1.- Rotor-section operating conditions.
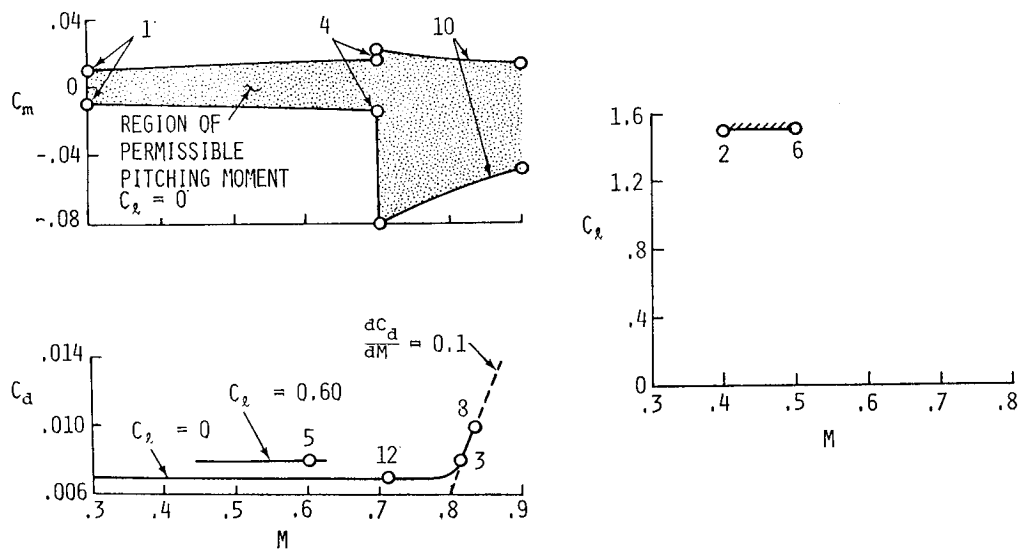
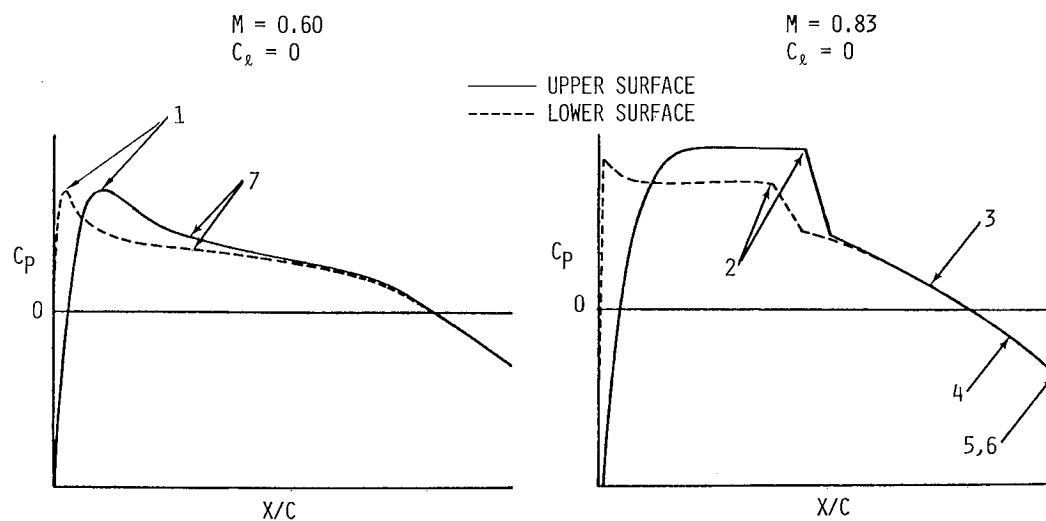Figure 2.- Aerodynamic performance objectives.
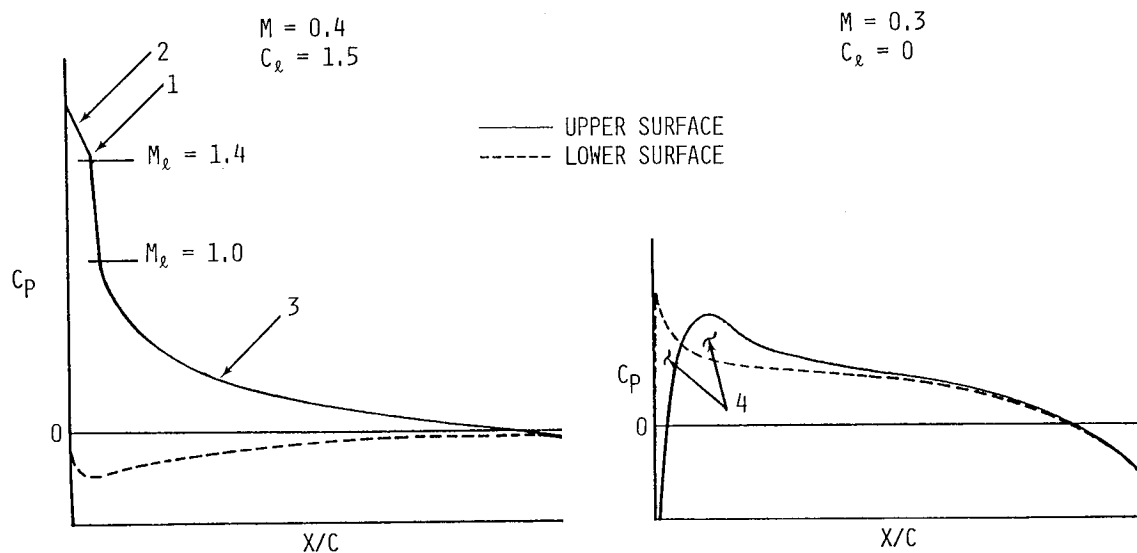
Figure 3.- Aerodynamic design criteria for Region I.

Figure 4.- Aerodynamic design criteria for Region II.
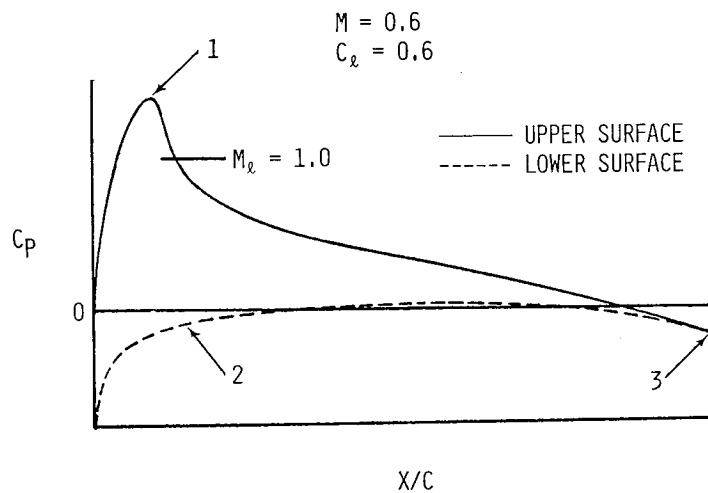
M = 0.6
C_ℓ = 0.6

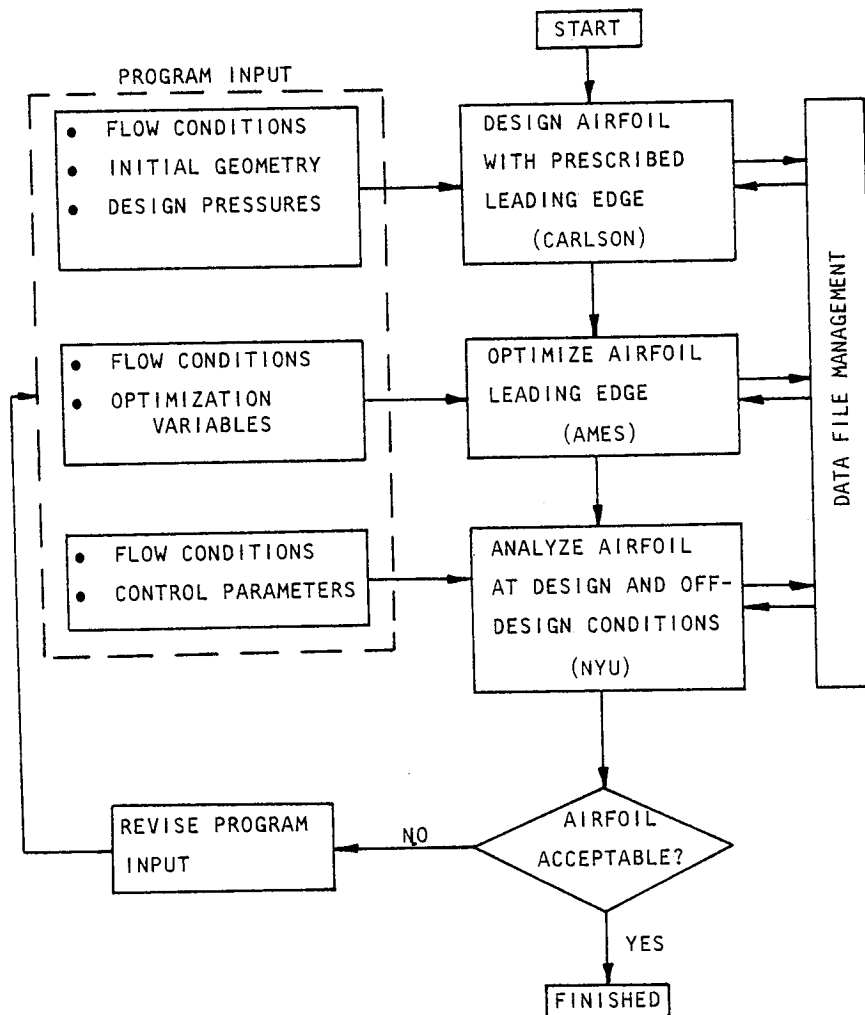Figure 5.- Aerodynamic design criteria for Region III.
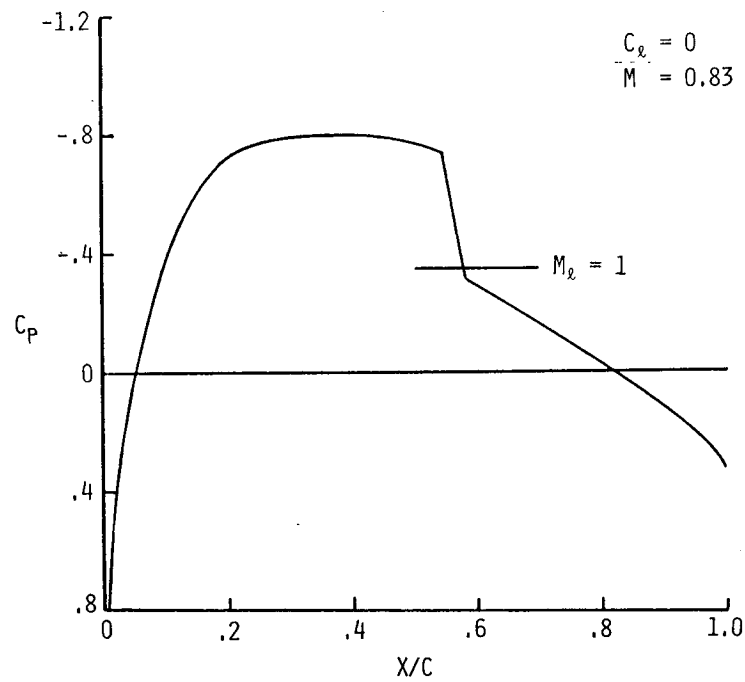

Figure 6.- Design and analysis procedure.

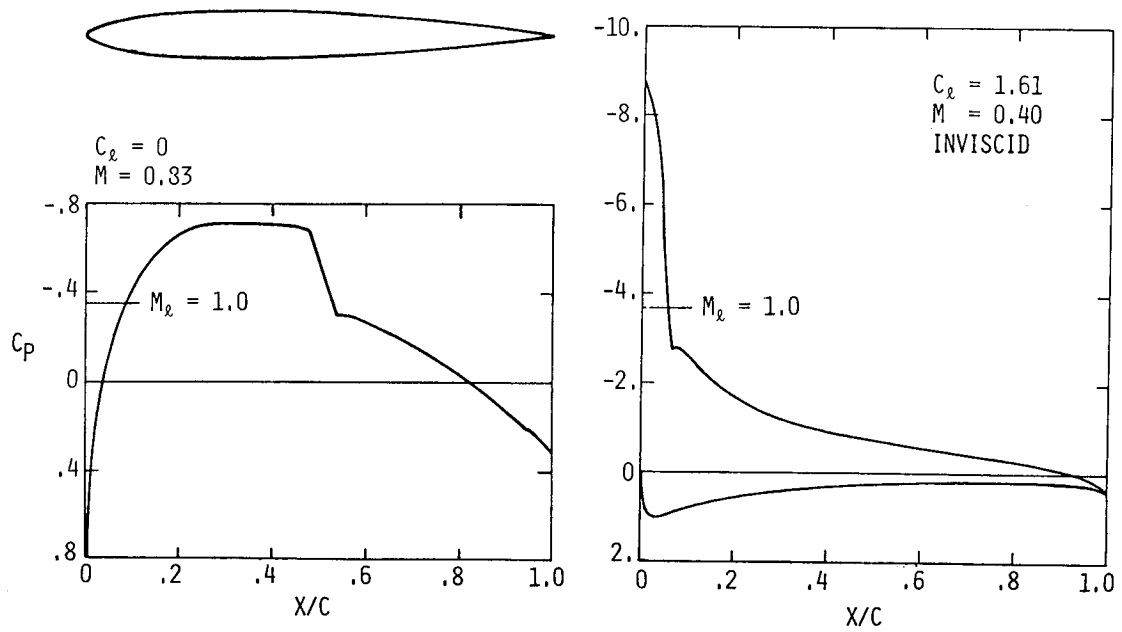Figure 7.- Initial input pressure distribution for Carlson program.

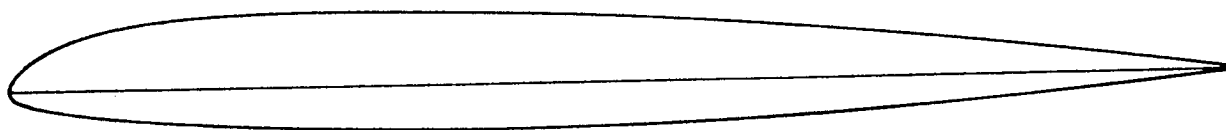Figure 8.- Final airfoil shape from Carlson program.
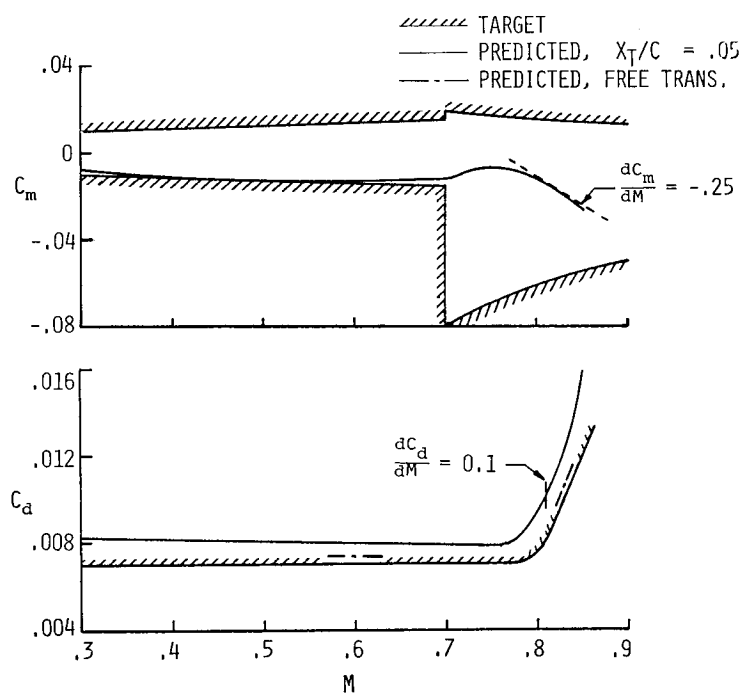
Figure 9.- Final rotor airfoil shape.

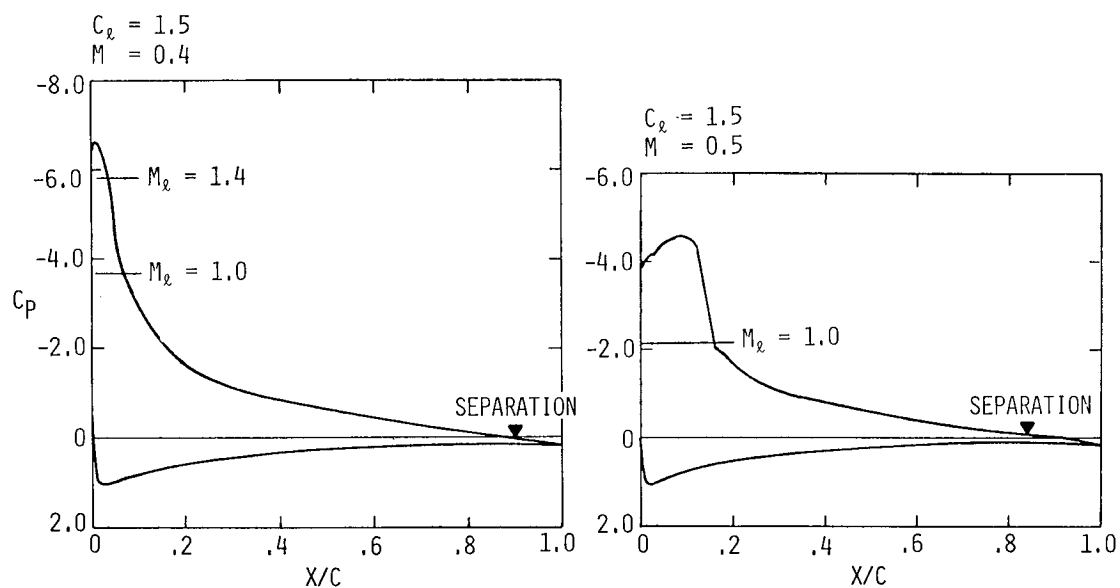Figure 10.- Comparison between predicted and target force data with $C_\ell = 0$.
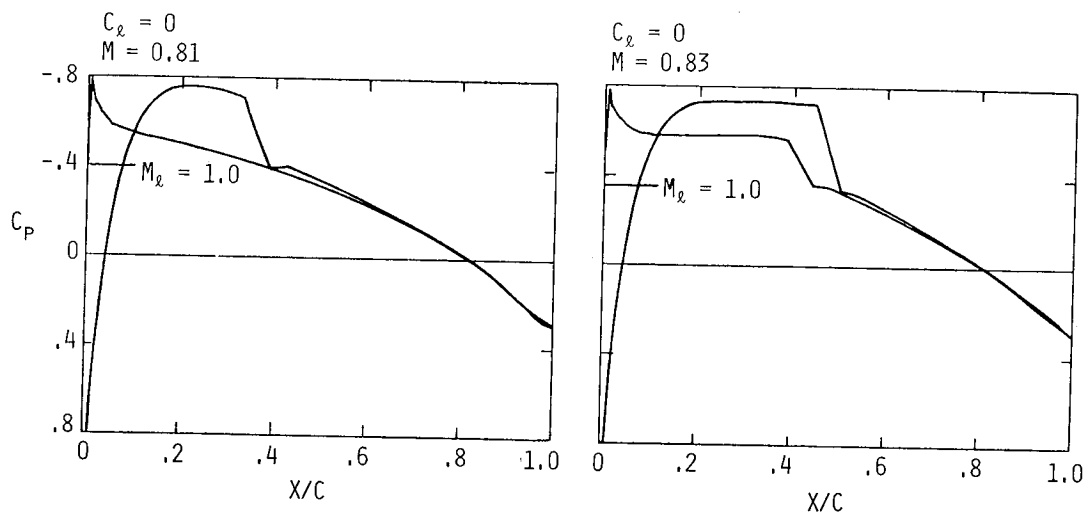
Figure 11.- Airfoil pressure distributions for Region II.
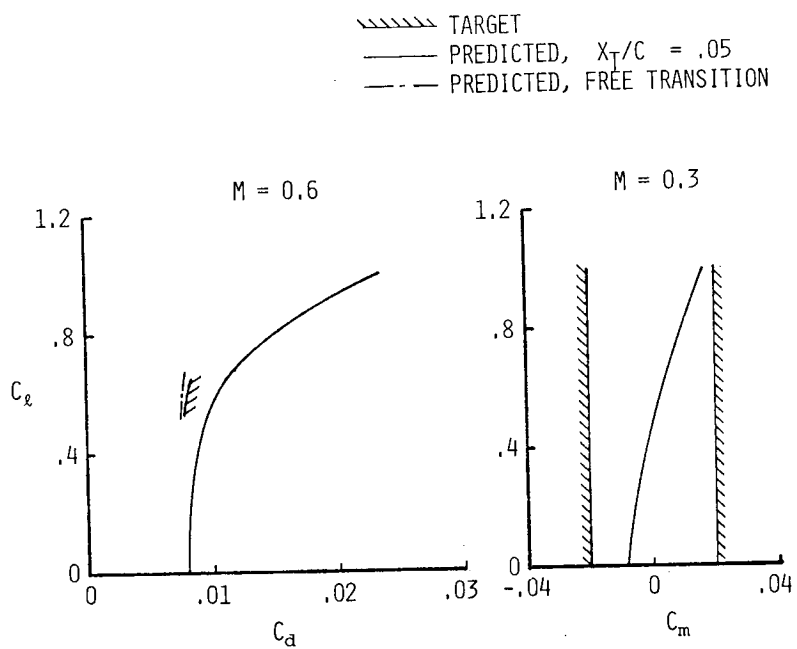

Figure 12.- Airfoil pressure distributions for Region I.

M = 0.6   M = 0.3

Figure 13.- Comparison between predicted and target force data.
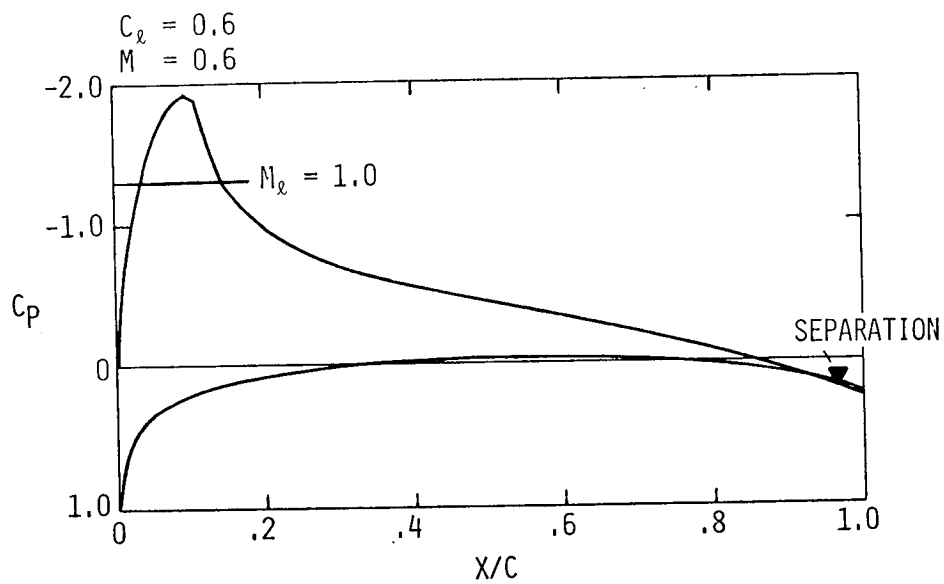
C_ℓ = 0.6
M = 0.6

Figure 14.- Airfoil pressure distribution for Region III.

A FLIGHT INVESTIGATION OF ROTOR AIRFOILS

Charles E. K. Morris, Jr.
NASA Langley Research Center

SUMMARY

A flight investigation has been conducted to study the behavior of advanced-technology airfoils in the three-dimensional, unsteady-flow environment of the helicopter rotor. The research system is described and some preliminary results are presented for the NLR-1 airfoil. The flight data show that rotorcraft airfoils must operate over a wide range of aerodynamic conditions. Some of the comparisons of pressure distributions from flight and from two-dimensional, steady-flow theory do show good correlation.

INTRODUCTION

Flight research is needed to guide the application of new airfoil technology to helicopter rotor blades. Although many of the currently available methods for airfoil design are powerful and sophisticated, each was developed with the assumption of two-dimensional, steady flow (refs. 1 and 2). However, in many flight conditions the blade sections of a helicopter rotor are subjected to significant effects of three-dimensional, unsteady flow (refs. 3 and 4). For example, when the helicopter is trimmed in high-speed forward flight, the outboard section of a rotor blade can encounter many phenomena: compressibility effects on the advancing blade, dynamic stall on the retreating blade, unsteady yawed flow and interactions with tip vortices trailed by preceding blades. Math-model simulations and wind-tunnel investigations are helpful, but flight testing is still required to determine the significance of the aerodynamic phenomena affecting rotor airfoils throughout the total flight envelope of the rotor (ref. 5). Such data can then be used to guide the development of improved design criteria for rotorcraft airfoils. Examples of flight tests for airfoil research are found in references 6, 7, and 8.

This paper presents preliminary results from the first of several flight investigations with advanced-technology rotorcraft airfoils. This first test was conducted with the NLR-1 airfoil (of refs. 9 to 12) on the main rotor of a fully-instrumented, high-performance helicopter. Data presentation is limited to results from measurements of airfoil pressure distributions at 90-percent blade radius, although performance parameters and rotor loads were also measured. Emphasis is given to high-speed forward flight.

SYMBOLS

Values are given in both SI and U.S. Customary Units. The measurements and calculations were made in the U.S. Customary Units.

c	airfoil chord, cm (in.)
c_n	section normal-force coefficient
$c_{m_{c/4}}$	section pitching-moment coefficient, referenced to section quarter chord
C_p	pressure coefficient, $\dfrac{p - p_\infty}{q_\infty}$
C_p^*	pressure coefficient corresponding to a local Mach number of 1.0
M	free-stream Mach number of blade section
p	local static pressure at a point on airfoil, N/m^2 (lb/ft^2)
p_∞	free-stream static pressure, N/m^2 (lb/ft^2)
q_∞	free-stream dynamic pressure of blade section, N/m^2 (lb/ft^2)
R	blade radius, m (ft)
R_c	Reynolds number based on total chord and free-stream conditions
r	radial distance to blade element, m (ft)
t	airfoil thickness, cm (in.)
V	true airspeed, knots
x	airfoil abscissa, cm (in.)
y	airfoil ordinate, cm (in.)
y_c	ordinate of airfoil mean line, cm (in.)
y_ℓ	airfoil lower-surface ordinate, cm (in.)
y_u	airfoil upper-surface ordinate, cm (in.)
y'	slope of airfoil surface, dy/dx
ψ	rotor azimuth, deg
Ω	blade rotational speed, m/sec (ft/sec)

TEST EQUIPMENT AND DATA SYSTEM

The experimental main-rotor blades had an airfoil section derived by truncating the NLR-1 airfoil of reference 10 at 99 percent of design chord. Coordinates of this airfoil are given in table I. The contour, thickness distribution, and mean line are shown in figure 1; surface slopes are shown in figure 2. The design of the airfoil is discussed in references 9 and 10. Results of "static" and oscillating-airfoil wind-tunnel tests are given in references 11 and 12. The airfoil has a drag-divergence Mach number of about 0.84 at zero lift and a static maximum lift coefficient of approximately 1.1 at a Mach number of 0.4.

The test vehicle was the fully instrumented AH-1G helicopter shown in figure 3. This high-speed vehicle had a two-bladed, teetering-hub main rotor. The basic vehicle was the same model aircraft as was used in the investigation of reference 13. The rotor had a radius of 6.71 m (22.0 ft), a constant chord of 0.686 m (2.25 ft), and linear twist about the quarter chord that reached -10° at the tip. Nominal tip speed of the rotor was 227.5 m/sec (746.4 ft/sec). The NLR-1 airfoil section was used on the outer 69 percent of each blade. Except for the airfoil contour, the experimental blades were designed to be as close as possible to the production-configuration blades in geometric and dynamic characteristics.

The data system was digital and had two major subsystems. The subsystem for basic aircraft data consisted of fuselage-mounted sensors and recording/ conditioning equipment that sampled 10-bit data signals from each channel at 80 samples per second. These sensors measured the aerodynamic flight state (with parameters such as angle of attack, dynamic pressure, and total temperature), inertial flight state, control positions, rotor speed, and engine power. The second major subsystem provided 8-bit measurements of rotor-mounted sensors at the rate of 1000 samples per channel per second. Thirteen absolute-pressure transducers were located at the 90-percent radial station of one blade. (They were located at chordwise stations of 2, 10, 20, 50, 70, and 90 percent for both surfaces and 80 percent for the upper surface.) Each transducer was mounted in a sealed cavity-and-cover-plate assembly so as to isolate it from blade structural loads; they measured local surface pressure through a 0.8 mm (0.03 in.) hole drilled in the cover plate. Each cover was faired to match the airfoil contour. Other rotor parameters that were measured included structural loads, hub angles, and temperatures for data correction.

The final steps in the data reduction operated on data for one blade revolution at each flight-test point. Parameter histories were studied to guide the selection of well-controlled test points. Due to sequential sampling of the rotor data, linear interpolation was used to obtain simultaneous values of airfoil pressure data. Corrected parameters from both data subsystems were then used to compute the set of 13 pressure coefficients for every 2° of azimuth. The curve-fitting and integration schemes of reference 14 were then applied to obtain the resulting coefficients of normal force and pitching moment.

DISCUSSION

Consideration of the flight measurements begins with the data on normal-force coefficient given in figure 4. The variation shown there helps to indicate that rotorcraft airfoils can experience a wide range of conditions within a single revolution. The data show that negative lift can occur on the advancing-blade (high-speed) side of the rotor disk. However, this loading is measured at only one spanwise location, and a substantial amount of positive lift is required on the disk to trim the rotor to this high-speed, level-flight condition. The higher level of normal-force coefficient on the retreating-blade side compensates for the lower dynamic pressure in that region.

Airfoil-coefficient data for the high-speed case and two other level-flight conditions can be compared in figure 5. Airfoil behavior in the low-speed case is seen to be strongly influenced by a tip-vortex interaction that occurs for the 90-percent radius at 270° of azimuth. An increase in vehicle airspeed to the cruise condition eliminates that phenomenon but introduces a region of very low or even negative lift near an azimuth of 100°. For the high-speed case, not only is the region of negative lift large, but the pitching-moment coefficient reaches magnitudes that are large in comparison to basic design levels.

Even with due consideration for the accuracy of airfoil coefficients calculated from flight data, the magnitude of pitching moments for the high-speed case are larger than is anticipated from wind-tunnel data for two-dimensional, steady flow. This can be seen in figure 6. The flight values of normal-force coefficient and Mach number have been used to enter tables of wind-tunnel data for the NLR-1 airfoil in steady flow (ref. 12). The associated wind-tunnel values of pitching-moment coefficient are plotted for comparison with the flight data. The differences between the two moment data curves should be explainable due to effects of the rotor environment on the airfoil pressure distribution.

Figure 7 presents pressure-distribution data for the high-speed case already considered in figures 4, 5, and 6. The theoretical pressure distributions were obtained with the computer program of reference 15. This program provides predictions of the aerodynamic characteristics of airfoils in subcritical and supercritical, two-dimensional, steady flow. The Mach number, Reynolds number, and normal-force coefficient calculated for flight were used as inputs. (One program option allows lift coefficient to be specified as input.)

Pressure coefficient data for moderate flow conditions at the rear and front of the rotor disk are shown in figures 7(a) and 7(b), respectively. Mach numbers are the same, and normal-force coefficients are very close; however, the yaw angle of the local flows should have the opposite sense and the flow environment in the rear of the disk is generally more influenced by the wake. Correlation between flight data and theory appears to be good except for the forward region of the airfoil for figure 7(a).

Data for the highest Mach number condition are shown in figure 7(c). With the exception of the shock location, correlation for the upper surface appears to be quite good; flight data for the lower surface do not agree as well, particularly at the leading and trailing edges. Differences in these regions should have a much larger effect on pitching moment than on normal force.

Data for the two other conditions with a high Mach number are also considered. Rotor azimuths of 60 and 120° both have a Mach number of 0.85 for the flow component normal to the blade leading edge. Figure 7(d) presents data from the negative lift region. Flight data indicate that more of the load is being carried in the rear of the airfoil than is predicted for two-dimensional, steady flow. The agreement between theory and flight measurements for an azimuth of 60° is comparatively poor (fig. 7(e)). In this case, the agreement for the lower surface is not good at the leading edge; also, the upper-surface data from flight indicate that the shock lies between 20 and 50 percent chord and not nearly 70 percent as predicted with the computer program. Reasonable adjustments to the program inputs and to values of pressure from flight measurements cannot provide any significant improvement in correlation. This shows that simplifying assumptions are inappropriate for predicting pressure distributions in some parts of the rotor disk.

A comparison of data for the condition with the lowest Mach number is shown in figure 7(f). Even though the low dynamic pressure degrades the accuracy of the flight data, the correlation shown can be judged to be good. As with all other figures with pressure distributions, further considerations should be given to the accuracy of all elements of the flight system, including contour deviations.

CONCLUDING REMARKS

Flight-test data are now becoming available to permit the study of the behavior of advanced-technology airfoils in a full-scale, operationally conventional rotor environment. Significant variations in operation conditions are observed in a small sampling of reduced data. Although correlation of pressure distributions from flight and simplified-flow theory was generally good, cases of poor correlation and the limited scope of the review preclude the formulation of strong conclusions at this point in the research.

REFERENCES

1. Reichert, G.; and Wagner, S. N.: Some Aspects of the Design of Rotor-Airfoil Shapes. Paper No. 14, AGARD CP-111, Sept. 1972.

2. Blackwell, James A., Jr.; and Hinson, Bobby L.: The Aerodynamic Design of an Advanced Rotor Airfoil. NASA CR-2961, 1977.

3. Ward, John F.; and Young, Warren H., Jr.: A Summary of Current Research in Rotor Unsteady Aerodynamics with Emphasis on Work at Langley Research Center. Paper No. 10, AGARD CP-111, Sept. 1972.

4. Landgrebe, Anton J.; Moffitt, Robert C.; and Clark, David R.: Aerodynamic Technology for Advanced Rotorcraft - Part II. J. Am. Helic. Soc., vol. 22, no. 3, July 1977, pp. 2-9.

5. Drees, Jan M.: The Art and Science of Rotary Wing Data Correlation. J. Am. Helic. Soc., vol. 21, no. 3, July 1976, pp. 2-12.

6. Pearcey, H. H.; Wilby, P. G.; Riley, M. J.; and Brotherhood, P.: The Derivation and Verification of a New Rotor Profile on the Basis of Flow Phenomena; Aerofoil Research and Flight Tests. Paper No. 16, AGARD CP-111, Sept. 1972.

7. Riley, M. J.; and Brotherhood, P.: Comparative Performance Measurements of Two Helicopter Blade Profiles in Hovering Flight. R.&M. No. 3792, British A.R.C., 1977.

8. Thibert, J. J.; and Gallot, J.: A New Airfoil Family for Rotor Blades. Paper No. 41, Third European Rotorcraft and Powered Lift Aircraft Forum (Aix-en-Provence, France), Sept. 1977.

9. Kemp, Larry D.: An Analytical Study for the Design of Advanced Rotor Airfoils. NASA CR-112297, 1973.

10. Sloof, J. W.; Wortmann, F. X.; and Duhon, J. M.: The Development of Transonic Airfoils for Helicopters. Preprint 901, 31st Annual National Forum, Am. Helic. Soc., May 1975.

11. Noonan, Kevin W.; and Bingham, Gene J.: Two-Dimensional Aerodynamic Characteristics of Several Rotorcraft Airfoils at Mach Numbers From 0.35 to 0.90. NASA TM X-73990, 1977.

12. Dadone, Leo: Two-Dimensional Wind-Tunnel Test of an Oscillating Rotor Airfoil, Vols. I and II. NASA CR-2914 and CR-2915, 1977.

13. Shockey, Gerald A.; Cox, Charles R.; and Williamson, Joe W.: AH-1G Helicopter Aerodynamic and Structural Loads Survey. USAAMRDL TR-76-39, 1977.

14. James, C. A.: A Suite of Computer Programs for the Automatic Analysis of Helicopter Rotor Blade Pressure Measurements. Tech. Memo. FS 47, British R.A.E., Oct. 1975.

15. Bauer, F.; Garabedian, P.; Korn, D.; and Jameson, A.: Supercritical Wing Sections II. Lecture Notes in Economics and Mathematical Systems, Vol. 108. Springer-Verlag (New York), 1975.

TABLE I.- COORDINATES OF TRUNCATED NLR-1 AIRFOIL

x/c	y_u/c	y_ℓ/c
0.00	0.00	0.00
.00259	.00704	-.00512
.00974	.01524	-.00867
.02185	.02296	-.01180
.03796	.02972	-.01465
.05675	.03588	-.01713
.07753	.04098	-.01929
.09845	.04469	-.02112
.12341	.04741	-.02299
.15412	.04986	-.02494
.18767	.05188	-.02671
.22313	.05345	-.02821
.26054	.05459	-.02944
.29979	.05531	-.03040
.34064	.05565	-.03104
.38269	.05560	-.03142
.42528	.05518	-.03150
.46849	.05438	-.03132
.51162	.05323	-.03080
.55383	.05175	-.02992
.59596	.04992	-.02867
.63728	.04774	-.02734
.67732	.04524	-.02580
.71079	.04291	-.02432
.73905	.04017	-.02305
.76946	.03644	-.02164
.80263	.03140	-.01996
.84055	.02533	-.01794
.87846	.01901	-.01571
.90845	.01421	-.01364
.93589	.01020	-.01087
.96199	.00651	-.00711
1.00000	.00104	-.00104
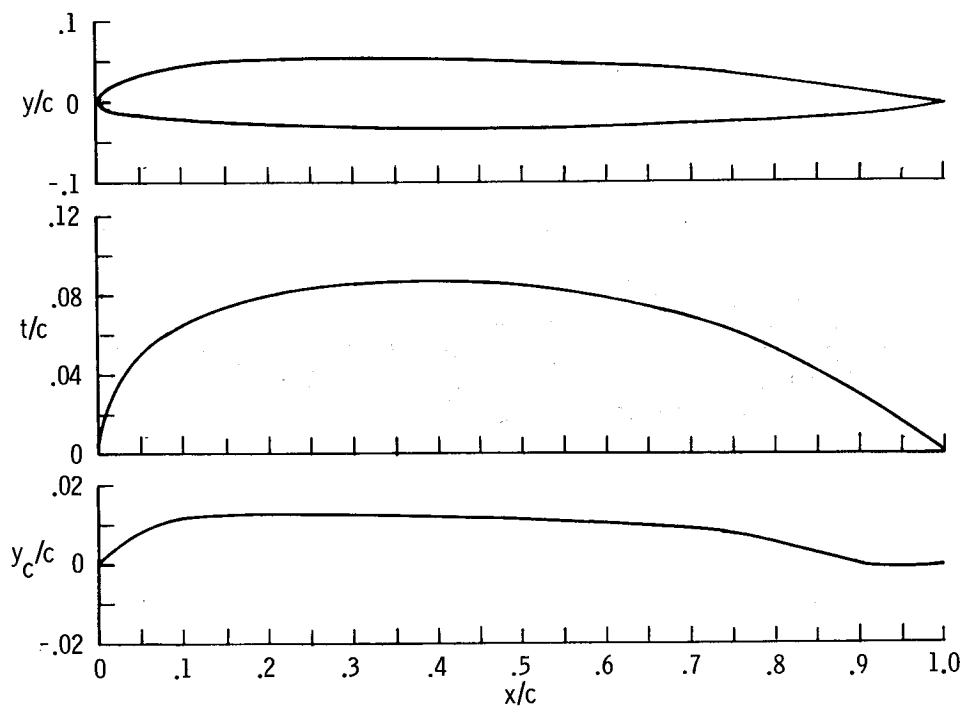
Figure 1.- Profile, thickness distribution and mean line of NLR-1 airfoil.
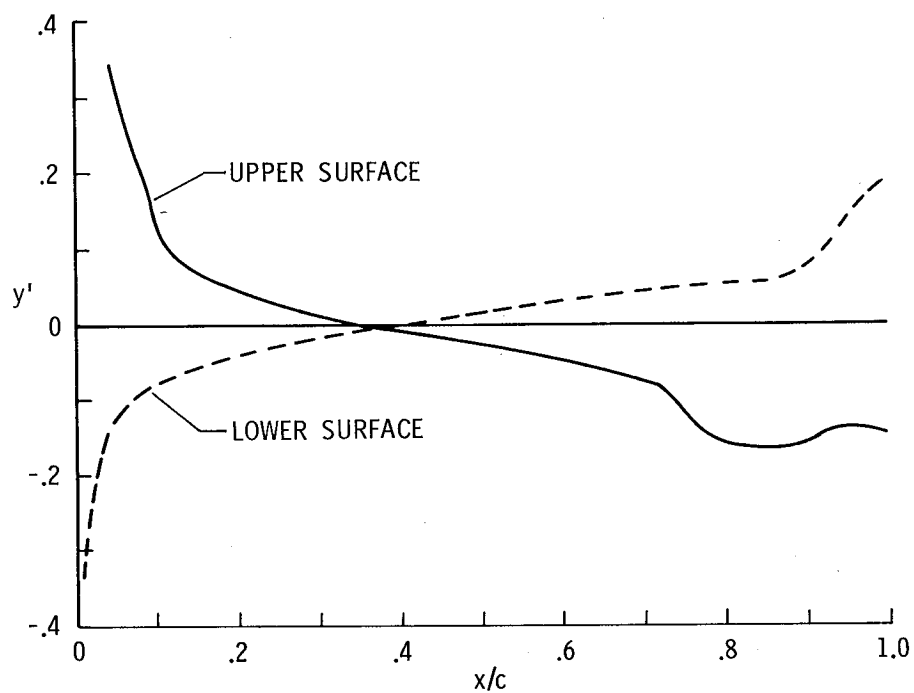
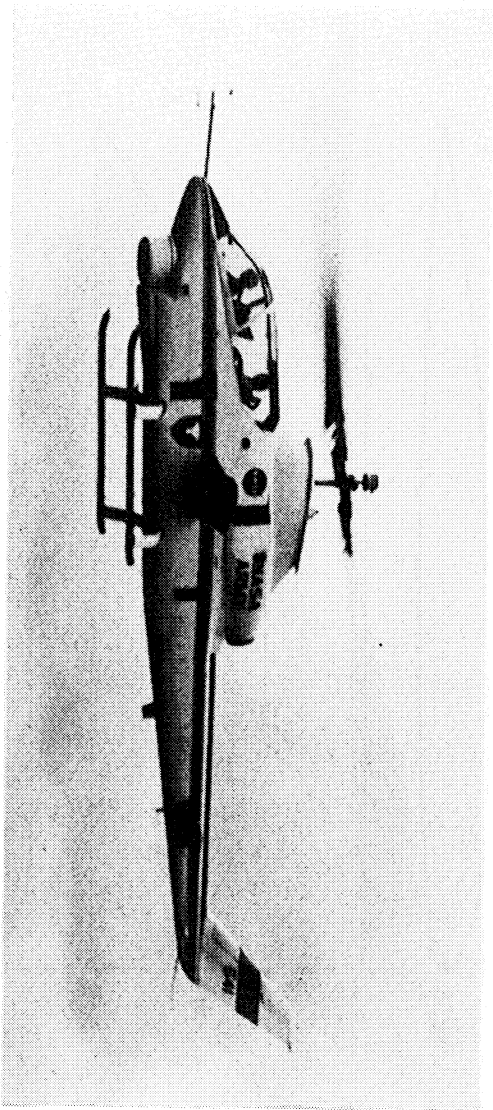Figure 2.- Chordwise distribution of profile slopes of NLR-1 airfoil.

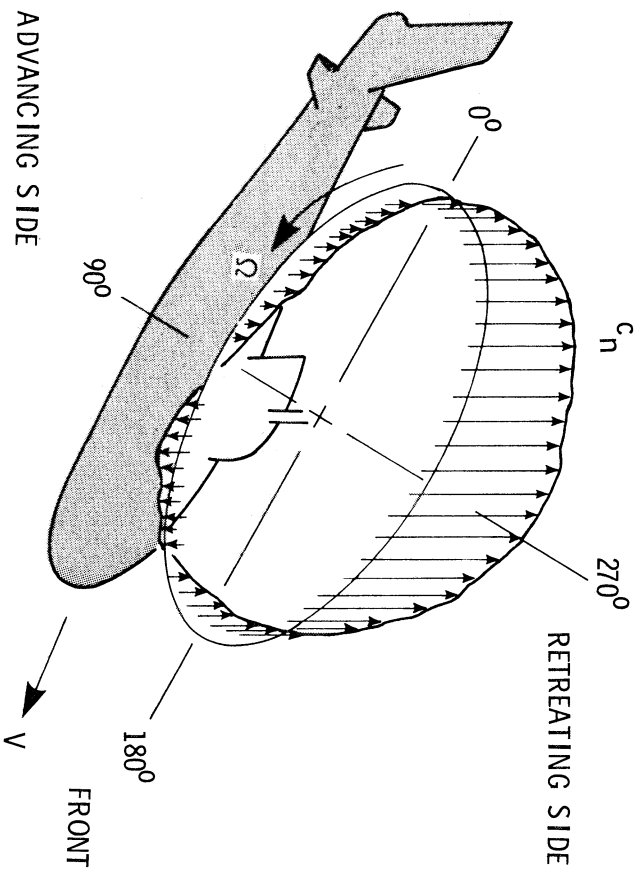Figure 3.- Flight-test vehicle for rotor-airfoil research.

Figure 4.- Distribution of normal-force coefficient at 90-percent blade radius; NLR-1 airfoil on AH-1G rotor, level flight, V = 164 knots.
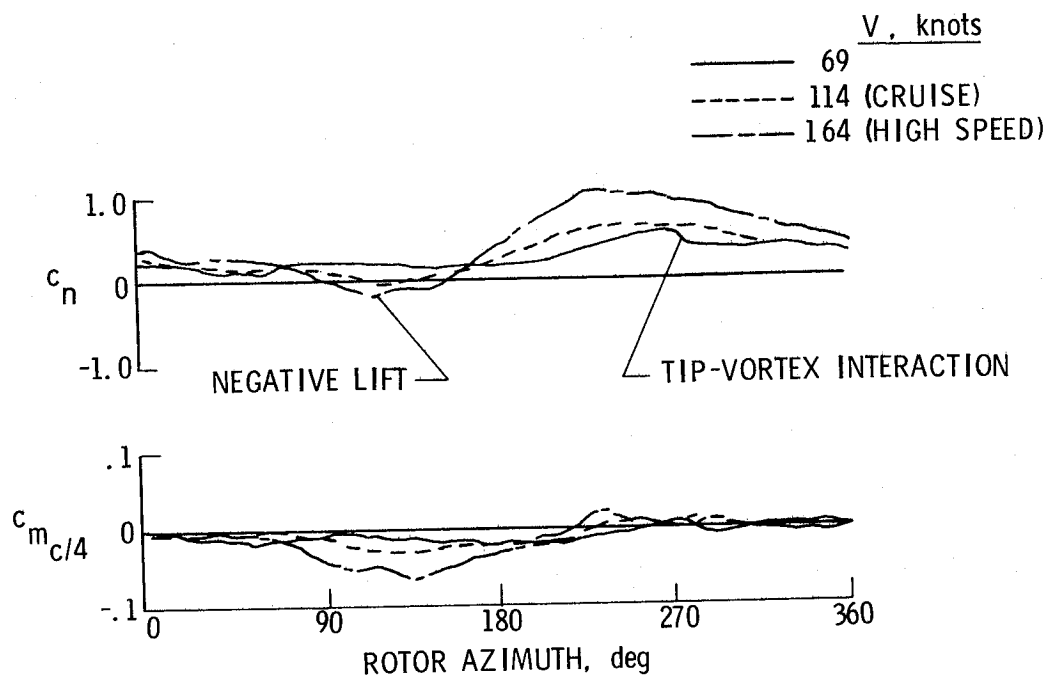
Figure 5.- Variation of airfoil behavior with rotor azimuth;
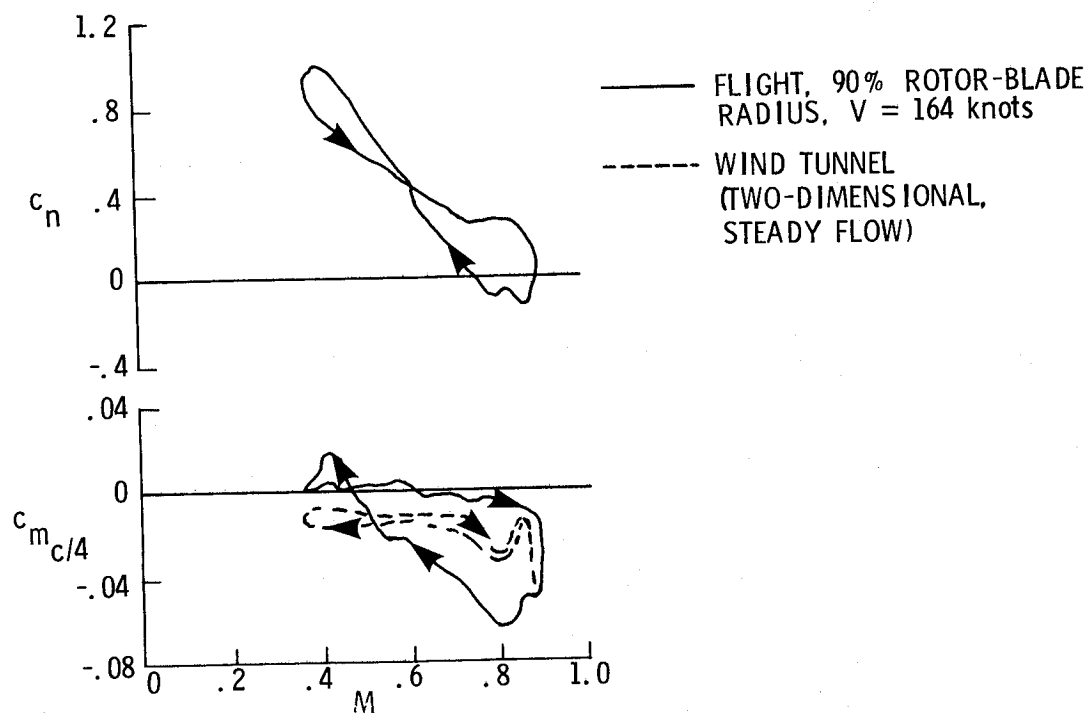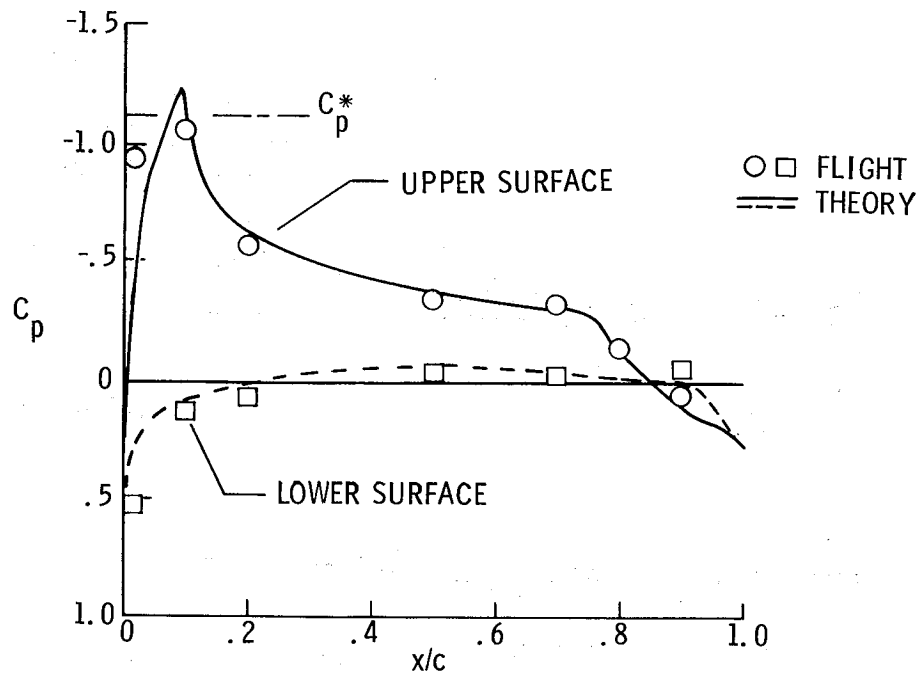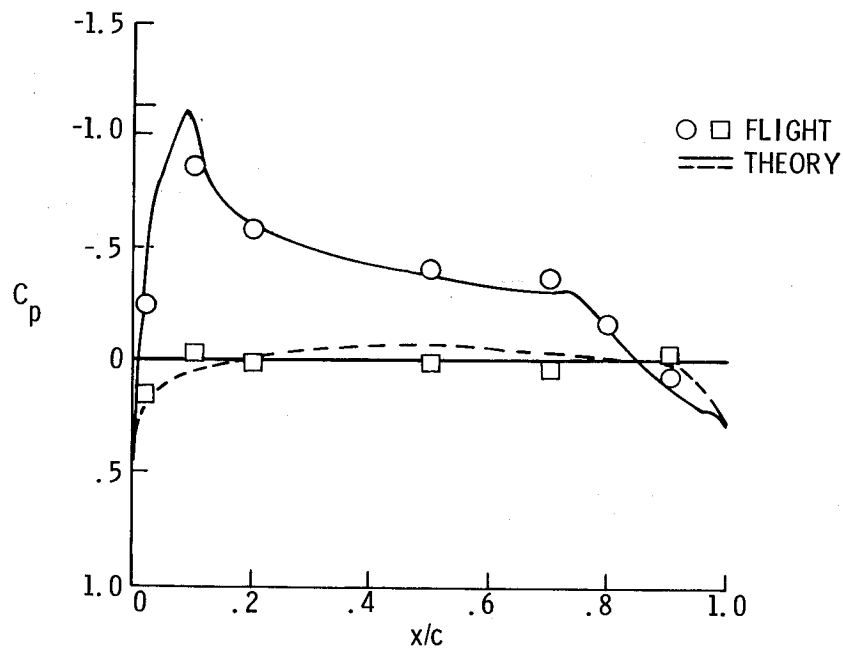NLR-1 airfoil on AH-1G rotor, r/R = 0.9, level flight.

Figure 6.- Comparison of flight and wind-tunnel data for NLR-1 airfoil.
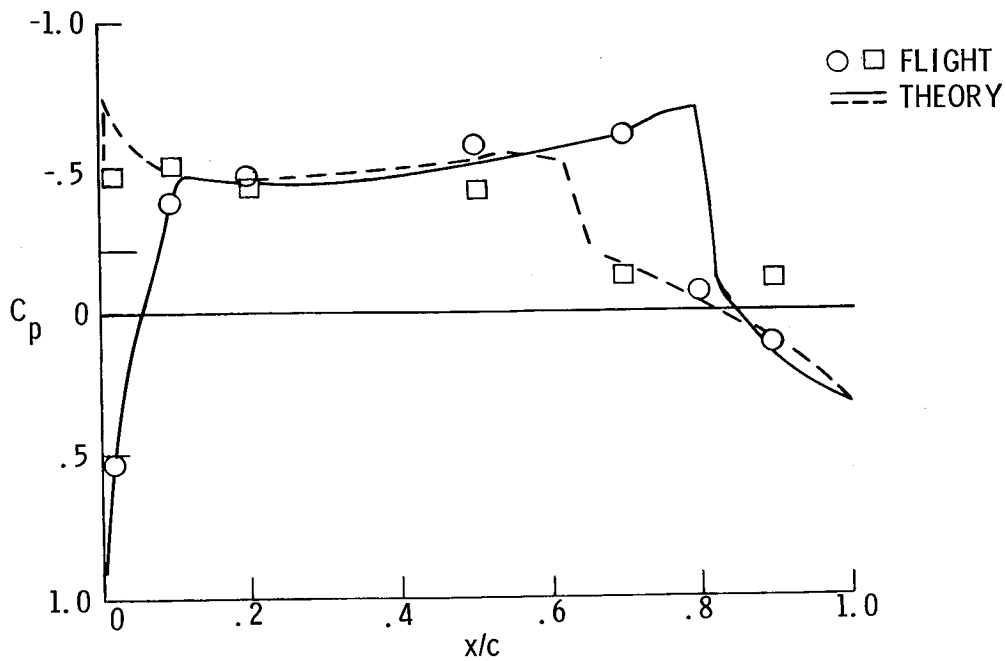
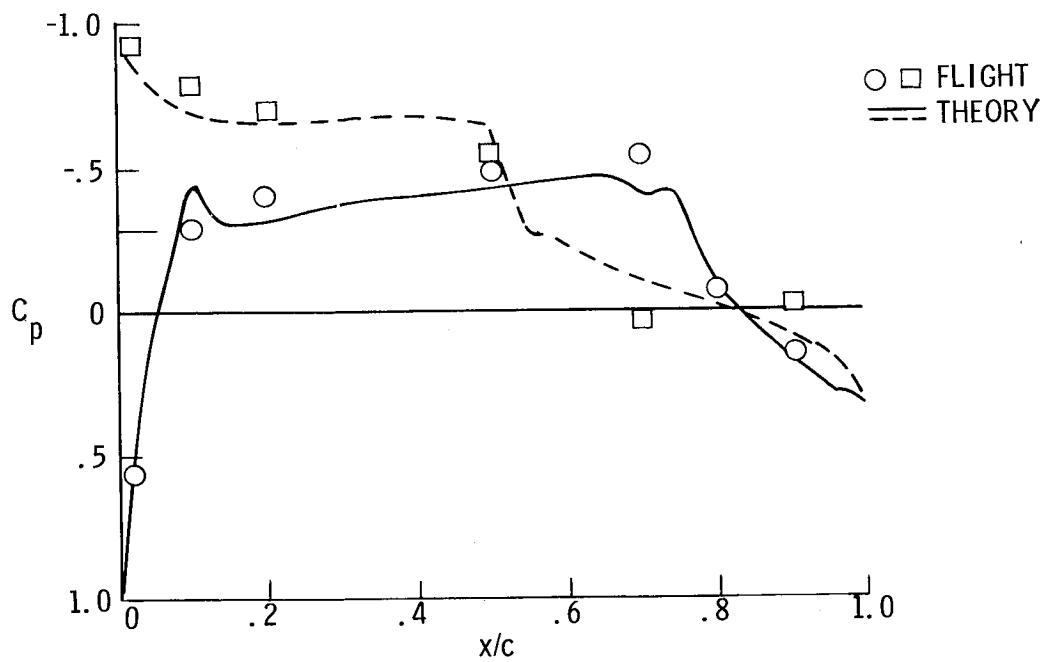(a) $\psi = 0^{\circ}$, $M = 0.63$, $c_n = 0.40$.

(b) $\psi = 180^{\circ}$, $M = 0.63$, $c_n = 0.36$.

Figure 7.- Comparison of flight data and pressure distribution calculated by NYU program; NLR-1 airfoil on AH-1G rotor, $r/R = 0.9$, level flight, $V = 164$ knots, $R_c/M = 16.8 \times 10^6$.
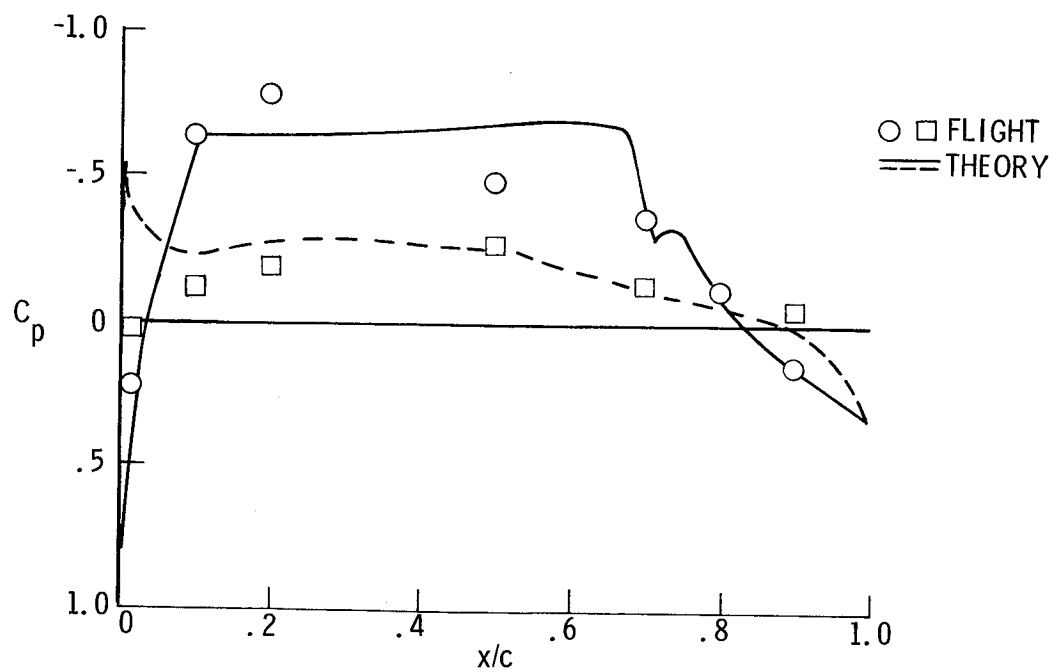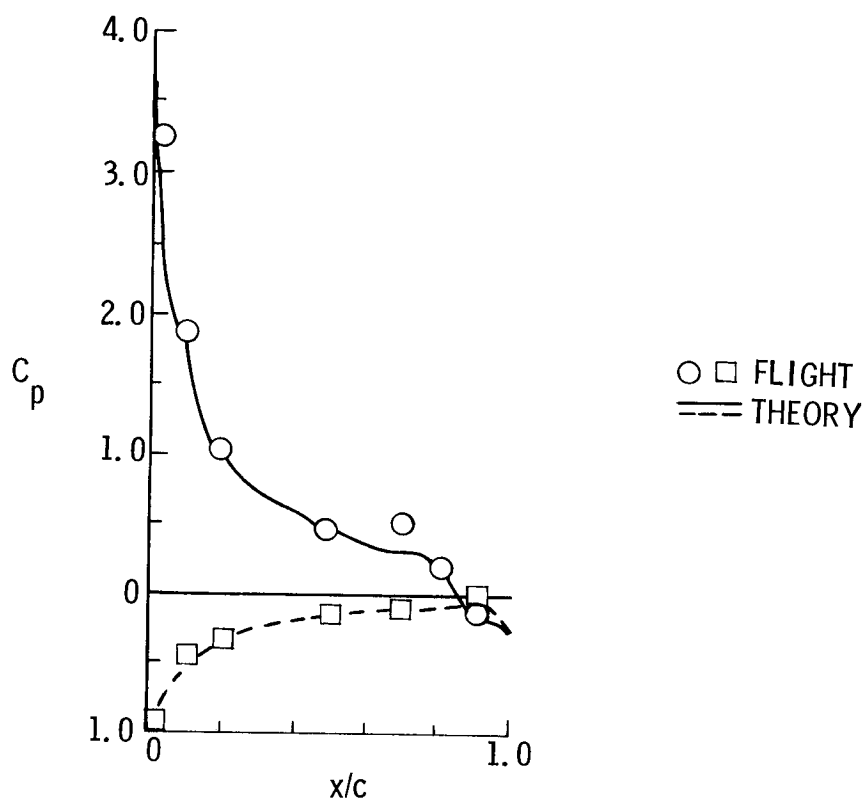
(c) $\psi = 90^{\circ}$, $M = 0.89$, $c_n = 0.02$.

(d) $\psi = 120^{\circ}$, $M = 0.85$, $c_n = -0.16$.

Figure 7.- Continued.

(e) $\psi = 60^{\circ}$, $M = 0.85$, $c_n = 0.23$.

(f) $\psi = 270^{\circ}$, $M = 0.37$, $c_n = 0.89$.

Figure 7.- Concluded.

AIRFOILS FOR WIND TURBINE APPLICATION

Melvin H. Snyder and William H. Wentz, Jr.
Wichita State University

SUMMARY

Desirable characteristics of airfoils for use as blade sections of wind-axis turbines include high maximum lift coefficient, high lift-drag ratio, and gentle stall. In order to design blades and to predict off-design performance, wind turbine designers need low Reynolds number data for new airfoils at extremely wide ranges of angle of attack. For cross-wind axis turbines, airfoil modifications to increase leading-edge suction are highly desirable.

INTRODUCTION

Wind energy is an alternate renewable energy source of considerable interest because it is a clean source having minimum impact on the environment. It appears there will be a steady effort to develop this energy source along the coasts and in the high plains area of the United States.

Some claim that efficiency of Wind Energy Conversion Systems (WECS) is not important because the source of the energy is relatively full and abundant. This reasoning is erroneous. Increasing the efficiency (C_p) of a unit reduces the diameter of the rotor for a given power output. Tailoring the airfoil characteristics to the requirements of the turbine blade results in smaller volume blades for a given diameter. Both of these reductions result in reduced weight of turbine rotor, reduced weight of support structure, and reduced capital cost.

Efficiency of turbines is expressed by power coefficient, C_p, which is the fraction of the energy in the air stream (the stream tube intercepted by the turbine) which is extracted by the turbine. As shown in figure 1, C_p is a function of the blade tip speed ratio, X.

Two types of wind turbines are referred to in figure 1--wind axis and cross-wind axis. Wind-axis turbines, sometimes called "horizontal axis" turbines, include the low efficiency, high-torque American farm windmill and the two-blade turbines of the NASA Plumbrook type. In general, the fewer the number of blades, the higher the operational speed and efficiency. The most effective cross-wind rotor turbine (vertical axis) is the Darrieus rotor.

SYMBOLS

A   area of streamtube intercepted by turbine

c   local chord of turbine blade

c_d section drag coefficient

c_ℓ section lift coefficient

$C_{L_{max}}$ maximum lift coefficient

C_p power coefficient, $\dfrac{P}{(\rho/2)A\,V_a^3}$

D   drag force

L   lift force

P   shaft power extracted by turbine

r   radius of local blade section

Res   resultant force acting on Darrieus rotor blade section

R.N.   Reynolds number

t/c   airfoil maximum relative thickness

V_a ambient wind velocity

X   blade tip peripheral speed/wind speed

α local section angle of attack

β local section pitch angle, a function of radius

θ angular position of a Darrieus blade, measured, in direction of rotation, from plane normal to wind

ρ air density

ω Darrieus angular speed

WIND-AXIS TURBINE

To test a concept of generating synchronous power with an on-line in-
uction generator driven by a wind turbine over a wide range of rotational
peeds, a prototype was designed, erected, and is currently being tested on

the Wichita State University campus. It is a two bladed turbine with a 5.5 m (18 ft) diameter.

In order to design the turbine blades, a design program was developed based on Wilson's work (ref. 1). The program was computerized as detailed in reference 2 and outlined in figure 2. The input to the program is the torque required, the design wind speed, the diameter required, the design rpm, and the relative blade planform. Other input to the program is the design angle of attack of the particular airfoil being considered, together with the coefficient of lift and the coefficient of drag developed at that angle of attack. Output is the blade pitch angle (a function of the radial position), local chord, total blade volume and weight, thrust (force which tends to blow the windmill away, i.e., force normal to the plane of rotation), centrifugal loads, and hub bending moment.

In using this sort of design program, it is possible to examine a number of things, e.g., effects of planform and of airfoil sections. A number of different promising airfoils, including Clark-Y, 2300-series, GA(W)-1, and others, were examined as candidates for blade section. It appeared that use of GA(W)-1 would result in smaller blade volume. For this reason, the turbine now operating has a GA(W)-1 section.

Various design angles of attack were chosen and the resulting blade volume was determined. As shown in figure 3, this study indicated that a design angle of attack of 16 degrees (GA(W)-1 section), corresponding to maximum c_ℓ, resulted in minimum blade volume.

A subsequent study, using the design program, compared a number of "paper airfoils" which were based on the GA(W)-1. The design angle of attack was retained at 16 degrees, but the profile drag coefficient was varied from 0.0038 to 0.006, so that L/D varied from 234 to 375. The results are shown in figure 4. It may be concluded that the blades should be designed so that the sections are operating at or near maximum lift coefficient, that high maximum lift coefficient is very desirable, and that high L/D is also desirable.

Having determined the design of the blade, it is desirable to calculate rotor performance at all the various wind speeds, blade rotational speeds, and blade pitch angles available. For this purpose, an off-design computer program was written (fig. 5). In this case, the input is wind speed, rotational speed, density, and radial distribution of pitch and of chord. In addition, a table of c_ℓ and c_d for the various ranges of angle of attack and Reynolds numbers must be supplied to the computer. Angle of attack is a problem because in any systematic investigation of wind speeds and rpm the computer requires information at angles of attack ranging well over ±90 degrees.

Reynolds numbers are also a problem. For example, on the 5.5 meter rotor, the Reynolds number, at design condition, varies from 18,000 inboard to about 620,000 outboard. Even on a larger rotor, such as the NASA Mod-0, which is 38 meters in diameter, Reynolds number varies from about 500,000 to 1,750,000 at design conditions. At off-design conditions the range is wider. There is

a paucity of recent data on the effects of Reynolds number and on wide ranges of angles of attack.

Reynolds number effects on lift coefficient are rather extreme. From unpublished data obtained by Jaroslav Lnenicka and provided to NASA Langley Research Center, figures 6 and 7 show the dependence of lift coefficient on Reynolds number and, in particular, the deleterious effect of very low Reynolds numbers on C_{Lmax}.

To obtain additional wide-range angle-of-attack data as well as effects of low Reynolds numbers, 2-D tests were conducted at Wichita State University.

Six airfoils were tested: GA(W)-1, GA(W)-2; and four symmetrical air-foils: NACA 0009, 0012, 0012 (modified), and 0015. These symmetrical airfoils were tested for Sandia Labs because of their interest in the Darrieus type rotor. The tests were performed through 360 degrees angles of attack. Test results were reported in reference 3, and figures 8, 9 and 10 are typical curves from reference 3. One of the problems for off-design performance cal-culation is the hysteresis at angles above the stall (fig. 10). It would be quite desirable if turbines could operate at $C_{L_{max}}$ for a wide range of angles of attack, because the wind velocity continually fluctuates forcing contin-ually changing angles of attack at constant rpm and constant pitch angle. It is hoped that the very desirable high-lift characteristics of some of the new low-speed airfoils (fig. 11) will carry down into the very low Reynolds number range.

Figure 12 illustrates the type of performance predictions provided by the off-design program. Observed points are from tests currently underway. Pitch angle, β, is nominal blade angle and it equals actual section angle at 75% of tip radius.

CROSS-WIND AXIS TURBINE

The Darrieus rotor is a cross-wind axis rotor which is of considerable interest because of structural advantages. A 1-meter diameter Darrieus rotor was recently wind tunnel tested at WSU. Figure 13 is a sectional view show-ing the forces which are acting when the blades are moving across wind. When the resultant is ahead of the center of rotation, positive torque is developed. The leading edge suction provides the driving force. A multiple-tube analysis of the Darrieus type rotor, named "DART," has been developed at Sandia Labs. It does a reasonable job of predicting performance (fig. 14). Fukuda used this program to predict effects of changing from a 0012 section to various airfoils which were thought to have better leading edge suction characteris-tics (ref. 4). His results (fig. 15) seem to show that using a thicker air-foil (particularly the one that he specified, which was a kind of symmetri-cal attempt at a GA(W)-type distribution) would give better performance. A 1-meter diameter Darrieus with two sets of blades, 12% thick and 21% thick, was built and tested in the wind tunnel (ref. 5).

Contrary to predictions, the thicker airfoil did not improve performance. Performance of the Darrieus rotor with 12% blade sections is shown in figure 16. The power developed was measured using an eddy-current dynamometer developed for the test (ref. 6). The chord of the blades is only about 5 cm and the tunnel speed was only 6.7 m/sec so that the section Reynolds numbers were less than 24,000.

CONCLUDING REMARKS

Some of the new general aviation airfoils which produce high maximum lift coefficients and new airfoils being designed for low Reynolds number operation are of interest to wind turbine designers. Designers' needs include:

For Wind-Axis Turbine Application--

    Wide range of angle of attack data
    Low Reynolds number data
    Effects of radial acceleration on boundary layer and stall

For Cross-Wind Axis Turbines--

    High leading-edge suction airfoils
    Application of cambered airfoils to Darrieus

REFERENCES

1. Wilson, Robert E. and Lissaman, P.B.S.: Applied Aerodynamics, May 1974.

2. Snyder, M.H.: Airfoil Data for Use of Wind Turbine Designers. Proceedings of the Fourth Annual UMR-DNR Conference on Energy, University of Missouri-Rolla, 1977.

3. Satran, Dale and Snyder, M.H.: Two-Dimensional Tests of GA(W)-1 and GA(W)-2 Airfoils at Angles-of Attack from 0 to 360 Degrees. WER-1, Wichita State University, Wichita, KS, Jan. 1977.

4. Fukuda, Takao: New Airfoil Sections for a Darrieus Wind Turbine. M.S. Thesis, Aeronautical Engineering Department, Wichita State University, Wichita, KS, Dec. 1977.

5. Axtell, Coutee, and Wilson: Performance of NACA 0012 and WSU 0021 Airfoils on a Darrieus Wind Turbine. Senior Projects Report, Aeronautical Engineering Department, Wichita State University, Wichita, KS, Dec. 1977.
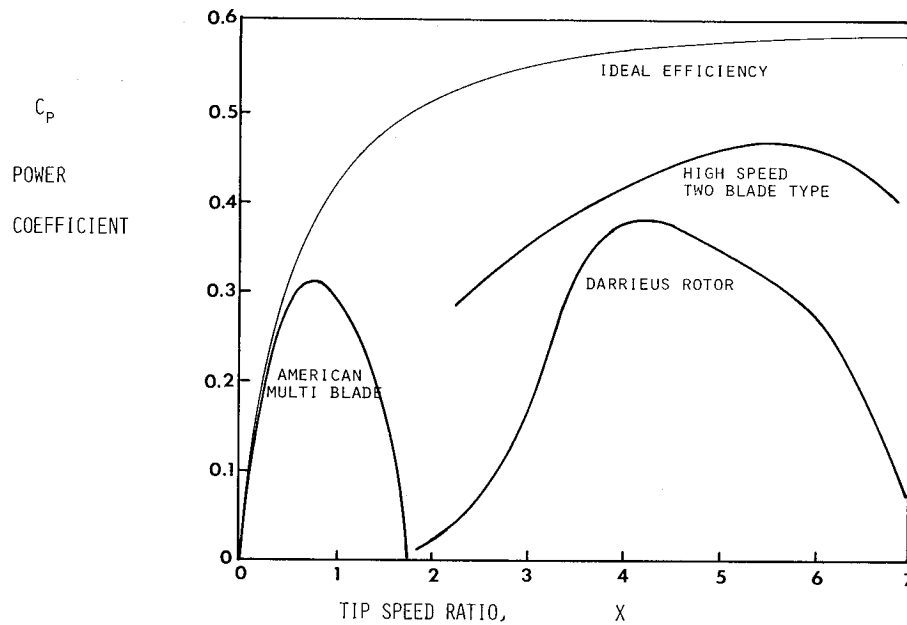
Figure 1.- Wind-turbine power coefficients.
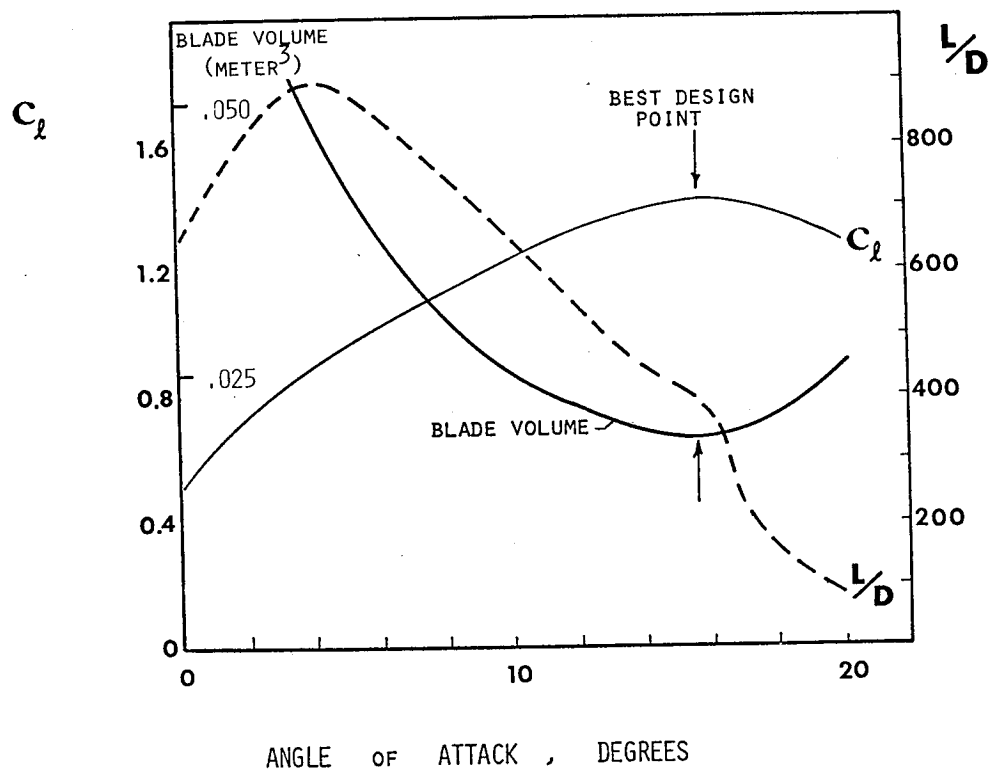

Figure 2.- Blade design program.

Figure 3.- Effect of design angle of attack on blade size. W.S.U. 5.5 meter
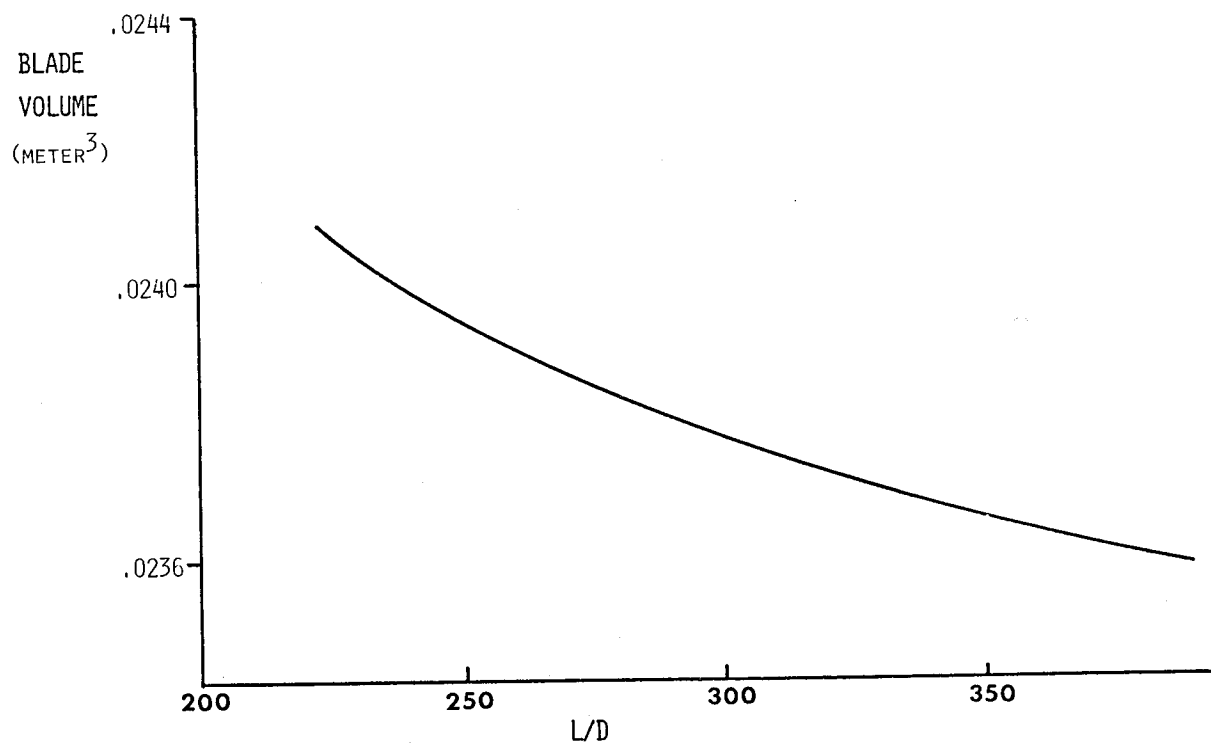turbine; GA(W)-1 airfoil section.

Figure 4.- Effect of L/D on blade size.

INPUT:

WIND SPEED, RPM, DENSITY

RADIUS, $\beta(r)$, $\mathbf{c}(r)$

TABLE OF $\mathbf{C}_\ell$ & $\mathbf{C_d}$

FOR VARIOUS RANGES OF REYNOLDS NUMBERS

OUTPUT:

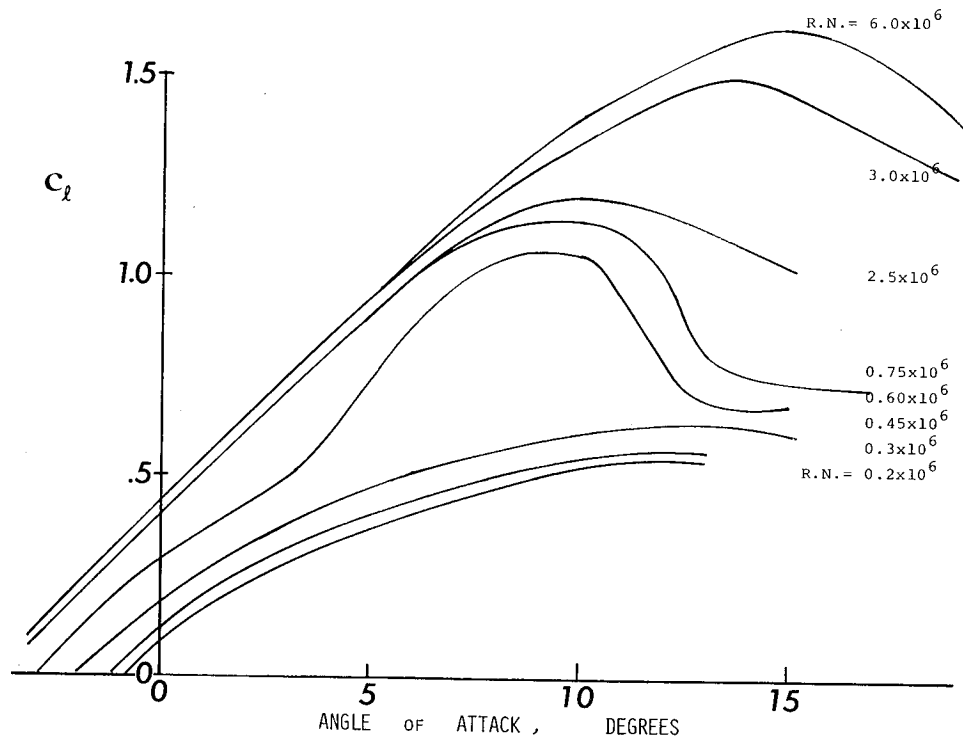TORQUE, POWER, THRUST

Figure 5.- Off-design performance program.
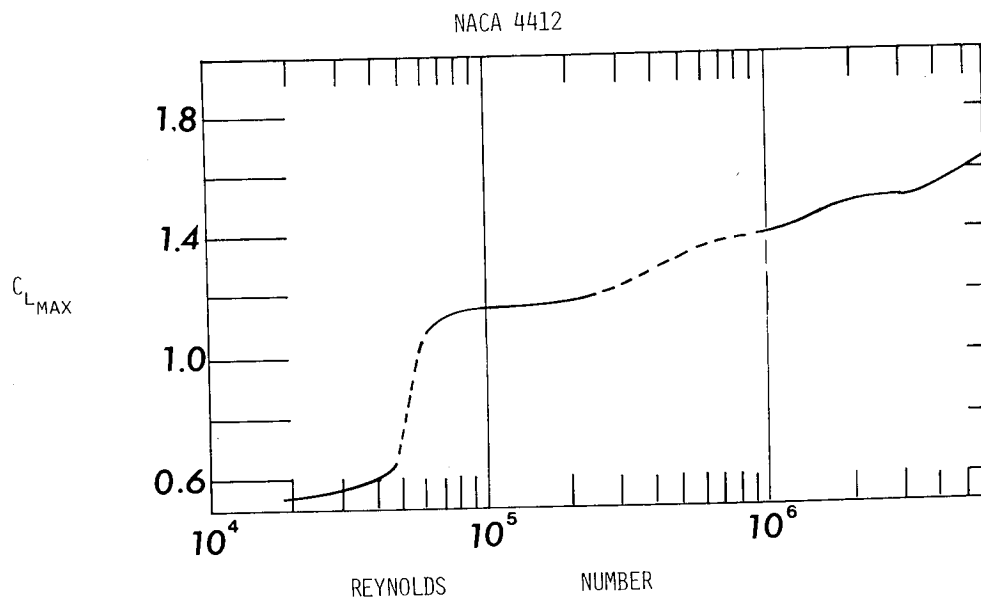

Figure 6.- Reynolds number effects on NACA 4412 airfoil.

NACA 4412

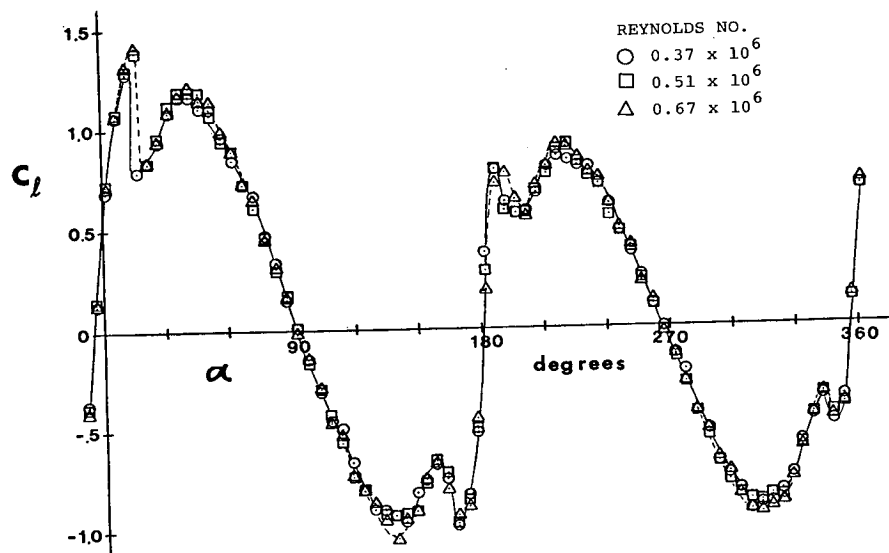Figure 7.- Variation of $C_{L_{MAX}}$ with Reynolds number.

Figure 8.- 2-D test of GA(W)-1 airfoil for C_ℓ plotted against α.
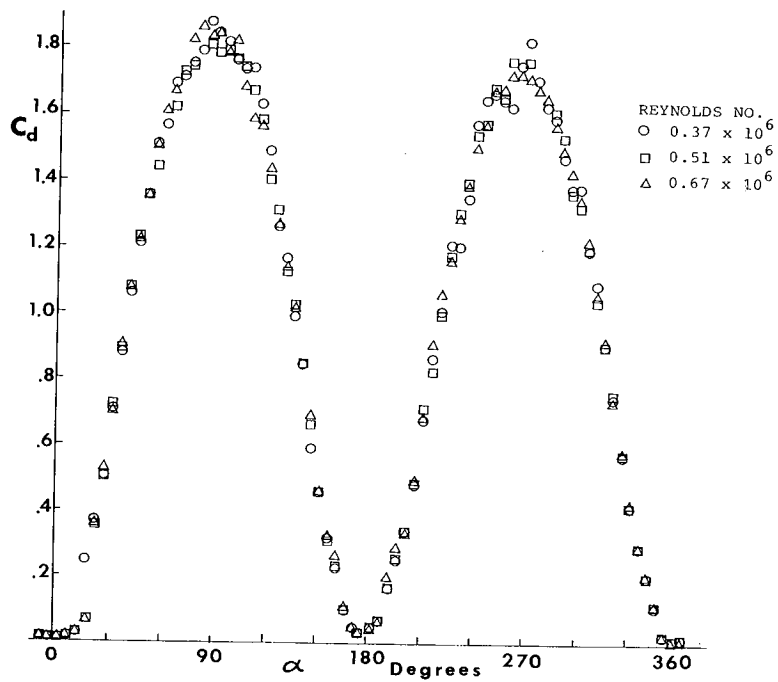
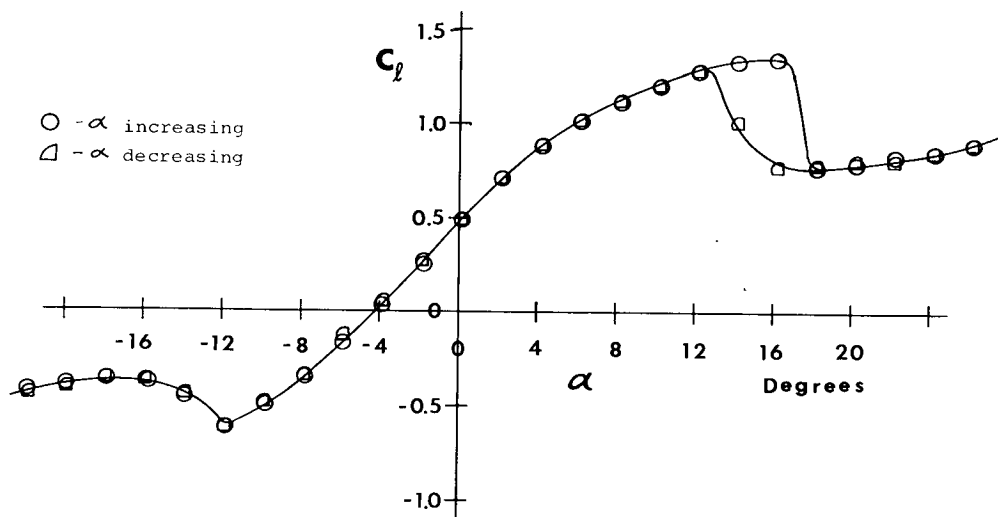Figure 9.- 2-D test of GA(W)-1 airfoil for C_d plotted against α.

Figure 10.- 2-D test of GA(W)-1 airfoil with R.N. $= 0.37 \times 10^6$.
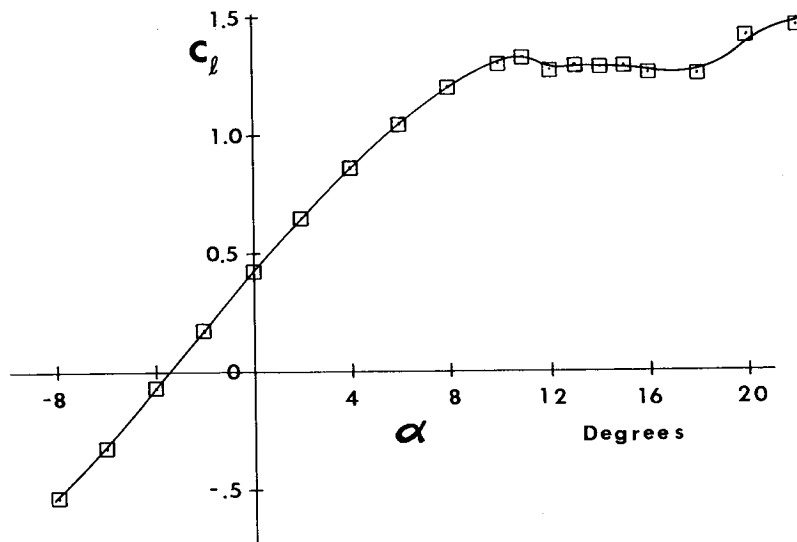
164

Figure 11.- 2-D test of LS(1)-0421 airfoil with R.N. $= 2.2 \times 10^6$.
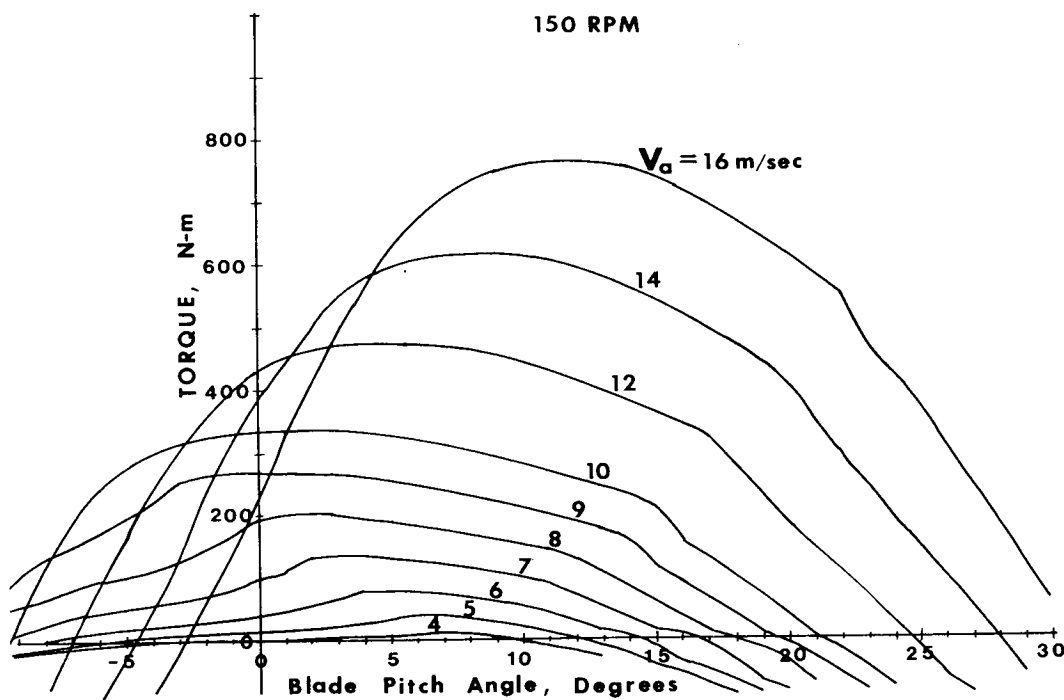

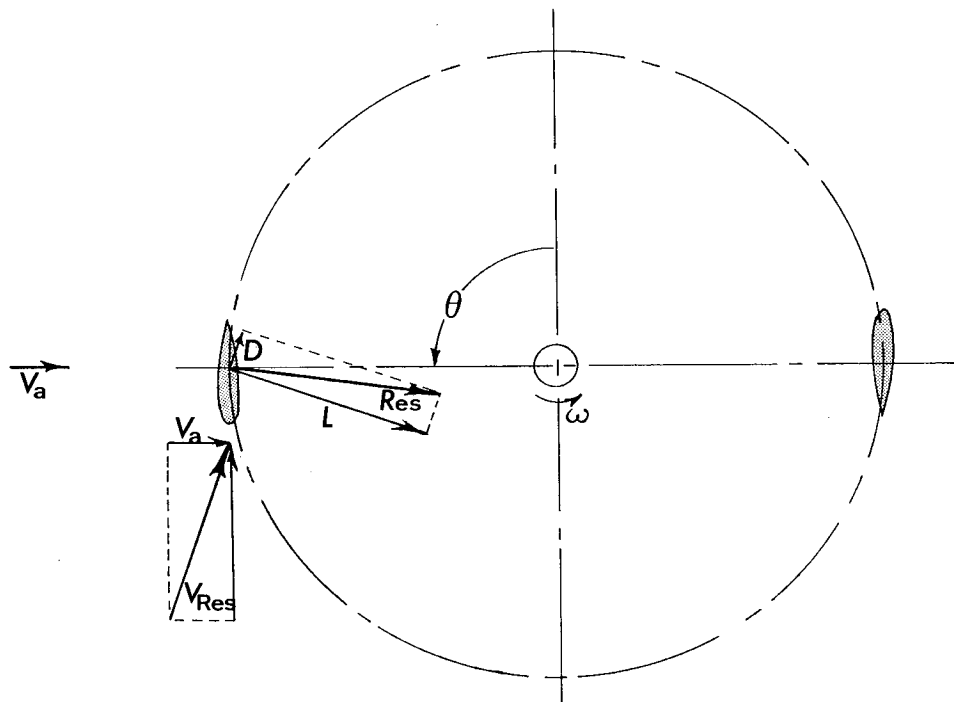Figure 12.- Computer-predicted torque characteristics at 150 rpm with W.S.U. 5.5-meter turbine.

Figure 13.- Darrieus wind turbine.

DART Program Prediction Compared with Experimental Data
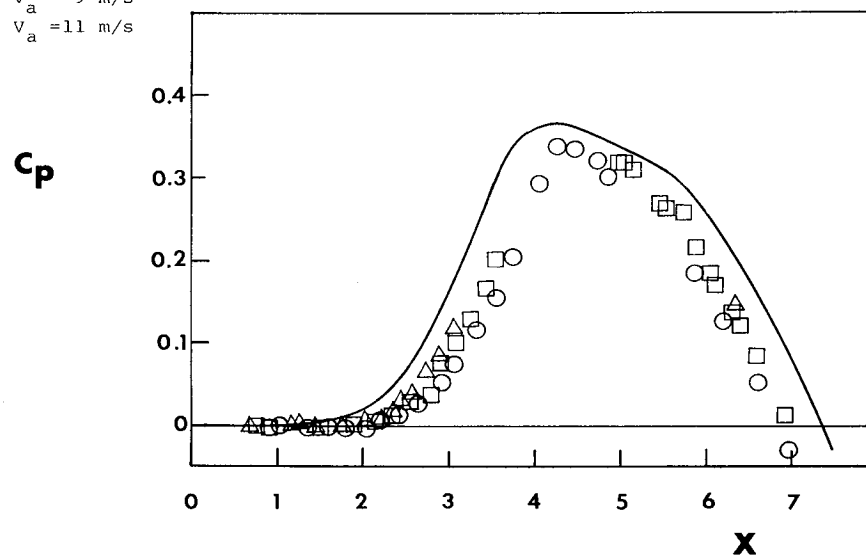
V_a = 7 m/s
V_a = 9 m/s
V_a =11 m/s

Figure 14.- Sandia Darrieus turbine performance.

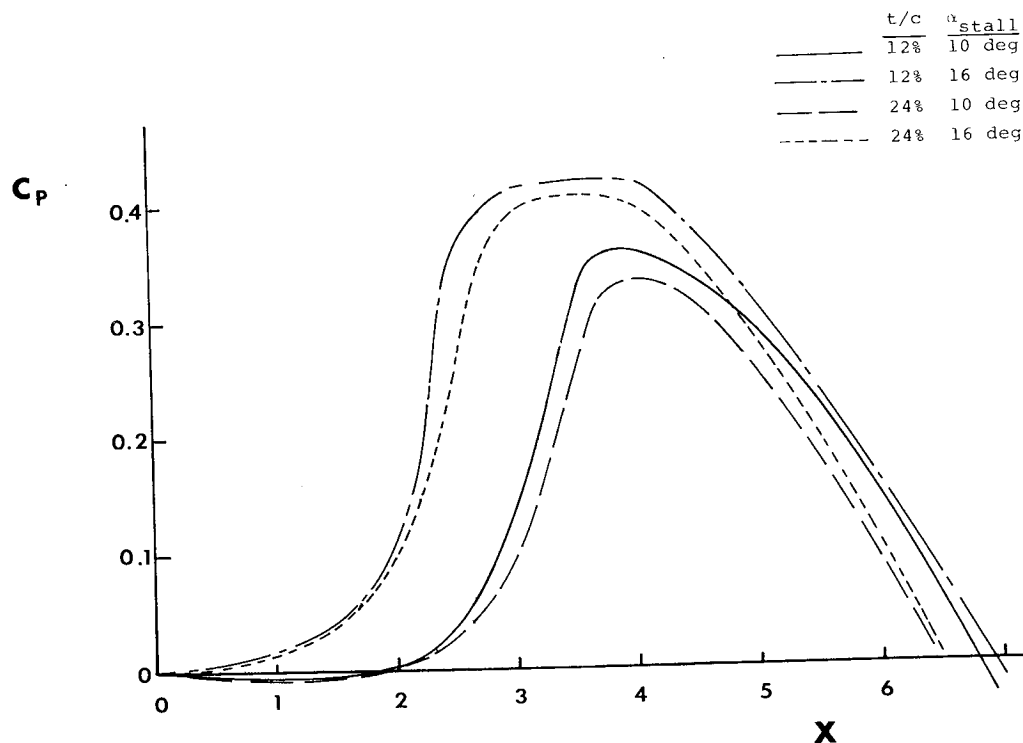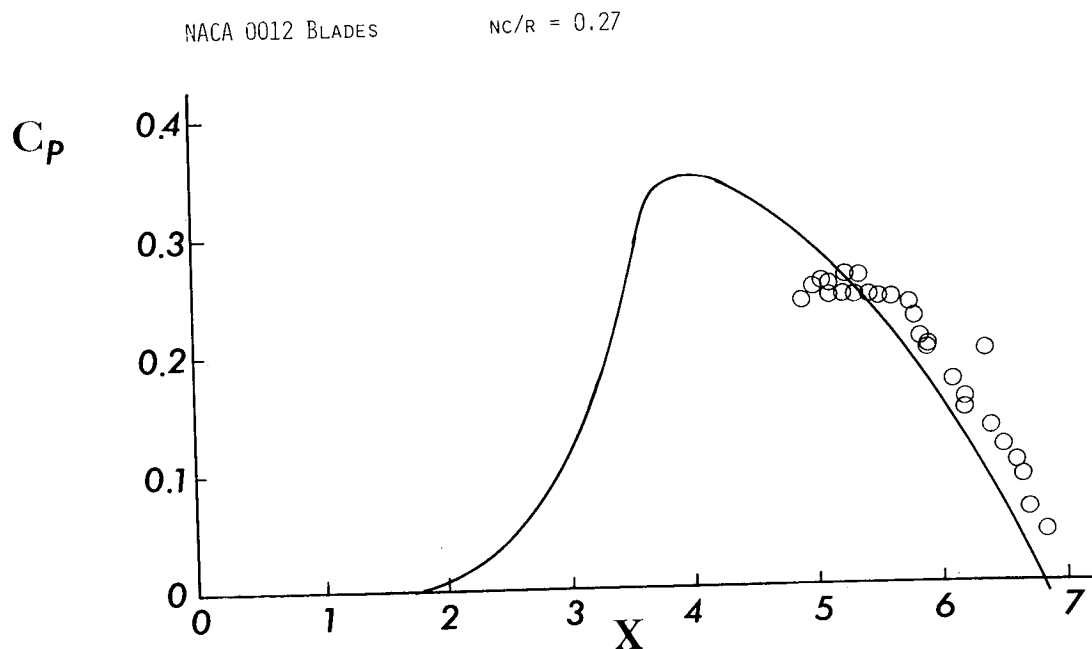Figure 15.- Computer-predicted effects of varying blade section on Darrieus turbine performance.

NACA 0012 Blades   NC/R = 0.27

Figure 16.- W.S.U. 1-meter Darrieus turbine. Comparison of performance with prediction. V_A = 6.6 m/sec.

CHARACTERISTICS AND DEVELOPMENT OF THE

CIRCULATION CONTROL AIRFOIL

Robert J. Englar
David W. Taylor Naval Ship Research and Development Center

SUMMARY

The Circulation Control airfoil, a promising concept in blown aerodynamics, has been under development and has exhibited a number of unique aerodynamic properties. This concept employs tangential blowing from a thin upper surface slot over the airfoil's rounded trailing edge. The jet sheet remains attached to and turns around the trailing edge, thus controlling the circulation around the airfoil. Experimental results are presented for numerous airfoils of this type which show high lift augmentation and lift coefficients exceeding those predicted for inviscid flow. Benefits of the CC airfoil thus include high lift from low values of momentum (blowing) coefficient, lift essentially independent of airfoil incidence, and equivalent aerodynamic efficiencies on the same order as conventional unblown airfoils but at considerably higher lift coefficient. These primary characteristics have led to three ongoing full scale flight demonstration programs: a STOL fixed wing aircraft, an advanced rotary wing vehicle, and a combination fixed wing-rotary wing V/STOL aircraft. The CC airfoil has also been applied experimentally as a water-blowing control surface for submarines, blades in a lifting fan for a surface effect vehicle, and as a transonic rotor tip section. The present paper describes and presents the characteristics and operation of these airfoils, experimental results, comparison to theoretical predictions, and ongoing development leading to advanced versions of the CC airfoil.

INTRODUCTION

The Circulation Control (CC) airfoil concept has been under development since 1968 at the David W. Taylor Naval Ship Research and Development Center (DTNSRDC). The basic technology was derived from earlier research in the United Kingdom (ref. 1 for example) where blowing on circular cross section rotor blades was of interest for stopped-rotor aircraft application. The basic derived concept is shown in figure 1, where the sharp trailing edge of an otherwise conventional airfoil is replaced with a rounded or bluff surface with a thin tangential slot located on the aft upper surface. A jet sheet issuing from this slot remains attached to and traverses the rounded surface due to a balance between centrifugal force and sub-ambient static pressure within the jet, a phenomenon frequently referred to as the Coanda effect. At very low total pressures and blowing rates, the jet acts as a boundary layer control (BLC), entraining the upper surface boundary layer and preventing its separation. At

increasing values of momentum coefficient C_μ, the knee in the C_ℓ vs. C_μ curve of figure 1 is reached. This is theoretically the critical C_μ at which the airfoil static pressure distribution returns to the inviscid potential flow predicted for that incidence. At greater C_μ, values of lift greater than those from potential flow are generated in the Circulation Control regime. Here, the jet controls the location of the airfoil stagnation points, and thus the circulation around it and the associated lift. The primary mechanism is the increased streamline deflection produced by the movement of both stagnation points toward the centerchord; the overall effect is to produce an effective camber considerably greater than the geometric value without use of external moving parts.

Typical lifting capabilities of CC airfoil sections are shown in figure 2 for a 30 percent-thick CC ellipse with 1.5 percent camber, from reference 2. Not only are large values of lift generated at very moderate blowing coefficient (i.e., high lift augmentation, $\Delta C_\ell / C_\mu$), but positive lift is produced at negative angles of attack of -20° or lower. The implications are that lift can be achieved essentially independently of airfoil incidence merely by variations in blowing rate; mechanical pitch (as in rotary wing systems) or mechanical flaps can be replaced by air supply modulation. In addition, profile drag may be varied with C_μ, from unblown C_d values that are considerably higher than those of conventional airfoils to zero or even negative values at moderate C_μ (see ref. 2). Figure 3 compares equivalent airfoil efficiencies (ℓ / d_e) of several CC airfoils (from ref. 3) to the NACA 0012 airfoil, a typical rotor blade section. Here, the equivalent drag term d_e includes a conservative penalty for compressor power required to produce the air supply. As can be seen, the 20% cambered airfoil (ref. 4) is slightly more efficient than the 0012 at 50 percent greater C_ℓ, but produces a $C_{\ell_{max}}$ almost 6 times that of the conventional airfoil.

The above characteristics of the CC airfoil make it a unique device for application to a number of concepts where efficient high lift airfoils capable of lift independent of incidence offer a number of interesting solutions. The following sections will discuss results of basic investigations into these airfoil properties, a number of present application programs, comparison to theoretical results, and ongoing programs for further development on the CC airfoil.

SYMBOLS

Values are given in SI and U.S. Customary Units, but measurements and calculations were made in the latter.

C_d airfoil drag coefficient

c_f/c flap-chord-to-wing-chord ratio

C_ℓ, C_L airfoil or wing lift coefficient

C_m quarter-chord pitching moment coefficient

C_μ momentum or blowing coefficient, $\dot{m}V_j/qc$

h jet slot height, cm (in.)

ℓ/d_e airfoil lift-drag efficiencies

$\dot{m}$ jet mass efflux, kg/sec (slugs/sec)

P_d, P_D duct (plenum) total pressure, N/m^2 absolute (lb/ft^2 absolute)

P_∞ freestream static pressure, N/m^2 absolute (lb/ft^2 absolute)

q, q_∞ freestream dynamic pressure, N/m^2 (lb/ft^2)

R, r Coanda trailing edge radius, cm (in.)

V_j isentropic jet velocity, m/sec (ft/sec)

α airfoil or wing incidence, deg

Subscripts:

LE, TE   leading edge or trailing edge

EXPERIMENTAL AIRFOIL INVESTIGATIONS

During the ongoing CC programs at DTNSRDC since 1968, a number of two-dimensional airfoil investigations have been conducted to understand the basic properties of these devices and to provide input data for their applications. Included in these are more than 25 CC airfoils intended for use on rotary wing vehicles, 15 for application to high lift STOL aircraft, 3 transonic CC airfoils and several unique airfoils for specific additional applications to be discussed in a later section. Reference 3 is a bibliography of published reports on these investigations up through mid 1977. Some basic properties of the CC airfoil were mentioned in the Introduction, but many additional interesting properties were revealed in investigations on a basic CC research airfoil.

CC Research Airfoil

This airfoil, shown in figure 4, was designed and tested (references 5 and 6) to investigate the properties of higher jet velocity and pressure ratio, and contained some special instrumentation for those purposes. Static pressure distributions over the airfoil are shown in figure 5 and give some insight into the airfoil loading produced by blowing. The "saddle-back" shape is fairly typical of CC airfoils at $\alpha = 0^\circ$; at positive incidence the leading edge suction peak is more pronounced, while at negative incidence, the rear adverse pressure gradient is further aft and the peak greater. Once the sonic (choked, $P_d/P_\infty = 1.89$) pressure ratio is reached, a noticeable pressure rise occurs just downstream of the slot, but lift continues to increase with blowing. Figure 6 depicts airfoil lift for these conditions and slot height h = 0.033 cm (0.013 in.), as well as for 4 other slot heights. Whereas jet impingement on the tunnel floor was denoted by flow visualization and precluded determination of exact corrected

values of lift coefficient, the trends are that C_ℓ approaching 8 to 9 is obtainable with the CC airfoil and C_μ less than 1/2. The effect of varying slot height is seen, where for a constant value of momentum coefficient, reduced h produces reduced mass flow but increased jet velocity and kinetic energy due to the higher pressure ratios required. The result is increased circulation and lift produced by improved jet turning. This is confirmed in figure 7, where the separation point of the jet from the trailing edge has been located by use of a hot film anemometer (ref. 5). The jet is seen to turn through more than 170° from the slot even in the face of the oncoming freestream beneath the airfoil.

Transonic CC Airfoils

Primarily intended as rotor tip sections, a series of three blown 15 percent thick ellipses was tested transonically (ref. 7). The CC ellipses were able to generate far greater lift than the jet flap configuration over the entire speed range tested, as shown in figure 8. (Here, C_μ available from the tunnel air supply varied with dynamic pressure and M_∞, but was the same for all 3 configurations at any given Mach number. An upper limit for the test of 0.08 was available at $M_\infty = 0.3$.) However, the superior lift-generating ability of the rounded trailing edge at low Mach numbers was surpassed at transonic speeds by the elliptic trailing edge with its considerably larger radius downstream of the slot. This pure ellipse was also able to relocate the upper surface shock wave from 75 to 93 percent chord by blowing ($C_\mu = .012$) at $M_\infty = 0.9$, while the shock was not moved under similar conditions by either of the other airfoils. It had been suspected by a number of investigators (see ref. 5) that under certain conditions of high jet pressure ratio, large slot height, and small radius, the Coanda phenomenon would deteriorate into one of jet-detachment (immediate jet separation at the slot with no turning). Apparently, at transonic speeds, blown performance is deteriorated by similar conditions of geometry and pressure Whereas no definite criteria were established for transonic performance improvement, the trend towards larger radii at higher speeds was apparent. Recently conducted (J.B. Wilkerson, et al.) in-house transonic tests of a 2-D airfoil wit a spiral trailing edge downstream of the slot were undertaken to generate an airfoil capable of reasonable transonic as well as subsonic performance by proper tailoring of the radius to the corresponding flow regime.

THEORETICAL COMPARISON

Whereas a large collection of work has been completed by numerous investigations on details of the wall jet (see Appendix A of ref. 3), very little theoretical work has been completed which accurately handles the wall jet at the rounded trailing edge of a high lift airfoil where viscous effects are a predominant factor. Two such theoretical works are references 8 and 9. However, a method developed recently under Navy contract (ref. 10) requires no empirical inputs concerning jet characteristics. This technique employs potential flow and boundary layer analyses connected by an iterative procedure. The jet is modeled by a finite difference method employing an eddy viscosity model. The iterative scheme modifies the potential flow and continues until the calculated pressures

at the separation points from the upper and lower airfoil surfaces are equal, thus locating the aft stagnation point and the airfoil circulation, lift, drag, and pitch. The analysis has been used to calculate characteristics for a number of CC airfoils tested at DTNSRDC; figure 9 shows some sample calculations for a 29 percent thick ellipse airfoil at -5° incidence. Here, for $C_\mu = 0$ and 0.088, the agreement between calculated (subscript c) and measured (M) pressure distribution and lift coefficient is excellent, while quarter-chord pitching moment shows some slight discrepency. The agreement in the case of $C_\mu = 0$ is especially encouraging, considering the large viscous separated wake behind the bluff trailing edge. The analysis thus becomes a valuable tool in predicting characteristics of CC airfoils and in designing advanced versions where variation in trailing edge shape may produce significant performance improvements.

APPLICATIONS

Benefits of the CC airfoil discussed above have suggested a number of applications where the airfoil's characteristics promise a variety of improvements in aerodynamic performance, simplicity, and weight. A significant amount of detailed experimental and analytical work has led to three ongoing full scale flight demonstration programs, as well as a number of other experimental applications.

Circulation Control Rotor (CCR)

The rotary wing application makes full usage of lift modulation by blowing instead of cyclic or collective mechanical pitch variation of the rotor blades. The result is a simplified rotor mounted on a very simple hub and capable of reduced vibration due to higher harmonic cyclic control by modulation of air flow to the individual blades. In-house effort since 1968 (refs. 3, 11, 12, and 13) has led to a prototype H-2 helicopter with a CC Rotor (figure 10) now being constructed by Kaman Aerospace Corporation and scheduled for first flight by December 1978. Figure 11 shows a cross section of one rotor blade of four. The airfoil is very similar in geometry and performance to the 20 percent CC cambered section of figure 3. Here, a particular advantage of the CC airfoil is its ability to operate at negative angles of attack as shown; negative α can provide rotor trim by using no or low blowing on outboard blade sections over certain portions of the rotor azimuth.

Circulation Control Wing (CCW)

The ability of CC sections to generate quite high lift coefficients at the moderate blowing coefficients obtainable from bleed of present-day turbine engines offers a very promising STOL high lift system. As figure 12 shows, many of the CC airfoils tested at DTNSRDC come quite close to achieving the limiting $C_{\ell_{max}} = 2\pi (1 + t/c)$ based on coincidence of front and rear stagnation points (ref. 14) and exclusive of any vertical component of C_μ. Based on this potential, a program was undertaken to determine the effectiveness of the CC trailing

edge on airfoils more characteristic of high performance aircraft. Figure 13 shows a 2-D wind tunnel model of a CC trailing edge applied to the wing-fold lin airfoil section (NACA 64A008.4 Mod) of the Grumman A-6A aircraft (ref. 15). The rotor blade airfoils had shown problems with leading edge separation at high C_ℓ and incidence, and thus considerable attention was given in these tests to effec tive leading edge devices. Figure 14 shows CCW lifting effectiveness in compari son to an NACA collection of 2-D data on blown flap airfoils (ref. 16). Here the comparison is in terms of minimum C_μ required to produce a given increment i C_ℓ due to blowing at $\alpha = 0^\circ$, and both CCW airfoils require far less blowing than their corresponding chord blown flaps. (The 64A212/CCW airfoil is from ref. 17. The A-6/CCW airfoil results led to modification of a 1/8.5 scale model A-6A to the configuration in figure 15. The model and the jet turning effectiveness are shown in figure 16 (which is wind off); more than 180° of turning from the upper surface slot is observed. The supercirculation capabilities are quite evident. Over 600 hours of tunnel testing of this configuration led to the trimmed lift data of figure 17, where, for $C_\mu = 0.30$, trim $C_{L_{max}}$ is 2.1 times that for the conventional A-6 high lift system. These results have led to a full scale A-6/ CCW flight test program, with the aircraft now being modified by Grumman Aero space Corporation and with first flight scheduled for November 1978.

X-Wing

High speed limitations on present-day helicopters are caused by ineffective ness of the retreating blade in the reverse velocity flow region of the rotor, where forward velocity of the craft is greater than the rotational velocity of the blade airfoil section. Thus the relative velocity approaches the blade from its sharp trailing edge, resulting in no lift or corresponding pitch and roll control of the vehicle. CC airfoils offer a very promising alternative to this problem: the dual slotted airfoil as shown in figure 18. Slots are located in both ends of the airfoil and fed by two separate plenums. Thus, depending on where the blade is operating around the rotor azimuth, the effective trailing edge is blown. The reverse flow field no longer results in liftless airfoils, thus allowing lift and rotor trim at much higher forward velocities. Figure 19 (from ref. 18) shows lift generated with both leading and trailing edge blowing, which is the intermediate condition in blowing transfer from one end to the other, and is critical because the leading edge blowing tends to counteract that at the trailing edge. However, the worse cases show a maximum lift loss of 25 percent of that with no leading edge blowing, a tremendous improvement over 100 percent lift loss due to flow into the trailing edge of a conventional blade. Reference 19 presents data on a four-bladed rotor model successfully employing this concept. This work has led to a third ongoing flight demonstration program the X-Wing aircraft, reference 20. This vehicle (fig. 20) will employ a four bladed dual slotted rotor for VTOL or STOL operation, and will then slow and stop the rotor at forward and aft sweep angles of 45°, thus providing a high subsonic speed fixed wing aircraft. At present, a full size rotor and control system for the demonstration vehicle are being constructed by Lockheed Califor nia Co., with testing in the NASA Ames 40 x 80 tunnel planned for summer of 1978 and anticipated vehicle construction and flight to follow at a later date.

Additional Applications

An alternate dual plenum CC airfoil is shown in figure 21, where the two slots on the trailing edge of the airfoil provide a non-deflecting stern plane for a submarine (ref. 21), blowing water instead of air. This concept was tested in a towing basin and found quite effective in generating positive and negative pitching moments at zero incidence, thus eliminating the possibility of jamming at high deflections, since no incidence is required to produce the necessary control forces. CC airfoils were also employed as blade elements in a lifting fan intended for open-ocean surface effect ship use (ref. 22). Lift depending only on blowing yielded a fan capable of variable performance at fixed blade incidence and constant RPM.

With most of the above applications, continuing analysis and experimentation is being conducted to provide advanced CC airfoils capable of providing improved performance for the corresponding concept. Examples of this are the improved transonic airfoil discussed earlier, and the modification shown in figure 22 to reduce the drag on a subsonic CCR airfoil section by modifying the trailing edge shape. As this figure shows, deviating from the rounded trailing edge reduces the suction pressure normal to the airfoil surface at the trailing edge, and thus reduces the pressure drag on the airfoil. This data is from reference 23, which discusses 5 recently designed and tunnel-tested airfoils and presents an airfoil designation system. The number of parameters describing and affecting CC airfoils is far greater than for conventional airfoils, and generation of complete families of airfoils becomes an involved and difficult task, but present efforts are providing a base from which further development of the Circulation Control Airfoil can occur.

CONCLUDING REMARKS

The Circulation Control airfoil investigations described have demonstrated the ability of this concept to generate: high lift from low values of momentum coefficient, lift essentially independent of incidence, equivalent aerodynamic efficiencies similar to conventional airfoils but at higher lift coefficients, and improved transonic capabilities over other blown airfoils. These properties have been developed into a number of unique applications, including ongoing flight demonstrations of an advanced rotary wing vehicle, a fixed wing STOL aircraft, and a combination fixed wing-rotary wing V/STOL aircraft. Theoretical analyses capable of predicting the characteristics of the CC airfoil flow regime are now available, and are part of a continuing effort to develop advanced versions of the airfoil and performance improvements for many types of vehicles employing aerodynamic surfaces for lift or control.

REFERENCES

1. Cheeseman, I.C.: Circulation Control and Its Application to Stopped Rotor Aircraft. Presented at Tenth Anglo-American Conference, Los Angles (Sept 1967). Published as AIAA Paper 67-747 (1967).

2. Englar, R.J.: Two-Dimensional Subsonic Wind Tunnel Tests of a Cambered 30-Percent Thick Circulation Control Airfoil. Naval Ship R and D Center Tech Note AL-201 (AD 913-411 L), May 1972.

3. Englar, R.J.; Stone, M.B.; and Hall, M.: Circulation Control - An Updated Bibliography of DTNSRDC Research and Selected Outside References. David W. Taylor Naval Ship Research and Development Center Report 77-0076, Sept 1977.

4. Williams, Robert M.; and Howe, Harvey J.: Two-Dimensional Subsonic Wind Tunnel Tests on a 20-Percent Thick, 5-Percent Cambered Circulation Control Airfoil. NSRDC Technical Note AL-176 (AD 877-764), Aug 1970.

5. Englar, Robert J.: Experimental Investigation of the High Velocity Coanda Wall Jet Applied to Bluff Trailing Edge Circulation Control Airfoils. NSRDC Technical Note AL-308 (AD 771-690), June 1973. Also published as M.S. Thesis, University of Maryland, Department of Aerospace Engineering, June 1973, and as NSRDC Report 4708 (AD-A-019-417), Sept 1975.

6. Englar, R.J.: Circulation Control for High Lift and Drag Generation on STOL Aircraft. AIAA Journal of Aircraft, Vol. 12, No. 5, May 1975, pp. 457-463.

7. Englar, Robert J.: Two-Dimensional Transonic Wind Tunnel Tests of Three 15-Percent-Thick Circulation Control Airfoils. NSRDC Technical Note AL-182 (AD 882-075), Dec 1970.

8. Ambrosiani, J.P.; and Ness, N.: Analysis of a Circulation Controlled Elliptical Airfoil. West Virginia University, Department of Aerospace Engineering, TR-30 (AD 726-434), Apr 1971.

9. Levinsky, E.S.; and Yeh, T.T.: Analytical and Experimental Investigation of Circulation Control by Means of a Turbulent Coanda Jet. NASA CR-2114, Sept 1972.

10. Dvorak, Frank A.: A Viscous/Potential Flow Interaction Analysis for Circulation-Controlled Airfoils. Analytical Methods, Inc. Report No. 7710, Nov 1977.

11. Wilkerson, Joseph B.: Design and Performance Analysis of a Prototype Circulation Control Helicopter Rotor. NSRDC Technical Note AL-290 (AD 912-213L), Mar 1973.

12. Wilkerson, J.B.; Reader, K.R.; and Linck, D.W.: The Application of Circulation Control Aerodynamics to a Helicopter Rotor Model. Preprint No. 704, 29th Annual National Forum of the American Helicopter Society, Washington, D.C., May 1973.

13. Wilkerson, Joseph B.; and Linck, Drew W.: A Model Rotor Performance Validation for the CCR Technology Demonstrator. Preprint 902, 31st Annual National Forum of the American Helicopter Society, Washington, D.C., May 1975. Also published in Journal of the American Helicopter Society, Vol. 21, No. 4, Oct 1976.

14. Whittley, D.C.: Maximum Lift Coefficient for STOL Aircraft: A Critical Review. Third CAL/AVLABS Symposium on Aerodynamics of Rotary Wing and V/STOL Aircraft, Cornell University, Buffalo, New York, Vol. 2 of Proceedings, 18-20 June 1969.

15. Englar, R.J.; Trobaugh, L.A.; and Hemmerly, R.A.: Development of the Circulation Control Wing to Provide STOL Potential for High Performance Aircraft. Paper No. 77-578 presented at AIAA/NASA Ames V/STOL Conference, Palo Alto, California, 6-8 June 1977.

16. Riebe, J.M.: A Correlation of Two-Dimensional Data on Lift Coefficient Available with Blowing-, Suction-, Slotted-, and Plain-Flap High Lift Devices. NACA RM L55D 29a, Oct 1955.

17. Englar, R.J.: Subsonic Two-Dimensional Wind Tunnel Investigations of the High Lift Capability of Circulation Control Wing Sections. NSRDC Report ASED-274, Apr 1975.

18. Ottensoser, Jonah: Two-Dimensional Subsonic Evaluation of a 15-Percent Thick Circulation Control Airfoil with Slots at Both Leading and Trailing Edges. NSRDC Report 4456, July 1974.

19. Reader, Kenneth R.; and Wilkerson, Joseph B.: Circulation Control Applied to a High Speed Helicopter Rotor. Preprint No. 1003, 32nd Annual National V/STOL Forum of the American Helicopter Society, Washington, D.C., May 1976.

20. Williams, R.M.; Leitner, R.T.; and Rogers, E.O.: X-Wing: A New Concept In Rotary Wing VTOL. Presented at the American Helicopter Society Symposium on Rotor Technology, Philadelphia, PA, Aug 1976.

21. Englar, Robert J.; and Williams, Robert M.: Design of a Circulation Control Stern Plane for Submarine Applications. NSRDC Technical Note AL-200 (AD 901-198), Mar 1971.

22. Furey, R.J.; and Whitehead, R.E.: Static Evaluation of a Circulation Control Centrifugal Fan. DTNSRDC Report 77-0051, June 1977.

23. Wilkerson, Joseph B.: An Assessment of Circulation Control Airfoil Development. DTNSRDC Report 77-0084, Aug 1977.
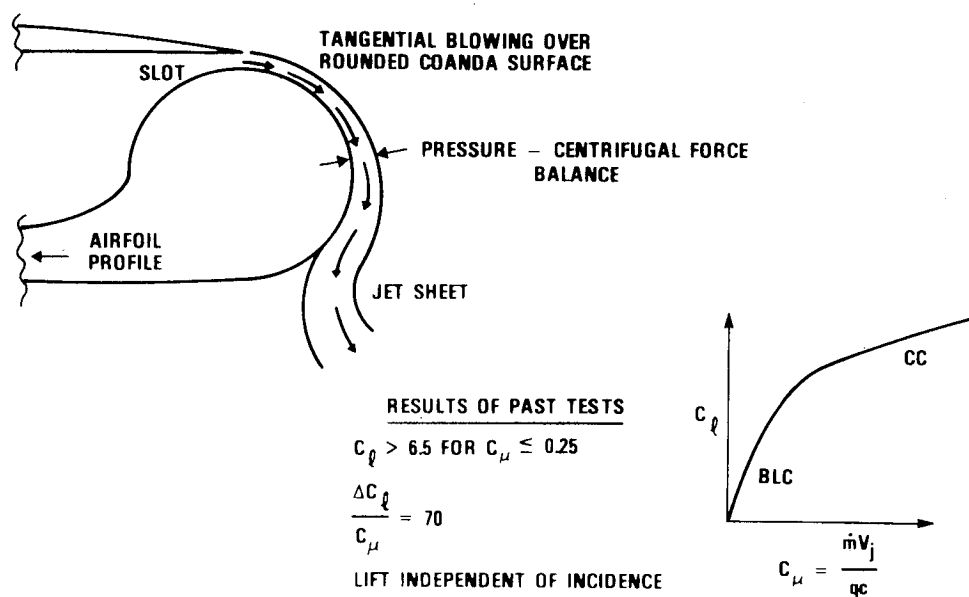
Figure 1.- Basic Circulation Control (CC) aerodynamics.
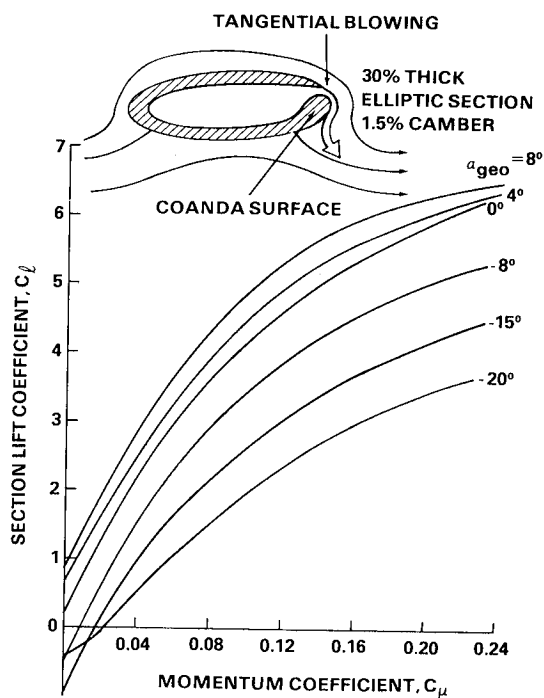

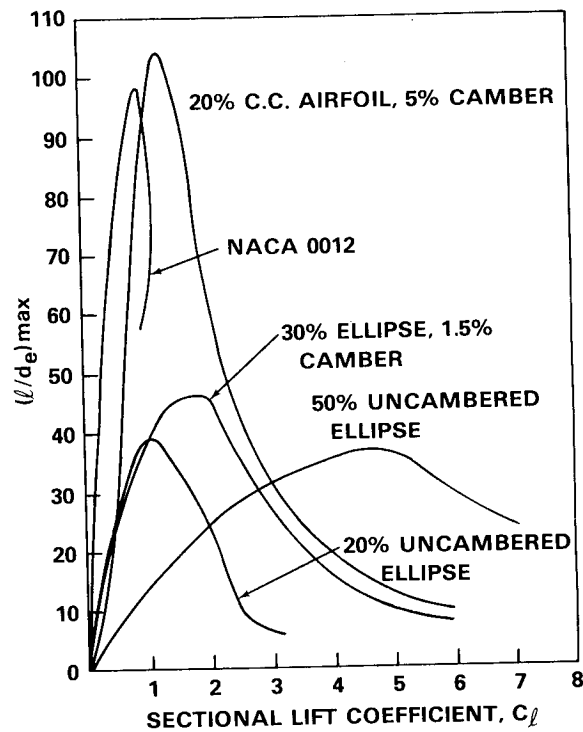Figure 2.- Typical Circulation Control (CC) airfoil lift capability.

Figure 3.- Comparative efficiencies for conventional and CC airfoil sections.
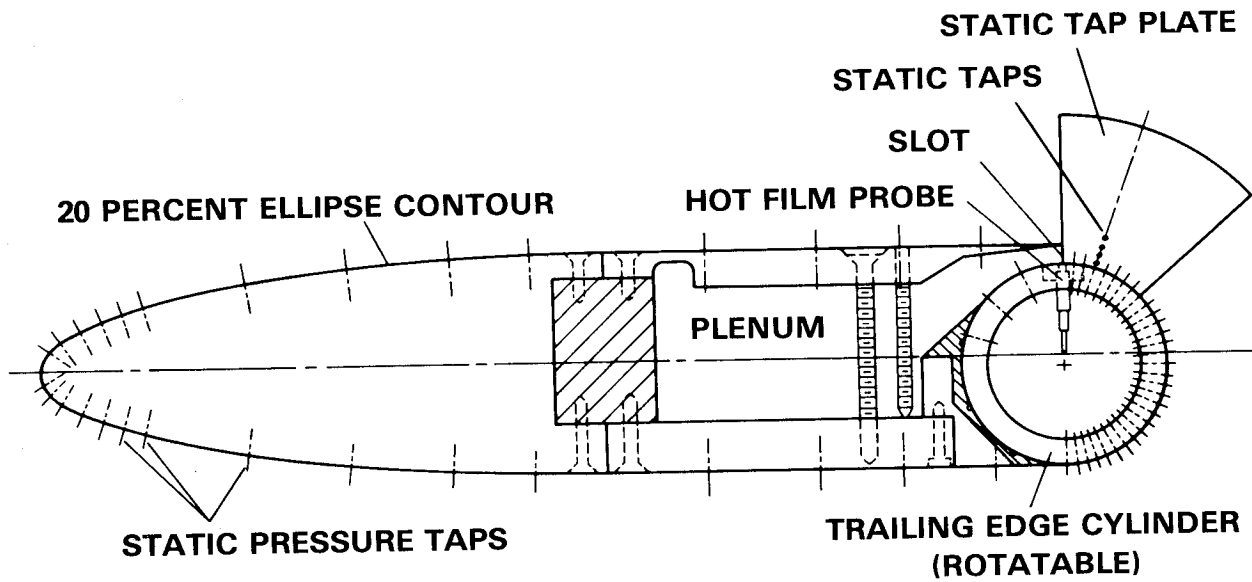

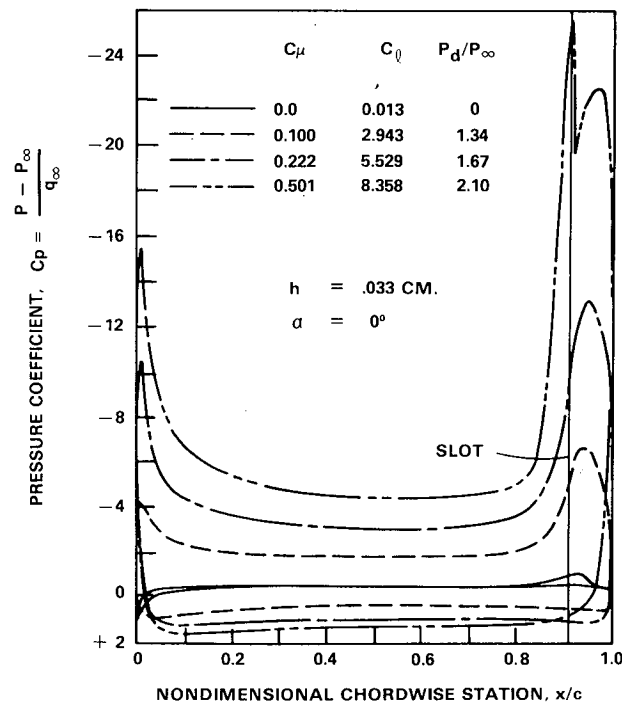Figure 4.- Geometry of 2-D CC research airfoil.

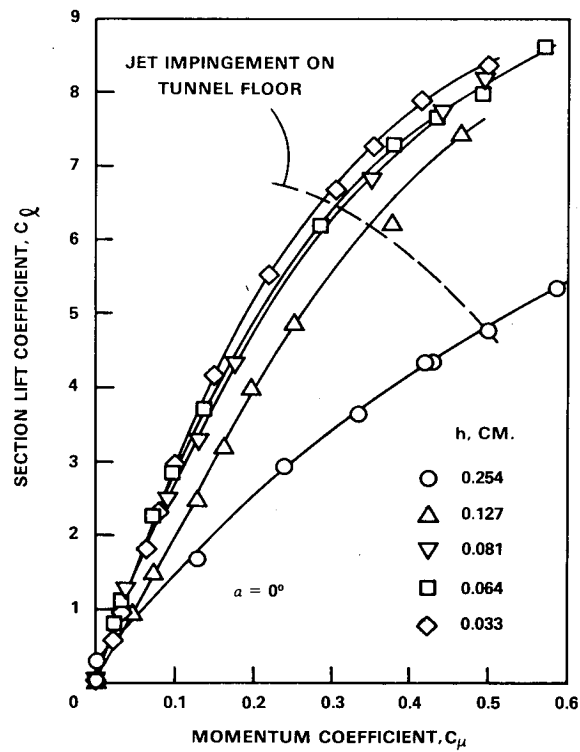Figure 5.- CC airfoil static-pressure distributions.

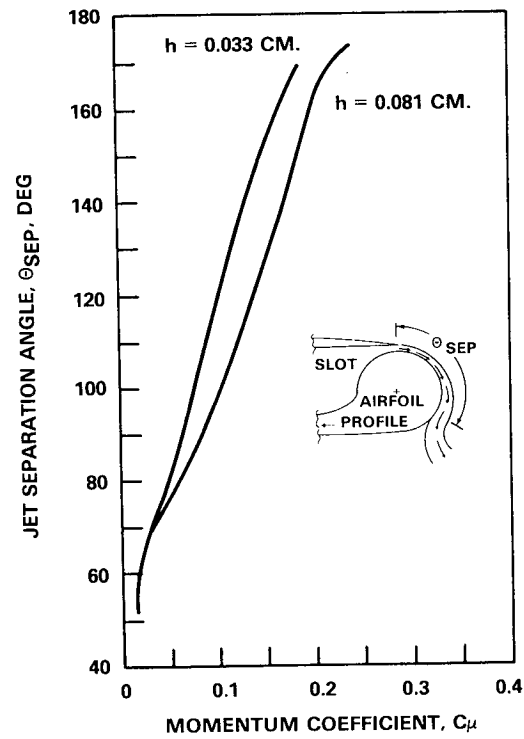Figure 6.- CC airfoil lift as a function of slot height and C_μ.

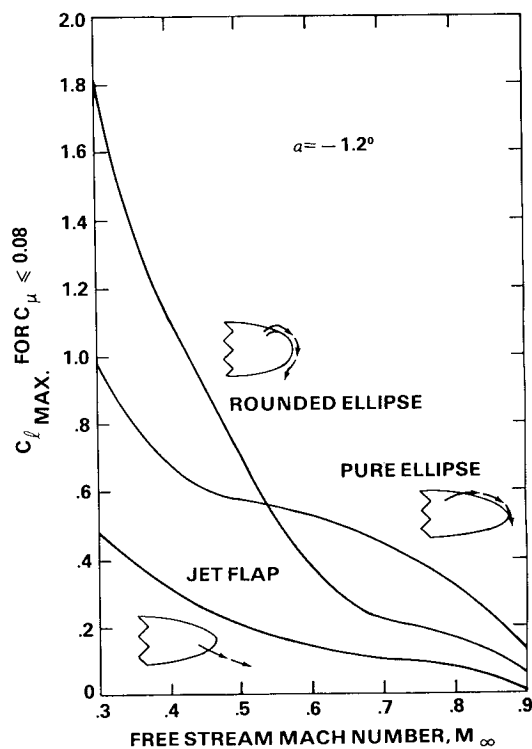Figure 7.- Location of jet separation point.
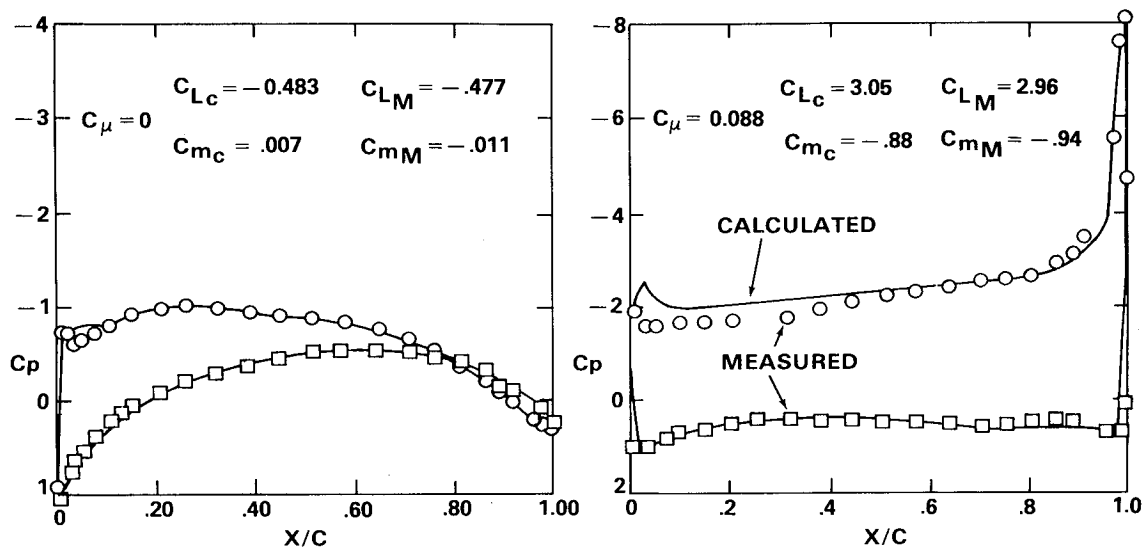

Figure 8.- Lifting capabilities of transonic CC and jet-flap airfoils.

Figure 9.- Comparison between calculated and measured pressure distributions for a 29% thick CC ellipse. $\alpha = -5^\circ$.
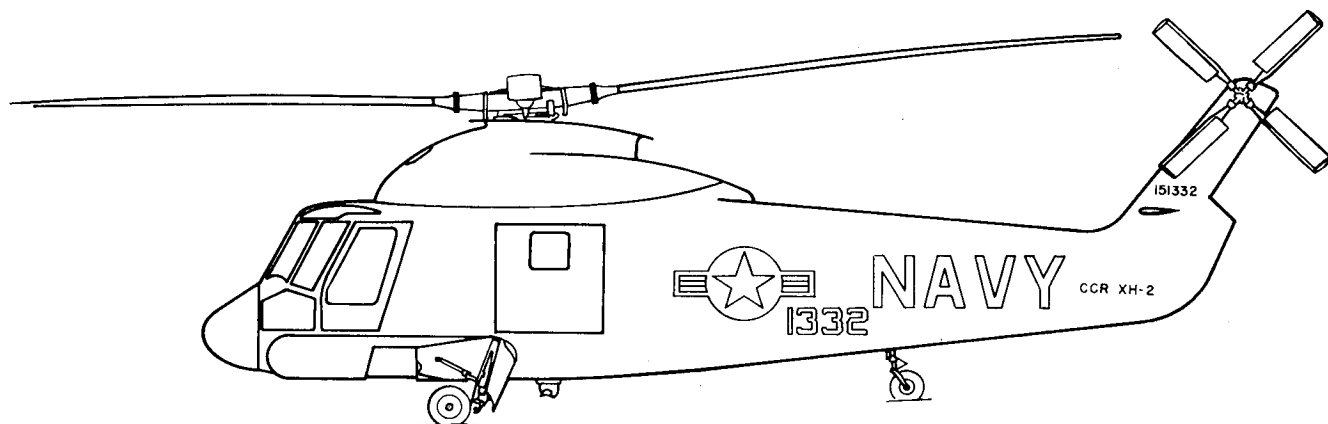
Figure 10.- XH-2/CCR flight-demonstrator vehicle.
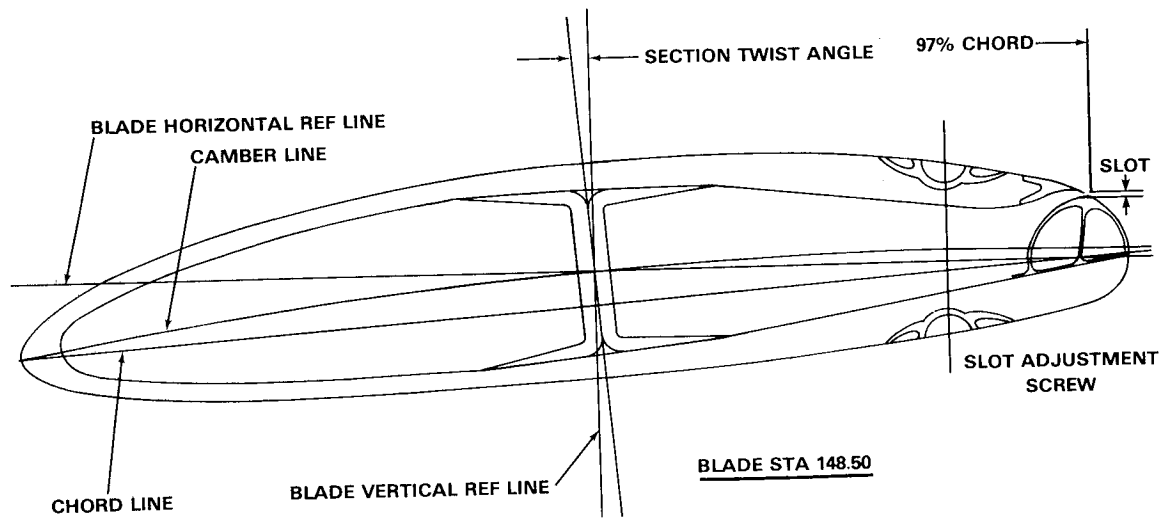
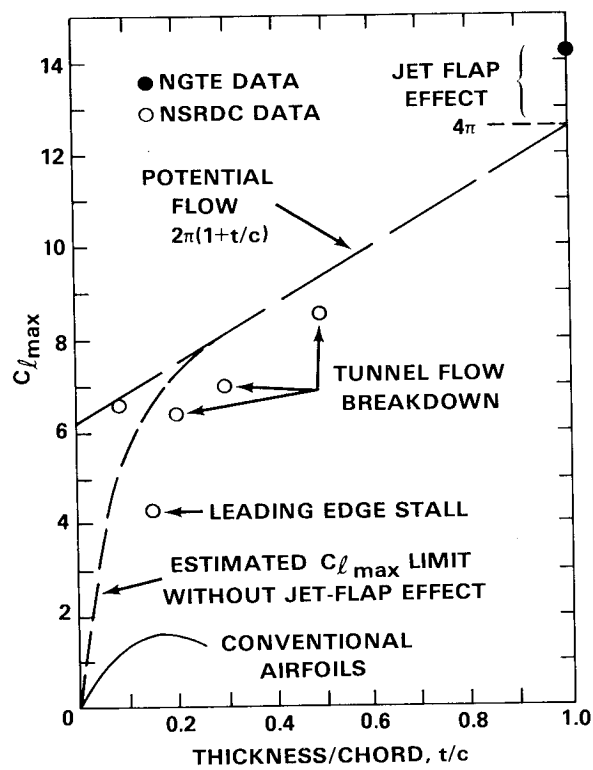Figure 11.- Circulation Control rotor-blade cross section (XH-2/CCR).

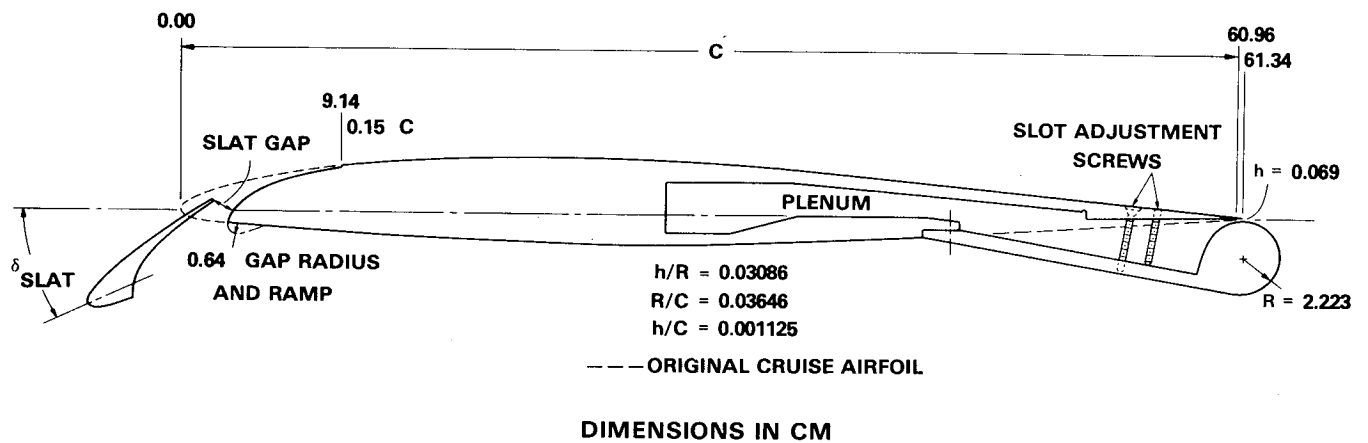Figure 12.- Section maximum lift characteristics.

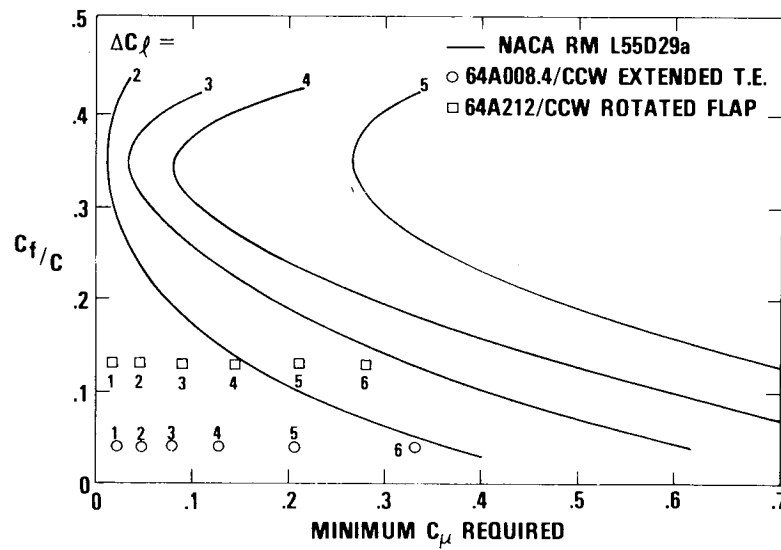Figure 13.- Circulation Control wing cross section (NACA 64A008.4 Mod).

Figure 14.- 2-D CCW comparison with NACA blown-flap data. $\alpha = 0^{\circ}$.

ADD BLEED AIR
SYSTEM CONTROLS

BLEED AIR SYSTEM

ADD FIXED
KRUEGER L.E. FLAP

ADD FLOW FENCE

ADD FIXED
L.E.

WING

STABILIZER

SLAT FIXED
AT 25°

ADD BLEED
AIR SYSTEM

INCR. RADIUS

ADD COANDA T.E.
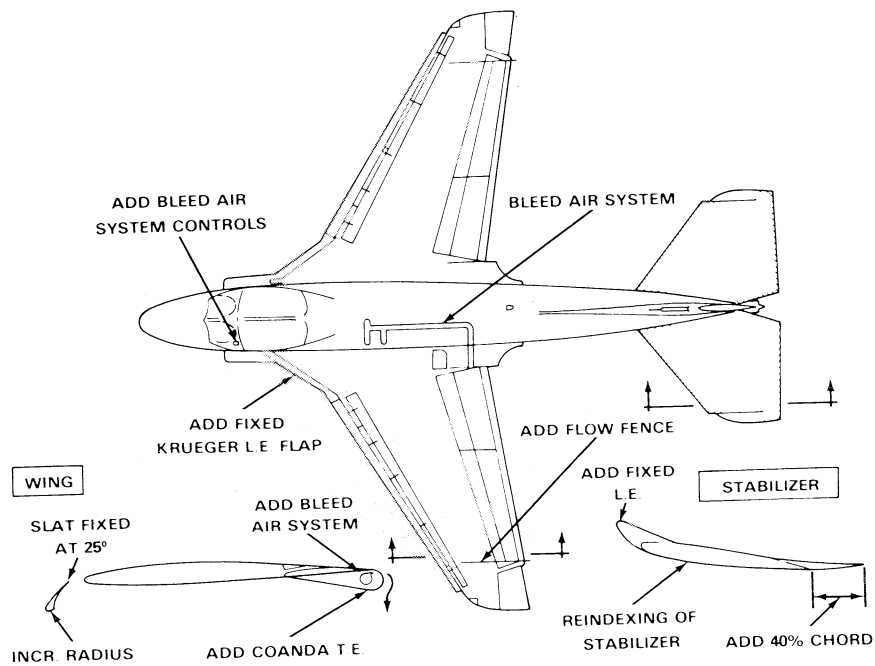
REINDEXING OF
STABILIZER

ADD 40% CHORD

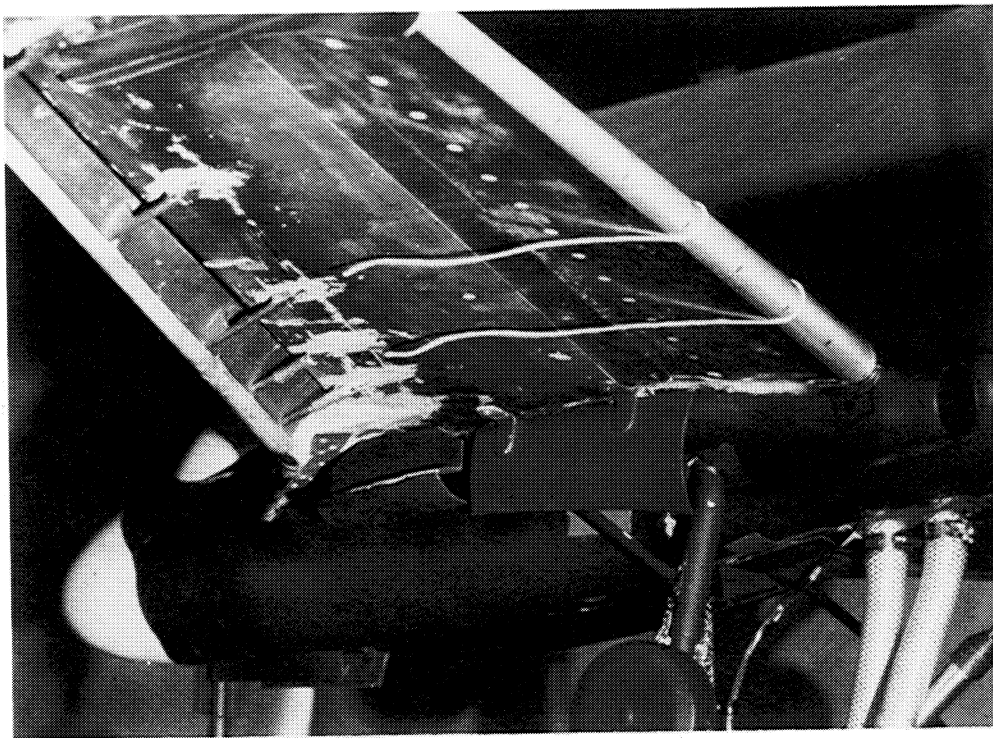Figure 15.- CCW modifications to A-6A aircraft.

Figure 16.- Tufts showing jet turning on A-6/CCW model. Wind off.

Figure 17.- Trimmed-lift data for the A-6/CCW model.
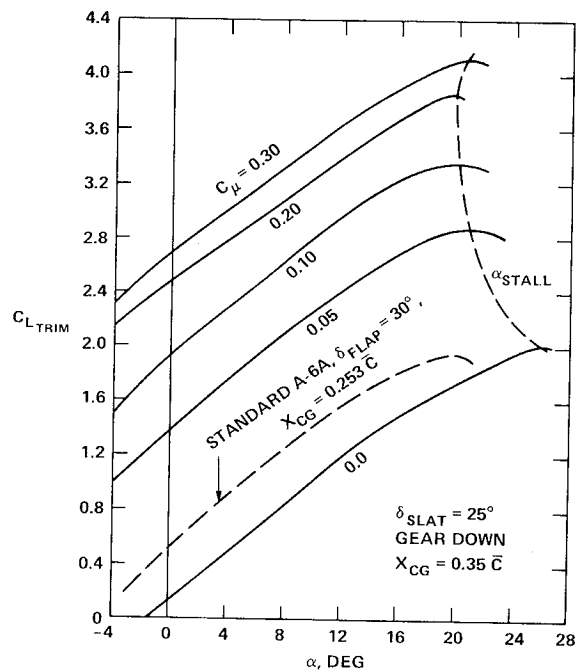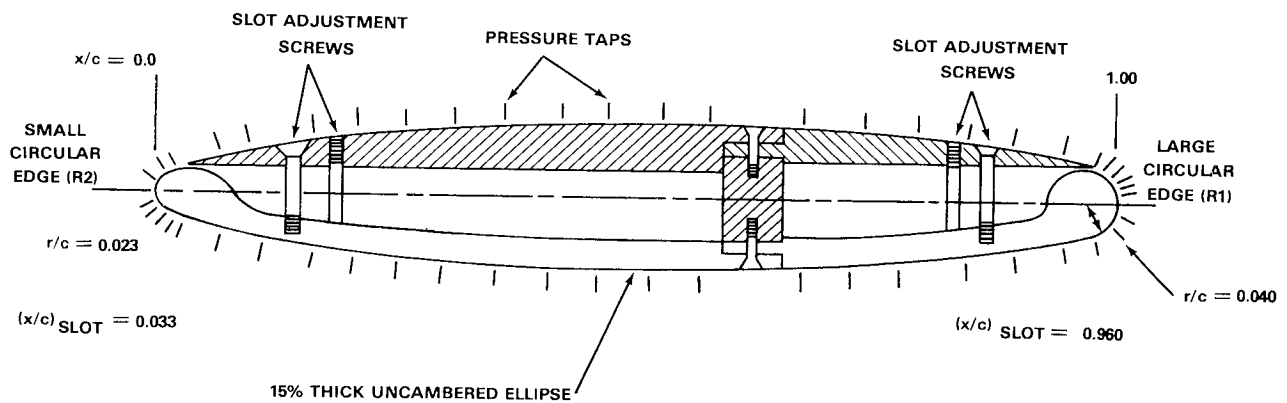

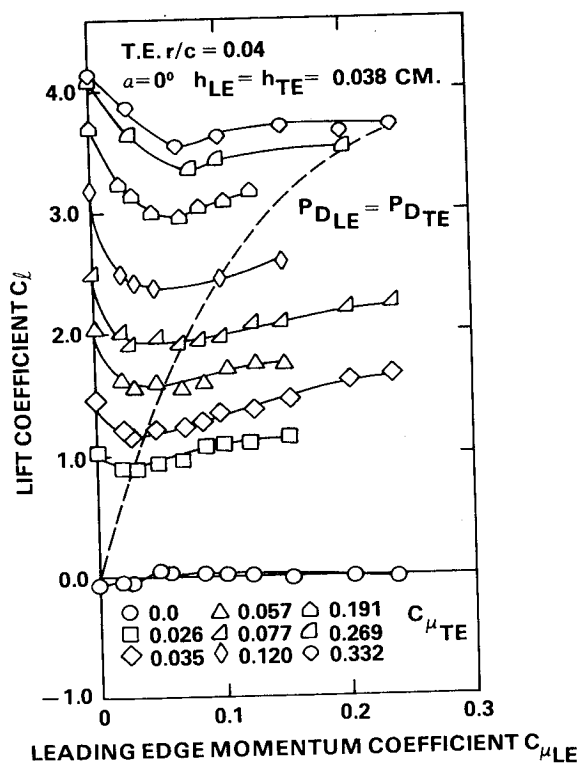
Figure 18.- Dual-slotted CC airfoil.

T.E. r/c = 0.04
$a = 0°$ $h_{LE} = h_{TE} = 0.038$ CM.

$P_{D_{LE}} = P_{D_{TE}}$

$C_{\mu_{TE}}$		
○ 0.0	△ 0.057	⬠ 0.191
□ 0.026	◁ 0.077	⬡ 0.269
◇ 0.035	◇ 0.120	◇ 0.332

LEADING EDGE MOMENTUM COEFFICIENT $C_{\mu_{LE}}$

Figure 19.- Lift variation for dual-slotted CC airfoil.
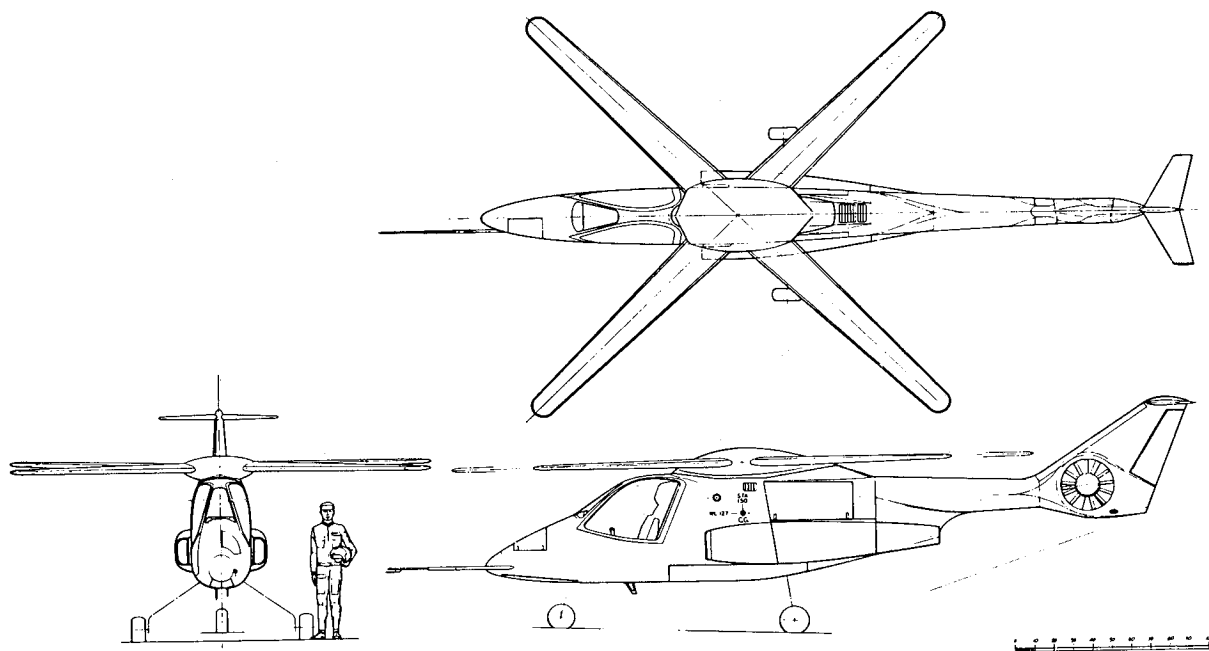
Figure 20.- General arrangement of X-wing demonstrator aircraft.

ROOT SECTION

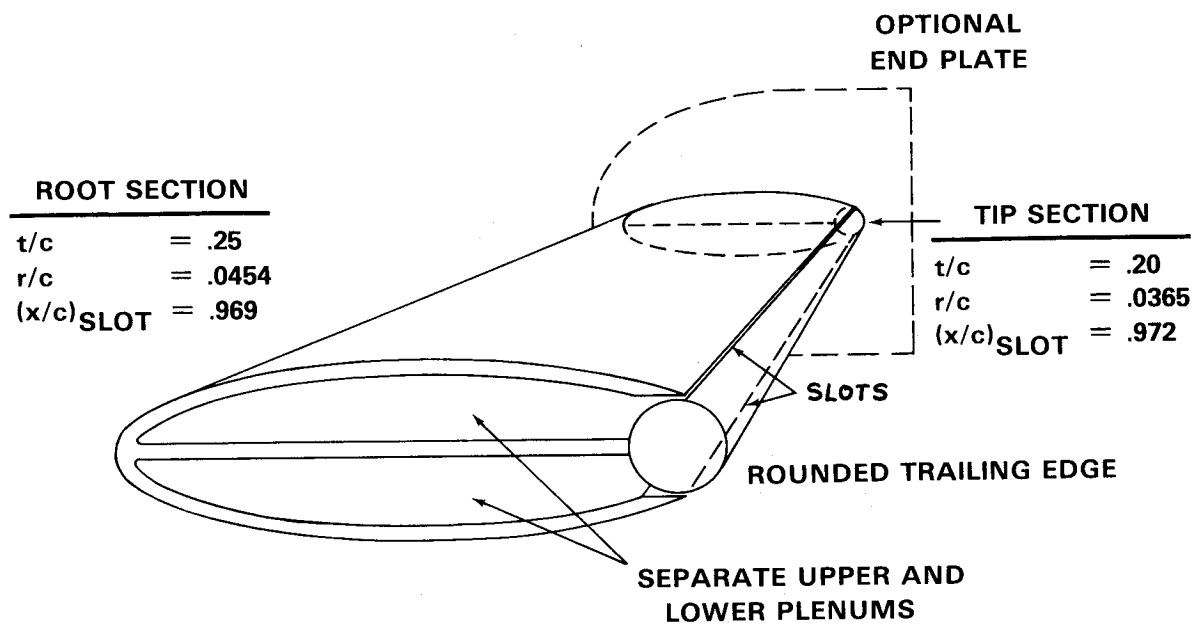|	
t/c	= .25
r/c	= .0454
$(x/c)_{SLOT}$	= .969

OPTIONAL END PLATE

TIP SECTION

t/c	= .20
r/c	= .0365
$(x/c)_{SLOT}$	= .972

SLOTS

ROUNDED TRAILING EDGE

SEPARATE UPPER AND LOWER PLENUMS

Figure 21.- Dual-plenum submarine stern-plane model.

	CIRCULAR T.E.	MODIFIED T.E.
C_ℓ	3.042	2.802
C_d	−0.035	−0.054
C_m	−0.984	−0.901

$C_\mu = 0.11, \alpha = -2°$

CIRCULAR T.E.

MODIFIED T.E.

$-C_p$

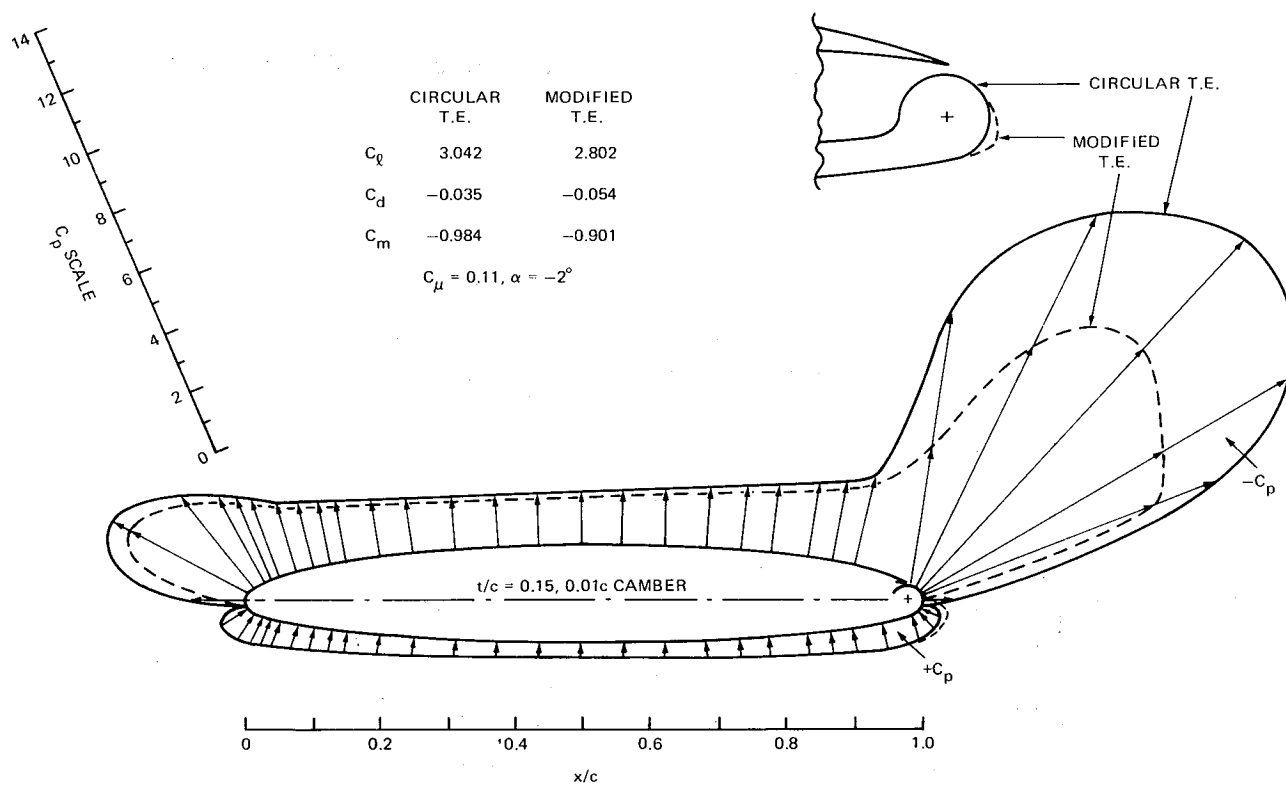t/c = 0.15, 0.01c CAMBER

$+C_p$

x/c

Figure 22.- Normal pressure distribution on improved subsonic CC airfoil.

SLATTED AIRFOILS FOR AGRICULTURAL AIRCRAFT

Karl H. Bergey and R. Leon Leonard
Aerospace, Mechanical and Nuclear Engineering
University of Oklahoma

Agricultural aviation has a number of distinctions. It is important to the economy, it is dangerous, and it is growing at a rapid rate.

Figure 1 shows the farm receipts for a five year period from 1970 to 1974. It also shows the growth in agricultural aviation during that period of time. Clearly all the indicators are up. In addition, the variety of ag aircraft in use has never been wider, ranging from modified J-3 Cubs to large turbo-prop-powered aircraft that sell at prices above $200,000.

One of the largest of these agricultural aircraft is the Rockwell S-2R, shown in figure 2. As with other modern ag aircraft, the design is tailored specifically for crash protection, featuring a strong turn-over structure, a 40-g cockpit, a forward-located hopper to absorb energy in a crash, and a well-designed pilot restraint system.

Accident statistics show that these features have been effective in protecting pilots. Figure 3 shows the accident and fatality rate for the complete general aviation population. As one might expect, the accident rate for agricultural aviation is relatively high, five times that of business and corporate flying, and about the same as pleasure flying. The fatality rate, on the other hand, is only about two times as high as the business and corporate fatality rate and only 40% of the pleasure flying fatality rate. What this means is that an ag pilot is 2 1/2 times more likely to live through a crash than you and I are in conventional general aviation aircraft.

Even so, more can be done to improve the safety of agricultural aviation. Ag aircraft operate in a demanding environment and in flight regimes that are probably more critical than those of any other commerical operations. Clearly the safety and utility of agricultural aircraft should be improved if stall speeds were to be reduced and stall characteristics rendered more innocuous. In addition, improvements in payload, fuel efficiency, and take off and landing distances are desirable for all good and familiar reasons.

Leading edge slats have the potential for providing many of the above benefits without degrading other critical performance characteristics.

About two years ago, the University of Oklahoma proposed a slat development program to Rockwell International for application to their S-2R Thrush agricultural airplane. Rockwell agreed to fund the development program and, after some discussion, a decision was made to concentrate on fixed leading edge slats to be fitted to the existing airfoil (NACA 4412). For this particular application, fixed slats are preferable to automatic or movable slats

because of their reliability, their low cost, and their potential for retrofit to airplanes in the field. The major disadvantage, high speed drag, is relatively unimportant for agricultural aircraft. Gordon McMahon, project engineer on the S-2R airplane for Rockwell, and Richard Brummett, chief of aerodynamics for the General Aviation Division of Rockwell, were involved in this decision and played an active role throughout the project.

Part way through the slat program, NASA initiated its agricultural aviation program. Since many of the goals were similar, it seemed reasonable to make common cause on this particular development, and the S-2R slat program became a joint effort between the University of Oklahoma, Rockwell International, and NASA. The NASA contribution included a test of the prototype airplane in the full-scale NASA-Langley tunnel.

At the time of this conference, the S-2R test airplane is installed in the full-scale tunnel and testing is to begin next week (March 13, 1978).

Returning to the start of the project, the question immediately arose; how do you start the design of an add-on fixed slat system that will improve take-off, landing, and turning performance without significantly reducing the maximum rate-of-climb or degrading handling characteristics?

The answer is very simple. As with almost every other aircraft design project, the first thing to do is to consult the NACA/NASA indexes. Fortunately, during the 1920's and 1930's, NACA researchers had carried out an extensive series of tests on a variety of slat shapes and locations. We identified a total of 32 pertinent references. Of these, five Reports and Notes were particularly helpful and are listed as references 1 through 5. Using these reports, we attempted to separate the effects of various slat geometry parameters. From this information, we generated what appeared to be an optimum slat shape; that is, one that was compatible with the NACA 4412 section, and one that would provide good high lift characteristics without unacceptably high drag in the critical climb regime. This initial configuration is shown in figure 4.

At the same time, we were in touch with Ray Hicks and Larry Olson at NASA-Ames, both of whom were working on analytical programs to calculate the pressure distribution over airfoil sections. Larry Olson volunteered to run our preliminary slat shape and location on the multi-element program he was then developing. As part of his investigation, he checked various slat positions and several cut-away shapes on the underside of the slat. The purpose of these latter shape variations was to determine whether a simple "thin" slat might be aerodynamically acceptable. The potential improvement in cost, weight, and overall simplicity is apparent.

Dr. Olson ran both potential and viscous flow solutions, as shown in figure 5. Although the absolute value of the lift coefficients for the viscous flow solutions were higher than one might expect in practice, the ratios between the plain airfoil and the slatted airfoil appeared to confirm our earlier estimates. In addition, the preliminary choice of slat shape and location based on the early NACA tests appeared to be very close to an optimum for our

purposes. It was apparent, of course, that higher lift coefficients could be obtained by lowering the slat relative to the wing, but this change tended to increase the drag at lift coefficients corresponding to climb conditions. It was also apparent that larger slats extending futher ahead of the basic airfoil would increase the effective wing area and therefore the total lift. Unfortunately, this approach tends to move the wing center of pressure forward, and thus decreases the airplane's static margin.

The NASA-Ames calculations also showed that there was very little change in normal force characteristics as a result of cutting away the under-surface of the slat.

A further benefit of the analysis was to show the fractional load on the slat. As shown in figure 6, the slat accounts for up to 30% of the total lift of the wing at high angles of attack. This information was particularly useful for stress analysis of both the wind tunnel model and the prototype slat system.

Figure 7 shows lift coefficient and drag coefficient versus angle of attack for the standard Rockwell S-2R airplane and for the S-2R airplane equipped with fixed leading edge slats (ref. 6). Note that the cross-over point for the two drag coefficient curves occurs at an angle-of-attack of approximately 8° and at a lift coefficient of approximately 0.8. This corresponds to the best rate of climb conditions for the airplane at high gross weights. Another potential advantage of the slat system is apparent from the graph. By limiting elevator authority, it is possible to make the slatted airplane essentially stall-proof while retaining most of the benefits of the increased lift coefficient.

Figure 8 shows the relative performance of the standard and slatted aircraft. The approved gross weight for the S-2R under FAR 23 requirements is 6000 pounds. Part 8 of the regulations permits agricultural aircraft to be flown at even higher gross weights, and it is no secret that the S-2R is sometimes flown at very high weights indeed. It is therefore important that the performance be checked at representative overloads. The results of the performance analysis showed that there would be significant improvements in stall speed, take-off distance, and time to turn. Specifically, calculations showed that the stall speed of the S-2R with slats would be reduced by 16%, the take-off ground run by 27%, and the time for a 360 degree turn by 12%. The climb performance would remain essentially the same, and the top speed would be reduced by approximately 3%.

As a part of the development program, wind tunnel tests of a one-fifth scale model were carried out in the University of Oklahoma four-by-six foot tunnel. Both the "thick" and "thin" slats were tested. Their contours are shown in figures 9 and 10. The half-span reflection plane model is shown in figure 11. A majority of the tests were carried out at a dynamic pressure q of 25.6 psf, which corresponds to a Reynold's number of approximately 1.5×10^6. A typical plot of the data is shown in figure 12 (ref. 7).

The results confirmed the NASA-Ames conclusion that the "thin" slat is as good or better than the conventional "thick" slat. Both slats, however, showed

a smaller lift-coefficinet increment ΔC_L than had been expected. We believe this is due to Reynold's number effects. Subsequent flight testing has tended to confirm this conclusion.

As a result of the wind tunnel test program, a decision was made to proceed with the "thin" slat design. To simplify manufacture and the replacement of damaged slats in the field, the installation consists of four slats per side, each approximately 64 inches long (ref. 8). Figure 13 shows the slats installed on the test airplane. The first flight tests were run with only the two outboard slats in place. Since there was no handling or stall problems, the full slat system was installed and the flight tests continued. Unfortunately, the flight tests were limited by a need to fly the airplane to Langley Field in time for preparation and installation in the full-scale tunnel. It was possible, however, to draw some conclusions from the limited flight tests.

1. The measured increase in lift coefficient was approximately 0.30 and was limited by elevator travel rather than by wing stall. It appears that the original estimates shown in figure 8 were essentially correct.

2. At the most forward center of gravity, the static longitudinal and directional stability were both satisfactory.

3. At a center of gravity position of 26.5% mac, the power off stability was satisfactory but the power-on stability in climb was negative at all speeds below trim speed. As noted before, the addition of fixed slats will tend to move the neutral point forward and thereby decrease the static margin.

4. Several experienced agricultural pilots reported favorably on the airplane's operational potential. All noted the high deck angles at "stall".

As I indicated earlier, the Rockwell S-2R airplane is now in the Langley full-scale tunnel. A number of tests will be run over the next eight to ten weeks, and we are looking forward to further slat optimization based on tests run at full-scale Reynold's numbers. An accurate evaluation of the downwash effects over the tail section will also be helpful in defining elevator limits aimed at reducing the likelihood of stalls in a turn.

The crashworthiness features now incorporated in most modern agricultural aircraft have saved hundreds of lives during the past 15 years. We expect that fixed slat systems, through improved performance and more docile handling characteristics, could have an equally important effect on agricultural aviation operations in the future.

REFERENCES

1. Weick, F.E. and Wenzinger, C.J., "The Characteristics of a Clark Y Wing Model Equipped with Several Forms of Low-Drag Fixed Slots", NACA TR 407, 1931.

2. Bamber, M.J., "Wind Tunnel Tests of Several Forms of Fixed Wing Slot in Combination with a Slotted Flap on an NACA 23012 Airfoil", NACA TN 702, 1939.

3. Wenzinger, C.J. and Shortal, J.A., "The Aerodynamic Characteristics of a Slotted Clark Y Wing as Affected by the Auxiliary Airfoil Position", NACA TR 400, 1931.

4. Weick, F.E. and Shortal, J.A., "The Effect of Multiple Fixed Slots and a Trailing Edge Flap on the Lift and Drag of a Clark Y Airfoil", NACA TR 427, 1932.

5. Weick, F.E. and Platt, R.C., "Wind Tunnel Tests on Model Wing with Fowler Flap and Specially Developed Leading Edge Slot", NACA TN 459, 1933.

6. Bergey, K.H. and Leonard, R.L., "Wind Slat Development Program, Rockwell S-2R, Phase I: Analysis and Performance Estimates." University of Oklahoma General Aviation Research Center, Norman, Oklahoma, September, 1976.

7. Leonard, R.L., Bergey, K.H. and Gardner, T.G., "Wing Slat Development Program, Rockwell S-2R, Phase II: Wind Tunnel Test Program." University of Oklahoma General Aviation Research Center, Norman, Oklahoma, August, 1977.

8. Bergey, K.H., Weiss, W.C. and Leonard, R.L., "Wing Slat Development Program, Rockwell S-2R, Phase III: Prototype Design and Installation." University of Oklahoma General Aviation Research Center, Norman, Oklahoma, August, 1977.
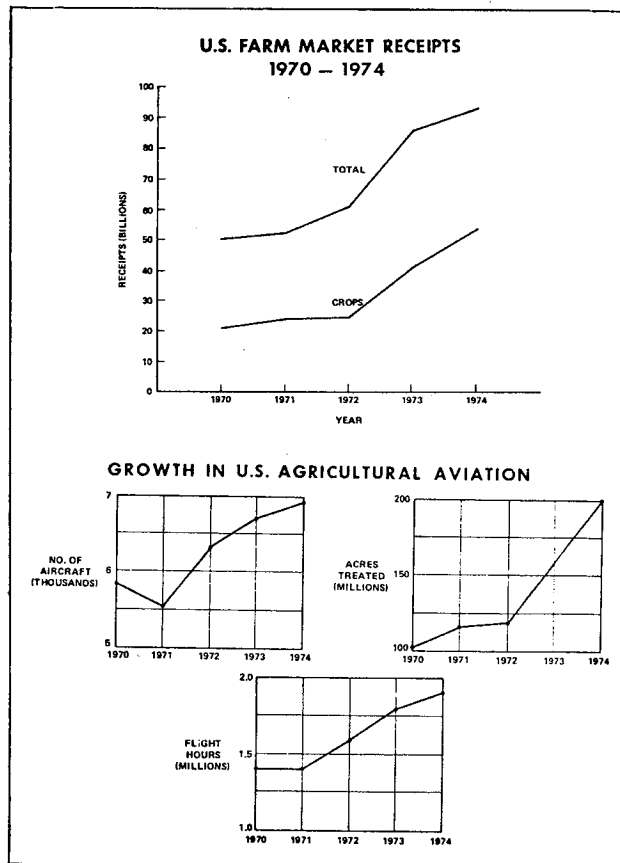
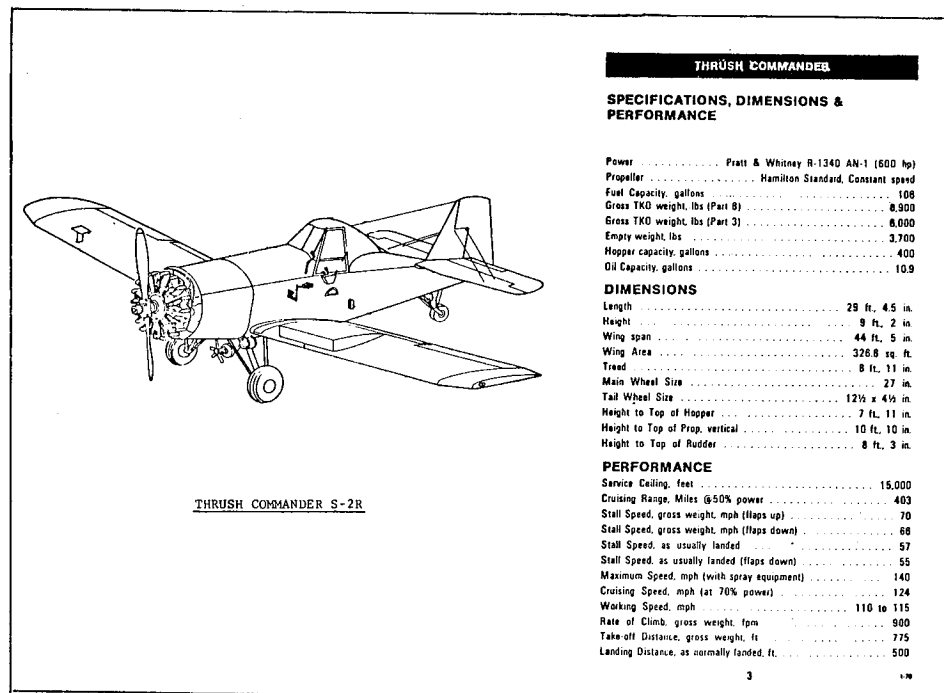Figure 1.- Farm receipts and agricultural aviation history.
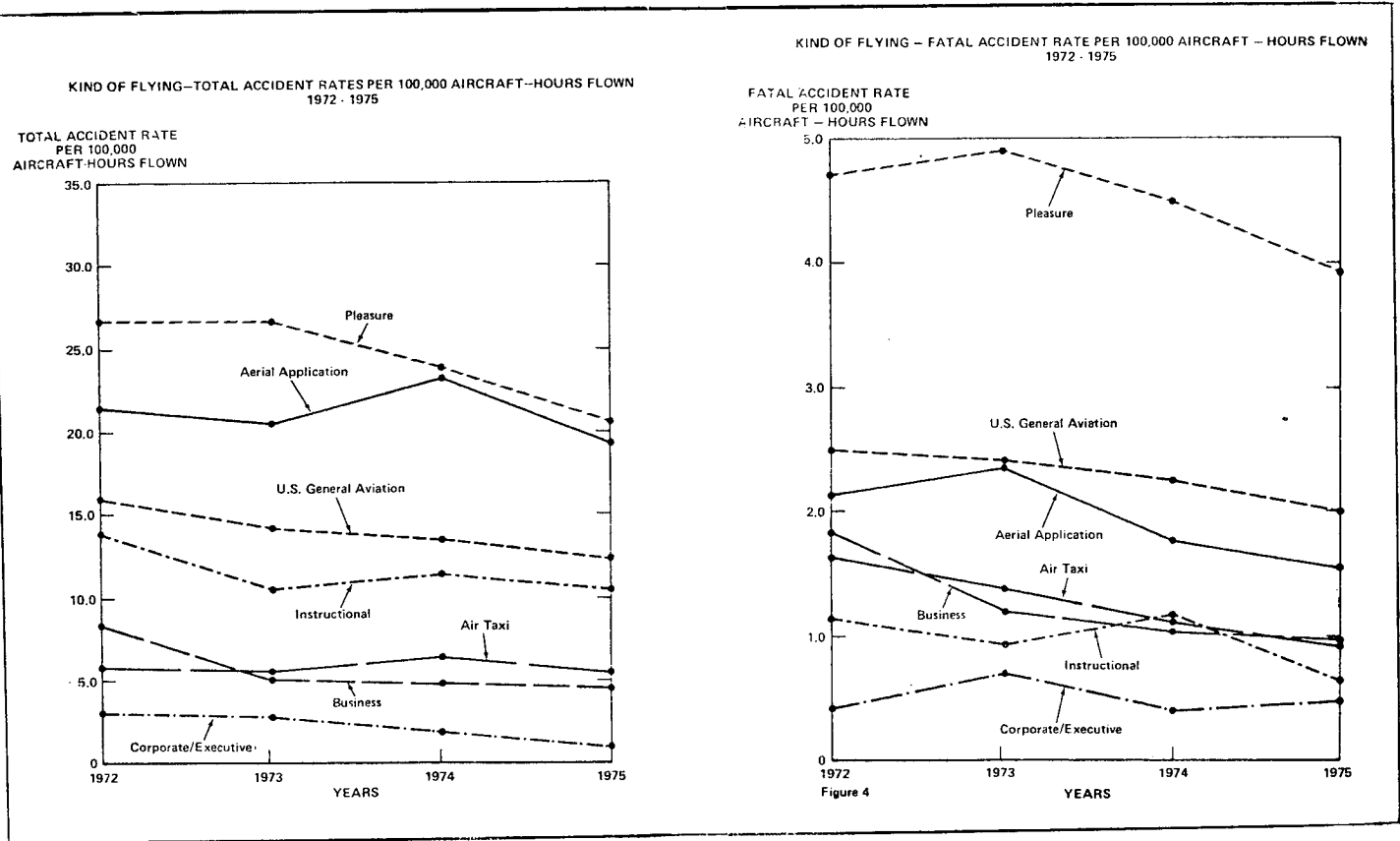

Figure 2.- Thrush Commander characteristics.

KIND OF FLYING—TOTAL ACCIDENT RATES PER 100,000 AIRCRAFT--HOURS FLOWN
1972 - 1975

TOTAL ACCIDENT RATE
PER 100,000
AIRCRAFT-HOURS FLOWN

FATAL ACCIDENT RATE
PER 100,000
AIRCRAFT – HOURS FLOWN

Figure 3.- Accident history.
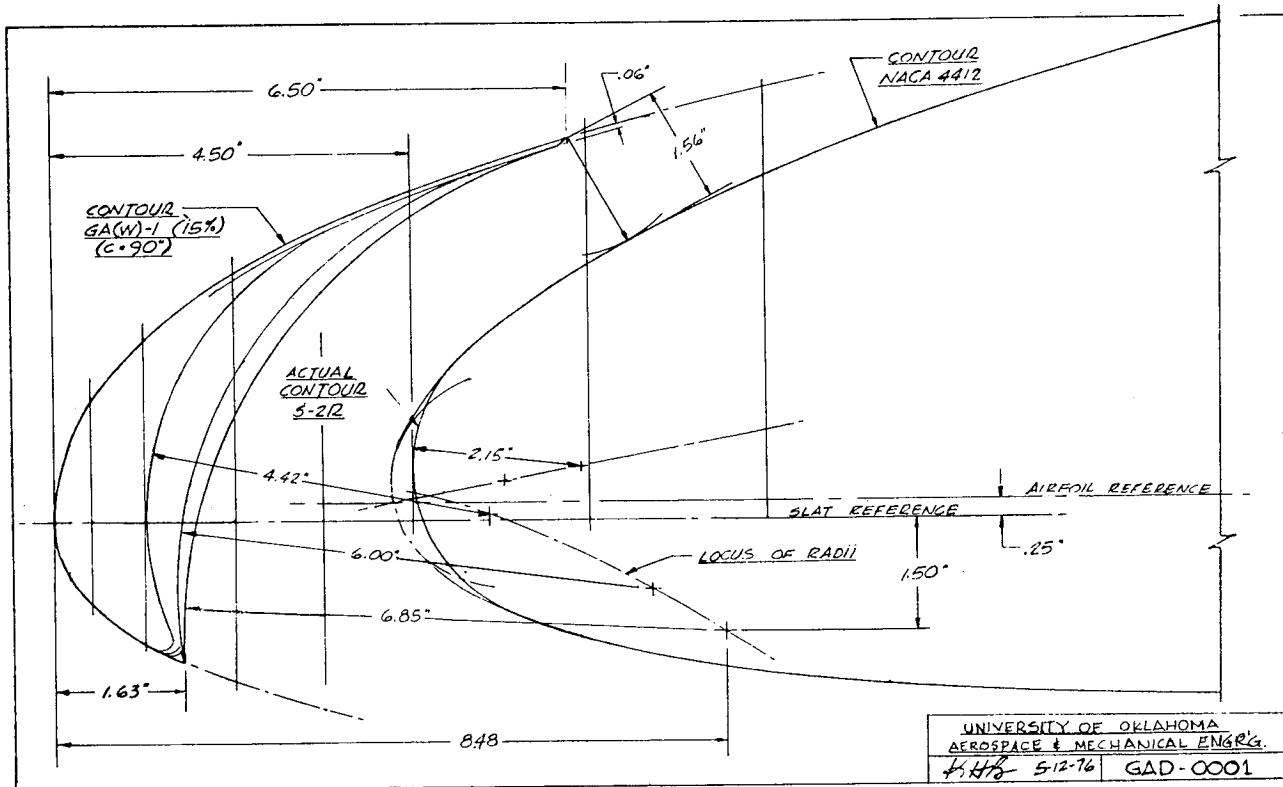
Figure 4.- Initial slat configuration.

UNIVERSITY OF OKLAHOMA
AEROSPACE & MECHANICAL ENGR'G.
5-12-76   GAD-0001
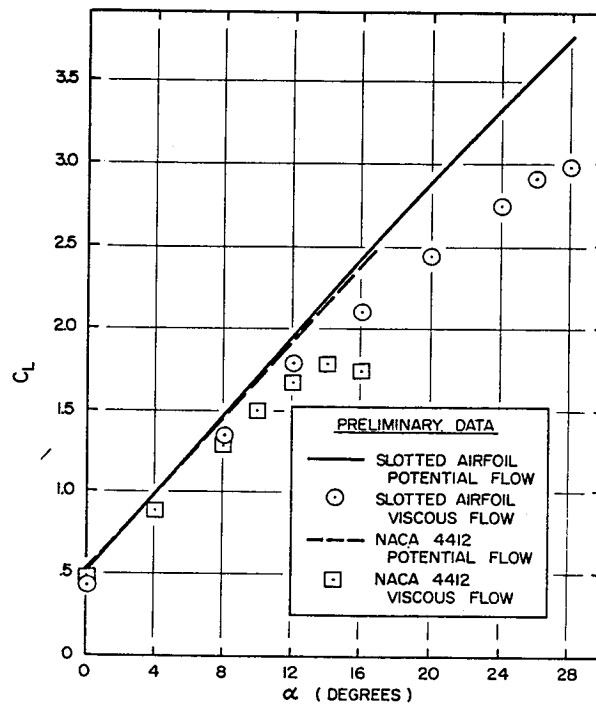
Figure 5.- Calculated lift curves with and without slats where α denotes angle of attack and C_L denotes lift coefficient.
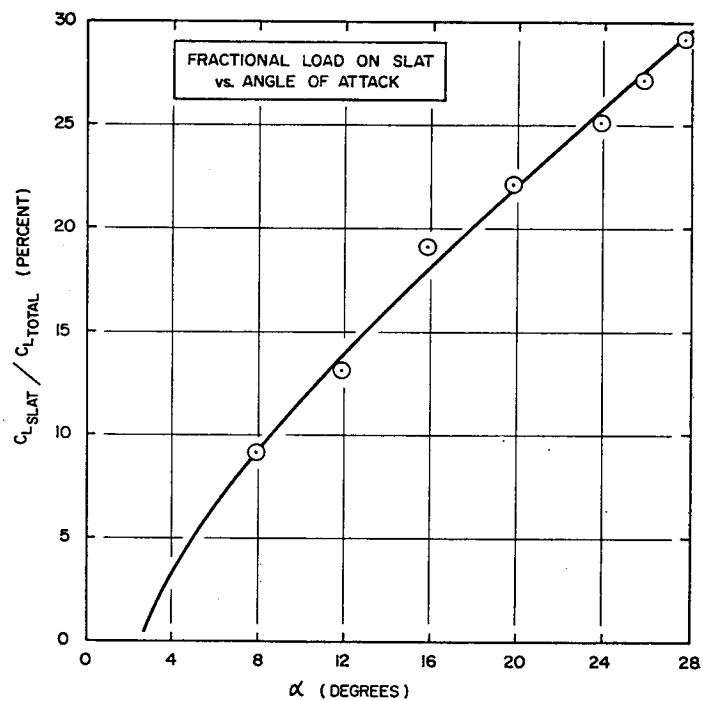
Figure 6.- Fractional load on slat.
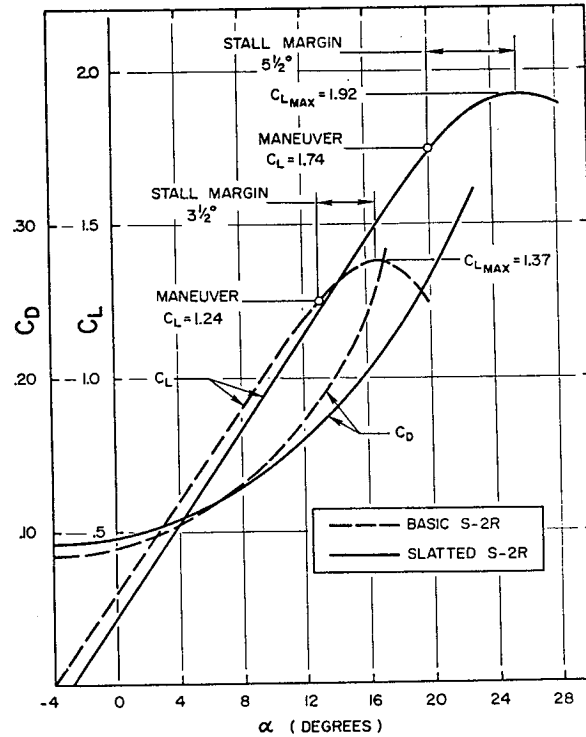
Figure 7.- Effect of fixed leading-edge slat on Thrush Commander lift C_L and drag C_D characteristics.

RELATIVE PERFORMANCE
STANDARD S-2R vs SLATTED S-2R
AT THREE WEIGHTS

WEIGHT	6000#		8500#		10,000#	
CONFIGURATION	STD.	SLATS	STD	SLATS	STD	SLATS
STALL SPEED (flaps up)(mph)	72.5	61.2	86.3	72.3	93.5	78.9
STALL SPEED (flaps 28°)(mph)	69.0	59.3	82.1	70.6	89.0	76.6
MAXIMUM SPEED (mph)	142	138	137	133	132	129
RATE-OF-CLIMB (fpm)	1380	1390	695	700	410	425
SPEED FOR BEST R/C (mph)	99	94	103	98	107	102
T.O. GROUND RUN (ft)	940	680	2520	1775	3600	2440
DISTANCE TO 50 FT (ft)	1380	1110	4050	3290	8000	7150
RADIUS OF TURN (ft)	460	335	880	650	1630	1345
TIME TO TURN (sec)	19.2	16.8	36.7	32.5	68.3	62.7
ANGLE OF BANK (deg)	57.0	55.5	38.6	37.0	23.2	22.7

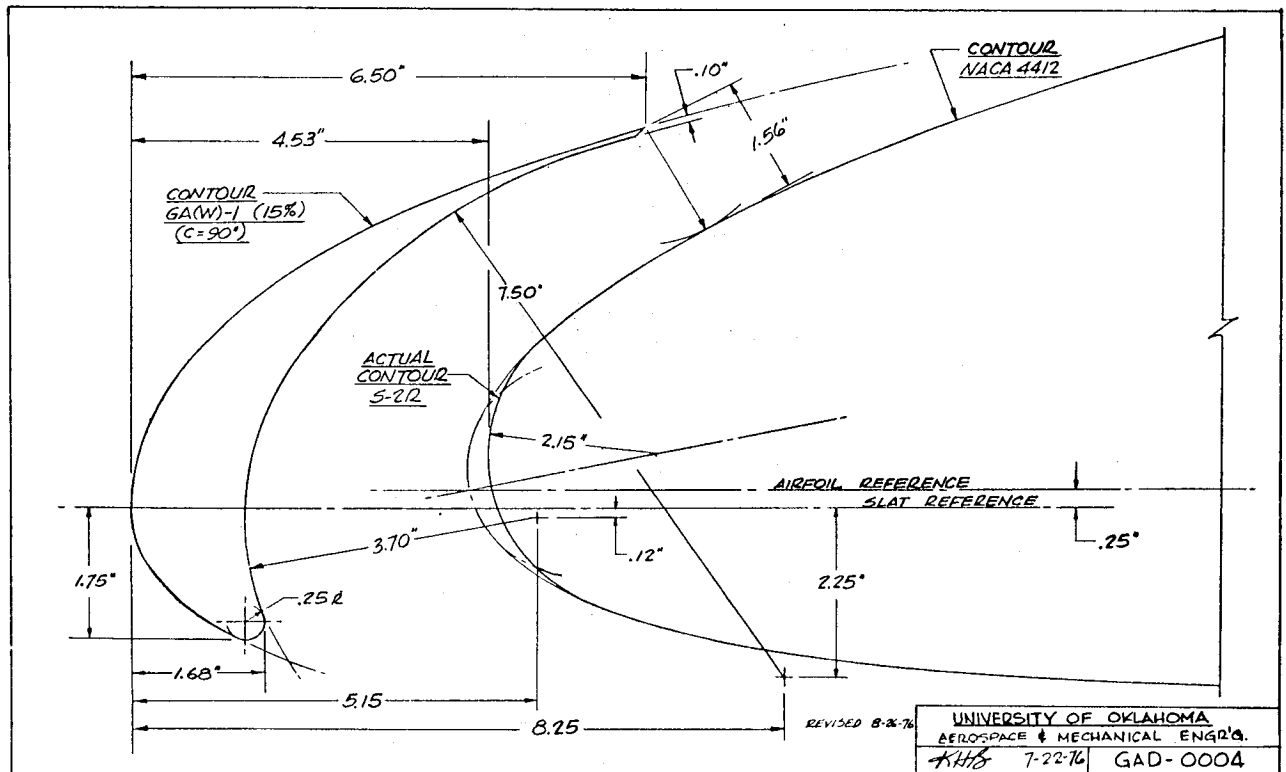Figure 8.- Effect of fixed slat on Thrush Commander performance.

197

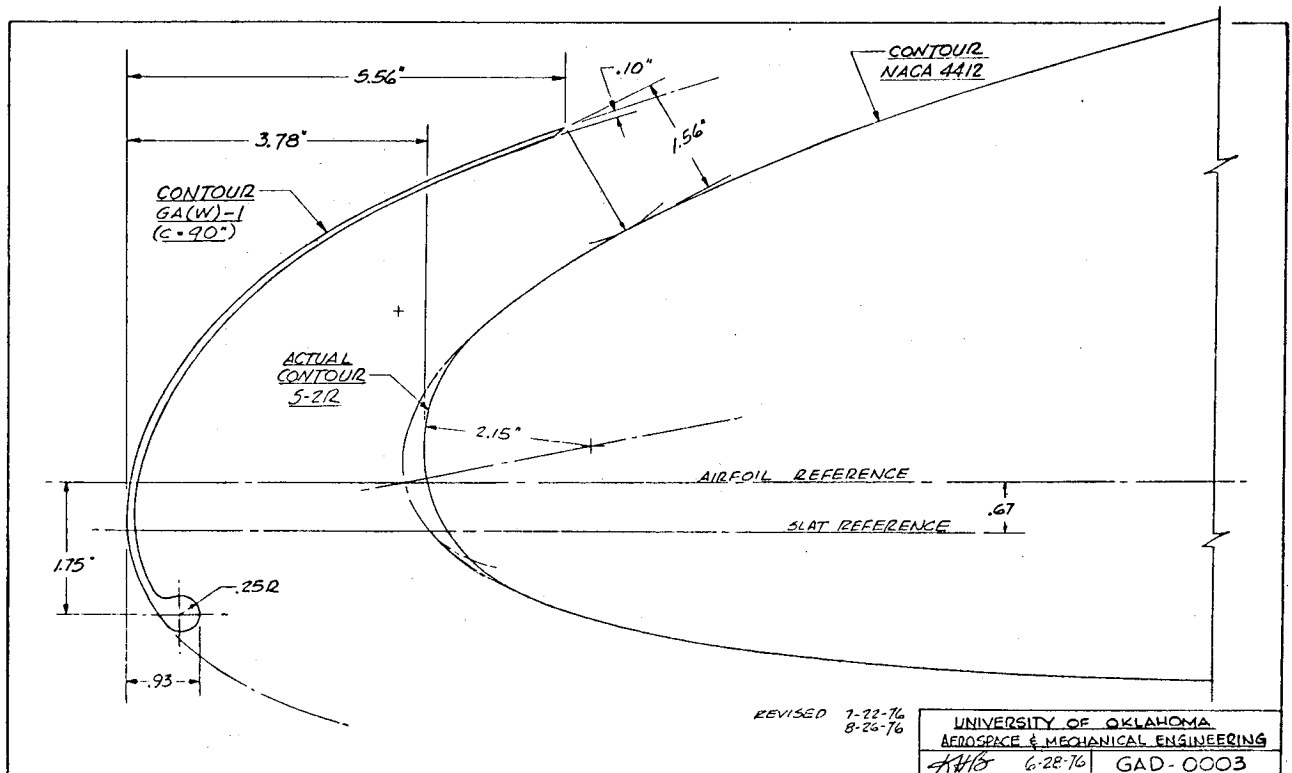Figure 9.- Proposed thick-slat design where c denotes chord.
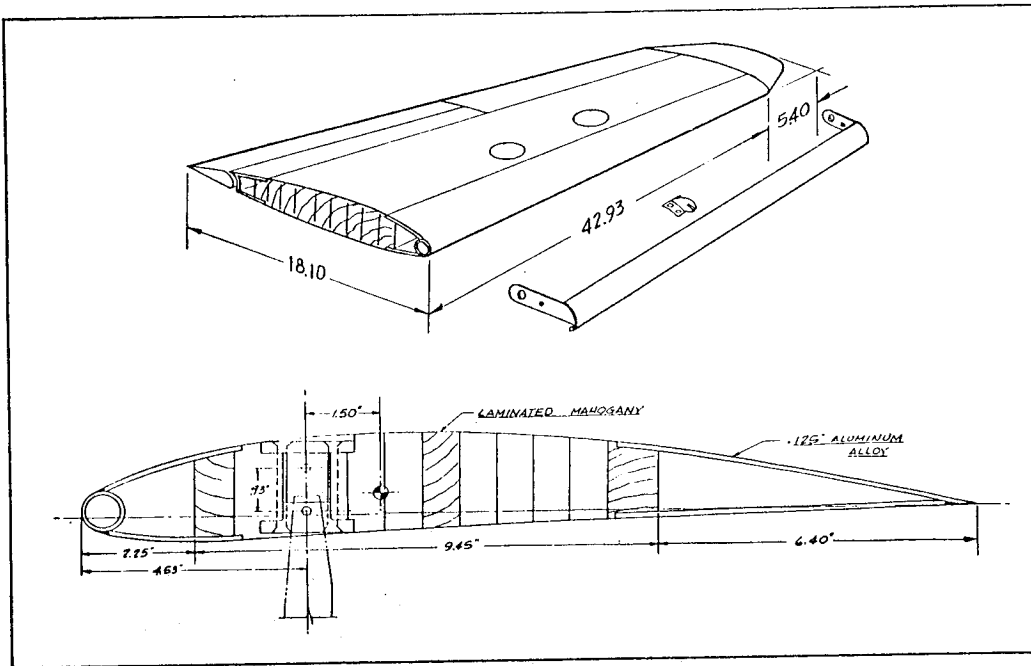

Figure 10.- Proposed thin-slat design.

198

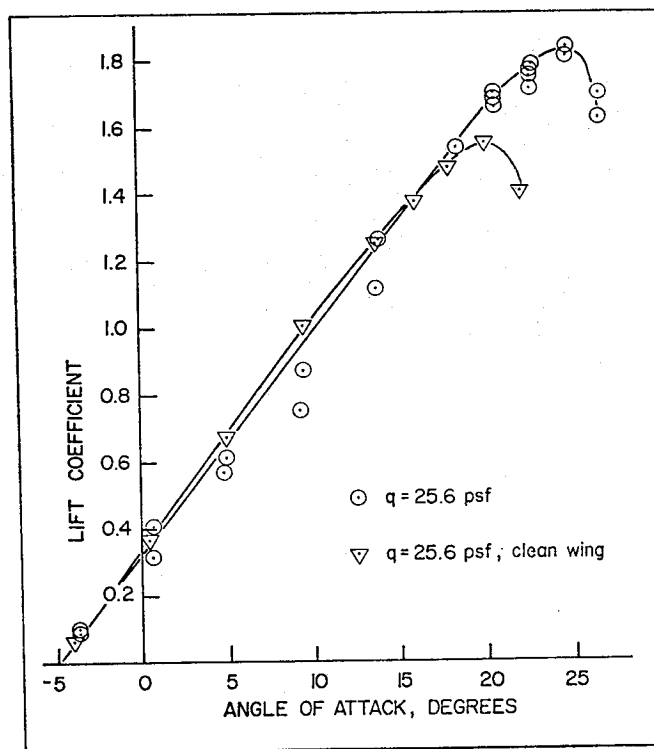Figure 11.- Reflection-plane model dimensions.

Figure 12.- Measured lift characteristics with reflection-plane model.

Figure 13.- Thin slats installed on Thrush Commander.

SHOCK OSCILLATION AND PRESSURE FLUCTUATION MEASUREMENTS

ON SUPERCRITICAL AND CONVENTIONAL AIRFOILS[*]

Frederick W. Roos
McDonnell Douglas Research Laboratories

SUMMARY

Measurements of surface pressure fluctuations and shock wave oscillations have been made as part of an investigation into the detailed nature of transonic airfoil flowfields. Comparable sets of data were taken on both a Whitcomb-type supercritical airfoil and a conventional NACA 0012 section. Emphasis was placed on the ranges of M_∞ and c_l in which transonic buffeting occurred. Standard statistical techniques were employed in the analysis of the unsteady data, with the results serving to reveal the similarities and differences in the way flow unsteadiness and buffeting developed for the two classes of airfoils.

Intense pressure fluctuations on both airfoils were associated with shock wave motion, boundary layer separation, and the presence of upstream-propagating shocklets in regions of nearly-sonic flow. Overall features of fluctuating pressure power spectra were similar for the two airfoils, but power spectra of lift fluctuations and shock oscillations in buffeting showed some definite differences between the two types of sections. The oscillating shock wave was discovered to be a much-less-important element of the unsteady flowfield for the supercritical airfoil than for the conventional section. This difference was related to differences in the upper-surface pressure distributions developed by the two airfoils.

INTRODUCTION

Transonic buffeting continues to be a limiting factor in the maneuverability of combat aircraft. Correspondingly, there continues to exist appreciable interest and activity in the study of transonic buffeting (refs. 1 and 2). McDonnell Douglas Research Laboratories has been involved in an investigation of transonic airfoil aerodynamics in a cooperative effort with the Douglas Aircraft Company and the Ames Research Center of NASA. One element of this program has been research into the unsteady aerodynamics responsible for buffeting. The initial series of experiments dealt exclusively with a Whitcomb-type supercritical airfoil; details of these tests have already been reported (refs. 3 and 4). More recently, further measurements were made in the

---

unsteady flowfield of the supercritical airfoil, and corresponding tests were performed on a conventional airfoil to provide a basis of comparison for the supercritical data. Results of these recent experiments will be discussed here. The symbols used herein are defined in an appendix.

EXPERIMENTAL SETUP AND PROCEDURES

The two airfoil sections studied during these experiments are illustrated in figure 1. The DSMA 523 section is identical to Whitcomb's original one-piece supercritical airfoil (ref. 5); the particular model tested was modified to have a 1% thick trailing edge to permit installation of static and dynamic pressure instrumentation in the trailing edge region. The conventional airfoil tested was the NACA 0012 section. Each model had a chord of 15.24 cm.

Experiments were all performed in the NASA-Ames Two- by Two-Foot Transonic Wind Tunnel, a continuous-flow facility. The test section of the tunnel had been modified specifically for the testing of two-dimensional airfoil sections, which spanned the tunnel as shown in figure 2.

Located at mid-span on each airfoil model was a chordwise row of static pressure orifices. Adjacent to the pressure taps on both upper and lower surfaces of the airfoils were installed a number of high-frequency-response, semiconductor strain gage pressure transducers. Signal conditioning equipment for these transducers included an analog summing circuit which allowed the formation of an approximation to the instantaneous lift force.

Additional instrumentation included a high-frequency-response, static pressure-type probe attached to the test section wall for monitoring background disturbances, and a sting-mounted probe traversing unit. The traversing rig was capable of movements in the streamwise and vertical directions, and was used to calibrate and locate an MDRL-developed shock-position sensing probe. A sketch of this probe appears in figure 3, along with a typical in situ calibration curve. The probe is based on hot-film anemometer technology and is operated similarly to an anemometer probe in connection with a standard constant-temperature anemometer unit. The great sensitivity of the probe is evident, as is an ambiguity in shock-position indication resulting from shock excursions upstream of the probe's intended operating range. This ambiguity could have been alleviated had it been possible to construct longer probes, but fabrication and operating problems prevented this. As a result, the shock displacement data were affected by the ambiguity, especially in the heavy buffeting cases (where shock displacement amplitudes tended to be large). However, data analysis procedures included the screening of shock probe data to eliminate those cases that were significantly degraded by the probe ambiguity.

Dynamic data were recorded on FM tape during the wind tunnel tests for later analysis. Digital equipment was employed in the data analysis, which followed standard statistical procedures (ref. 6). Root-mean-square levels of unsteady variables were evaluated, and auto- and cross-correlations were computed. Power spectra were generated by Fourier transformation of autocorrelation functions.

202

RESULTS AND DISCUSSION

Mean Flowfield

The primary differences in the transonic flowfields of the NACA 0012 and DSMA 523 airfoils are evident in figures 4 and 5. Pressure distributions on the conventional NACA 0012 airfoil for a sequence of increasing Mach numbers, at constant lift, are shown in figure 4. The forward location of the shock, the gradual chordwise movement and rapid strength increase of the shock with increasing Mach number, and the strong chordwise pressure gradients are all typical of this type of airfoil. Flow separation, which begins with the appearance of a bubble at the shock foot, extends from the shock to the trailing edge at the highest Mach number.

Figure 5 illustrates the development with increasing lift, at constant Mach number, of the pressure distribution on the supercritical DSMA 523 section. (The constant-lift, increasing-Mach-number series is very similar.) Of particular importance are the substantial aft loading, the mild pressure gradients over much of the upper surface, the moderate shock strengths, and the reaccelerated, nearly-sonic flow downstream of the shock at lower lift coefficient, c_l, levels. Separation appears first at the trailing edge and progresses upstream, having reached the shock for $c_l = 0.91$.

Surface Pressure Fluctuations

Pressure fluctuation intensity on the upper surface of the conventional NACA 0012 airfoil, as a function of increasing Mach number at constant c_l, is shown in figure 6. Unsteadiness of the shock produces the most intense pressure fluctuations, indicated by the peak that shifts downstream somewhat with increasing freestream Mach number, M_∞. The low amplitude of pressure fluctuations upstream of the shock is associated with the limited ability of pressure disturbances generated downstream to penetrate the supersonic zone. Fluctuating pressure intensity downstream of the shock remains low until separation effects appear at the higher Mach numbers.

Corresponding data for the supercritical airfoil are given in figure 7. The M_∞ range and the value of c_l are not identical to those of the previous figure because each airfoil was tested at conditions near a reasonable c_l-M_∞ operating point for that airfoil. Pressure fluctuations on the supercritical section show a shock-related peak and a low intensity upstream of the shock that are similar to the conventional airfoil results, although the extent of the chordwise shock shift is much greater for the supercritical airfoil. While the high-Mach-number buildup of fluctuating pressure intensity aft of the shock results from separation effects, as it did on the conventional airfoil, there appears an unusually-high pressure fluctuation level between the shock and the trailing edge at lower M_∞ on the supercritical airfoil. This is produced by upstream-propagating "shocklets" in the region of nearly-sonic flow pointed out in figure 5. (The shocklet phenomenon is discussed more fully in reference 3.)

To clarify the upper-surface pressure fluctuations in terms of coherence and propagation direction, two-point pressure cross-correlations were used. The cross-correlation coefficient is defined as

$$R_{p_1 p_2}(\tau) = \frac{1}{[\overline{p^2(\vec{x}_1)} \cdot \overline{p^2(\vec{x}_2)}]^{1/2}} \lim_{T \to \infty} \frac{1}{2T} \int_{-T}^{T} p(\vec{x}_1, t) p(\vec{x}_2, t + \tau) dt, \qquad (1)$$

where $\vec{x}_1$ and $\vec{x}_2$ are position vectors of the two points. A typical set of cross-correlations for attached flow on the supercritical airfoil is given in figure 8. The pressure coefficient, C_p, distribution shows a region of nearly-sonic flow downstream of the shock, and the pressure fluctuation, $C_{p_{rms}}$, distribution shows a corresponding region of moderately intense pressure fluctuations. The pressure measured at 90% chord is used as the reference for all cross-correlations. Peak correlation levels are substantial, and are associated with increasingly negative values of time delay τ as the separation between the measuring points is increased. According to the definition of the cross-correlation, the pressure disturbances between the shock and the trailing edge are well-correlated and are propagating upstream at a speed that is consistent with the acoustic mode.

A set of cross-correlations for the supercritical airfoil in heavy buffeting appears in figure 9. The C_p distribution shows flow separation from the shock to the trailing edge, and the $C_{p_{rms}}$ distribution shows that pressure fluctuations are intense over the same region. Values of τ associated with the correlation peaks have the opposite sign in this case, indicating that pressure disturbances are traveling downstream. The low propagation speed indicates a convective mode, and this is substantiated by the cross-correlation between the pressure at 90% chord and downwash fluctuations measured by a hot-film anemometer in the wake just downstream of the trailing edge: a slight peak exists at a value of τ that confirms the convection speed defined by the pressures.

This behavior was true of both airfoils. That is, for either airfoil, whenever the flow was attached from the shock to the trailing edge, the pressure signals in that region propagated upstream acoustically. On the other hand, whenever the flow was separated from the shock to the trailing edge, the pressure disturbances were convected downstream. An unusual case, presented in figure 10, appeared in the NACA 0012 data. Although the C_p distribution indicates that flow was attached, some intermittent separation must have existed, for the cross-correlations show evidence of both the upstream and downstream modes.

Shock Oscillations

Shock oscillation amplitude data $((x_s/c)_{rms}$, where x_s is shock displacement and c is airfoil chord) for the NACA 0012 airfoil are given in figure 11, where they are compared with lift fluctuation levels and with the trailing edge pressure coefficient, a commonly-used indicator of flow separation effects.

All three variables are consistent in identifying the onset of flow separation and buffeting.

In contrast, the variables show no consistency in the case of the supercritical airfoil (fig. 12), whereas $C_{p_{te}}$ does correctly identify the appearance of flow separation effects such as drag rise (see figure 13), the shock oscillation amplitude and unsteady spanwise bending, c_{m_b}, of the airfoil model both show divergence at an appreciably-higher Mach number. (The lift fluctuations, which are not plotted, showed even less of a divergence than c_{m_b}.) This indicates that the supercritical airfoil not only has a higher drag-rise Mach number than do conventional airfoils, but it also can penetrate farther into the drag rise before encountering significant buffeting.

For completeness, it is noted that the high $(x_s/c)_{rms}$ level at the lower Mach numbers in figure 12 is associated with the ease of chordwise shock movement resulting from the low pressure gradients existing in the midchord region.

A distinct difference existed between the supercritical and conventional airfoils in the degree of coupling between shock oscillations and lift force fluctuations. Both airfoils exhibited a characteristic peaking in the unsteady lift power spectrum when M_∞ and/or c_l had been increased to the point where appreciable buffeting existed, as shown in figure 14. Shock oscillation measurements made in the conventional airfoil flowfield showed a pronounced spectral peak at the same frequency as the peak in the unsteady lift spectrum. However, despite the fact that the shock oscillation amplitude in the supercritical airfoil flowfield increased significantly with the development of buffeting, the shock displacement power spectrum showed no tendency to develop a peak corresponding to the peak in the unsteady lift spectrum. The cross-correlations of shock oscillation with unsteady lift, given in figure 15, reinforce this, the (negative) peak being definitely stronger for the conventional airfoil, even though the buffeting is less intense. Also evident in figure 15 is a greater periodicity to the shock:lift correlation in the case of the conventional section.

Correlation of Pressure and Lift Fluctuations

To properly characterize the buffeting process, it is necessary to establish which regions of the pressure field are, and which are not, significant contributors to the lift force fluctuations, as it is the latter that usually act as the forcing function in the buffeting of an aerospace vehicle (although pitching moment fluctuations are also, or alternatively, responsible for producing buffeting in some cases, according to reference 7). This was accomplished through study of cross-correlations of the various pressures measured on the airfoil upper surface with the unsteady lift force acting on the airfoil.

A space-time cross-correlation map representing high-M_∞ buffeting of the NACA 0012 airfoil is shown in figure 16. For the purpose of interpreting this map, it can be considered as an x-t diagram of the averaged pressure disturbances that correlate with the unsteady lift. It is important to realize that

the function plotted is in coefficient form, i.e., the cross-correlation has been normalized by the root-mean-square of the two correlated variables (as was indicated in equation (1)).

Several features of figure 16 are both prominent and highly important. To begin with, it is quite evident that only the pressures from about 25% chord back to the trailing edge are significant in terms of input to buffeting. It should be noted that, owing to sign conventions on pressure and c_l, a positive pressure change on the upper airfoil surface produces a negative change in lift. Pressure fluctuations near the leading edge not only have a weak correlation with c_l, but are of low intensity as well (figure 6). The pressure fluctuations most highly correlated with c_l are those associated with the chordwise movement of the shock wave and related boundary layer separation in the region of 30% to 40% chord. This is also the region in which the most intense pressure fluctuations are found: the strong shock produces $C_{p_{rms}}$ levels as high as 0.30 in the vicinity of 30% chord (figure 6).

The pronounced periodicity of the pressure:lift correlation is also evident in figure 16. Although randomness in phase and amplitude causes the correlation to damp out rather rapidly as τ increases, it is nevertheless apparent that the correlation exists over at least three cycles in either direction from $\tau = 0$. It should be noted that there is no connection between this periodicity and spanwise bending vibrations of the airfoil model. The frequency appearing in the cross-correlation changes with flow conditions and is always greater than the spanwise bending mode frequency.

Another significant feature of the correlation map is the manner in which the pressure:lift correlation develops away from the shock region. The convention used in this correlation is such that $\tau > 0$ means a delay of the lift force relative to the pressure, so the correlation map shows that the strong pressure fluctuations in the shock region occur slightly before the related changes in lift take place. The pressure changes associated with a change in lift are almost exactly in phase from 30% to 60% chord. With increasing chordwise distance away from this region, either up- or downstream, the phase difference grows to almost 180° at the leading and trailing edges of the airfoil. At the trailing edge, the strongest correlation between local pressure and lift fluctuations is not negative but positive, occurring slightly before the negative correlation peak in the shock region. The magnitude and phase of the correlation right at the trailing edge strengthen the suggestion that the flow in this region is a central element of the buffeting process. Upstream of the shock region, the phase change takes place rapidly as a result of the low velocity (relative to the airfoil) of pressure wave propagation in the upstream direction, since these waves must in effect pass around the region of supersonic flow.

A similar space-time cross-correlation map for the supercritical DSMA 523 airfoil is shown in figure 17. This case corresponds to buffeting of the airfoil at high lift ($c_l = 0.91$) and the nominal operating Mach number ($M_\infty = 0.82$). Many similarities exist between this correlation map and that of figure 16 (e.g., the regions of strong correlation near the shock and trailing edge, the phase changes up- and downstream of the shock, and the insignificance of pressure

fluctuations near the leading edge), suggesting that these features are general characteristics of airfoils in transonic flow.

The most striking difference between the two cross-correlation maps is the relative lack of periodicity in the supercritical airfoil correlation, compared to the correlation for the NACA 0012 section. Only one cycle is evident on either side of $\tau = 0$, and these are faint relative to the correlation peak. Lift fluctuations on the supercritical airfoil in buffeting are significantly more random than they are on the conventional airfoil, as was earlier suggested by the broader peak in the DSMA 523 unsteady lift power spectrum in figure 14. One further difference between the two cross-correlation maps is that the negative peak is slightly weaker and the positive peak somewhat stronger for the supercritical airfoil, indicating weaker lift fluctuations but stronger pitching moment fluctuations for that airfoil relative to the conventional section.

CONCLUDING REMARKS

The experimental study of unsteady transonic airfoil aerodynamics reported here has defined several important features of buffet-related transonic airfoil flowfield fluctuations. These tests have established that, for both a conventional and a supercritical airfoil, the surface pressure and lift force fluctuations are associated primarily with the upper-surface shock, the region of separated flow, and the appearance of "shocklets" downstream of the shock. It is also true of both airfoils that pressure disturbances in the important region between the shock and the trailing edge propagate upstream if the flow is attached, but are convected downstream when the flow is separated.

Two principal differences between the airfoils were identified. Compared to the conventional airfoil, the supercritical section shows a reduced tendency to develop buffeting fluctuations as flow separation effects grow; this is especially true as drag divergence is penetrated. When buffeting does develop on the supercritical section, it is decidedly less periodic than it is with the conventional airfoil.

APPENDIX – LIST OF SYMBOLS

C_a unsteady variable $a(t)$ in coefficient form

C_p pressure coefficient, $C_p = (p - p_\infty)/q_\infty$

$C_{p_{crit}}$ pressure coefficient for locally sonic flow

$C_{p_{te}}$ pressure coefficient at trailing edge

c airfoil chord, m

c_d section drag coefficient, $c_d = D/q_\infty c$

c_l section lift coefficient, $c_l = L/q_\infty c$

c_{m_b} unsteady bending moment coefficient, $c_{m_b} = m_{b_{rms}}/M_b$

D drag force per unit span, N/m

f frequency, Hz

L lift force per unit span, N/m

M_∞ Mach number

M_b mean spanwise bending moment at mid-span, m-N

m_b fluctuating spanwise bending moment at mid-span, m-N

P static pressure, N/m^2

q dynamic pressure, $q = \rho U^2/2$

R_{ab} cross-correlation coefficient relating unsteady variables $a(t)$ and $b(t)$,

$$R_{ab}(\tau) = \frac{1}{a_{rms} \, b_{rms}} \lim_{T \to \infty} \frac{1}{2T} \int_{-T}^{T} a(t) \, b(t+\tau) \, dt$$

Re_c Reynolds number, $Re_c = U_\infty c/\nu_\infty$

U streamwise flow speed, m/s

x chordwise distance, m

x_s chordwise displacement of shock, m

ν kinematic viscosity, m^2/s

ρ density, kg/m^3

τ cross-correlation time delay, s

Φ_a power spectral density of unsteady variable a(t),

$$\Phi_a(\omega^*) \equiv \frac{2U_\infty}{\pi c} c_{a_{rms}}^2 \int_0^\infty R_{aa}(\tau) \cos\omega\tau \, d\tau$$

ω^* dimensionless frequency, $\omega^* = 2\pi fc/U_\infty$

$( )_{rms}$ root-mean-square value

$( )_\infty$ freestream value

REFERENCES

1. Unsteady Airloads in Separated and Transonic Flow. Conference Proceedings No. 226, AGARD, April 1977.

2. Aircraft Stalling and Buffeting. Lecture Series No. 74, AGARD, March 1975.

3. Roos, F. W.; and Riddle, D. W.: Measurements of Surface-Pressure and Wake-Flow Fluctuations in the Flow Field of a Whitcomb Supercritical Airfoil. NASA TN D-8443, 1977.

4. Roos, F. W.: Surface Pressure and Wake Flow Fluctuations in a Supercritical Airfoil Flowfield. AIAA Paper 75-66, January 1975.

5. **Whitcomb, Richard T.: Review of NASA Supercritical Airfoils. ICAS Paper No. 74-10, Aug. 1974.**

6. Bendat, J. S.; and Piersol, A. G.: Random Data: Analysis and Measurement Procedures. Wiley-Interscience, 1971.

7. Jones, J. G.: A Survey of the Dynamic Analysis of Buffeting and Related Phenomena. TR 72197, British R.A.E., September 1972.

DSMA 523 Supercritical
(modified with 1%-thick trailing edge)

NACA 0012 Conventional

Figure 1.- Airfoils studied during joint MDRL-DAC-NASA program.

Optical glass
window

Vertical
traversing
rig

Tunnel sting

Monitoring
probe

Instrumentation leads
(both ends of airfoil)
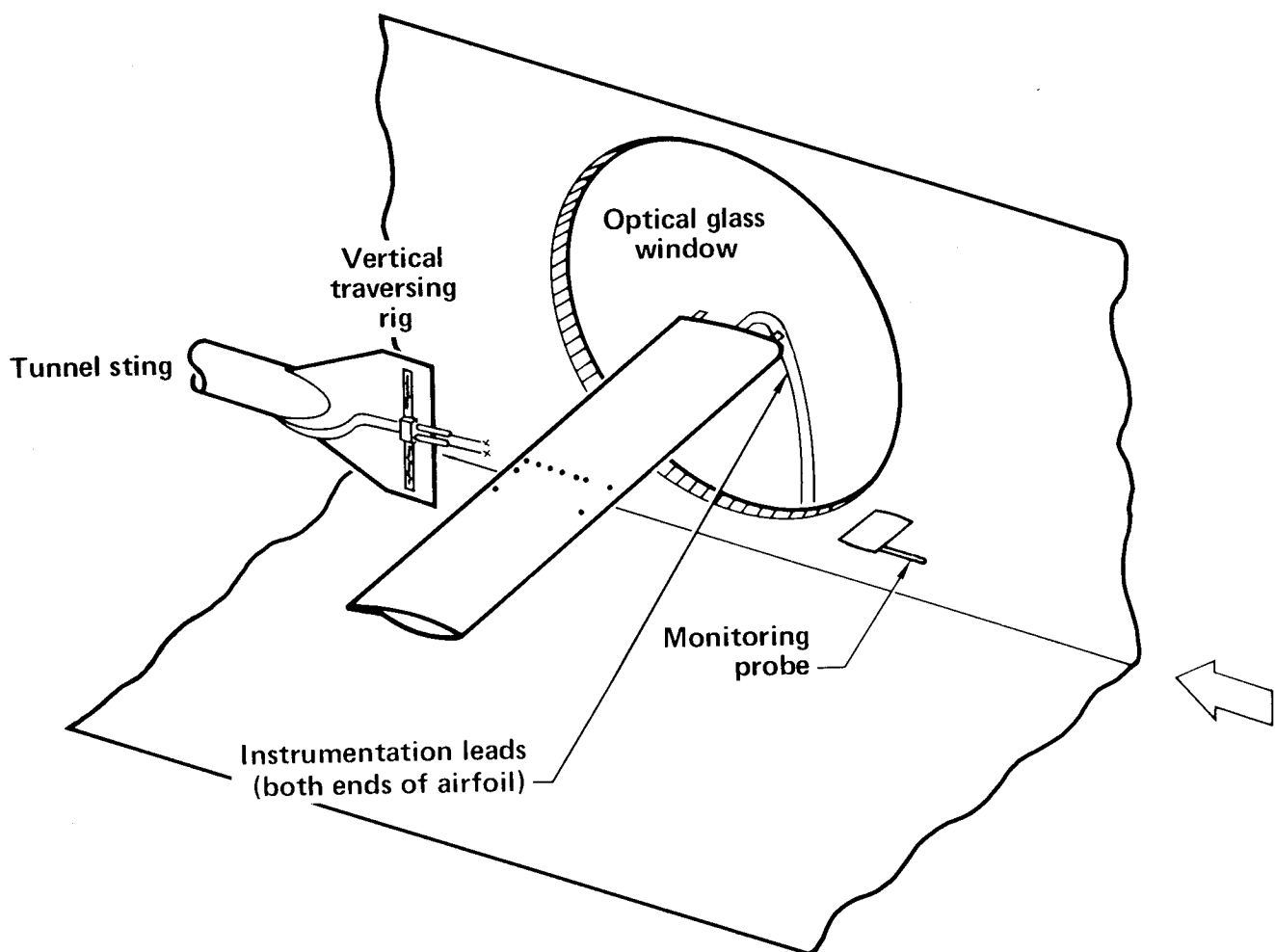
Figure 2.- Test-section setup for dynamic measurements.
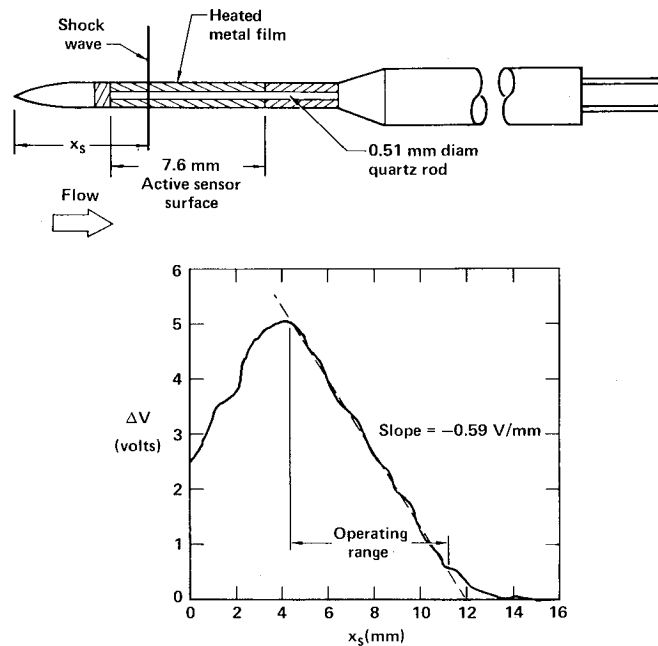
Figure 3.- MDRL-developed shock-position sensing probe.
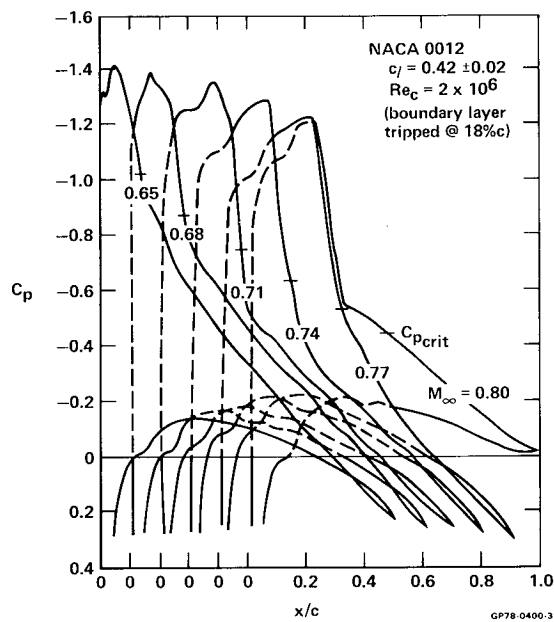
Figure 4.- Development with increasing Mach number of pressure distribution on conventional NACA 0012 airfoil.
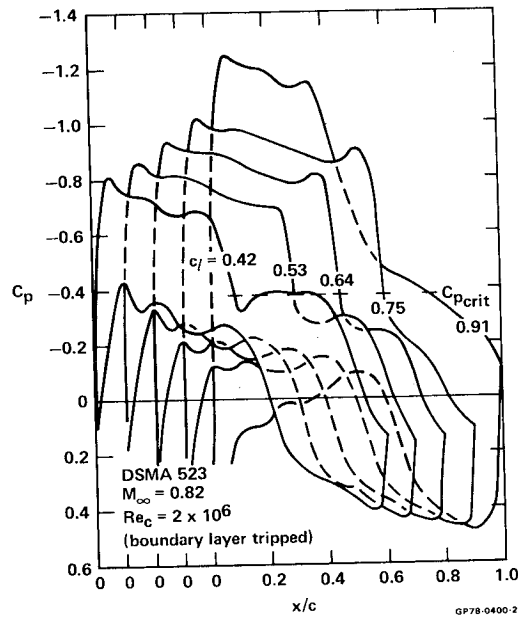
Figure 5.- Evolution with increasing lift of pressure distribution on super-
critical DSMA 523 airfoil.
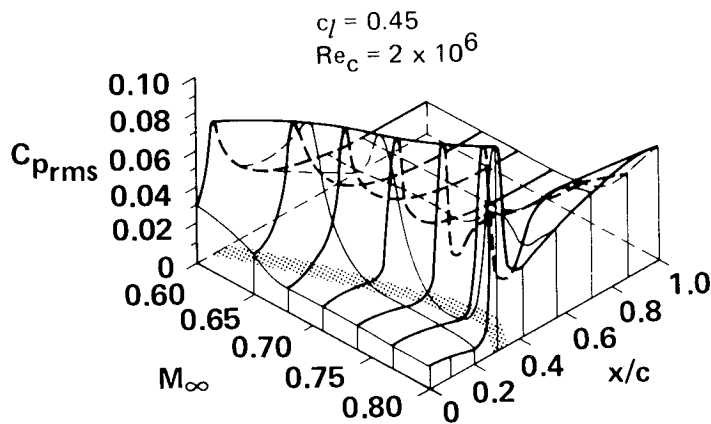
Conventional airfoil (NACA 0012)

Figure 6.- Chordwise fluctuating pressure distribution on NACA 0012 airfoil:
evolution with Mach number variation. Shaded area indicates location of
shock region.

$c_l = 0.55$
$Re_c = 2 \times 10^6$
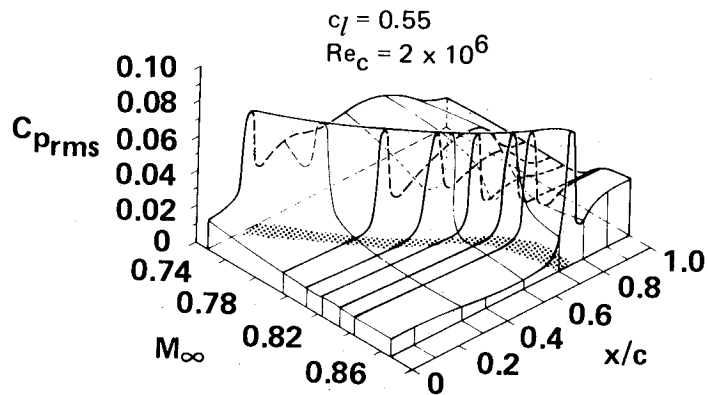
Supercritical airfoil (DSMA 523)

Figure 7.- Chordwise fluctuating pressure distribution on DSMA 523 super-critical airfoil: variation with increasing Mach number. Shaded area indicates shock region.

$M_\infty = 0.80$
$c_l = 0.54$
$c_{l_{rms}} \approx 0.011$
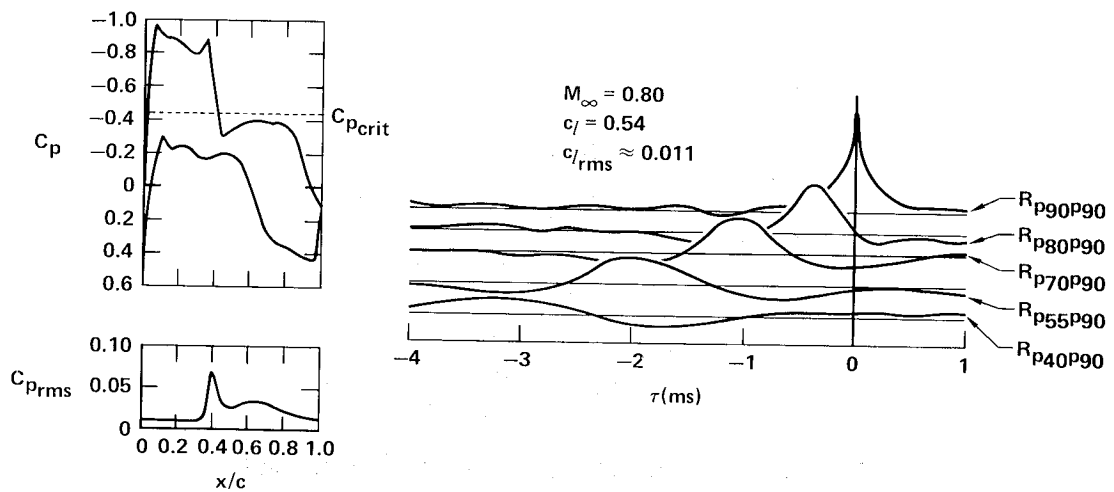
Figure 8.- Disturbance propagation in a supercritical airfoil flowfield: normal case (no separation).
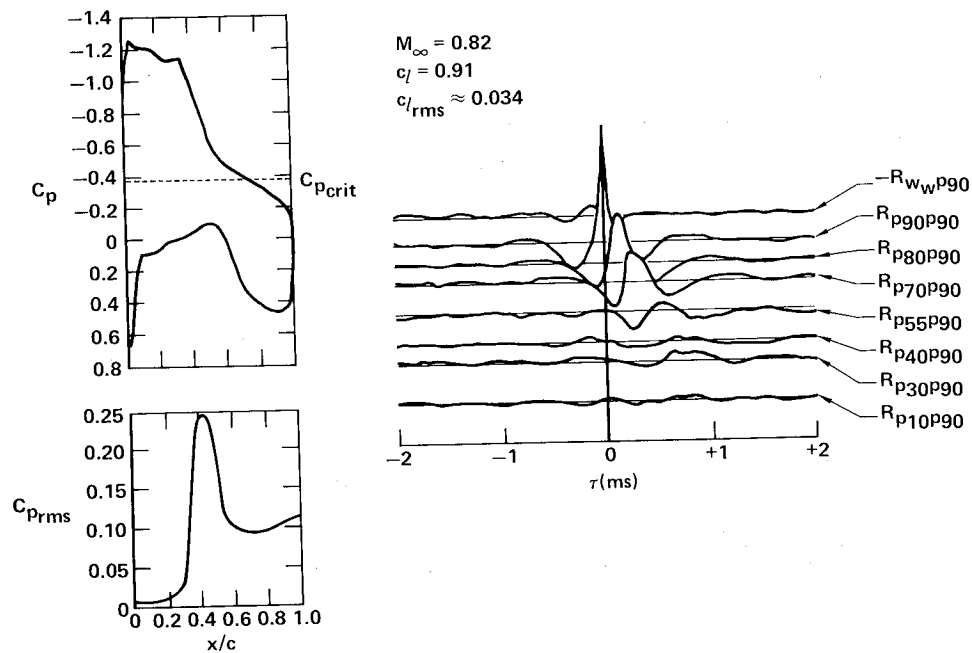
Figure 9.- Disturbance propagation in a supercritical airfoil flowfield: heavy buffeting case.
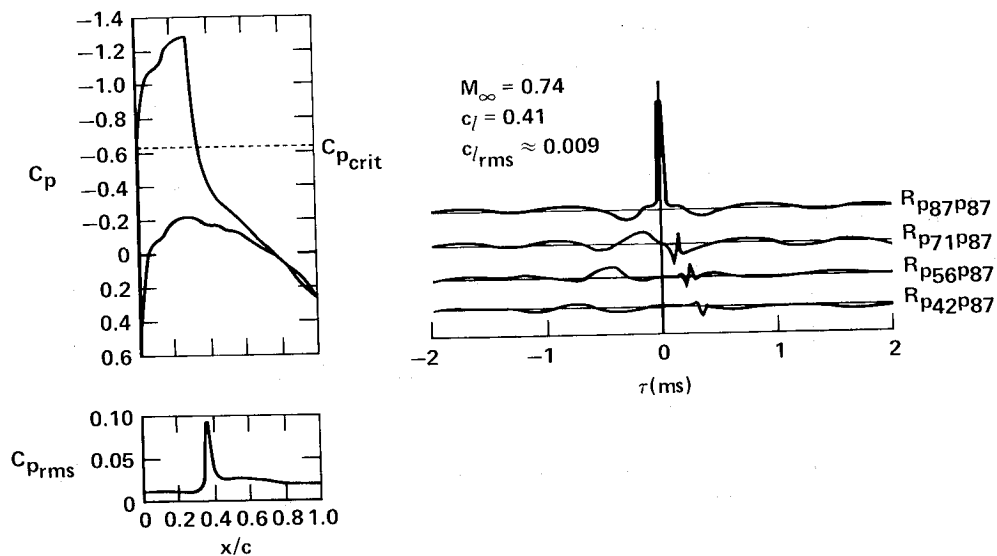
Figure 10.- Disturbance propagation in a conventional airfoil flowfield: mixed case (intermittent separation).
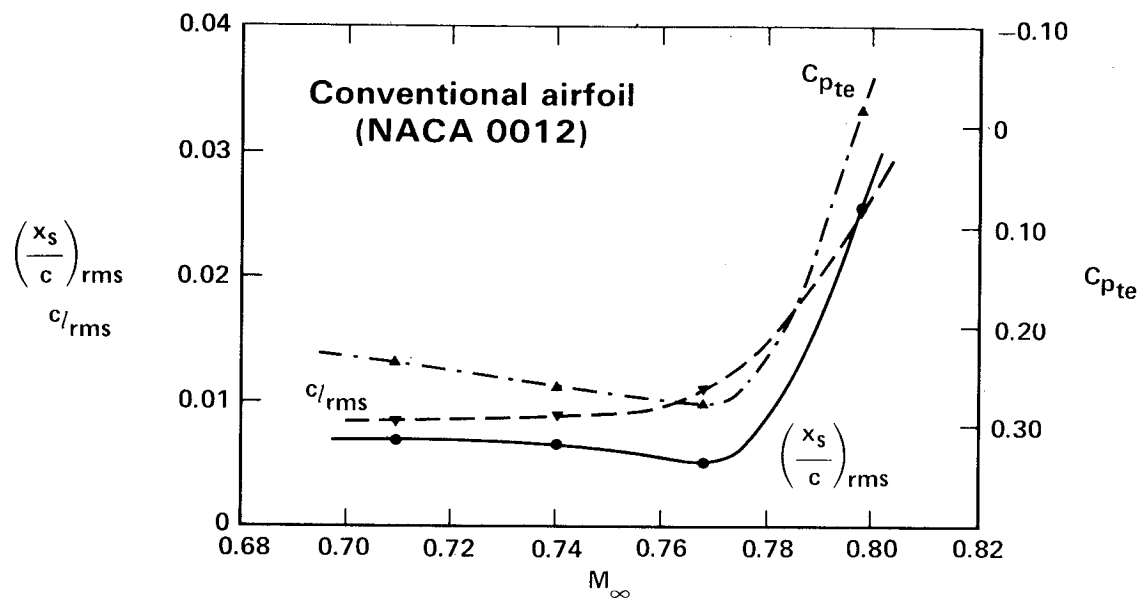
Figure 11.- Shock-oscillation intensity as a function of Mach number for a conventional airfoil.
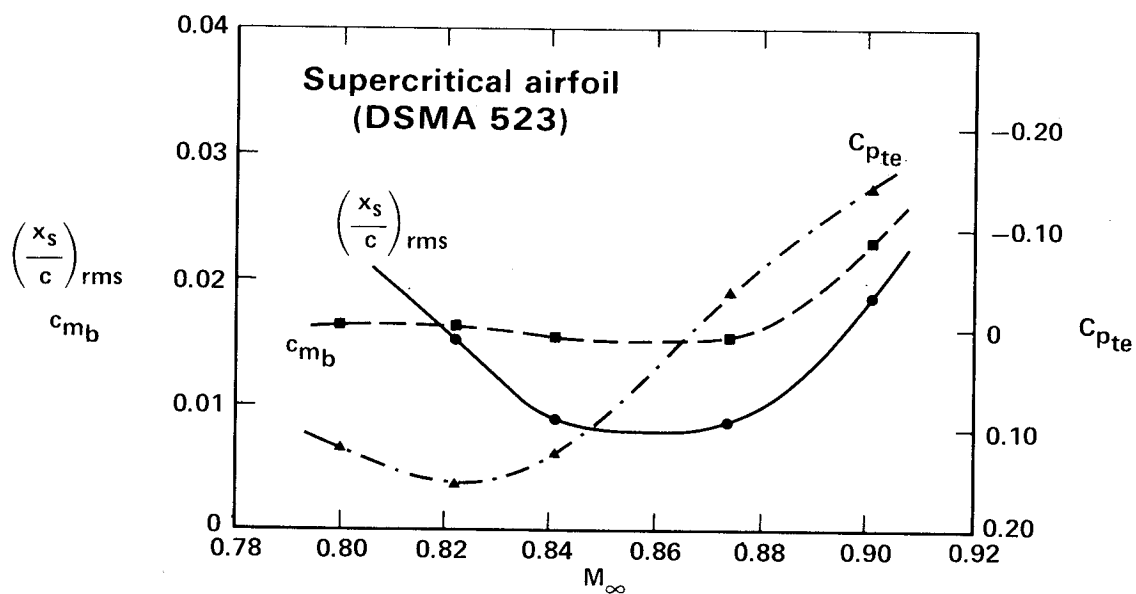
Figure 12.- Intensity of shock oscillations as a function of Mach number for a supercritical airfoil.
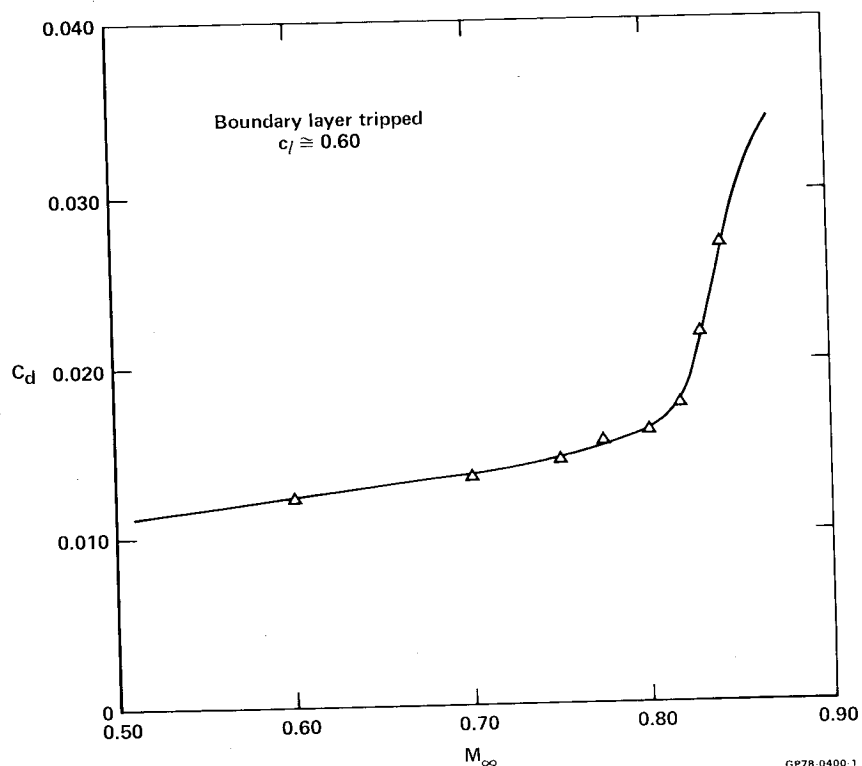
Figure 13.- Drag rise of the DSMA 523 airfoil.
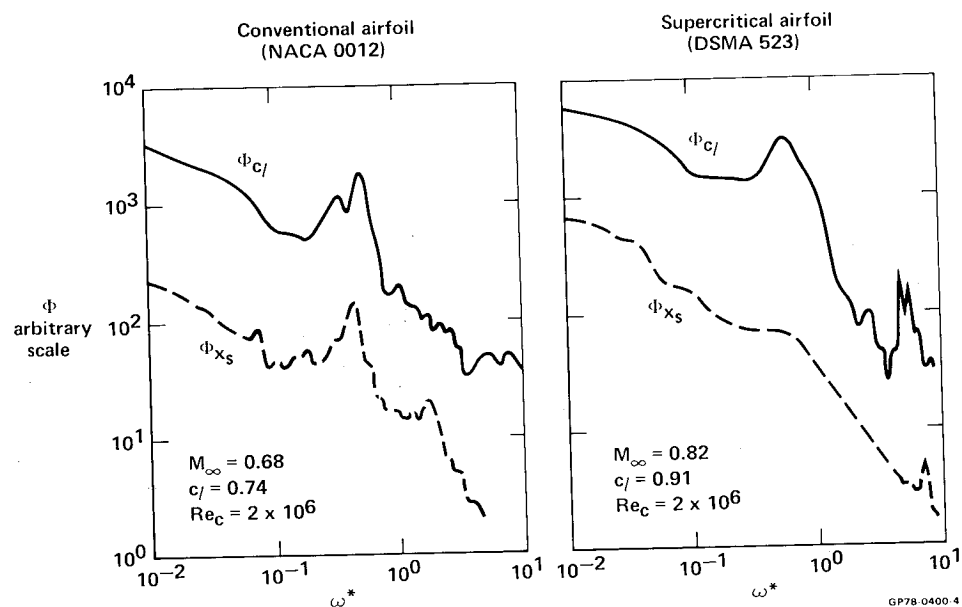
Figure 14.- Power spectra of lift fluctuations and shock oscillations. Reduced frequency $\omega^* = 2\pi fc/U_\infty$, where f is frequency and U_∞ is freestream velocity.

NACA 0012

$R_{x_s c_l}$

$M_\infty = 0.798$

$c_l = 0.441$

$c_{l_{rms}} = 0.027$

0.6
0.4
0.2
−20   −10   −0.2   10   20
−0.4
−0.6

$\tau(ms)$

DSMA 523

$R_{x_s c_l}$

$M_\infty = 0.822$

$c_l = 0.910$

$c_{l_{rms}} = 0.034$

0.4
0.2
−20   −10   −0.2   10   20
−0.4

$\tau(ms)$
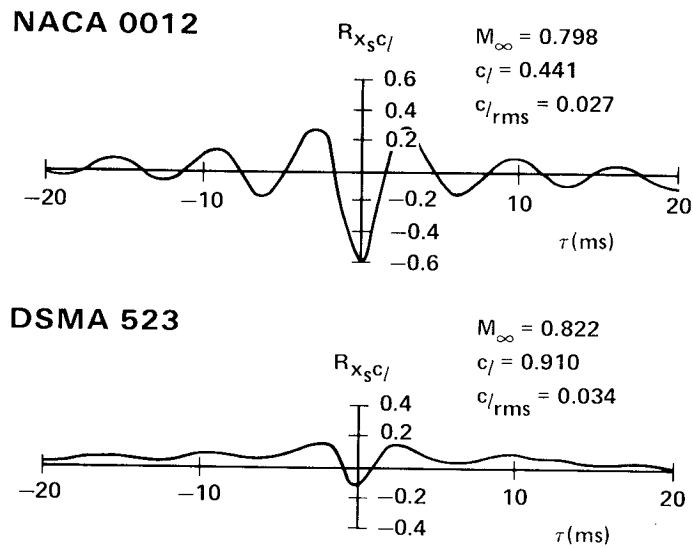
Figure 15.- Cross correlations of shock oscillations and lift fluctuations in buffeting.

Contours represent increments of 0.1 in cross-correlation coefficient
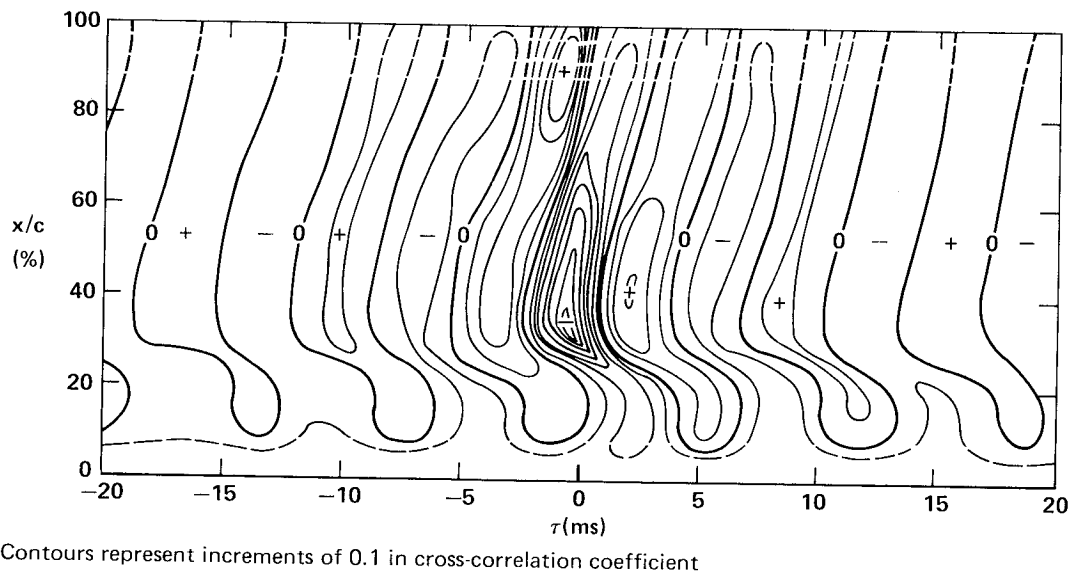
Figure 16.- Cross correlation of lift and local surface-pressure fluctuations on a conventional airfoil in high Mach number buffeting.

218
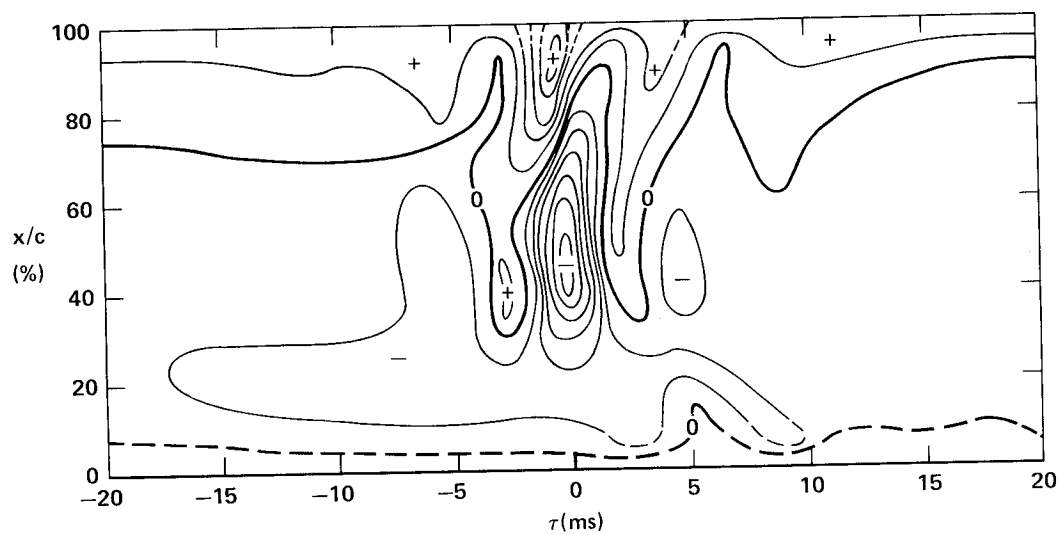
Contours represent increments of 0.1 in cross-correlation coefficient

Figure 17.- Cross correlation of lift and surface-pressure fluctuations on a supercritical airfoil in high-lift buffeting.

EFFECT OF AIRFOIL SECTIONS

ON ACOUSTIC PERFORMANCE OF PROPELLERS

Kenneth D. Korkan, Chung-jin Woan, and Gerald M. Gregorek
The Ohio State University

SUMMARY

In the present study three representative airfoil sections have been chosen for use in a propeller acoustic analysis - Clark Y, NACA 16 series, and ARA-D series sections. Comparisons of their basic aerodynamic characteristics and pressure distributions have been made for both sub- and supercritical flow conditions representative of conditions experienced by propellers equipped with airfoils having a maximum thickness-to-chord ratio of 6% and 10%. Each of the airfoil sections are then utilized in a two-bladed propeller acoustic analysis to determine the effects of airfoil blade sections on propeller thickness noise.

SYMBOLS

B	blade width, m
C_D	drag coefficient, dimensionless
C_L	lift coefficient, dimensionless
$C_M(c/4)$	moment coefficient about quarter chord, dimensionless
C_p	pressure coefficient, dimensionless
D	propeller diameter, m
H	maximum blade thickness, m
M	Mach number, dimensionless
$|1-M_r|$	Doppler factor
$p-p_o$	acoustic perturbation pressure, N/m^2
$p_{ij}n_j$	local force at blade surface, N/m^2
r	distance between an observer and source point at time τ_e, m
R_H	hub radius, m
R_p	propeller radius, m
S	blade surface area, m^2
SPL	sound pressure level, dB(re: 2×10^{-5} N/m^2)
t	observer time, sec
V	blade surface convection velocity, m/sec
V_n	normal (outward) component of V, m/sec
X	observer position vector, m
x_1, x_2, x_3	three Cartesian coordinates of the position vector X, m
x/c	distance along airfoil axis non-dimensionalized by chord, c
z/c	vertical coordinate non-dimensionalized by chord, c
β	blade angle, deg
ξ	blade section radius, m

ρ_o undisturbed air density, kg/m^2

τ source time, sec

τ_e emission time, sec

INTRODUCTION

The increased emphasis on fuel conservation in the world and the continued pressure of communities and regulatory agencies to reduce noise levels in the vicinity of airports have increased the needs for computational methods that can design propellers having quiet operation yet high efficiency. This requires an accurate determination of the flow over the propeller blade in addition to the acoustic field induced by the propeller blade. Basic to the evaluation of a propeller from a performance as well as a noise standpoint is the selection of the airfoil sections which make up the propeller blade. With new airfoils - such as those designed to operate efficiently in the supercritical flows - a gain in performance may be possible. Further, if in propeller redesign an acoustic analysis is employed, the potential exists to optimize the propeller for minimum noise with little impact on propeller aerodynamic performance.

A recent paper by Bocci (ref. 1) indicates some of the improvements that can be obtained in propeller performance using a new series of airfoils especially designed for supercritical flow as well as good low speed performance. The results indicate that the new propeller airfoil family known as the ARA-D series derived from these criteria provided performance improvements. A comparison between a 6% ARA-D series and the 6% NACA series in terms of C_L vs. α, C_D vs C_L, and $C_{L_{max}}$ boundaries are shown in figure 1 for a free stream Mach number of 0.5. As can be seen, the ARA-D airfoil section does provide a significant improvement over the NACA 16 section at this Mach number. However, in Bocci's analysis (ref. 1), no acoustical analysis was performed.

It is the purpose of this study to investigate the aerodynamic characteristics obtained on three representative propeller airfoil sections under sub- and supercritical flow conditions, and then to utilize each of the airfoil sections in a propeller acoustical analysis to determine the effects of these airfoil blade section characteristics on propeller thickness noise.

AIRFOIL SECTIONS

The three airfoil sections selected for this analysis, i.e., the Clark Y, NACA 16 series, and the new ARA-D series are shown in figure 2. The Clark Y airfoil is a propeller section that has been used prior to 1940, whereas the NACA 16 series family has been preferred in post-war years. The ARA-D series family is the most recent attempt to improve the aerodynamic performance by relaxing several of the constraints that have been imposed in past propeller section designs. This series, for example, has an increased leading edge radius and cambered under-surface when compared with the Clark Y and NACA 16 series.

Aerodynamic Characteristics of 6% Airfoil Sections

As noted in figure 2, the maximum thickness to chord ratio has been fixed at 6% for each of the airfoil sections under study. Selecting a flow condition as suggested by Bocci (ref. 1) that would be compatible with a propeller section of 6%, a $M = 0.6$ and $Re = 2 \times 10^6$ condition was chosen and the pressure distributions for each of the airfoil sections computed using the numerical analysis of Smetana, et. al. (ref. 2) at angles of attack of 0 and 2°. For these conditions, flows for each of the airfoils were subcritical. The Clark Y and NACA 16 series sections exhibit a very narrow leading edge suction pressure spike as a result of the small leading edge radius. This may be compared to the ARA-D series pressure distribution (fig. 3) which has a larger leading edge radius that broadens the leading edge suction pressures.

Figures 3 through 5 also indicate the natural transition locations for the three airfoils. The Clark Y section displays the usual forward movement of the transition location on the upper surface as the angle of attack is increased while the lower surface transition point remains fixed at the trailing edge resulting in a long laminar run. These results may be compared to the NACA 16 series (fig. 5) for which the transition locations remain relatively fixed as the two angles of attack investigated are within the drag "bucket" for this airfoil. As α is increased from 0 to 2° for the ARA-D series (fig. 3), the transition location on the bottom surface moves from the leading edge region to the trailing edge resulting in a significant laminar run and a lower drag coefficient. When the L/D ratio is calculated for each of the three sections at the two angles of attack, the L/D increases regularly from the Clark Y to the NACA 16 series and finally the ARA-D series. The price for this increased performance is increased moment coefficient, which changes significantly increasing by a factor of three when comparing the Clark Y to the ARA-D section.

The supercritical properties of these airfoils have been investigated using the numerical analysis of Bauer, et. al. (ref. 3) at a Mach number of 0.8. The C_L value has been fixed at 0.4 and a Reynolds number of 2×10^6 chosen as representative propeller flow conditions. The results are shown in figures 6 through 8 for the leading edge transition fixed case. The pressure distributions show the shock locations for the three airfoils. Surprisingly, the 6% Clark Y section appears quite acceptable at this condition with a mild shock near the mid-chord and a low moment coefficient. According to theory the shock for the NACA 16 airfoil has moved aft, the moment more than doubled and flow separation has occurred upstream of the trailing edge. The ARA-D series airfoil suffers the greatest at this test condition with shocks on the upper and lower surfaces causing flow separation. It should be noted that the ARA-D section is at approximately -2° for this lift coefficient, and at higher lift coefficients and angles of attack the lower surface shock may disappear resulting in improved performance.

Aerodynamic Characteristics of 10% Airfoil Sections

To represent an inboard station propeller section, the three airfoils previously investigated were scaled to 10% thickness to chord ratio and evaluated

at M = 0.4 and a Reynolds number of 10^6. The pressure distributions obtained from the Smetana analysis (ref. 2) at angles of attack of 0° and 2° are shown in figures 9 through 11. As illustrated in these figures, the suction pressure spikes have been attenuated by the increased leading edge radius of the thicker sections, while the natural transition behavior of all three 10% sections exhibit the same behavior as on the 6% sections.

The overall performance of the 10% Clark Y, NACA 16 and ARA-D sections are compared in figure 12 for both natural and fixed transition. If laminar flow can be maintained, the NACA 16 series is clearly superior in L/D; however, with transition fixed at 10% this section suffers the greatest loss in performance. The Clark Y and ARA-D sections have comparable L/D, as indicated with the ARA-D being more favorable at the higher lift coefficients. These airfoil sections will now be employed in an acoustic analysis of a two bladed propeller.

ACOUSTIC PERFORMANCE

Mathematical Model

Following Ffowcs Williams and Hawkings (ref. 4), the acoustic pressure, $p-p_0$, due to a rigid moving propeller at the field point X and time t neglecting the effects of Lighthill stress tensors, is given by:

$$4\pi(p-p_0)(X,t) = - \frac{\partial}{\partial x_i} \int \left[\frac{p_{ij}n_j}{r|1-M_r|} \right]_{\tau=\tau_e} dS + \frac{\partial}{\partial t} \int \left[\frac{\rho_0 V_n}{r|1-M_r|} \right]_{\tau=\tau_e} dS \qquad (1)$$

Here $p_{ij}n_j$ is the force per unit area exerted on the air by the blade surface of the propeller S; V_n is the outward normal component of the surface convection velocity V; ρ_0 is the undisturbed air density; r is the distance between the field point and the source point at emission time $\tau = \tau_e$; and $|1-M_r|$ is the Doppler factor. These integrals are taken over the entire blade surface and the acoustic density perturbation has been replaced by the acoustic pressure, $p-p_0$. The first term of this equation is the noise generated by the blade force, i.e., loading noise, and the second term represents the effects of blade thickness commonly referred to as thickness noise.

In the present study, the effects of blade airfoil sections on the propeller thickness noise are investigated and therefore only the second term of equation (1) is considered.

Computational Method

The thickness acoustic pressure signature is computed based on the method developed by Woan and Gregorek (ref. 5). The result is then utilized in a Fourier series analysis program based on the method outlined by Ralston (ref.

6) to obtain the noise spectrum. The performance of these programs is demonstrated in figures 13 through 15. The good agreement between experimental measurements and predicted results are shown in both time and frequency domains (fig. 14).

Effects of Blade Airfoil Sections on Thickness Noise

Six propellers were used in this investigation; two with Clark Y, two with NACA 16, and two with the combination of Clark Y and ARA-D (ref. 1) sections. The outer third of all propeller blades have sections of constant thickness/chord ratio. It is to be noted that the propellers which have the combination of Clark Y and ARA-D sections use only the outer third of the propeller blade with ARA-D airfoil sections and the remaining region with Clark Y sections. Figure 16 shows the blade-form curve and blade angle distribution along the propeller radius. These curves are obtained from reference 7 and only the ten percent thickness/chord ratio distribution curve is shown (fig. 16).

For means of comparison, the system for identifying the blades is illustrated by the following two examples. Blade No. NACA 16 06-35-06-06 has propeller blades with NACA 16 sections; six percent thickness/chord ratio distribution; observer located in the propeller disc plane 35 R_p from the rotational axis; and operates at a tip rotational Mach number of 0.6 and tip helical Mach number of 0.6. Blade No. Clark Y 10-2-06-08 utilizes Clark Y blade airfoil sections; ten percent thickness/chord ratio distributions; observer located in the propeller disc plane 2 R_p from the rotational axis and moving with propeller; and operates at a tip rotational Mach number of 0.6 and a tip helical Mach number of 0.8.

In the computation of acoustic pressure signatures, it is assumed that all propellers are operating in free space at sea level. The computed propeller acoustic pressure signatures and spectra due to blade thickness effects are presented in figures 17 through 24 for all propellers investigated.

The effects of thickness on the near and far field sound pressure levels are presented in figures 17 and 18. Reducing blade thickness from 10% to 6% results in a 60% reduction in the peak acoustic pressures. The influence of Mach number on the acoustic pressure is shown in figure 19; as the Mach number at the tip is lowered from M = 0.8 to M = 0.6, the near field acoustic pressure is reduced by more than 90% for all three sections. Note, however that no account has been made of the impact of these tip speed reductions on the aerodynamic performance of the propeller.

As the forward speed of the propeller is increased, the acoustic signature is altered as shown in figures 20 and 21. With the helical Mach number fixed at 0.8 which can be obtained by reducing the rotational tip speed to 0.6 as the forward Mach number is increased to M = 0.53, the acoustic level is one half that of the zero speed case. When the rotational speed is fixed at M = 0.6 and the forward speed increased to M = 0.53, the acoustic signature is increased by a factor of five. Both results illustrate the strong dependence of acoustic environment on the helical Mach number.

In addition to these acoustic pressure signatures, a spectral analysis in the frequency domain for each of the cases has been conducted. These results are given in figures 22 through 24 allowing comparisons of the effects of airfoil shapes in terms of sound pressure level and frequency.

CONCLUDING REMARKS

An analytic study to determine the effects of airfoil shape on propeller blade thickness noise has been conducted. The aerodynamic characteristics of three airfoils - the Clark Y, NACA 16 series, and the ARA-D family of 6% and 10% thickness to chord - were examined for use in an acoustic analysis of a two bladed propeller. The study shows the importance of lowering the tip Mach number and reducing blade thickness to minimize both the near and far field noise. Of the configurations evaluated, the Clark Y propeller exhibited the most acceptable acoustic performance.

REFERENCES

1. Bocci, A. J., "A New Series of Airfoil Sections Suitable for Aircraft Propellers", Aeronautical Quarterly, February 1977, pp. 59-73.

2. Smetana, F. O., Summey, D. C., Smith, N. S., and Carden, R. K., "Light Aircraft Lift, Drag, and Moment Prediction - A Review and Analysis", NASA CR-2523, 1975.

3. Bauer, F., Garabedian, P., Korn, D., and Jameson, A., Supercritical Wing Sections II, A Handbook, Lecture Notes in Economics and Mathematical Systems, V. 108, Springer-Verlag, New York (1975).

4. Ffowcs Williams, J. E., and Hawkings, D. L., "Sound Generation by Turbulence and Surface in Arbitrary Motion", Philosophical Transactions of the Royal Society A264, 1969, pp. 321-343.

5. Woan, C. J., and Gregorek, G. M., "The Exact Numerical Calculation of Propeller Noise", AIAA Paper No. 78-1122, AIAA 11th Fluid and Plasma Dynamics Conference, Seattle, Washington (July 1978).

6. Ralston, A., A First Course in Numerical Analysis, McGraw-Hill Book Company (1965).

7. Freeman, H. B., "Comparison of Full-Scale Propellers Having R.A.F. 6 and Clark Y Airfoil Sections", NACA Report No. 378, 1931.
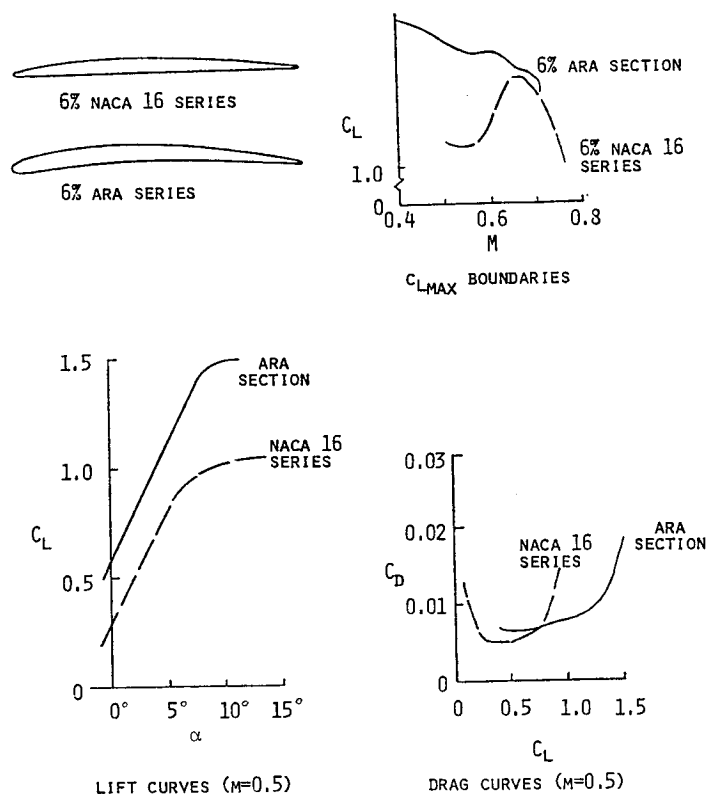
Figure 1.- Comparison of airfoil performance of 6% NACA 16- and ARA-D series.
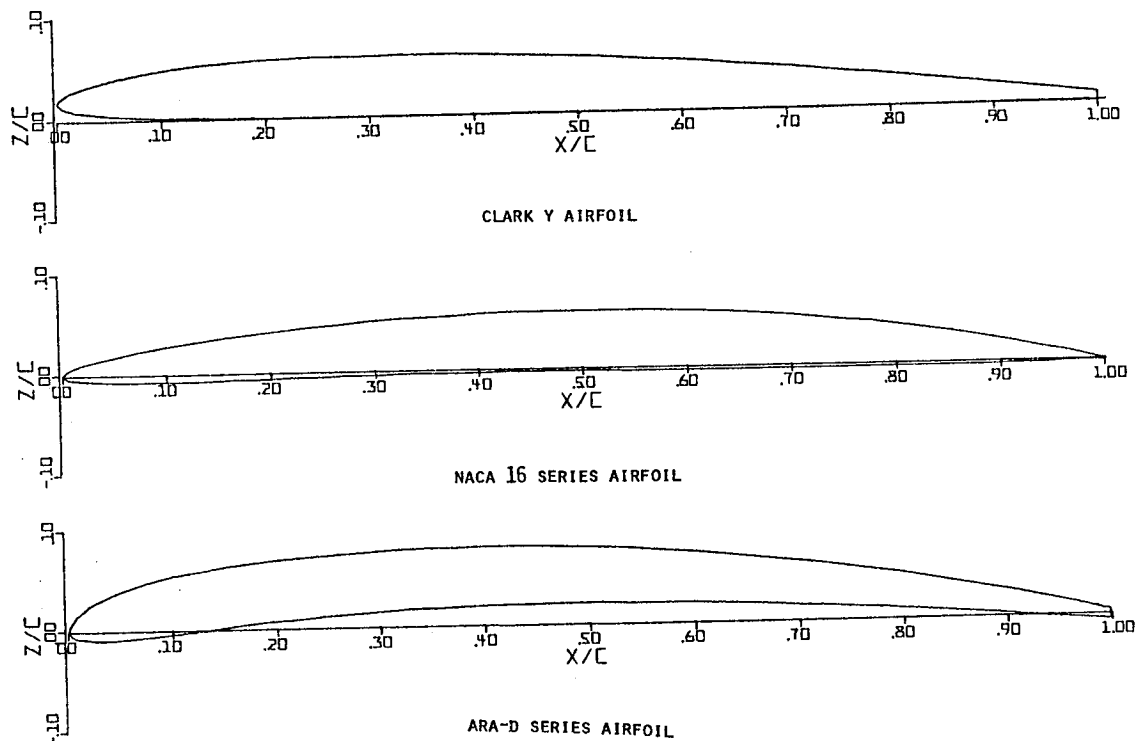
Figure 2.- Airfoil sections used in present analysis with 6% maximum thickness/chord ratio.
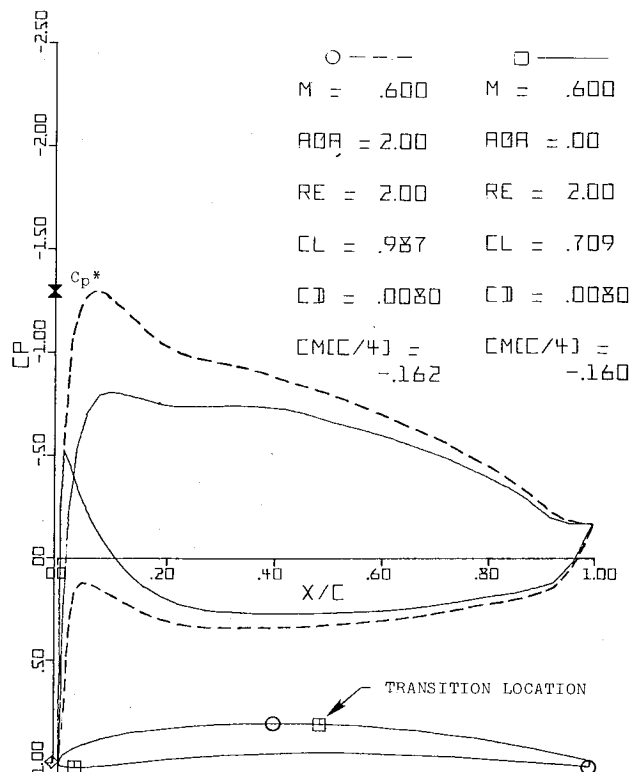
Figure 3.- Subcritical pressure distributions about ARA-D series airfoil with 6% maximum thickness/chord ratio.
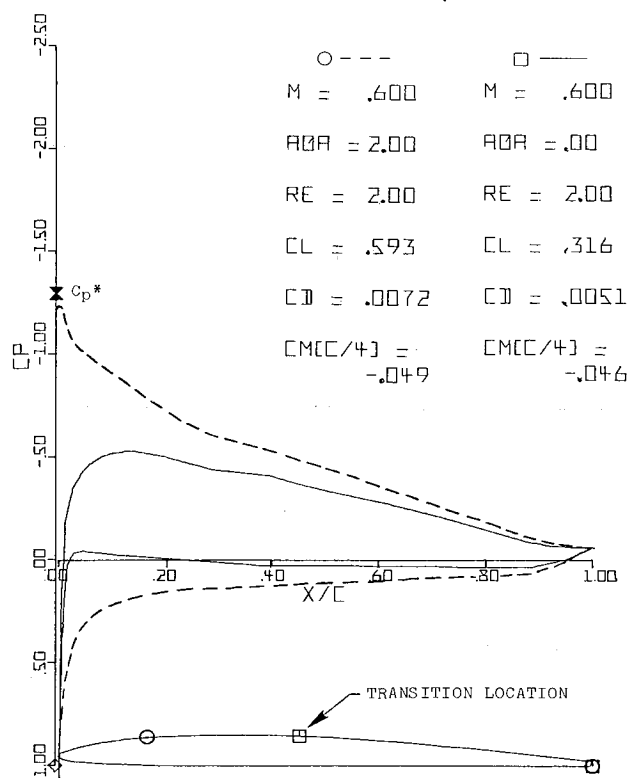
Figure 4.- Subcritical pressure distributions about Clark Y airfoil with 6% maximum thickness/chord ratio.
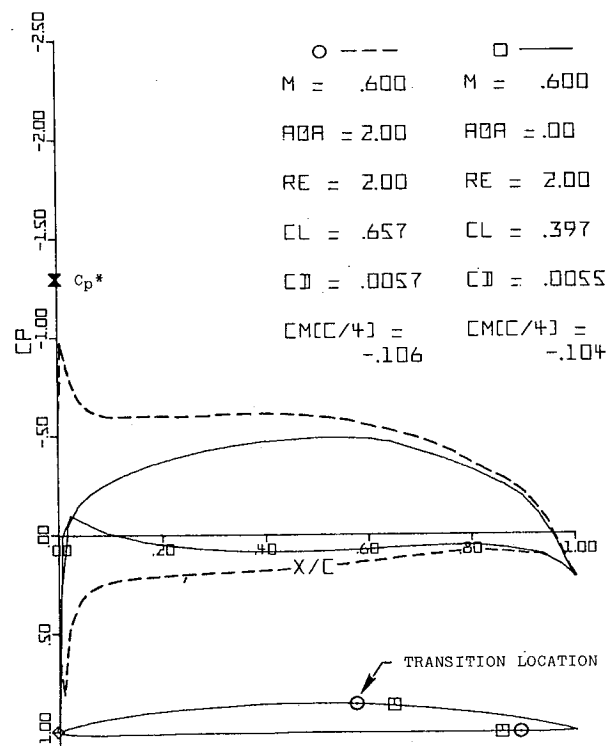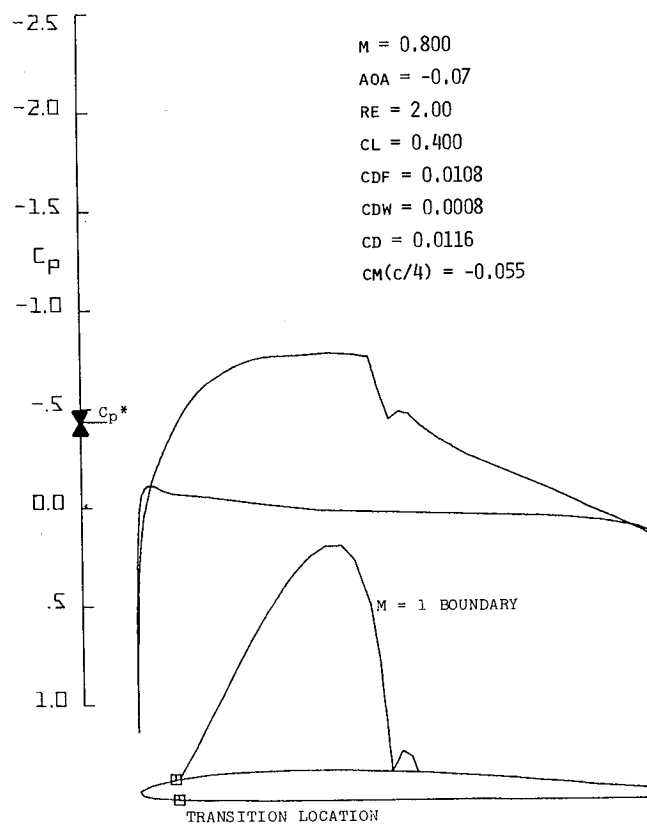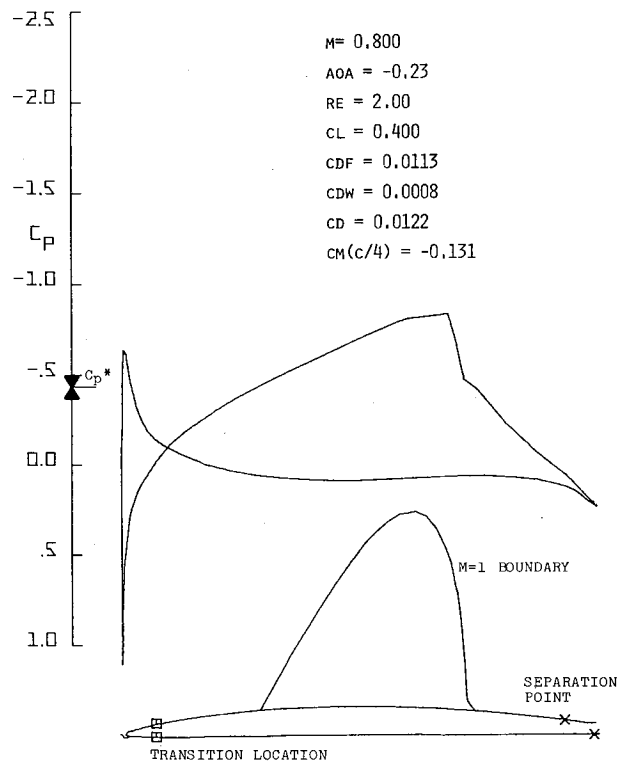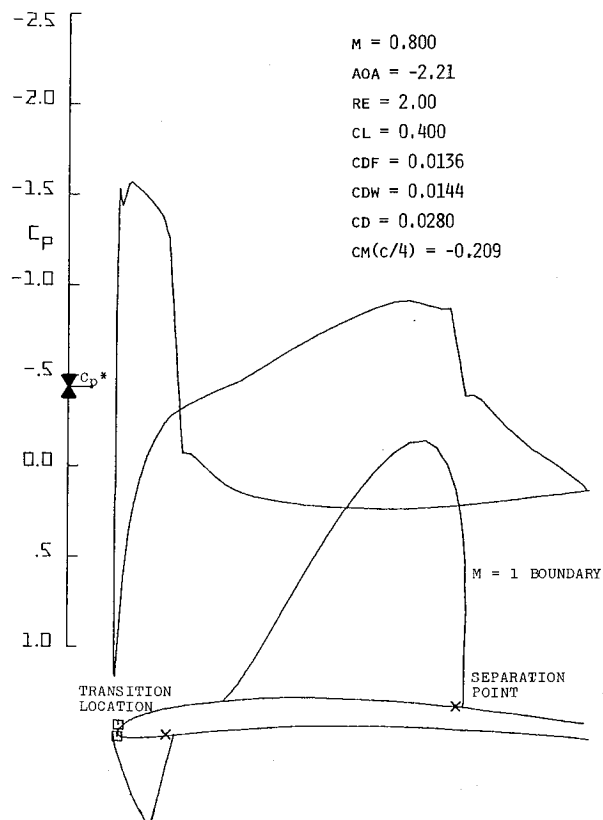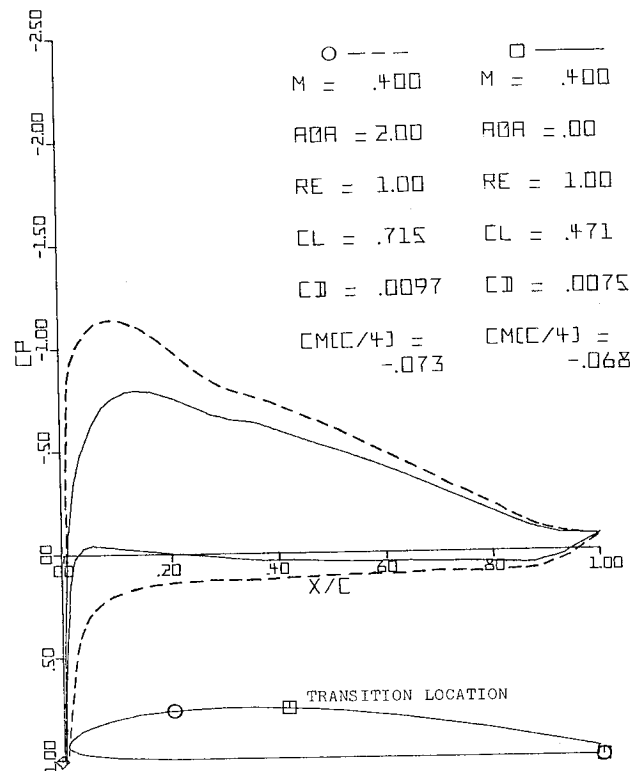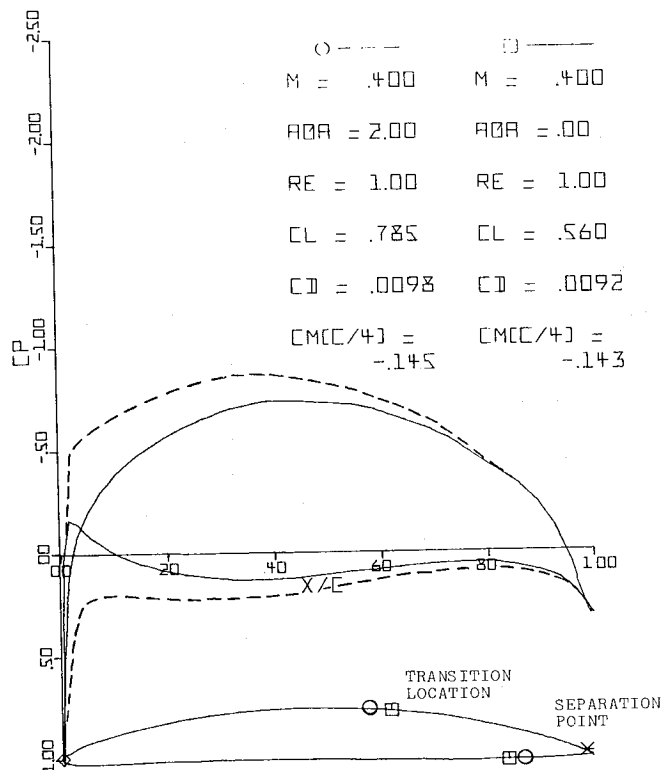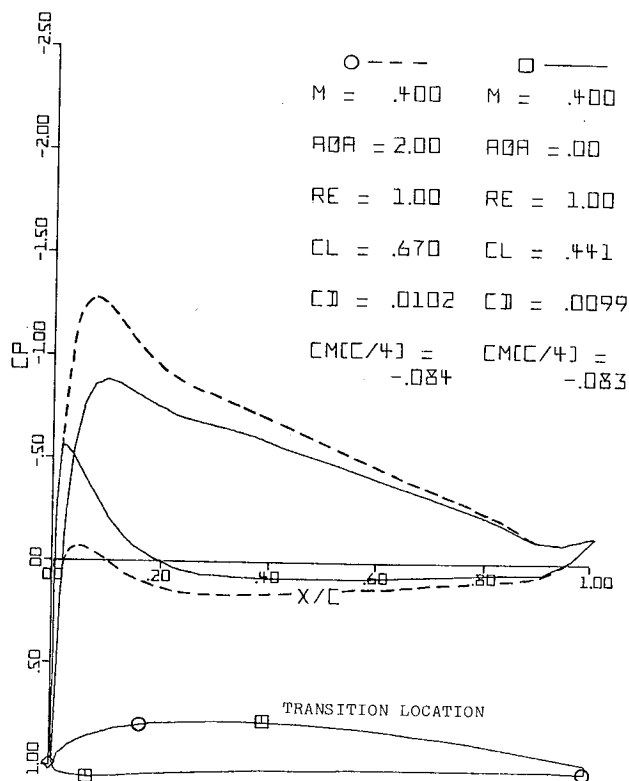
Figure 5.- Subcritical pressure distributions about NACA 16-series airfoil
with 6% maximum thickness/chord ratio.

Figure 6.- Supercritical pressure distribution about Clark Y airfoil at
C_L = 0.4 with 6% maximum thickness/chord ratio.

Figure 7.- Supercritical pressure distribution about NACA 16-series airfoil at C_L = 0.4 with 6% maximum thickness/chord ratio.

Figure 8.- Supercritical pressure distribution about ARA-D series airfoil at C_L = 0.4 with 6% maximum thickness/chord ratio.

Figure 9.- Subcritical pressure distributions about Clark Y airfoil with 10% maximum thickness/chord ratio.

Figure 10.- Subcritical pressure distributions about NACA 16-series airfoil with 10% maximum thickness/chord ratio.

Figure 11.- Subcritical pressure distributions about ARA-D series airfoil with 10% maximum thickness/chord ratio.
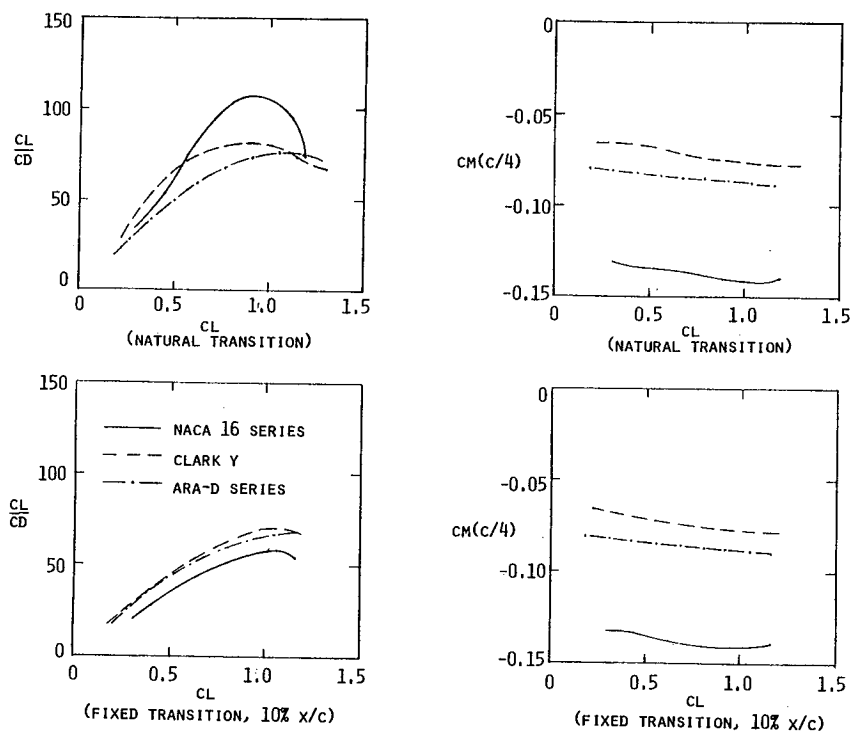
Figure 12.- Comparison of aerodynamic characteristics of the Clark Y NACA 16 and ARA-D 10% airfoil sections for natural and fixed transition. M = 0.4; Re = 1 × 10^6.

(A) - PROJECTED BLADE OUTLINES;
$R_P = 1.30$ m, $R_H = 0.3575$ m.

(B) - BLADE FORM CURVES; B - BLADE
WIDTH, D = PROPELLER DIAMETER,
H = MAXIMUM BLADE THICKNESS,
ξ = SECTION RADIUS, R_P = PRO-
PELLER RADIUS, β = BLADE ANGLE.

(C) - PROFILES OF BLADE
SECTIONS
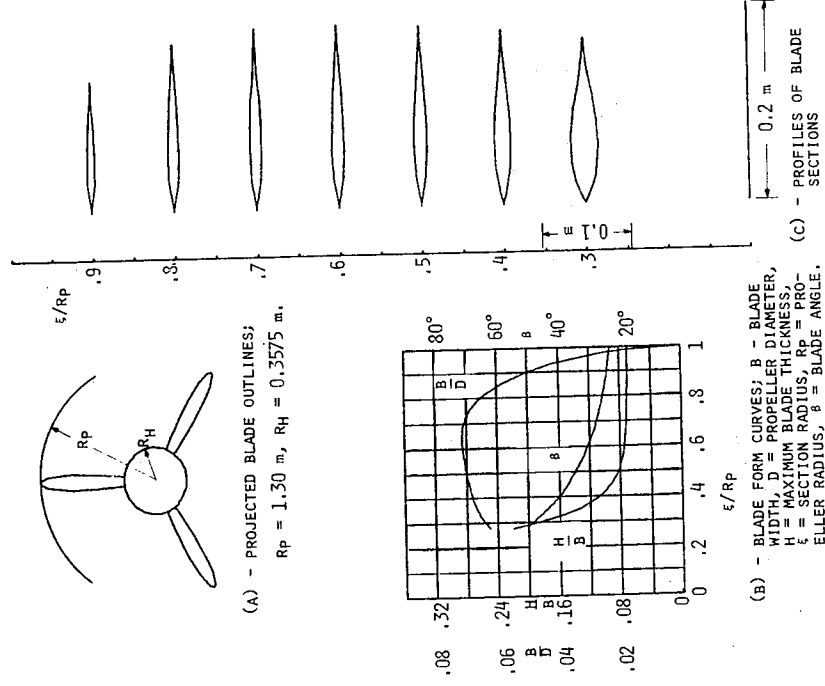
Figure 13.— 3-bladed propeller geometry.
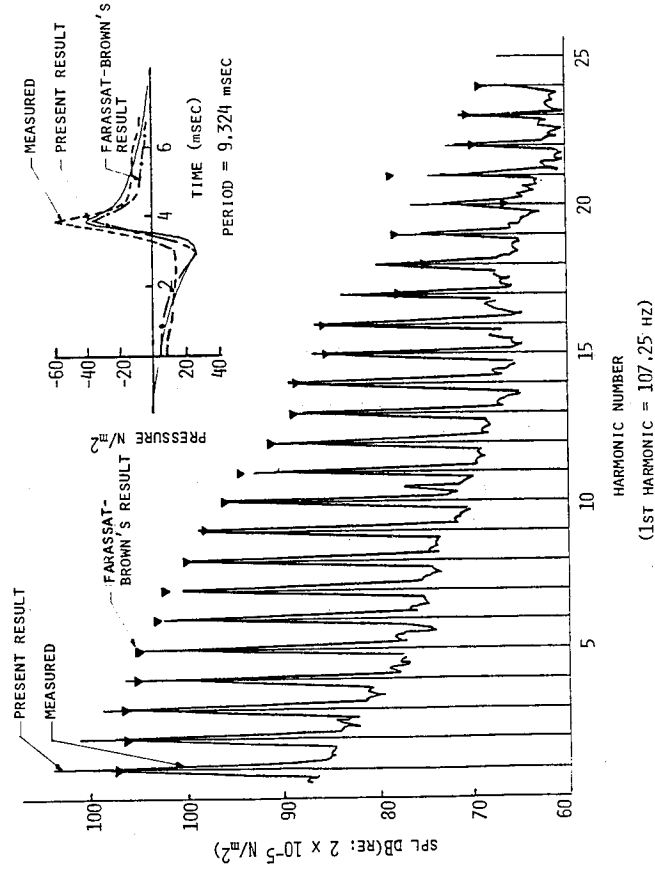
Figure 14.— Comparison between experimental measurement and predicted
computational results.
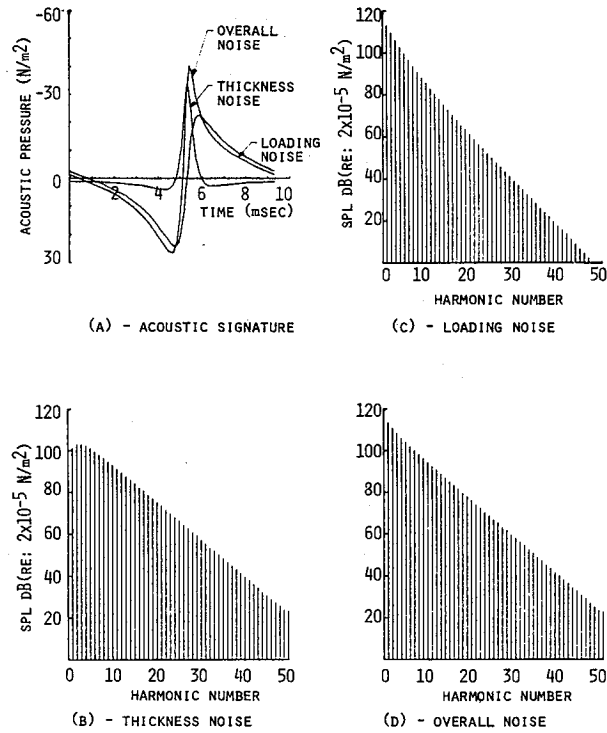
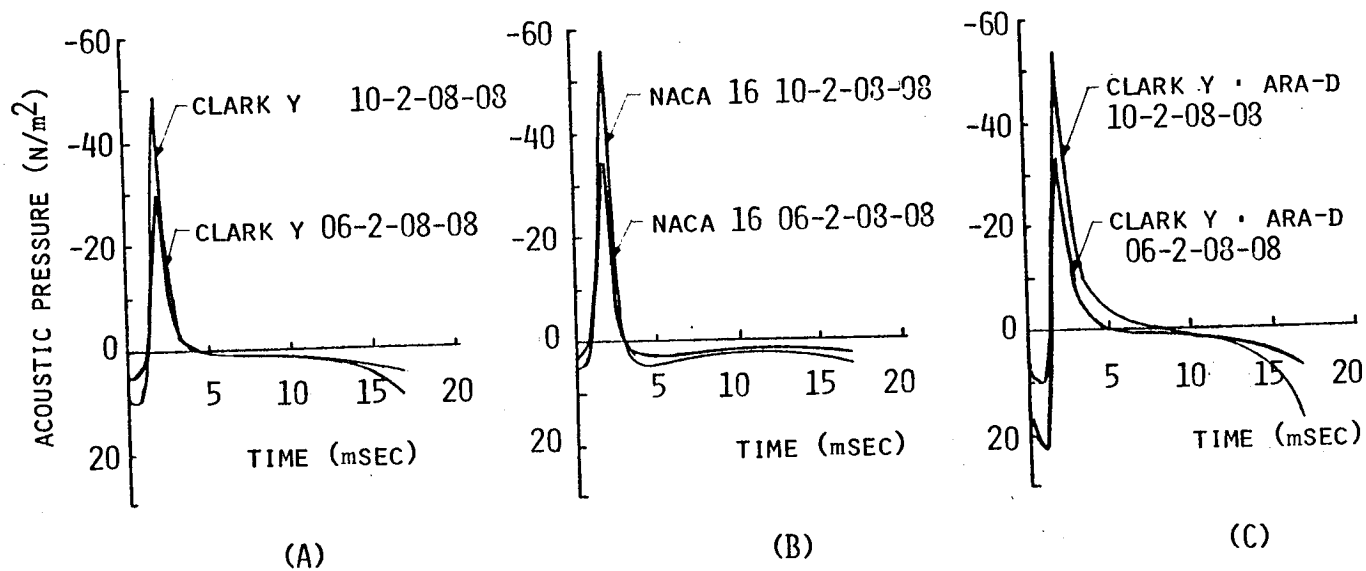Figure 15.- Acoustic pressure signature and spectrum.

PROJECTED BLADE OUTLINES;
R_P=1.4478m, R_H=0.28956 m

BLADE FORM CURVES; B = BLADE WIDTH,
D = PROPELLER DIAMETER, H = MAXIMUM
BLADE THICKNESS, $\mathcal{E}$ = SECTION RADIUS,
R_P = PROPELLER RADIUS, β = BLADE ANGLE.
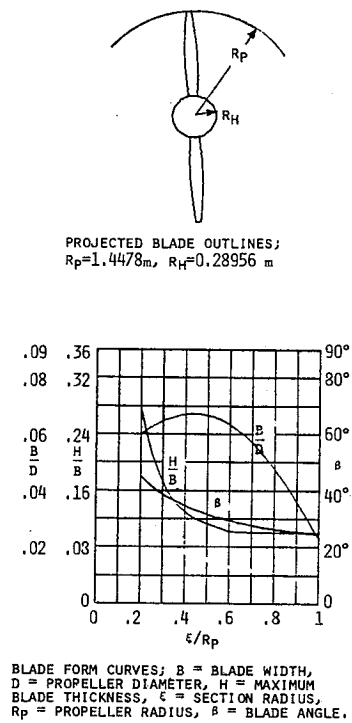
Figure 16.- 2-bladed propeller geometry.

Figure 17.- Near-field acoustic pressure signature. Effect of thickness.
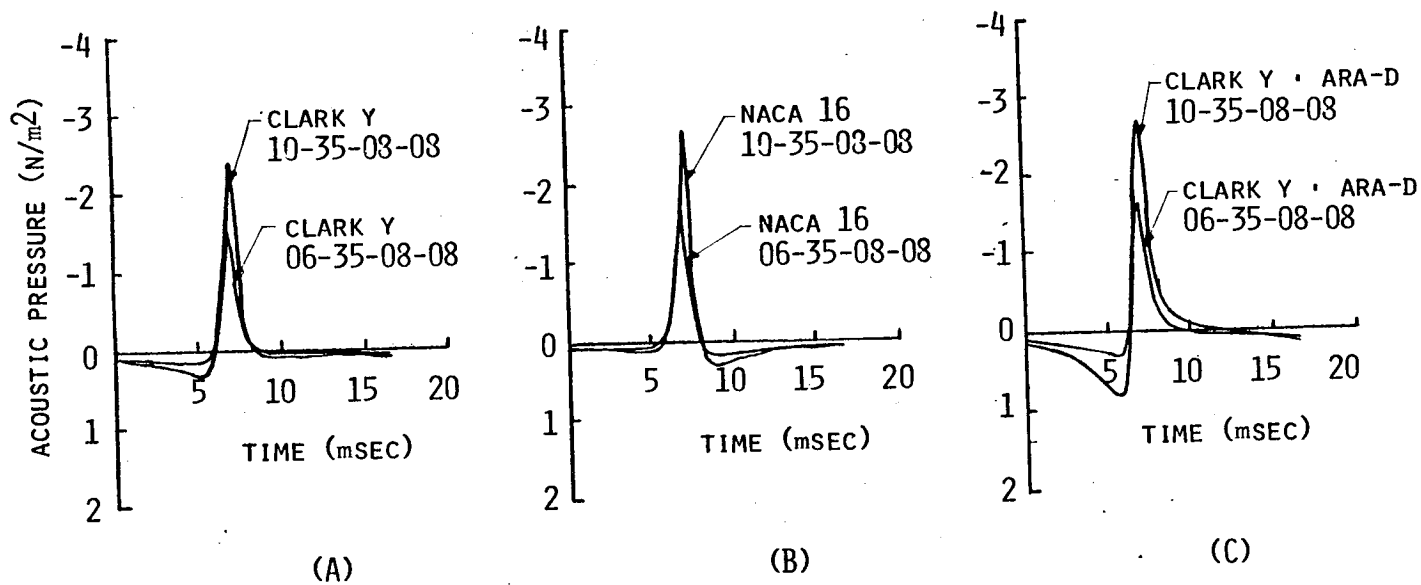
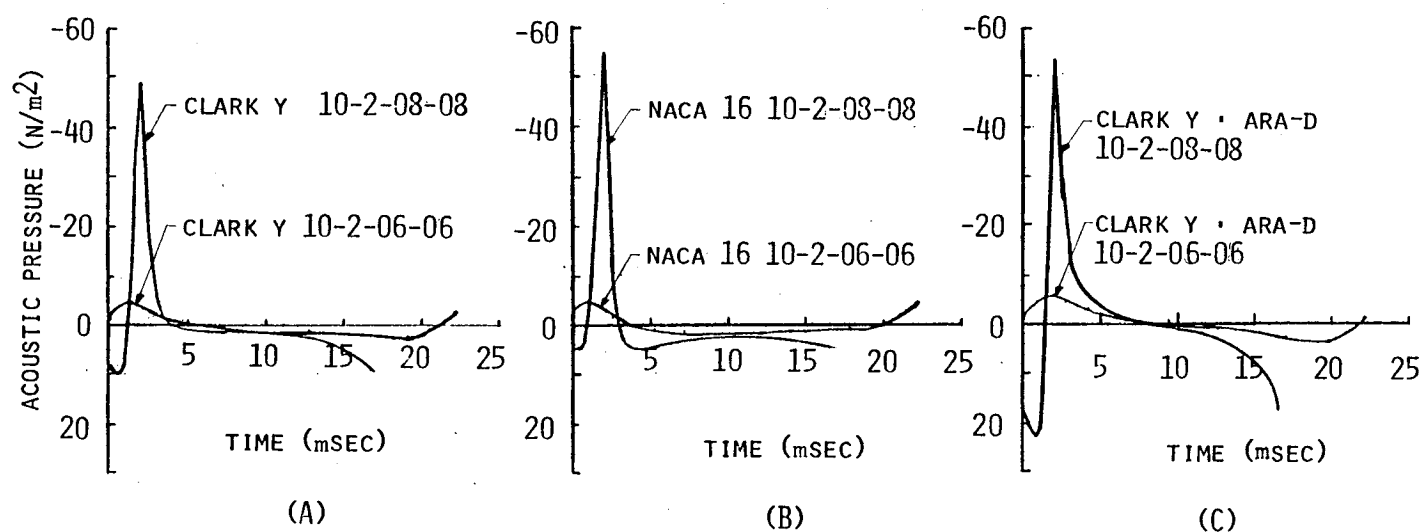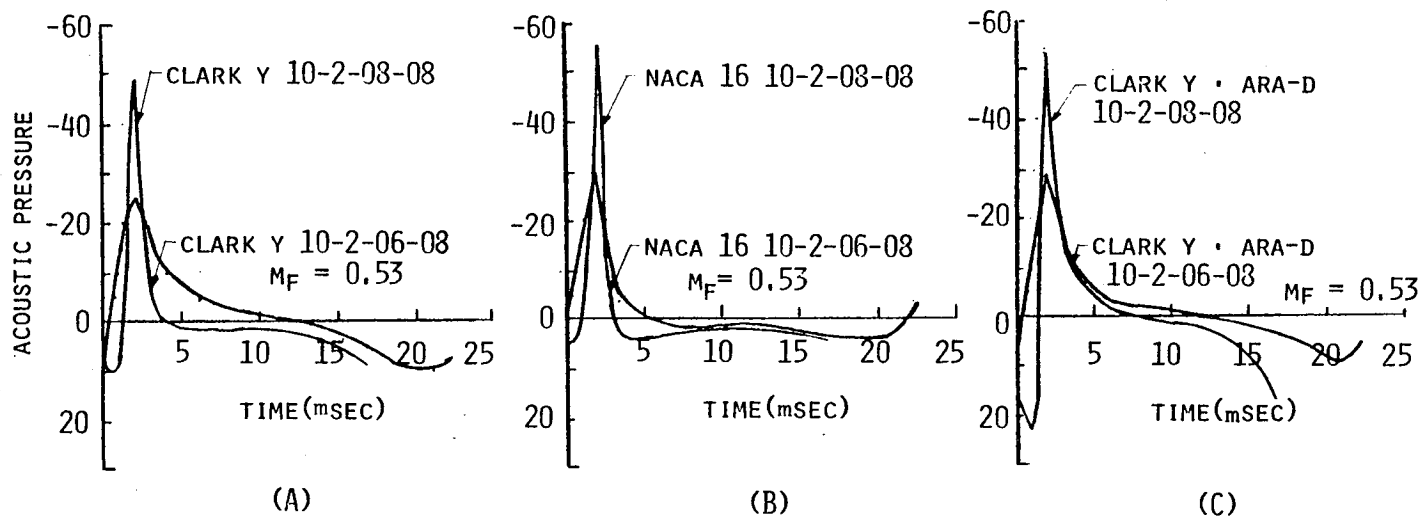Figure 18.- Far-field acoustic pressure signature. Effect of thickness.

Figure 19.- Near-field acoustic pressure signature. Effect of tip Mach number.

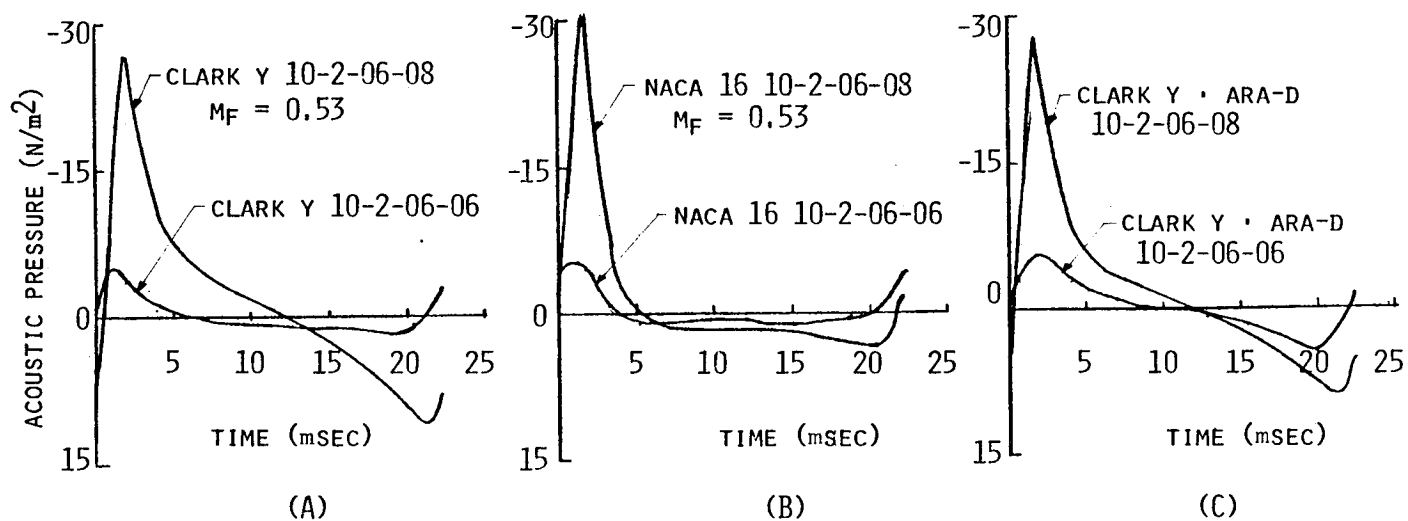Figure 20.- Near-field acoustic pressure signature. Effect of forward Mach number.

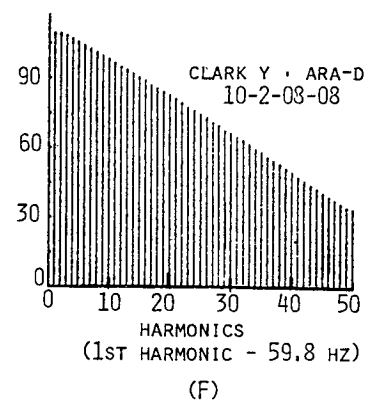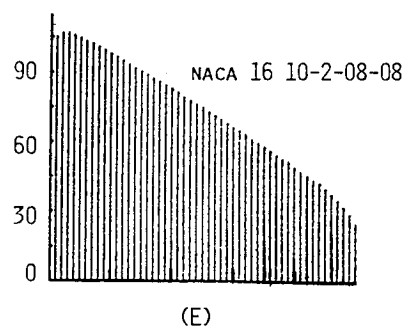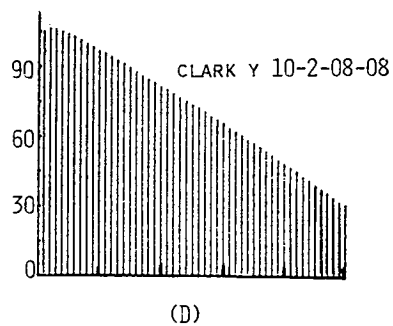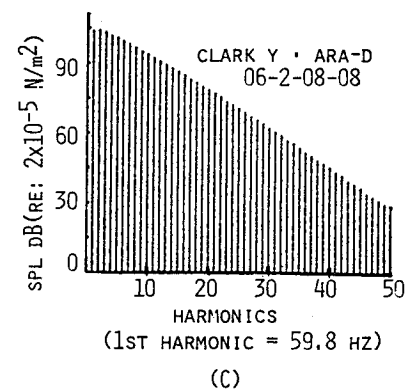Figure 21.- Near-field acoustic pressure signature. Effect of forward Mach number.
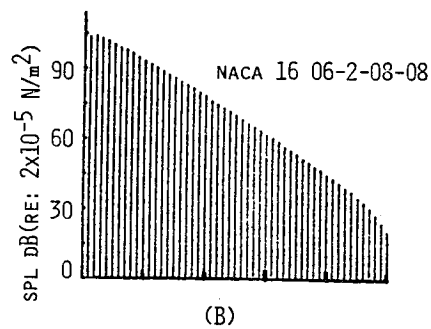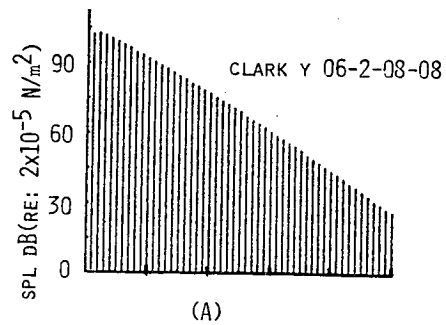
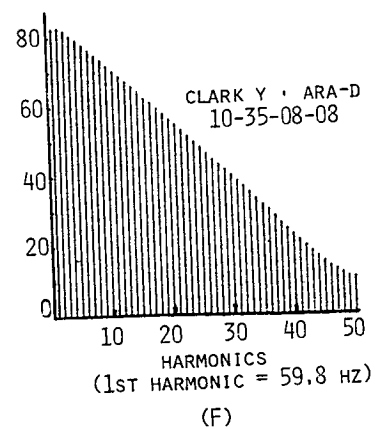Figure 22.- Near-field acoustic pressure spectrum. Effect of thickness.
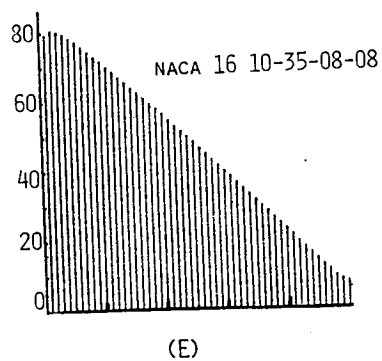
Figure 23.- Far-field acoustic pressure spectrum.   Effect of thickness.

SPL dB(RE: 2x10^{-5} N/m^2)

CLARK Y 10-2-06-08
M_F = 0.53

10   20   30   40   50
(A)

NACA 16 10-2-06-08
M_F = 0.53

10   20   30   40   50
(B)

CLARK Y · ARA-D
10-2-06-08
M_F = 0.53

10   20   30   40   50
HARMONICS
(1ST HARMONIC = 44.851 HZ)
(C)

CLARK Y 10-2-06-06

10   20   30   40   50
(D)

NACA 16 10-2-06-06

10   20   30   40   50
(E)

CLARK Y · ARA-D
10-2-06-06

10   20   30   40   50
HARMONICS
(1ST HARMONIC = 44.851 HZ)
(F)
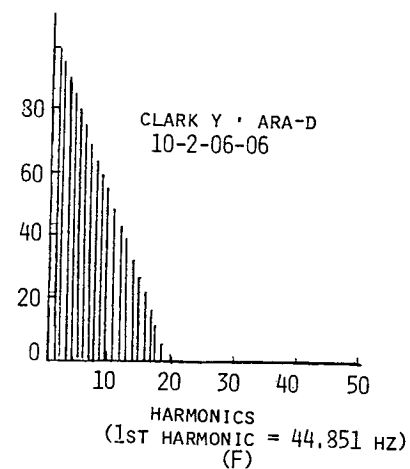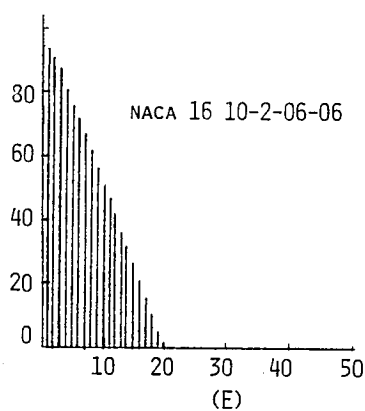
Figure 24.- Near-field acoustic pressure spectrum. Effect of forward Mach number.

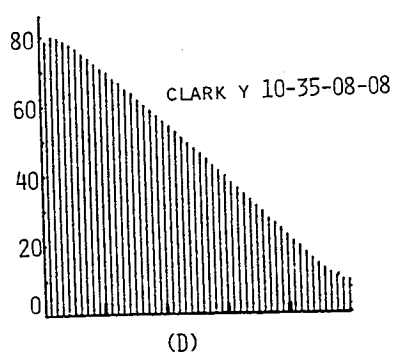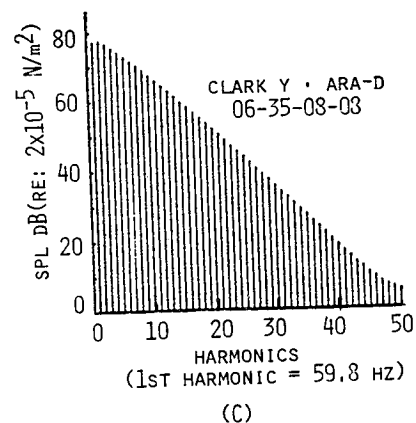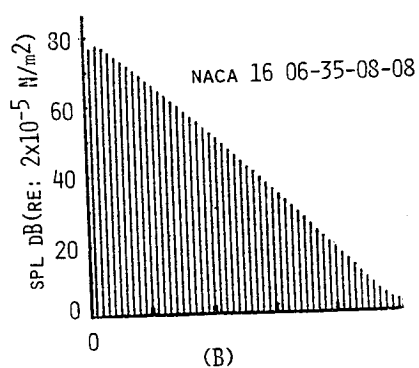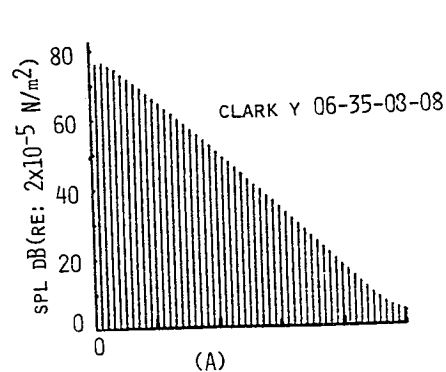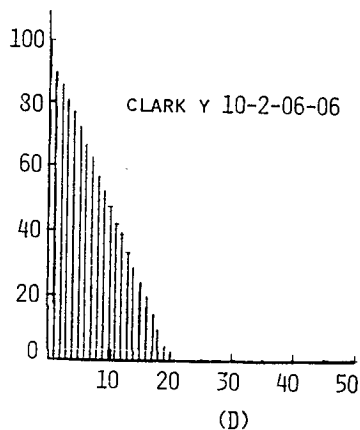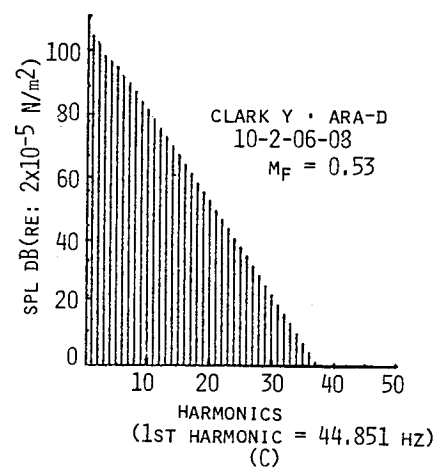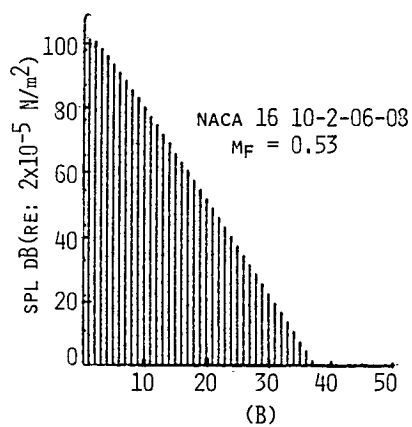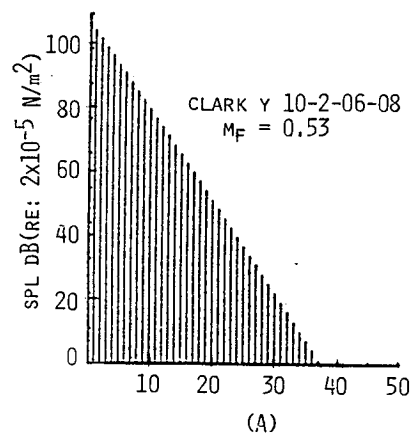# AIRFOIL CONSIDERATIONS FOR FANS, COMPRESSORS AND PROPELLERS

Henry V. Borst
Henry V. Borst & Associates

INTRODUCTION

With known two-dimensional airfoil characteristics, the performance of any lifting or propulsion system can be determined providing proper account is taken of the differences between the two- and three-dimensional flow conditions. The change between two- and three-dimensional flow conditions has been found by theoretical means for wings, so that it is generally possible to calculate the performance of any wing using two-dimensional airfoil data. However, for fans, axial flow compressors and propellers the changes between two- and three-dimensional conditions at any given station can only be found for propellers. Thus, only in the case of propellers can performance be determined using two-dimensional airfoil data. The performance of axial flow fans and compressors is found based on the use of cascade airfoil data to account for the induced losses and the mutual blade interference effects. Thus, for lifting and propulsion type rotors, the use of two-dimensional airfoil data has been restricted to helicopters and propellers. As a result of limited application of propellers there has been little need for the high-cambered airfoil data, such as used on propeller blades.

Although two-dimensional airfoil data has only been used as a basis for calculating performance and conducting design studies of propellers, the procedure has been very effective and accurate. Excellent agreement between test and calculated data has been achieved, as illustrated on figures 1 and 2. The agreement between the calculated and test thrust distribution for the propeller, for instance, is excellent, figure 1. The variation of efficiency with power is also calculated with good accuracy as is illustrated on figure 2. In general, the efficiency of propellers is calculated within ± 2 to 3% using two-dimensional airfoil data for finding the lift and profile drag characteristics at each blade station.

Although axial flow fans and compressors operate in a manner similar to a propeller, the methods for their design and analysis are quite different. Generally, cascade airfoil data are used for the analysis of fans and compressors, rather than two-dimensional airfoil data. The cascade data used includes many of the three-dimensional effects calculated by theory for propellers and, thus, it becomes difficult to separate out the true characteristics of the airfoils used. Further, two-dimensional cascade airfoil data are expensive and difficult to run, as it is necessary to test a wide range of parameters to obtain sufficient data for the design of axial flow fans and compressors. As a result, for instance, low solidity fans became difficult to analyze because of the lack of suitable test data. For these reasons and the success of the use of two-dimensional airfoil data in the design of propellers, a study was undertaken to

determine if the three-dimensional flow changes encountered with axial flow fans and compressors could be determined. If this were possible, two-dimensional airfoil data could then be used for the design and analysis of axial flow compressors and fans. If such a procedure could be developed, far more two-dimensional airfoil test data should be obtained than is normally run for the design of aircraft wings and helicopters, as axial flow compressors incorporate blade sections with very high design lift coefficients.

As propellers, axial flow fans and compressors operate in a similar manner, it would appear that the same approach could be used for the application of two-dimensional airfoil data in calculating performance. The propeller theory is, therefore, reviewed to provide a foundation for a unified theory that would apply to fans and axial flow compressors as well.

SYMBOLS

Values are given in both SI and U.S. Customary Units. Measurements and calculations were made in U.S. Customary Units.

A_1	area
B	blade number
c	blade chord, cm (ft)
C_D	drag coefficient
C_L	lift coefficient
C_Q	torque coefficient $= Q/\rho n^2 D^5$
C_T	thrust coefficient $= T/\rho n^2 D^4$
D	rotor or propeller diameter, cm (ft)
J	advance ratio $= V/nD$
$K(x)$	circulation function
m	mass flow
n	rotational speed, rps
P	pressure, N/m^2 (psi)
Q	torque, N-m (lb-ft)
q	$\frac{1}{2}\rho V^2$, N/m^2 (psi)

R	rotor or propeller radius, cm (ft)
r	blade station radius, cm (ft)
T	thrust, N (lb)
V	axial velocity, m/sec (ft/sec)
W_1	relative inlet velocity to rotor blade, m/sec (ft/sec)
W_m	relative mean velocity to rotor blade, m/sec (ft/sec)
w'	displacement velocity, m/sec (ft/sec)
$\bar{w}$	w/V
x	fractional blade radius $= r/R$
α	angle of attack
α_i	induced angle of attack
β_1	inlet angle
β_2	exit angle
β_m	mean angle of inlet and exit
γ	$\tan^{-1} C_D/C_L$
$\Gamma(x)$	strength of circulation
Δv	change in rotational velocity
ϕ	true wind angle, degrees
ϕ_o	apparent wind angle
λ	pitch of final wake $= V + (w/\pi n D_w)$
ρ	fluid density, kg/m^3 (slugs/ft^3)
σ	rotor solidity $= cB/\pi x D$

Subscripts:

w	wake

VORTEX THEORY OF PROPELLERS

The vortex theory of propellers as developed by Goldstein and refined by Theodorsen, references 1 and 2, has made possible the use of two-dimensional airfoil data for calculating performance. With this theory the two-dimensional vector is found knowing the three-dimensional velocity vector, W_o, and the induced velocity, w', due to the dimensional effects, figure 3. The induced velocity vector is calculated based on the loading developed on the blade section, the blade number and the advance ratio. In this method, the spanwise loading is assumed to be optimum and is specified for the entire blade for any given station loading.

Based on the given blade angle setting and the two-dimensional velocity vector as determined above, the equivalent two-dimensional angle of attack can be found from which the lift and drag can be determined from two-dimensional airfoil data. Because the velocity vector is a function of the lift, it is necessary to iterate to find the true operating lift coefficient. Once the true operating lift and drag vectors are determined, the thrust force and torque are obtained by a resolution of the forces as shown on figure 3.

Using the concept of the displacement velocity, w, which with the rotational and axial velocity vectors describes the pitch of the final wake of the vortices shed by the propeller, the relative loading at each blade station can be determined from the equation as derived by Theodorsen, reference 2:

$$\sigma\,C_L = \frac{1 + \bar{w}}{(1+\tfrac{1}{2}\bar{w})(1+\tfrac{1}{2}\bar{w}\,\cos^2\phi)}\,2\bar{w}K(x)\frac{\sin^2\phi}{\cos\phi} \qquad (1)$$

The circulation function $K(x)$ is a function of the relative blade station, x, blade number and the advance ratio of the final wake as illustrated for a three-blade propeller on figure 4. In equation (1) it should be noted that the true wind angles are measured at the propeller disk and it is assumed the displacement velocity in the final wake is equal to $\tfrac{1}{2}$w at propeller disk.

DUCTED FANS

The theory for calculating three-dimensional effects of ducted fans can also be handled in the same way as open propellers. The main difference between the two is the effect of the duct and how it influences the magnitude of the change between the two- and three-dimensional relative velocity vectors at each blade station.

Following the theory of propellers by Theodorsen, Gray and Wright, references 2 through 5, assume an optimum load distribution between the rotor and duct, and set up conditions in the final wake so that the circulation function could be calculated. This was done by replacing the duct with vortices with

sufficient strength so that the radial flow at the duct wall is zero. Then, based on the conditions in the final wake, the circulation function K(x) was calculated for ducted propellers with 2 to 12 blades for a range of advance ratios. An example of the variation of K(x) with the wake advance ratio is given on figure 5. A comparison of K(x) for open and ducted propellers is given on figure 6. Note how the duct allows a finite value of K(x) to be supported at the blade tip.

Like an open propeller, the variation of the loading parameter σC_L can be determined knowing the circulation function and the advance ratio in the final wake. To do this it is necessary to convert the conditions in the final wake to those at the fan disk. Consider the velocity diagram of a ducted fan as illustrated on figure 7. The shape of the duct is assumed to be such that the velocity on the upstream side of the fan, station 1, is equal to the free stream velocity. Due to the expenditure of power, the fan is rotated and the blade sections develop lift. The lift force reacts on the airstream causing an increase of pressure from station 1 to 2, with no change in the axial velocity component since the area of the duct does not change. The lift force does react on the airstream to increase the rotational velocity component by Δv at station 2. At the duct exit station 3, the velocity expands so that in the fan wake where the pressure returns to free stream on the ambient pressure, the velocity change is equal to u. The displacement velocity with the axial and rotational components determine the pitch of the wake from which the circulation function K(x) is determined, such as in figure 5.

From the definition of the circulation function, the strength of the circulation can be expressed by the equation

$$\Gamma = \frac{K(x)(V+w)w}{Bn} \tag{2}$$

Referring to the mean velocity vector relative to the airfoil, W_m, as the velocity representing two-dimensional conditions, the lift per unit span produced by the airfoil equals

$$L = C_L \tfrac{1}{2}\rho W_m^2 c = \rho \Gamma W_m \tag{3}$$

so

$$\Gamma = C_L \tfrac{1}{2} W_m c \tag{4}$$

From equations 3 and 4 and the definitions $\sigma = Bc/\pi n D$ and $\bar{w} = w/V$

$$\sigma C_L = \frac{2K(x)(1+\bar{w})w}{\tan\beta_1 \, W_m} \tag{5}$$

For the case of an infinite number of blades, Theodorsen, reference 2, shows that the circulation function is equal to

$$K(x) = \frac{x^2}{x^2+\lambda^2} = \cos^2\phi_w = \sin^2\beta_{2w} \tag{6}$$

A comparison of $K(x)$ for an infinite blade number with that calculated by Wright and Gray for a 12-blade ducted propeller showed little difference. Thus, assumming for the moment that the $K(x)$ given in equation (6) can be used, equation (5) becomes

$$\sigma\, C_L = \frac{2\sin^2\beta_{2w}(1+\bar{w})\bar{w}\,\cos\beta_m}{\tan\beta_1} \tag{7}$$

Referring to figure 7

$$\tan\beta_2 = \frac{\pi nDx - \Delta v}{V_1} = \frac{\pi nDx}{V_1} - \bar{w}\,\sin\beta_{2w}\,\cos\beta_{2w} \tag{8}$$

$$\tan\beta_1 = \frac{\pi nDx}{V_1} \quad ; \quad \tan\beta_{2w} = \frac{\pi nDx}{V_1(1+\bar{w})} = \frac{\tan\beta_1}{1+\bar{w}} \tag{9}$$

so

$$\bar{w} = \frac{\tan\beta_1 - \tan\beta_2}{\sin\beta_{2w}\cos\beta_{2w}} \tag{10}$$

Substituting these relations in equation (7) we obtain

$$\sigma\, C_L = 2\cos\beta_m(\tan\beta_1 - \tan\beta_2) \tag{11}$$

Equation (11) can be corrected to account for blade number by multiplying it by the ratio of the circulation functions for a finite blade number to an infinite blade number; thus,

$$\sigma\, C_L = 2\cos\beta_m(\tan\beta_1 - \tan\beta_2)\frac{K(x)}{K(x)} \tag{12}$$

Equation (12) now makes possible the calculation of the performance of ducted propellers using theory to find the two-dimensional velocity vector and two-dimensional airfoil data for finding the lift and drag characteristics. In applying the two-dimensional airfoil data to the ducted fan, the effects of the change in the slope of the lift curve due to high values of solidity must be included as well as any drag increase due to interference. Also, in the application of equation (12) it should be noted that only conditions directly upstream and downstream of the rotor need to be considered.

In the case of an axial flow compressor, it is necessary to know the three-dimensional conditions at the disk to apply two-dimensional airfoil data. Since the duct would influence the rotor in the same manner as in the case of the ducted fan, it would appear that equation (12) would also apply to an axial flow compressor. As cascade airfoil data is generally used to calculate the performance of axial flow compressors and these data include both two- and three-dimensional effects, a study was undertaken to determine if the two-dimensional effects could be separated out and an equation similar to equations (11) or (12) be developed. Then, as in the case of propellers and ducted fans, the performance could be calculated based on two-dimensional airfoil data with any modifications necessary to include interference effects.

Basic Theoretical Considerations

As shown on figure 8, the flow conditions of a cascade are identical to the rotor; the flow is turned through an angle $\Delta\beta$ and the inlet and exit velocities in each case are W_1 and W_2. Assuming the duct has a constant area in the axial direction, the relative velocity can only change in the rotational direction since continuity must be maintained. As a result, the lift and drag forces on the airfoil are partly reacted by a velocity change and partly by a pressure change. If the flow were allowed to expand, the pressure rise across the cascade and rotor results from the lift and drag forces, which also give the flow a rotational velocity component.

In the cascade tunnel the forces on the blade sections can be related to the measured turning angle $\Delta\beta$ using the momentum equation, since the mass flow is known based on the inlet conditions. Thus, the mass flow in the tunnel is

$$m = \rho A_1 W_1 \tag{13}$$

By the momentum equation, the mass flow times the change in velocity in the torque direction is equal to the resultant forces on the blades, figure 8:

$$\rho A_1 W_1 \Delta v = R \cos(\beta_m - \gamma) \tag{14}$$

The angle β_m is the angle of the mean velocity vector W_m. This velocity vector is considered to be the true velocity of the two-dimensional airfoil section with the lift measured normal to W_m. The lift and drag coefficients are, therefore, based on $q_m = \frac{1}{2}\rho W^2_m$.

The force vector R' includes the profile drag force, so

$$R' = L/\cos\gamma \tag{15}$$

and

$$\rho A_1 W_1 \Delta v = L \cos(\beta_m - \gamma)/\cos\gamma \tag{16}$$

At any given station, x, on the rotor the equivalent cascade area is

$$A_1 = \pi \, xD \Delta xR \, \cos\beta_1 \tag{17}$$

Now, as indicated on figure 8

$$\sin\beta_1 = \pi nDx/W_1 \quad \text{and} \quad \sin\beta_2 = (\pi nDx - \Delta v)/W_2$$

so

$$\Delta v = W_1 \sin\beta_1 - W_2 \sin\beta_2 \tag{18}$$

Combining equations (16), (17) and (18) and letting

$$L = C_L \frac{\rho}{2} W^2_m Bc \Delta xR \quad \text{and} \quad \sigma = \frac{Bc}{\pi \, xD}$$

the expression is obtained for the loading parameter σC_L

$$\sigma C_L = \frac{2\cos\gamma \, \cos\beta_1 W_1^2 (\sin\beta_1 - \cos\beta_1 \tan\beta_2)}{W_m^2 \cos(\beta_m - \gamma)} \tag{19}$$

Since

$$W_m = W_1 \cos\beta_1 / \cos\beta_m \tag{20}$$

Equation (19) becomes

$$\sigma C_L = \frac{2\cos^2\beta_m \cos\gamma(\tan\beta_1 - \tan\beta_2)}{\cos(\beta_m - \gamma)} \tag{21}$$

For the case of zero drag, $\gamma = 0$ and equation (21) reduces to

$$\sigma C_L = 2 \cos\beta_m(\tan\beta_1 - \tan\beta_2) \tag{22}$$

Equation (22) is identical to equation (11) developed on the basis of propeller theory for a ducted fan with an infinite blade number.

Theoretical vs Test Cascade Data Comparisons

Based on the concept that the induced angle α_i can be expressed as

$$\alpha_i = (\beta_1 - \beta_2)/2 \tag{23}$$

and β_m as

$$\beta_m = \beta_1 - \alpha_i \tag{24}$$

248

then the variation of σC_L as a function of the induced angle of attack α_i was calculated from equation (22) for inlet angles β_1 of 30, 45, 60 and 70 degrees. The results of these calculations are compared with the cascade test data for NACA 65 series sections, reference 6, operating below the stall and indicate excellent agreement as illustrated on figure 9 for cases of $\beta_1 = 45^o$. Plotted in this form, the cascade test data is reduced to lines that are only a function of the solidity as the effect of camber is essentially zero. It should be noted that data for variations of design C_L from 0 to 2.7 are included on these plots. To obtain the proper comparison it was necessary to convert the lift coefficient given in reference 5 to the value based on the lift defined normal to W_m and a q corresponding to W_m. The C_L given in reference 5 was defined as normal to the vector W_m with the q based on W_1.

The comparison of the variation of σC_L vs the induced angle of attack, illustrated on figure 9, is for the case of zero drag at all solidities except $\sigma = 1.5$. In this case, the drag is included in the test data to show its effect. At a given induced angle of attack the drag vector decreases the σC_L or increases the turning angle, so the change in the apparent induced angle and that calculated using equation (22) is equal to

$$\Delta\alpha_i = \frac{\gamma}{2} = \tfrac{1}{2}\tan^{-1}C_D/C_L \tag{25}$$

The close agreement between the calculated values of σC_L calculated using equation (22) and the measured quantities from cascade data shows the induced angle is a reliable measure of the three-dimensional effects. This would indicate that two-dimensional airfoil data can also be applied to calculate the performance of axial flow compressors as long as proper account is taken of any drag increase due to interference between airfoils operating in a cascade.

INTERFERENCE EFFECTS

It is well known, references 7 and 8, that in the case of cascades of airfoils with a high solidity there are blockage and interference effects that increase the drag, reduce the slope of the lift curve, reduce the maximum lift coefficient, and in some cases change the angle of zero lift. Theoretical methods are available for calculating the change in the lift curve slope due to the cascade effects. However, comparisons of these theoretical results with results from test data indicate that the agreement is only poor to fair. For this reason it is necessary to use cascade test data for estimating the slope of the lift curve of the airfoils. The operating lift coefficient can then be found at the two-dimensional angle of attack corresponding to the same angle found knowing the blade setting angle, inlet angle and induced angle of attack, calculated using equation (12).

At solidities of the order of 0.5 the drag variation with lift for isolated airfoils is in good agreement with the cascade test results of reference 6, considering the differences in Reynolds number between the two sets of tests. With an increase of solidity of the cascade above 0.5, the available test data

indicates the drag coefficient increase due to blade interference is of the order of 0.003 to .0035. This drag coefficient change is encountered when the solidity of the cascade is between 0.5 and 1.5 and the airfoils are operating below stall. Although this change does not appear to be large, it is of the order of one-third to one-half of the profile drag coefficient of the section and, therefore, must be considered when calculating the performance.

COMPARISONS WITH TEST

A comparison of the test and calculated performance of a 12-blade axial flow compressor rotor of reference 9 is given on Table 1. This rotor was designed with a pressure ratio of 1.15 and has a tip solidity of 0.5, which increases to approximately 1.0 at the rotor hub. The comparison of the test and calculated performance indicates that the methods described predict the performance with good accuracy when the blades are operating in the unstalled region. Comparisons with other test data show similar results, indicating that the theoretical procedures for applying two-dimensional airfoil data to find the performance of propellers also can be used for the analysis of ducted fans and low solidity axial flow compressor rotors.

CONCLUDING REMARKS

A unified theory and method of analysis has been developed which is suitable for calculating the performance of axial flow rotors operating with or without a duct. This analysis method applies for solidities up to 1.5, and so covers the range of rotors between that of propellers and axial flow compressors. Using the procedure of analysis, the induced losses are identified and can be calculated by theory. This allows the use of two-dimensional airfoil data with corrections for mutual blade interference to be used for calculating performance. The methods of analysis developed are suitable for finding the performance over the entire operating range, as well as at the rotor's design condition. The methods developed can also be applied for the design and analysis of prerotation and stator vanes. Good agreement between the test and calculated performance has been obtained. Further work is necessary to extend the range of operation where the methods of analysis apply. To do this, additional two-dimensional airfoil data are needed, particularly data for airfoils operating with high design lift coefficients of the type used in axial flow compressors.

REFERENCES

1. Goldstein, Sydney: On the Vortex Theory of Screw Propellers. Proceedings of the Royal Society Of London, Ser. AV123, 1929.

2. Theodorsen, T.: Theory of Propellers. McGraw-Hill Book Company, 1948.

3. Wright, T.: Determination of the Design Parameters for Optimum Heavily-Loaded Ducted Fans. Georgia Institute of Technology, Report 69-3, Nov. 1969.

4. Gray, Robin B. and Wright, Terry: A Vortex Wake Model for Optimum Heavily-Loaded Ducted Fans. Journal of Aircraft, Vol. 7, No. 2, 1970.

5. Wright, Terry: Evaluation of the Design Parameters for Optimum Heavily-Loaded Ducted Fans. Journal of Aircraft, Vol. 7, No. 6, 1970.

6. Emery, J.C., et al.: Systematic Two-dimensional Cascade Tests of NACA 65-Series Compressor Blades at Low Speeds. NACA TR 1368, 1958.

7. Wallis, R. A. and Aust, F. I. E.: A Rationalized Approach to Blade Element Design, Axial Flow Fans. Institute of Engineers, Australia Conference on Hydraulic and Fluid Mechanics, 1968. Paper No. 2599.

8. Bullock, R. O. and Johnsen, I. A.: Aerodynamic Design of Axial-Flow Compressors. NASA SP-36, 1965.

9. Osborn, W. M. and Steinke, R. J.: Performance of a 1.15 Pressure Ratio Axial-Flow Fan Stage With a Tip Blade Solidity of 0.5. NASA TM X-3052, 1974.

TABLE 1. – COMPARISON OF TEST AND CALCULATED ROTOR PERFORMANCE OF REFERENCE 9

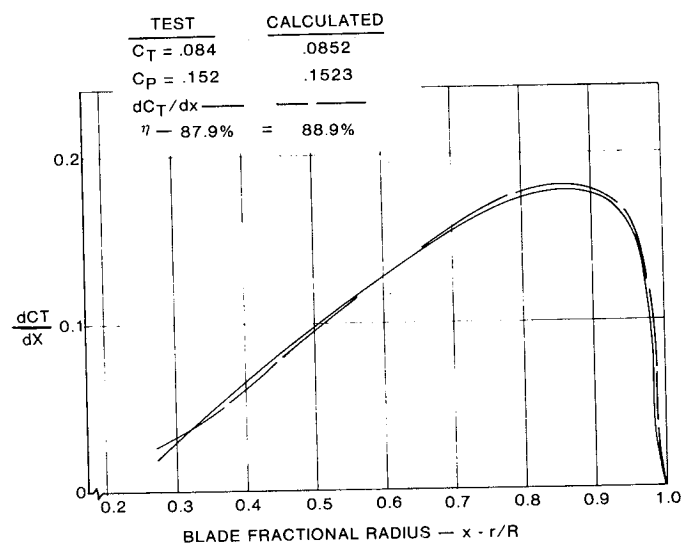| % Design Speed	Run No.	Test C_P	Test C_T	Cal C_P	Cal C_T	Test/Cal $C_T/C_P/C_T/C_P$
100	1532	1.837	.4491	1.894	.5838	0.793
	1400	2.255	.7807	2.237	.7730	1.002
	1402	2.357	.8664	2.348	.8588	1.005
	1404	2.393	.9073	2.408	.9211	0.991
	1405	2.448	.8139	2.392	.9317	0.854
90	1540	1.859	.4302	1.641	.4733	0.802
	1411	2.055	.7602	2.184	.7488	1.079
	1412	2.201	.8445	2.320	.8330	1.068
	1413	2.309	.9101	2.422	.9144	1.044
	1415	2.391	.9331	2.423	.9796	0.965
110	1533	1.725	.4383	2.079	.6778	0.779
	1534	2.180	.7038	2.232	.7687	0.938
	1418	2.329	.8524	2.322	.8380	1.014
	1420	2.505	.9538	2.406	.9091	1.008
	1421	2.479	.9300	2.391	.9365	0.958

Figure 1.- Comparison of test vs. calculated load distribution.
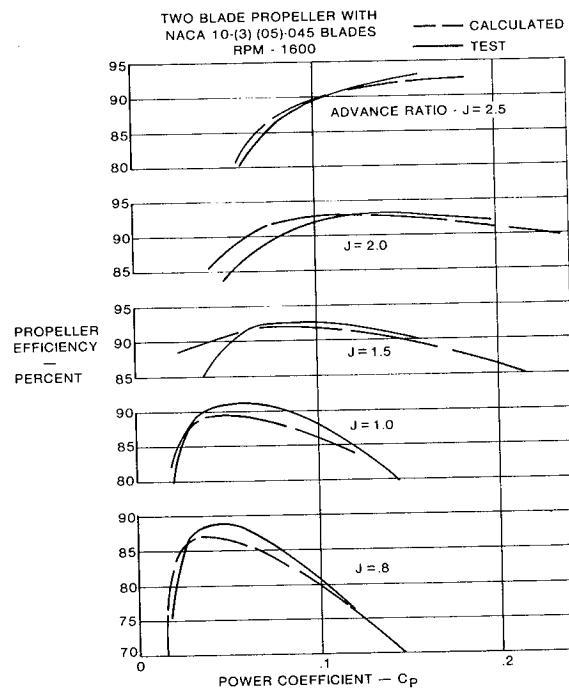
Figure 2.- Propeller calculated data vs. test efficiency.

dQ/r = SECTION TORQUE
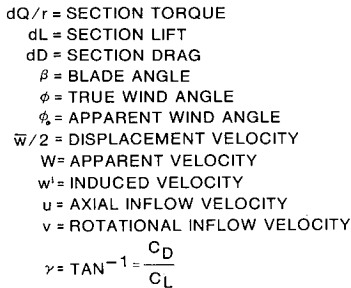dL = SECTION LIFT
dD = SECTION DRAG
β = BLADE ANGLE
ϕ = TRUE WIND ANGLE
ϕ_a = APPARENT WIND ANGLE
$\bar{w}/2$ = DISPLACEMENT VELOCITY
W = APPARENT VELOCITY
w' = INDUCED VELOCITY
u = AXIAL INFLOW VELOCITY
v = ROTATIONAL INFLOW VELOCITY

$$\gamma = TAN^{-1} = \frac{C_D}{C_L}$$

Figure 3.- Propeller velocity and force diagram. Single rotation propellers.

$$\sigma C_L = \frac{1 + \bar{w}}{(1 + 1/2\,\bar{w})(1 + 1/2\bar{w}\,COS^2\,\phi\,)} \; 2\bar{w}K(x) \; \frac{SIN^2\,\phi}{COS\phi}$$

WAKE ADVANCE RATIO — $J(1 + \bar{w})$
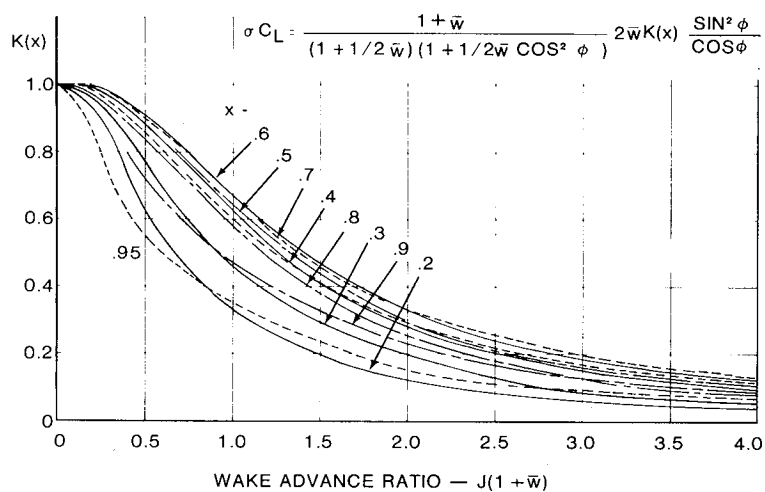
Figure 4.- Circulation function K(x) vs. wake advance ratio for a three-blade open propeller.

254

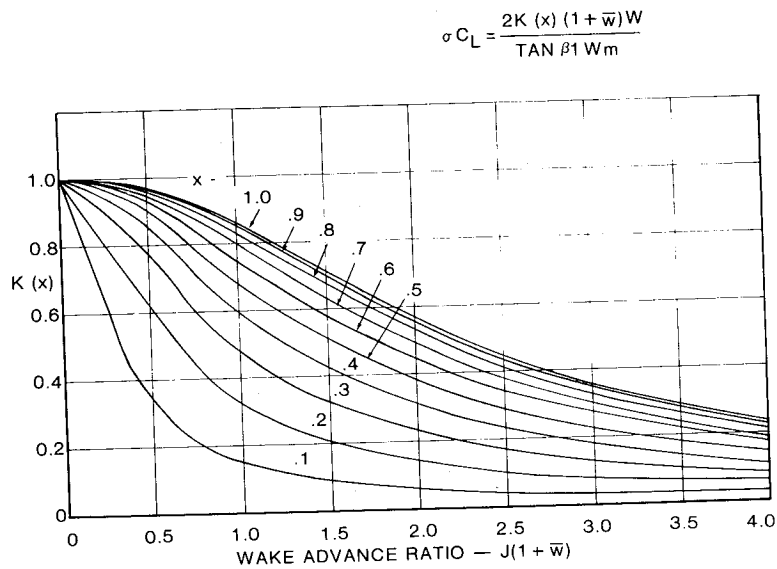$$\sigma C_L = \frac{2K(x)(1+\overline{w})W}{TAN\ \beta1\ Wm}$$

Figure 5.- Circulation function K(x) vs. wake advance ratio for a three-blade ducted propeller.
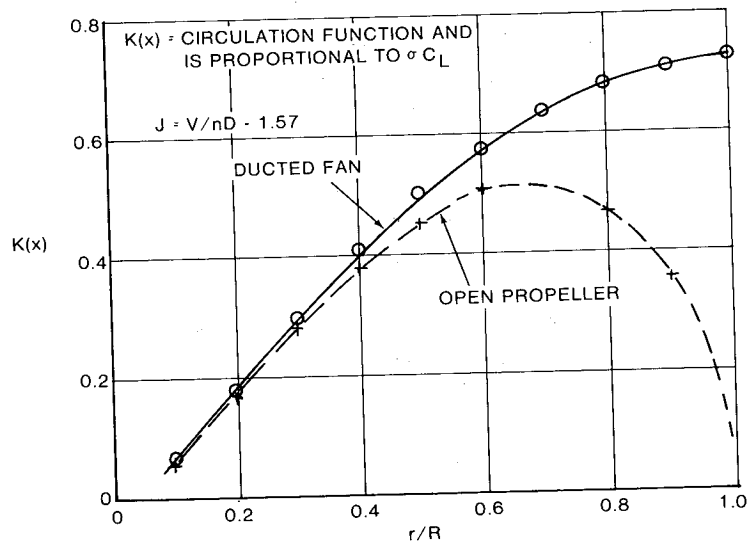

Figure 6.- Comparison of the load distribution of a ducted fan and an open propeller.
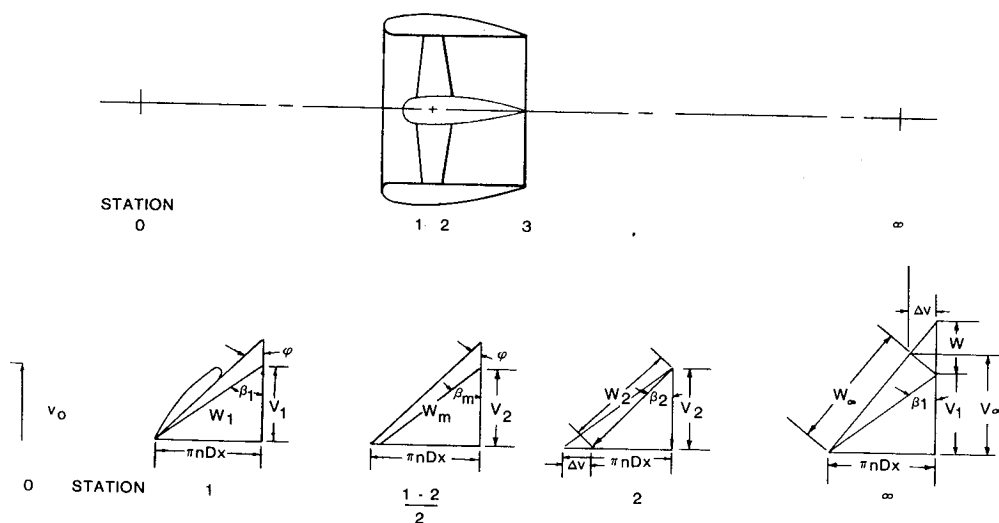
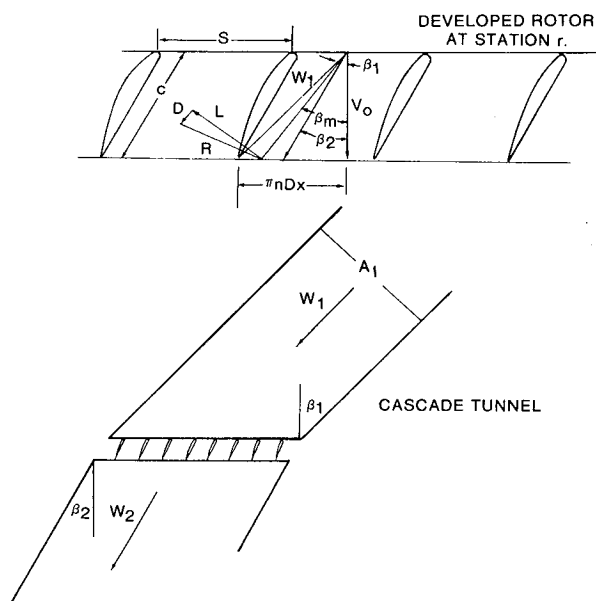Figure 7.- Velocity triangles for ducted fans.

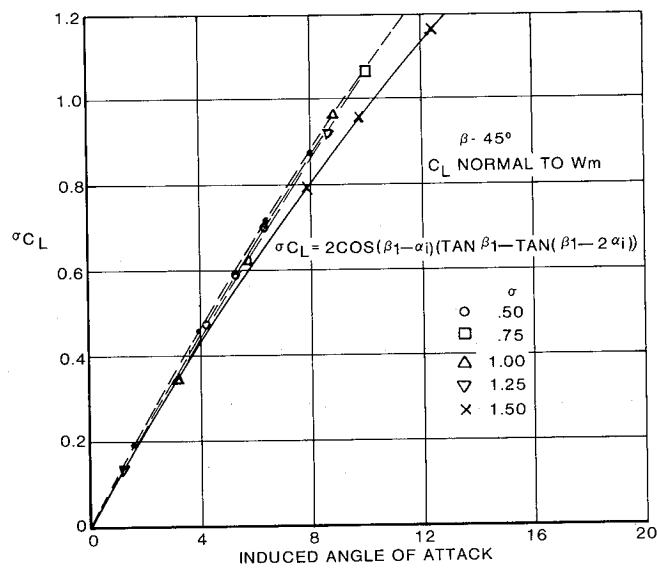Figure 8.- Duplication of the flow through a rotor using a cascade of airfoils.

Figure 9.- Blade-section loading parameter vs. induced angle of attack. Inlet angle, 45°.

1. Report No. NASA CP-2046	2. Government Accession No.	3. Recipient's Catalog No.
4. Title and Subtitle ADVANCED TECHNOLOGY AIRFOIL RESEARCH - VOLUME II		5. Report Date March 1979
		6. Performing Organization Code
7. Author(s)		8. Performing Organization Report No. L-12232
9. Performing Organization Name and Address NASA Langley Research Center Hampton, VA 23665		10. Work Unit No. 505-06-33-10
		11. Contract or Grant No.
12. Sponsoring Agency Name and Address National Aeronautics and Space Administration Washington, DC 20546		13. Type of Report and Period Covered Conference Publication
		14. Sponsoring Agency Code

15. Supplementary Notes
   Conference held at NASA Langley Research Center, Hampton, Va.,
   March 7-9, 1978.

16. Abstract

This compilation contains papers presented at the NASA Conference on Advanced
Technology Airfoil Research held at Langley Research Center on March 7-9, 1978,
which have limited distribution. This conference provided a comprehensive review
of all NASA airfoil research, conducted in-house and under grant and contract. A
broad spectrum of airfoil research outside of NASA was also reviewed. The major
thrust of the technical sessions were in three areas: development of computational
aerodynamic codes for airfoil analysis and design, development of experimental
facilities and test techniques, and all types of airfoil applications. In addition,
results of technical workshops were presented at a concluding roundtable discussion.

17. Key Words (Suggested by Author(s)) Aerodynamic theory Airfoils, multielement Supercritical airfoils Rotorcraft airfoils General aviation, low speed	Aerodynamics Airfoils Airfoil design High lift Wind turbines Propellers		
19. Security Classif. (of this report) Unclassified	20. Security Classif. (of this page) Unclassified	21. No. of Pages 263	22. Price